Interaction of Transition Metal Adatoms and Dirac Materials investigated by Scanning Tunneling Microscopy and X-ray Magnetic Circular Dichroism

Dissertation zur Erlangung des Doktorgrades
am Fachbereich Physik
der Universität Hamburg

vorgelegt durch
Dipl.-Phys. Thomas Eelbo

Hamburg
2013

Gutachter der Dissertation:
Prof. Dr. Roland Wiesendanger
Prof. Dr. Ulrich Merkt
Gutachter der Disputation:
Prof. Dr. Roland Wiesendanger
Prof. Dr. Kornelius Nielsch
Datum der Disputation:
24.01.2014
Vorsitzender des Prüfungsausschusses:
PD Dr. Michael Martins
Vorsitzender des Promotionsausschusses:
Prof. Dr. Peter Hauschildt
Dekan der MIN-Fakultät:
Prof. Dr. Heinrich Graener
Leiterin des Fachbereichs Physik:
Prof. Dr. Daniela Pfannkuche

Zusammenfassung

In der vorliegenden Arbeit wurden zwei neuartige Materialklassen, Graphen und topologische Isolatoren, untersucht. Diese wurden mit Einzeladsorbaten und Nanostrukturen der Übergangsmetalle Fe, Co und Ni kombiniert. Die Wahl begründet sich durch deren hohe technologische Relevanz, basierend auf ihren ferromagnetischen Eigenschaften. Die Studien umfassten sowohl experimentelle Methoden, vornehmlich die Rastertunnelmikroskopie und die Röntgenspektroskopie, als auch theoretische Berechnungen. Die Ergebnisse erlauben wesentliche Rückschlüsse auf die elektronischen und magnetischen Eigenschaften der Adatome, bzw. deren Auswirkungen auf das jeweilige Substrat.

Graphen ist eine monatomar dicke, flexible und ungemein belastbare Struktur, die aus Kohlenstoffatomen aufgebaut ist. Es weist besondere elektronische Eigenschaften auf (z.B. hohe elektrische Leitfähigkeiten), die aus der Bindung der C-Atome untereinander resultieren. Es wurden zwei verschiedene Graphen-Typen auf einem SiC Substrat präpariert und untersucht.

In der ersten Studie wurde die Entkopplung des Graphens durch eine zusätzliche Kohlenstofflage erreicht (Graphen/SiC). In diesem Fall wurden einzelne spezifische Adsorptionspositionen für Co und Ni Atome, sowie paramagnetisches Verhalten für Fe und Co aufgedeckt. Im Gegensatz dazu sind Ni-Cluster nichtmagnetisch, solange sie aus maximal vier Atomen bestehen. In der zweiten Studie wurde die Entkopplung durch eine Wasserstoff-Passivierung erreicht (quasi-freistehendes Graphen/SiC), was zu überraschend stark abweichenden Ergebnissen führte. In diesem Fall wurden für Co und Ni Atome zwei simultan existierende Adsorptionspositionen beobachtet. Das weist auf einen wesentlichen Einfluss des unterliegenden Substrats hin, der für eine realistische Beschreibung beachtet werden muss.

Topologische Isolatoren zeigen ebenfalls sehr ungewöhnliche elektronische Eigenschaften. Optimalerweise weisen dreidimensionale Kandidaten keine Leitfähigkeit im Inneren auf. Allerdings besitzen sie leitfähige spin-polarisierte Oberflächenzustände.

Für Co Atome auf einem Bi_2Se_3 Substrat wurden zwei verschiedene Adatomarten, gebunden in der fcc/hcp Position, gefunden. Eine Vorzugsrichtung der magnetischen Momente parallel zur Oberfläche wurde beobachtet. Bei höherer Bedeckung drehte die gemittelte Ausrichtung senkrecht zur Oberfläche. In diesem Fall wird ein erheblicher Einfluss auf die Oberflächenzustände erwartet, welcher aber nicht detektiert wurde. Die letzte Untersuchung befasste sich mit Fe Adsorbaten auf Bi_2Te_3. In diesem Fall wurden ebenfalls zwei verschiedene Sorten der Atome gefunden, wiederum adsorbiert in der fcc/hcp Position. Deren magnetische Momente zeigten schon für geringste Bedeckungen eine starke uniaxiale Anisotropie, senkrecht zur Oberfläche. Allerdings wurden die erwarteten Auswirkungen auf die Eigenschaften des topologischen Isolators auch in diesem Fall nicht detektiert.

Abstract

In the work at hand two novel classes of materials, graphene and topological insulators, were investigated. These were combined with single adsorbates and nanostructures of the transition metals Fe, Co, and Ni. The choice is motivated by their high technological importance, based on their ferromagnetic properties. The studies comprised both experimental methods, in particular scanning tunneling microscopy and X-ray spectroscopy, as well as theoretical calculations. The results allow for substantial conclusions concerning the electronic and magnetic properties of the adatoms and their influences on the respective substrate.

Graphene is a monatomic thick, flexible, and extraordinarily robust structure, built of carbon atoms. It exhibits peculiar electronic properties (e.g. high electrical conductivities), which originate from the bonding among the C atoms. Two different types of graphene on a SiC substrate were prepared and investigated.

In the first study, the decoupling of graphene was achieved by an additional carbon layer (graphene/SiC). In this case, single specific adsorption sites for Co and Ni and paramagnetic behavior of Fe and Co were found. In contrast, Ni-clusters are nonmagnetic as long as they consist of maximum four atoms. In the second study, the decoupling was achieved by hydrogen-passivation (quasi-free-standing graphene/SiC), which led to surprisingly strong deviating results. In this case, two simultaneously existing adsorption sites were observed for Co and Ni. This hints toward a significant influence of the underlying substrate, that needs to be considered for realistic modeling.

Topological insulators also show very unusual electronic properties. Ideally, three dimensional candidates exhibit no bulk conductivity. On the contrary, they feature conductive spin-polarized surface states.

For Co atoms on a Bi_2Se_3 substrate, two different adatom species were found, bound in the fcc/hcp position. A preferential orientation of the magnetic moments parallel to the surface plane was observed. At higher coverage, the average alignment of the moments rotated to a direction perpendicular to the surface plane. In this event, a heavy influence on the surface states is expected that, however, was not detected. The final investigation concerned Fe adsorbates on Bi_2Te_3. In this case, two different species of the atoms were found as well, again bound in the fcc/hcp position. Their magnetic moments showed a strong uniaxial anisotropy, perpendicular to the surface plane, already for the lowest coverage. The expected consequences on the topological insulator's properties were not detected in this case though, too.

Table of Contents

Title **i**

Zusammenfassung **iii**

Abstract **v**

Table of Contents **vii**

List of Acronyms **ix**

1 Introduction **1**

2 Experimental Techniques **7**
2.1 Scanning Tunneling Microscopy 7
2.1.1 The Basic Principle of Operation 8
2.1.2 The One-Dimensional Tunneling Effect 10
2.1.3 The Tunneling Current 12
2.1.4 The Bardeen Approach 13
2.1.5 The Tersoff-Hamann Model 14
2.2 Scanning Tunneling Spectroscopy 16
2.3 Spin-Polarized Scanning Tunneling Microscopy 17
2.4 X-ray Absorption Spectroscopy 20
2.5 The X-ray Magnetic Circular Dichroism Effect 24
2.6 The Sum Rules 27

3 Measurement Setups **31**
3.1 The Triple Axes Magnet System 31
3.1.1 The Cryostat Chamber 32
3.1.2 The Scanning Tunneling Microscope 34
3.1.3 The Preparation Facilities 35
3.2 The ID08 Dragon Beamline 38
3.2.1 The X-ray Beam 38
3.2.2 The UHV Chamber System 39

4 Graphene **41**
4.1 Overview of Graphene 41
4.1.1 Properties 43
4.1.2 Preparation Methods 45

4.1.3 Potential Applications . . . 46
4.2 Graphene on SiC . . . 47
4.2.1 Graphene on SiC(0001) . . . 48
4.2.2 Quasi-free-standing Monolayer Graphene on SiC(0001) . . . 49
4.2.3 Graphene on SiC(000$\bar{1}$) . . . 50
4.3 Individual Transition Metal Adatoms on Graphene . . . 51
4.3.1 Pristine MLG . . . 51
4.3.2 STM on TM Adatoms on MLG . . . 52
4.3.3 XAS and XMCD on TM Adatoms on MLG . . . 54
4.4 The Influence of the Substrate . . . 59
4.4.1 STM/STS on Co/QFMLG . . . 60
4.4.2 STM/STS on Ni/QFMLG . . . 61
4.4.3 QFMLG vs. MLG . . . 62
4.4.4 Intervalley Scattering on QFMLG . . . 64
4.5 Summary . . . 65

5 Topological Insulators 67
5.1 Overview of Topological Insulators . . . 67
5.1.1 Properties . . . 69
5.1.2 Three-Dimensional Topological Insulators . . . 71
5.1.3 2nd Generation Topological Insulators . . . 71
5.1.4 Expected Effects and Potential Applications . . . 73
5.2 Experiments on TIs . . . 75
5.2.1 Pristine Bi_2Se_3 . . . 77
5.2.2 Pristine Bi_2Te_3 . . . 78
5.3 Co on Bi_2Se_3 . . . 79
5.3.1 STM on Co/Bi_2Se_3 . . . 80
5.3.2 STS on Co/Bi_2Se_3 . . . 82
5.3.3 XAS and XMCD on Co/Bi_2Se_3 . . . 84
5.3.4 Spin Reorientation Transition of Co/Bi_2Se_3 . . . 87
5.4 Fe on Bi_2Te_3 . . . 88
5.4.1 STM and STS on Fe/Bi_2Te_3 . . . 89
5.4.2 XAS and XMCD on Fe/Bi_2Te_3 . . . 92
5.4.3 Sum Rules of Fe/Bi_2Te_3 . . . 94
5.5 Summary . . . 95

6 Conclusions and Outlook 97
6.1 Graphene . . . 97
6.2 Topological Insulators . . . 100

Bibliography 103

Publications 121

Acknowledgements 123

List of Acronyms

AES	Auger electron spectroscopy
AFM	atomic force microscopy
ALE	atomic layer equivalent
ARPES	angle-resolved photoemission spectroscopy
CVD	chemical vapor deposition
DFT	density functional theory
DOS	density of states
DP	Dirac point
e-beam	electron beam
EG	epitaxial graphene
EMW	electromagnetic wave
FET	field-effect transistor
FFT	fast Fourier transform
GGA	generalized gradient approximation
GGA+U	generalized gradient approximation including an on-site Coulomb potential
HC	hydrocarbon
HOPG	highly oriented pyrolytic graphite
IGP	ion getter pump
LDA+U	local density approximation including an on-site Coulomb potential
LDOS	local density of states
LEED	low energy electron diffraction
MAE	magnetocrystalline anisotropy energy
MBE	molecular beam epitaxy
MLG	monolayer graphene
MRAM	magnetoresistive random access memory
OFHC	oxygen-free high conductivity
pBN	pyrolytic boron nitride
QED	quantum electrodynamics
QFMLG	quasi-free-standing monolayer graphene
QHE	quantum Hall effect
QPI	quasi-particle interference
SE	Schrödinger equation

SOI	spin-orbit interaction
SP-STM	spin-polarized scanning tunneling microscopy
SRT	spin reorientation transition
STM	scanning tunneling microscopy
STS	scanning tunneling spectroscopy
TI	topological insulator
TM	transition metal
TRS	time reversal symmetry
TSP	titanium sublimation pump
TSS	topological surface state
UHV	ultrahigh vacuum
XAS	X-ray absorption spectroscopy
XMCD	X-ray magnetic circular dichroism

Chapter 1

Introduction

Nowadays the hunt for innovations in the field of electronic devices is probably carried out with more intensity due to a higher competition than ever before. On the one hand, to increase the performance of these tools, either the existing preparation methods or device concepts have to be tested regarding possible improvements. On the other hand, from a more fundamental point of view, new device concepts including the variation of the participating materials are sought. Therefore, new material classes always attract considerable attention. They often raise the hope not only to exhibit new phenomena, but to possibly reveal properties that would improve the device efficiencies by orders of magnitude, too.

Presuming promising new materials are discovered, it is of course essential to initially investigate their basic properties regarding structural, electronic, and magnetic characteristics. Moreover, it has to be clarified whether the observed intrinsic properties can be modified, or even better, can be precisely tuned. This potentially enables the accurate tailoring of the properties of devices that base on such materials. Common parameters to check are sample qualities or the response to external influences, such as electric or magnetic fields. This way, new materials are usually characterized quite well on a relatively short time scale.

Supposing the rise of the opinion that the material might be seriously suitable for future devices among the scientific community, the efforts of these investigations are usually intensified even more. In addition to the possible studies mentioned before, the materials are subsequently investigated by including more complicated types of manipulations. Examples are given by structural modifications of the samples. These can be achieved by growing thin films of those materials on different supporting substrates or by restricting the materials to different shapes. Moreover, a further opportunity is given by growing nanostructures made of other species on such materials.

Especially the growth of nanostructures offers the possibility of mimicking different effects, such as statistically distributed electric donors or magnetic moments. This is potentially interesting for data storage devices. It enables the opportunity of storing information within small magnetic domains depending on their magnetization direction. That is the general concept of *spintronics*. In state-of-the-art proposals for magnetoresistive random access memory (MRAM) devices minimum edge lengths of about 50 nm are assumed, compare Fig. 1.1(a). These are basically given by the gate lengths of the implemented transistors, that are typically above 25 nm (about 100 atoms) nowadays. A basic scheme of a single MRAM cell is given

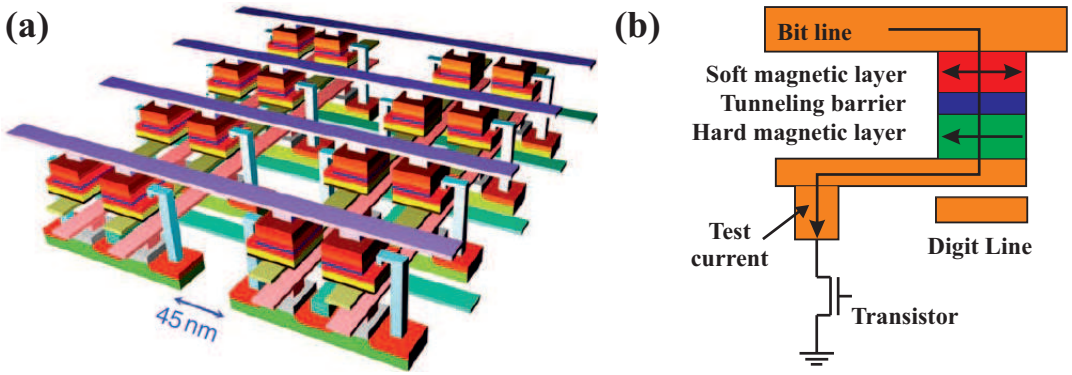

Figure 1.1: (a) Array of electric-field-controlled MRAM devices. The space between individual cells is given by the typical transistor channel lengths. Adapted from Hu *et al.*, 2011 with permission. (b) Basic principle of the MRAM with a hard magnetic domain and a soft magnetic layer. This can be switched utilizing induced magnetic fields or the spin transfer torque effect.

in Fig. 1.1(b). The magnetization of the soft magnetic layer can be switched by induced magnetic fields that are generated from currents applied to the bit and digit lines. The hard magnetic layer remains unaffected. Because this technique consumes comparably much power and causes unwanted stray field effects in adjacent cells, an alternative approach utilizes the *spin transfer torque* effect (Slonczewski, 1996; Berger, 1996). Here, a spin-polarized current directly applied to the soft magnetic layer straightforwardly influences its magnetization. This is due to the torque generated from the spin-polarized electrons if they do not match the layer's magnetization. However, the value of the information can be probed by a test current utilizing the *tunneling magnetoresistance*. The test current, guided through the soft and hard magnetic layer, is different depending on the relative orientations of their magnetizations.

In view of these fairly large and complex devices, material combinations with adsorbed nanostructures, that enable a robust information storage mechanism in units with only a few number of participating atoms, are highly interesting. Exemplary for the desired mechanism stands a recent study on atomic-scale magnets adsorbed on a Cu(111) substrate (Khajetoorians *et al.*, 2013a). At low temperatures (300 mK) and small applied biases, Fe clusters, that consist of only *five* atoms, exhibit magnetization-dependent mean lifetimes on the order of two hours. The information can thus be stored depending on the relative orientation of the cluster's magnetization. The decrease of the number of involved atoms finalizes with single atom magnets where the atomic spin is utilized to store information. A device based on this mechanism reflects the ultimate goal for the concept of spintronics. Achieving a similar mechanism at ambient conditions might therefore potentially revolutionize the setup of nowadays devices boosting their storage capacities by several orders of magnitude.

In contrast, the alternative proposed approaches of varying the substrate underneath thin films of the material or restricting its shape might influence its properties on a global scale. This is due to variations of the interactions between the materials upon this treatment. Of course, this can have significant influences on adsorbed nanostructures as well. Hence, decreasing the dimensionality goes hand in hand with an increasing importance of the interactions with the local environment (Bode, 2004). Such a confinement generally leads to new effects and

phases not observed before. To this end, distributions of adsorbed species require examinations of the basic interactions using high-resolution experimental approaches. Local probe techniques fulfill these needs and enable to precisely monitor the sample structure. They commonly simplify the data evaluation because influences due to imperfections or defects can be excluded. That depicts the major benefit of local probe techniques compared to spatially averaging techniques.

Motivated by the above discussion, the following work bases on combined experimental and theoretical studies. Those were performed on so-called 3*d transition metal* nanostructures adsorbed on different substrates of the novel material classes *graphene* and *topological insulators*. These materials were found to exist in reality only recently and are younger than ten years. Therefore, fundamental studies on their properties are still rare and highly desirable. The utilized *scanning tunneling microscope* (Binnig *et al.*, 1982) enables especially the aims of high spatial resolution and a well-defined sample structure. Thus, scanning tunneling microscopy (STM) observations on the structural and the electronic properties reflect a major part of the experimental findings. In view of the aforementioned advanced device concepts, a method, that is able to precisely manipulate the magnetization on an atomic scale, is of exceptional importance. Otherwise, the atomic scale magnets are not accessible. For this reason, the magnetism-sensitive add-on development of the STM, i.e. *spin-polarized scanning tunneling microscopy* (SP-STM) (Wiesendanger, 2009), is an important tool that fulfills these needs. SP-STM is able to simultaneously investigate and manipulate the magnetization on an atomic scale by means of the spin-transfer torque (Krause *et al.*, 2007; Krause *et al.*, 2011).

Unfortunately, in case of the investigations at hand, SP-STM experiments were not successful. Since for future applications the magnetic properties are of high interest, a complementary experimental approach by means of X-ray based experiments was applied. More precisely, *X-ray absorption spectroscopy* allows to examine the electronic properties of the sample, whereas the effect of *X-ray magnetic circular dichroism* (Schütz *et al.*, 1987) can be used to address its magnetic characteristics. On the one hand, due to their element sensitivities these approaches reveal major advantages compared to other techniques. On the other hand, they make use of focused X-ray beams with minimum beam sizes of $10 \times 50\ \mu\text{m}^2$. The results hence reveal the spatially averaged properties of a much larger area of the sample. However, the X-ray magnetic circular dichroism (XMCD) effect can be used without a specific layout of the sample structure. This is usually a disadvantage of the SP-STM if unambiguous conclusions are requested. Chap. 2 includes a detailed description of the theoretical principles of the experimental techniques. Subsequently, the experimental setups are specified in Chap. 3.

The combination with nanostructures made of the transition metals (TMs) Fe, Co, and Ni is motivated by their general technological importance in modern electronic devices. This is a consequence of their electronic configurations exhibiting non-completely filled 3*d*-shells. The *exchange interaction* among the electrons of TM elements provokes different densities of spin-up and spin-down states at the Fermi level E_F. Hence, the effective *density of states* $\tilde{D}(E_\text{F})$ is spin-polarized, compare Fig. 1.2(a). Furthermore, the Stoner integral I describes the strength of the exchange-correlation effects, shown as well in Fig. 1.2(a). Straightforwardly, the product of the density of states (DOS) and the Stoner integral: $\tilde{D}(E_\text{F}) \times I$ can be used to indicate the type of magnetism in these materials. For this product being larger than 1 the Stoner criterion (Stoner, 1938):

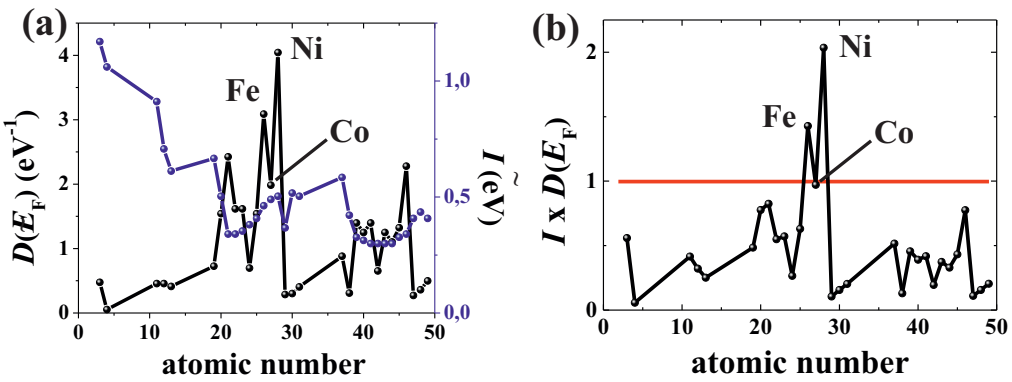

Figure 1.2: (a) Overview of the DOS (left *y*-axis) and exchange-correlation integral (right *y*-axis) for a collection of different elements depending on their atomic number. The data values were extracted from spin-polarized exchange-correlation calculations (Janak, 1977). (b) Product of DOS and exchange-correlation integral for each of the species. If the product is larger than one, the Stoner criterion is fulfilled and the bulk material is supposed to exhibit ferromagnetism.

$$\tilde{D}(E_\mathrm{F}) \times I > 1 \tag{1.1}$$

is fulfilled and ferromagnetism is expected, compare Fig. 1.2(b). This is generally the case for Fe, Co, and Ni. Of course, Fig. 1.2 reflects the calculations performed for bulk materials. The properties naturally vary for the case of individual atoms or clusters. Even more importantly, they vary depending on the local environment (Bode, 2004). To this end, for adsorbed nanostructures, the DOS has to be replaced by the local density of states (LDOS), that includes these effects. Thereby, the magnetic properties of the respective species can be modified. However, Fe, Co, and Ni nanostructures usually reveal peculiar magnetic properties which manifest their importance in modern devices.

Graphene is the first substrate investigated, whereas the related experiments and its basic characteristics are described in detail in Chap. 4. It exhibits a purely two dimensional lattice structure composed of two sublattices made of carbon atoms. These are arranged in a honeycomb lattice and account for its extraordinary mechanical robustness combined with high flexibility and high thermal conductivity. The robustness can also be seen by its inert-like behavior. Presuming a closed layer of graphene, the honeycomb lattice does not exhibit any points to attack. Hence, graphene is extremely robust even at ambient conditions. It mainly reveals the same properties if exposed to air.

Although the structural properties are already very exceptional, its electronic properties are even more astonishing. Graphene can be described as a *zero-band gap semiconductor*, because the intrinsic *spin-orbit interaction* of the light element C is small. The lattice structure generates a two-dimensional electron gas of massless Dirac fermions which originate from the delocalized p_z orbitals of the carbon atoms. This way, graphene exhibits *quasi-ballistic transport* with remarkably high charge carrier mobilities (Morozov *et al.*, 2008). These are expected to enhance the performance of state-of-the-art high frequency transistors by orders of magnitude. Furthermore, the p_z states cause π/π^*-bands with linear dispersions in the vicin-

ity of the *K*-points of the Brillouin zone (*Dirac points*), where the valence and conduction bands touch. This enables an easy tuning of graphene between electron and hole conductance, another desirable property regarding modern devices. In view of its robustness to ambient conditions, graphene therefore represents a promising candidate to be implemented in mass production of future electronic devices soon.

Opposite to its electronic properties, graphene exhibits only vary rare magnetic features. More precisely, only at its zig-zag edges a spin-dependent edge state is predicted. It seems thus promising to combine graphene's extraordinary electronic properties with the magnetic properties of TM nanostructures. Despite, graphene is also interesting in view of fundamental physics. It enables investigating effects of the *quantum electrodynamics* in *condensed matter physics*. Examples are given by the half-integer *quantum Hall effect* (Novoselov *et al.*, 2005; Zhang *et al.*, 2005) or the *Klein paradox* (Itzykson *et al.*, 2006). Further potential applications deal with its integration into solar cells or flexible displays. There, graphene might provide a flexible but robust conductive layer with high charge carrier mobilities, compare Chap. 6 for further details.

In contrast to graphene, topological insulators are a class of materials, that usually are alloys or compounds of multiple elements with relatively high atomic numbers, i.e. Bi, Se, Te. Chap. 5 deals with these materials and provides an overview of the experimental results, too. Topological insulators (TIs) are characterized by topological invariants, which, in a simple view, can be assigned to structural properties. In a detailed view, the topological invariants are better described by peculiarities of the band structure.

Owing to the high atomic numbers of the involved materials, the intrinsic spin-orbit interaction (SOI) is strong in these materials. Importantly, at interfaces where the topological invariants vary, SOI leads to a *band inversion* of the *p*-orbitals at the $\bar{\Gamma}$-points of the Brillouin zone of the reciprocal space. Although these materials exhibit insulating bulk states, this band inversion generates so-called *topological surface states*. They bridge the band gap between bulk valence and conduction states. On the one hand, topological surface states (TSSs), similar to graphene's π/π^*-bands, exhibit a linear band dispersion and form Dirac cones at the points they touch. On the other hand and contrary to graphene, the TSSs are not spin-degenerate. This has fundamental and important consequences by giving rise to spin-dependent transport properties. Since the SOI mimics the effect of an external magnetic field, charge carriers feel spin-dependent forces and propagate along specific trajectories. This way, backscattering is absent on topological insulator (TI) surfaces provided that effects due to finite temperatures are neglected.

The TSS are protected by *time reversal symmetry* and robust against nonmagnetic impurities. However, magnetic impurities do not respect time reversal symmetry (TRS), can generally destroy the TSSs and are hence of high importance. TIs are mainly interesting in view of fundamental physics because they offer a wide range of exciting effects. Examples are the *quantum spin Hall effect* (Murakami *et al.*, 2004), the *magnetoelectric effect* (Qi *et al.*, 2008; Essin *et al.*, 2009), or the possibility to generate *Majorana fermions* (Majorana, 1937). Although many of their properties are very interesting in view of future applications, according to Chap. 6, a realization seems to be challenging because TIs are highly reactive compared to, e.g., graphene. Of course, overcoming this major drawback would probably cause a run for their integration into future devices.

In summary, the performed investigations were motivated, on the one hand, by a lack of sufficient experimental data and, on the other hand, by fundamental reasons. The combination of graphene and TIs with 3*d* nanostructures in simple and defined samples might serve two purposes: Firstly, it offers to examine the interactions. Secondly, it potentially enables tailoring the band structure and realizing desired spin textures at the same time.

Chapter 2

Experimental Techniques

This chapter presents the working principles and procedures of the main experimental approaches used within the investigations. The chapter is basically divided into two parts. Starting with the general description of the STM, the theoretical background based on the tunneling effect including related models is explained in Sec. 2.1. Subsequently, Sec. 2.2 focuses on scanning tunneling spectroscopy (STS), that can be utilized to test the electronic properties of a sample. Afterward, the theory of the magnetically sensitive spin-polarized scanning tunneling microscopy (SP-STM) is presented in Sec. 2.3.

The basic principles and the theory of X-ray based measurements are treated beginning with the description of X-ray absorption spectroscopy (XAS) in Sec. 2.4. In the following section, Sec. 2.5, the magnetically sensitive XMCD effect is introduced in detail. The chapter finalizes in Sec. 2.6 with the sum rules, that can be used to evaluate the X-ray data.

2.1 Scanning Tunneling Microscopy

In 1897 the *tunneling effect* of electrons was first demonstrated during field emission experiments by R. W. Wood (Wood, 1897). Unfortunately, Wood was not able to interpret his observations correctly. Afterward, within the 20th century, physicists focused more and more on particles with smaller dimensions in order to keep the investigated systems simple and thereby to understand their basic mechanisms and interactions. Because the precise characterization of the systems is of crucial importance for the conclusions to be made, increasing resolution of the experimental techniques was highly desirable. Optical microscopes were a commonly used technique. But, they exhibit a spatial resolution restricted by the wavelength of the light used within their setups, typically some 100 nm. To gain the ability of resolving textures which reveal dimensions well below this limit, e.g. atomic resolution of crystal lattices (typically some 100 pm), a new experimental technique was sought. This aim was fulfilled in 1981 by *G. Binnig* and *H. Rohrer* (Binnig *et al.*, 1982). Soon after their invention of *scanning tunneling microscopy*, they were awarded the *Physics Nobel Prize* in 1986.

The STM crucially depends on a conductive sample and a metallic tip, that are approached nearby (typically 100 pm) without being in contact. The finite gap between tip and sample can be described as a potential barrier V_0. According to classical physics, no current flows if a

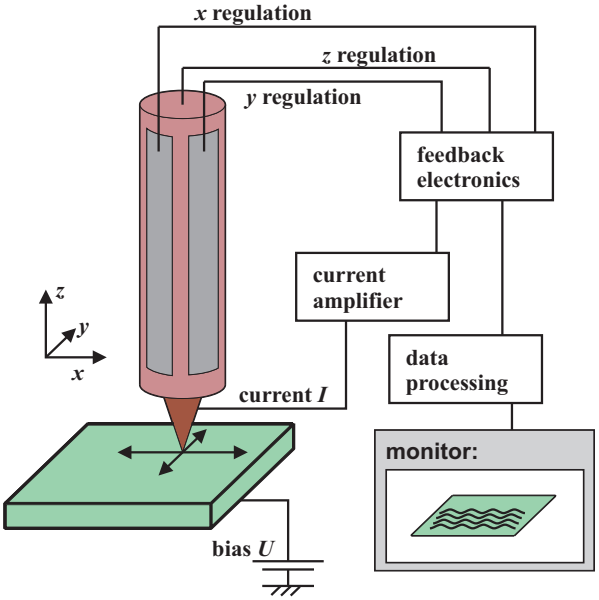

Figure 2.1: Schematic model of STM showing the basic setup. The tunneling distance is only a few angstroms. The current is amplified before it is used by the feedback loop to adjust the tip-sample separation in order to adapt the measured current to the setpoint current. Together with the x- and y-coordinates, the z-regulation enables the data processing unit to generate a map of the LDOS of the sample.

potential difference is applied between them and if the potential barrier exceeds the energy E of the electrons: $V_0 > E$. In contrast, *quantum mechanics* in principle allows the electrons to overcome the gap. By means of the *tunneling effect* the electrons can tunnel through this barrier, even if their energy E is lower than the barrier, i.e. $E < V_0$. As a result, a highly sensitive *tunneling current* is established, strongly depending on the tip-sample separation. In combination with an accurate adjusting mechanism, the tunneling current enables the operation of STM with extreme spatial resolution down to the atomic scale (Binnig *et al.*, 1985).

2.1.1 The Basic Principle of Operation

The general setup of STM is shown in Fig. 2.1. The investigated samples vary in a wide range from metal single crystals over semiconductors to modern materials, such as TIs. The tips are usually either ruptured or electrochemically etched from metal wires, e.g. PtIr, W, or Cr. The adjusting mechanism, that is used to control the tip position, bases on a bendable tube. The tube is covered by electrodes on its out- and inside and is made of piezoelectric ceramic. If potential differences are applied to the different electrodes, the tube can be precisely bent in the xy-plane or can be extended/shrunk in the z-direction.

The tunneling contact is achieved as follows: in a first step, a potential difference between tip and sample is applied. Secondly, the separation of tip and sample is decreased. Once the tunneling regime is reached, the initially applied potential difference causes different occupations of the electron reservoirs. Consequently, a net tunneling current arises. As will be shown in detail in Sec. 2.1.3, the tunneling current crucially depends on the transition coefficient T and,

this way, on the tip-sample distance z_0:

$$T = \mathrm{e}^{-2qz_0} \tag{2.1}$$

where q depicts the decay constant. The exponential dependence on the tip-sample separation in particular leads to the extreme sensitivity to height differences. For instance, in case of metals, the current varies approximately by one order of magnitude for a height difference of 0.1 nm. This is due to the decay constant, which is in the range of $q \approx 10\ \mathrm{nm}^{-1}$ for metals. Hence, the tunneling current increases during the approach. The approach mechanism is stopped once the tunneling current reaches a specified setpoint current. Usually the separation between tip and sample is in the range of several Å. Due to its smallness in the nA regime, the tunneling current is amplified by a factor of 10^9 using a FEMTO preamplifier (FEMTO, n. d.). As soon as the tunneling contact is successfully established two main modes of operation can be applied.

The most common operating mode is the *constant-current mode*. To interpret the STM data a combined hard- and software-based device is used, the Nanonis SPM electronics (Nanonis, n. d.). This module measures the tunneling current depending on the x- and y-coordinates. By means of a feedback loop the electronics keeps the tunneling current constant by modifying the tip-sample separation via the change of the z-voltage, that is applied to the piezoceramic tube. Potential modifications needed during this procedure are finally recorded together with the x- and y-coordinates. The Nanonis converts these data into an apparent height profile of the sample in Cartesian coordinates. The height profile can be seen as a map of the spatially resolved conductivity of the sample. More precisely, it depicts the spatially resolved sum of all unoccupied states between the Fermi level E_F and the stabilization voltage eV (*local density of states*). WSxM software (Horcas *et al.*, 2007; WSxM, n. d.) is available to further analyze the processed topographies with respect to their characteristic features.

Another mode of operation is the *constant-height mode*. In this event, a suitable tip-sample separation is chosen and the feedback loop is turned off afterward. Subsequently, the sample is scanned in the xy-plane with no correction applied to the z-electrode. Due to its extreme sensitivity, see Sec. 2.1.3, the tunneling current strongly varies as soon as the electronic structure of the surface is changed, e.g. by a step edge. For this operation mode, the tunneling current is recorded together with the xy-position to generate a map of constant height showing the variations in the tunneling current. The constant height mode has to be applied carefully because the tip might be severely damaged if the height differences on the sample exceed the initially adjusted tip-sample separation.

The quality of the measurements generally depends strongly on the quality of the tunneling tip. Although the etching procedure ensures fairly small radii ($\approx$ 100 nm), further tip treatment is usually needed to obtain an atomically sharp tip. Otherwise, the existence of multiple tunneling tips results in the multiple mapping of the sample's features. The tip treatment is commonly performed either by high temperature annealing or by voltage pulses on robust surfaces while being in tunneling contact. The pulsing procedure causes clusters of the tip to drop off and generally leads to an atomically sharp tip quite fast.

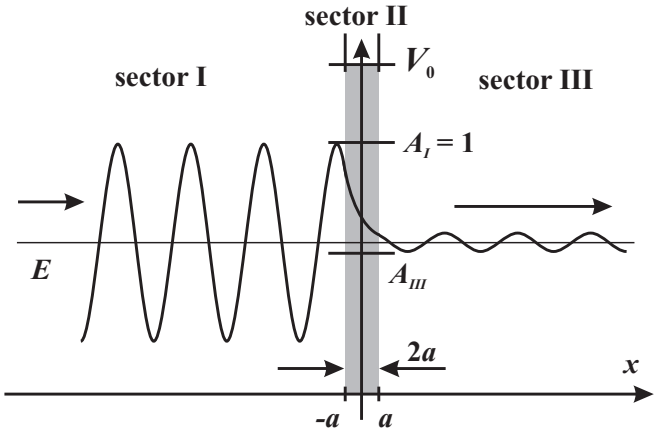

Figure 2.2: Illustration of the one-dimensional tunneling effect for a particle impinging on the potential barrier from the left.

2.1.2 The One-Dimensional Tunneling Effect

The tunneling effect is a consequence of quantum mechanics developed by *W. Heisenberg*, *E. Schrödinger*, *W. Pauli*, *P. Dirac*, and *F. Hund* and others in the third decade of the 20th century (Hund, 1925; Schrödinger, 1926; Heisenberg, 1927; Dirac, 1927). Quantum mechanics bases on Heisenberg's *uncertainty principle*, i.e. only a certain probability exists to find a particle in a particular state. Basically this means, that not all properties describing the particle can be precisely measured at the same time.

Considering Heisenberg's work, the tunneling effect is understandable because there must exist a finite probability that the particle can overcome the barrier, although $E < V_0$. Of course, this is valid only if the barrier is neither indefinitely wide nor high. The mechanism bases on the probability of the presence of the particle, which is not cut but exponentially damped by the potential barrier, compare Eq. 2.1. Since the tunneling effect is the main principle of STM, it is here introduced in detail. Without loss of generality, in the following, the tunneling effect is described for the one-dimensional case but can similarly be treated for the three-dimensional case.

A precise description of the tunneling effect makes use of the *wave-particle duality* postulated by *L. de Broglie*. Motivated by the uncertainty principle, it states, that each particle can be described as a matter wave, too (De Broglie, 1970). In view of this duality it is not surprising, that in quantum mechanics a particle and its properties are described by a *wave function* $\psi(x)$. The square of this wave function describes the probability of this particle to be located at the specific location x.

Using this wave function, the one-dimensional tunneling effect can be illustrated by a particle with energy E impinging on a rectangle potential barrier of height V_0 from the left, shown in Fig. 2.2. The effect is based on the finite overlap of the wave functions $\psi_{\mathrm{I}}(x)$ and $\psi_{\mathrm{III}}(x)$, that describe the particle on either side of the potential barrier. According to textbook physics (Demtröder, 2010), the wave function has to solve the *Schrödinger equation* for each sector (i = I, II, III):

$$\left(-\frac{\hbar^2}{2m}\frac{\mathrm{d}^2}{\mathrm{dx}^2} + V(x)\right)\psi_\mathrm{i}(x) = E\psi_\mathrm{i}(x) \tag{2.2}$$

where m is the mass of the particle, $\hbar$ is Planck's constant and V the strength of the potential barrier, which is nonzero only in sector II ($V(x) = 0$ for $x < -a$ and $a < x$; $V(x) = V_0$ for $-a \leq x \leq a$). The Schrödinger equation (SE) can be solved by the superposition of two plane waves, one propagating to the right and one to the left:

$$\psi_\mathrm{i}(x) = A_\mathrm{i}\mathrm{e}^{ik_\mathrm{i}x} + B_\mathrm{i}\mathrm{e}^{-ik_\mathrm{i}x} \tag{2.3}$$

Under the assumption of elastic tunneling, i.e. energy conservation during the tunneling process, the wave vectors outside the barrier are equal to each other. They are given by the kinetic energy of the particle:

$$k_\mathrm{i} = \sqrt{\frac{2m(E - V(x))}{\hbar^2}} \quad \Rightarrow \quad k_\mathrm{I} = k_\mathrm{III} = \sqrt{\frac{2mE}{\hbar^2}} = k \tag{2.4}$$

Inside the barrier, k_II would be imaginary and, thus, is substituted by the real quantity q:

$$k_\mathrm{II} = iq \quad \text{with} \quad q = \sqrt{\frac{2m(V_0 - E)}{\hbar^2}} \tag{2.5}$$

Without loss of generality, the amplitude of the impinging wave can be set to the maximum value, i.e. $A_\mathrm{I} = 1$. In addition, $B_\mathrm{III} = 0$, because no left-propagating wave exists in sector III. In summary, the wave function is given by:

$$\psi(x) = \begin{cases} \psi_\mathrm{I}(x) &= \mathrm{e}^{ikx} + B_\mathrm{I}\mathrm{e}^{-ikx} & \text{if:} \quad x < -a \\ \psi_\mathrm{II}(x) &= A_\mathrm{II}\mathrm{e}^{qx} + B_\mathrm{II}\mathrm{e}^{-qx} & \text{if:} \quad -a \leq x \leq a \\ \psi_\mathrm{III}(x) &= A_\mathrm{III}\mathrm{e}^{ikx} & \text{if:} \quad a < x \end{cases} \tag{2.6}$$

Another constraint is, that the wave functions and their first derivatives have to be continuous at the borders of the potential barrier to be physically meaningful:

$$\begin{aligned} \psi_\mathrm{I}(-a) &= \psi_\mathrm{II}(-a) \quad \text{and} \quad \psi_\mathrm{II}(a) = \psi_\mathrm{III}(a) \\ \psi'_\mathrm{I}(-a) &= \psi'_\mathrm{II}(-a) \quad \text{and} \quad \psi'_\mathrm{II}(a) = \psi'_\mathrm{III}(a) \end{aligned} \tag{2.7}$$

As a consequence, a set of four equations with four unknown amplitude factors is obtained. Hence, the *transmission coefficient* T, given by the ratio of transmitted current density to incident current density, can be evaluated. This quantity describes the efficiency of the tunneling process in dependence on the barrier height V_0 and width $2a$:

$$
\begin{aligned}
T &= \left| \frac{\psi_{\mathrm{III}}}{\psi_{\mathrm{I}}} \right|^2 \\
&= \frac{4k^2q^2}{4k^2q^2 + (k^2+q^2)^2 \sinh^2(2qa)} \\
&= \frac{4E(V_0 - E)}{4E(V_0 - E) + V_0^2 \sinh^2(2qa)}
\end{aligned}
\tag{2.8}
$$

2.1.3 The Tunneling Current

The precise description of the tunneling current needs a more appropriate explanation than the general concept of the tunneling effect. For simplicity reasons, in the following, the case of zero temperature ($T = 0$) is assumed.

The current results from all electrons tunneling from tip to sample and vice versa. Therefore, the *Fermi level* E_{F} and the *surface potential* U have to be introduced. The Fermi level is the upper limit of the occupied states. The surface potential is the lowest energy needed to detach an electron from the Fermi to the vacuum level and reflects thus the specific work function of the respective electrode. It is mainly given by the work function of the electrode's material but also includes effects induced by the specific shape of its surface. The latter can, for instance, be exemplarily shown by the crystallographic direction, which can have a sizable effect on U. As a result, the surface potentials of tip (U^T) and sample (U^S) are generally different.

If the conductive tip and sample are brought into the tunneling regime, their Fermi levels adapt to each other by a balancing initial current. Provided that both Fermi levels are equal, no net tunneling current occurs any more. At this point, electrons still tunnel between tip and sample but per time unit the amount in one direction equals the contrary direction. This is due to the absence of available unoccupied states ($E_{\mathrm{F}}^{\mathrm{sample}} = E_{\mathrm{F}}^{\mathrm{tip}}$), compare Fig. 2.3(a). In contrast, the Fermi levels are shifted with respect to each other, if a potential difference eV is applied between tip and sample, shown in Fig. 2.3(b). In this event, there is a net tunneling current depending on the applied bias voltage. The current depends on variations of the electronic properties with respect to the lateral position on the sample. This can be easily illustrated by the transmission coefficient. Supposing the applied bias voltage being small compared to the surface potentials ($eV \ll U^S, U^T$), Eq. 2.8 can be rewritten as:

$$
T = \mathrm{e}^{-2qz_0} \tag{2.9}
$$

where $q = \sqrt{m(U^S + U^T)/\hbar^2}$ is the decay constant near the Fermi level and z_0 depicts the tip-sample separation according to Fig. 2.3. The exponential decay describes the extreme sensitivity on variations of the separation assuming that the surface potentials remain fairly equal.

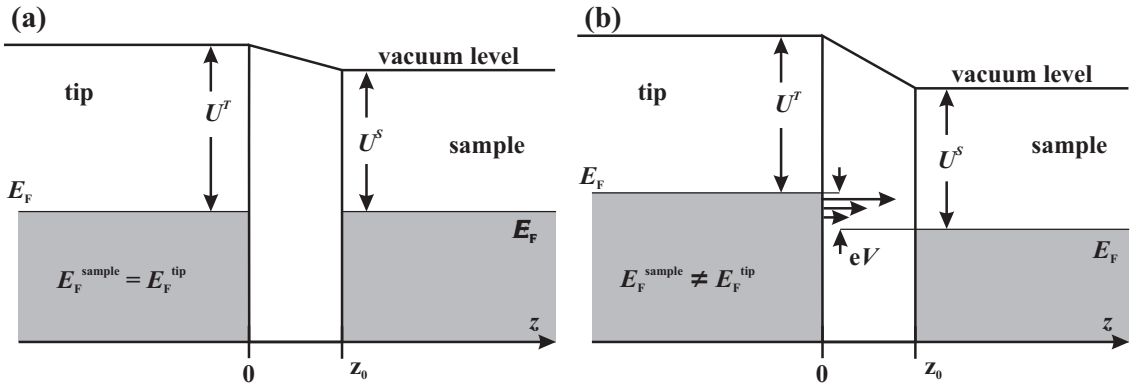

Figure 2.3: (a) Schematic model of the tunneling contact in view of the surface potentials of tip and sample without an applied bias voltage. In this case, no net tunneling current is established. (b) If a potential difference eV is applied between tip and sample, unoccupied sample states are available and a tunneling current occurs.

2.1.4 The Bardeen Approach

The formalism of the tunneling effect introduced in Sec. 2.1.2 was used by *J. Bardeen* to describe the principle of the tunneling junction using the *perturbation theory* in more detail (Bardeen, 1961). In his approach, sample and tip are similar to Fig. 2.3(b) described by two electrodes. If they are close to each other, the time-dependent SE of the entire system reads:

$$\left(-\frac{\hbar^2}{2m}\frac{\partial^2}{\partial \mathrm{z}^2} + U^S + U^T\right)\psi = \mathrm{i}\hbar\frac{\partial\psi}{\partial t} \tag{2.10}$$

where ψ depicts now the time-dependent wave function $\psi(x,t)$ of the combined system. The potential surfaces are assumed to be orthogonal to each other, i.e. $U^S U^T = 0$. This is reasonable owing to the electrical neutrality of the combined system. Hence, the vacuum potential at infinity is well defined. The solution of the SE is a linear combination of the solutions of the partial systems, given by:

$$\psi = A_\mu \mathrm{e}^{-\mathrm{i}E_\mu t/\hbar} + \sum_{\nu=1}^{\infty} c_\nu(t) A_\nu \mathrm{e}^{-\mathrm{i}E_\nu t/\hbar} \tag{2.11}$$

where $c_\nu(0) = 0$ and, thus, the first addend describes the solution for $t = 0$. In general, the coefficients $c_\nu(t)$ are determined by the SE. Inserting them, enables deriving the tunneling current depending on the bias voltage eV:

$$I = \frac{2\pi \mathrm{e}^2}{\hbar} \cdot V \cdot \sum_{\mu\nu} [f(E_\mathrm{F} - \mathrm{e}V) - f(E_\mathrm{F})] \cdot \left|M_{\mu\nu}\right|^2 \cdot \delta(E_\nu - E_\mu) \tag{2.12}$$

Here, f is the *Fermi distribution function*, given by: $f(E) = (1 + exp[(E - E_F)/k_\mathrm{B}T])^{-1}$. It includes finite temperature effects. The delta function in Eq. 2.12 describes the fact, that the

transition probability according to *Fermi's golden rule* is maximized, if the energies of initial and final state perfectly match (Dirac, 1927) ($E_\mu = E_\nu$). This is a result of the assumption of elastic tunneling. Furthermore, $M_{\mu\nu}$ depicts the *tunneling matrix element* describing the exact probability of the respective transition:

$$M_{\mu\nu} = \int_{z>z_0} A_\mu U_S A_\nu^* \mathrm{d}^3\boldsymbol{r} \tag{2.13}$$

Bardeen's major contribution was showing that the tunneling matrix element can be computed solely by the wave functions of tip and sample at the separation surface between them. Thereby, the particular properties of the potential barrier are eliminated from the formula. This is achieved by converting Eq. 2.13 into a surface integral of the unperturbed wave functions of both electrodes evaluated at the separation surface. In view of the energy conservation during the tunneling process $E_\mu = E_\nu$ and the fact that the sample potential U^S is zero at the tip side, the transition matrix element can be computed by:

$$M_{\mu\nu} = \int_{z=z_0} \left(A_\mu \frac{\partial A_\nu^*}{\partial z} - A_\nu^* \frac{\partial A_\mu}{\partial z} \right) \mathrm{d}x\mathrm{d}y \tag{2.14}$$

While M is not depending on the potential barrier itself, it is symmetric with respect to both electrodes, i.e. $M_{\mu\nu} = M_{\nu\mu}^*$. This is illustrating that the tunneling process is bidirectional and fulfills the principle of reciprocity. This means, that it is generally independent of the tunneling orientation (tip → sample or sample → tip).

In the limit of zero temperature and small applied bias voltages $\mathrm{e}V \ll U^S, U^T$, the tunneling current can be simplified to:

$$\begin{aligned} I &= \frac{2\pi\mathrm{e}^2}{\hbar} \cdot V \cdot \sum_{\mu\nu} \left|M_{\mu\nu}\right|^2 \delta(E_\nu - E_\mathrm{F})\delta(E_\mu - E_\mathrm{F}) \\ &= \frac{2\pi\mathrm{e}^2}{\hbar} \cdot V \cdot \sum_{\mu\nu} \left|M_{\mu\nu}\right|^2 \rho^S(E_\mathrm{F})\rho^T(E_\mathrm{F}) \end{aligned} \tag{2.15}$$

where the *density of states* of the tip $\rho_T(E_F)$ and the sample $\rho_S(E_F)$ were assumed to be constant near the respective Fermi level.

2.1.5 The Tersoff-Hamann Model

The Bardeen approach of tunneling between two electrodes bears a fundamental problem. The entire solution bases on the energy-dependent solutions of both partial systems. In case of STM, this is inconvenient since especially the DOS of the tip cannot be precisely determined owing to the missing knowledge about its exact structure. *J. Tersoff* and *D. R. Hamann* were able to elegantly circumvent this problem by simply assuming a specified structural layout for the tip apex (Tersoff *et al.*, 1983; Tersoff *et al.*, 1985). In the following, it was evidenced that their assumption is reasonably good and holds for a wide range of STM observations.

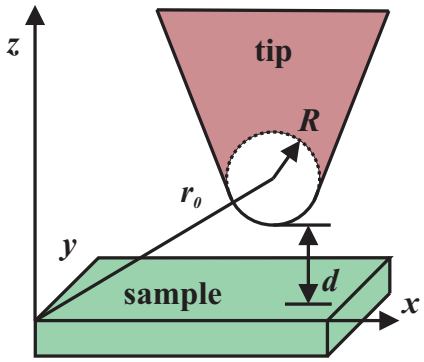

Figure 2.4: Schematic model of the *s* wave tip model according to the theory by Tersoff and Hamann. The distance of the atom's center to the sample z_0 is given by $z_0 = d + R$.

In this model the entire tip is reflected by a *s-type tip wave function*. This wave function exhibits an orbital momentum of zero ($l = 0$) and *spherical symmetry*. It is determined by $\psi_T(r) = 1/r \cdot \mathrm{e}^{-\kappa r}$, where κ is given by the surface potential of the tip: $\kappa = \sqrt{2mU^T}/\hbar$, compare Fig. 2.4. The sample wave vector q is given by its partial x- and y-components $q = (k_x, k_y)$. As a result, the sample wave function in the vacuum region is given by:

$$\psi_S(\boldsymbol{r}) = \int a(\boldsymbol{q}) \cdot \mathrm{e}^{-z\sqrt{\boldsymbol{q}^2+\kappa^2}+\mathrm{i}\boldsymbol{q}\boldsymbol{x}} \mathrm{d}^2\boldsymbol{q} \tag{2.16}$$

where $\boldsymbol{a}(q)$ are the coefficients of the Fourier components evaluated at the sample surface ($z = 0$). The tunneling matrix element can be straightforwardly computed according to Bardeen's theory:

$$M \propto \int a(\boldsymbol{q}) \cdot \mathrm{e}^{-z_0\sqrt{\boldsymbol{q}^2+\kappa^2}} \mathrm{d}^2\boldsymbol{q} \tag{2.17}$$

which demonstrates that M is essentially given by the sample wave function evaluated at the location of the tip. Consequently, the tunneling current is characterized by the sample's LDOS evaluated at the Fermi level at the origin of the tip's curvature:

$$I \approx \frac{4\pi\mathrm{e}}{\hbar} \cdot \rho^T \cdot \int_0^{\mathrm{e}V} \rho^S(E_\mathrm{F} + \epsilon, \boldsymbol{r}_0)\mathrm{d}\epsilon \tag{2.18}$$

Here, the tip's DOS is assumed to be constant for the bias interval eV, the tunneling matrix element is assumed to be energy-independent and the sample's DOS is assumed to be constant for the thermal energy given by $k_\mathrm{B}T$.

The advantage of the Tersoff-Hamann model is, that Eq. 2.18 can be easily used to simulate STM images. To this end, first-principles calculations can be applied, because the formerly unknown tip's DOS is modified to a constant factor. In general, the *s* wave tip model remains valid only if terms of higher order orbital momenta ($l > 0$) may be neglected. Tersoff and Hamann showed that for metals this constraint is fulfilled as long as the observed objects are larger than $\approx$ 0.3 nm. Otherwise, the image interpretation must be carefully performed

respecting possible higher order terms of the orbital momentum. A more realistic approach by calculating the transition matrix elements for *p*- and *d*-like tip wave functions helps explaining, e.g., an enhanced spatial resolution on metal surfaces (Chen, 1988; Chen, 1990a).

2.2 Scanning Tunneling Spectroscopy

Scanning tunneling spectroscopy is a very powerful mode of STM to obtain information about the electronic properties of the sample (Lang, 1886; Feenstra *et al.*, 1987; Hamers, 1989). If the tip's DOS is assumed to be featureless, the method enables to test the unoccupied and occupied states of the sample depending on the polarity of the applied bias. In view of the spatial resolution of the STM, this means, that the LDOS of the sample can be probed.

In general, the LDOS can be determined by differentiating the tunneling current with respect to the applied bias voltage U (Chen, 2008):

$$\left(\frac{\mathrm{d}I}{\mathrm{d}U}\right)_{(U=V)} \propto \rho^T(E_\mathrm{F}) \cdot \rho^S(E_\mathrm{F} + \mathrm{e}V)|M(\mathrm{e}V)|^2 + \int_0^{\mathrm{e}V} \rho^T(E_\mathrm{F} - \mathrm{e}V + \epsilon)\rho^S(E_\mathrm{F} + \epsilon)\frac{\mathrm{d}}{\mathrm{d}U}\left(|M(\epsilon)|^2\right)\mathrm{d}\epsilon \tag{2.19}$$

The application of a bias voltage leads to a shift of the Fermi levels of tip and sample by eV, compare Fig. 2.3(b). If a positive bias voltage is applied, the Fermi level of the sample is lowered with respect to the tip's Fermi level. As a result, the tunneling current primarily occurs from the states at the Fermi level of the tip. The cause is given by the tunneling matrix element that generally exhibits a dependence on the energy parameter ϵ:

$$M(\epsilon) = M(0) \cdot \exp\left(\frac{q\epsilon z_0}{(U^S + U^T)}\right) \tag{2.20}$$

This matrix element can be used to calculate the tunneling current via the integration over eV explicitly. As a result, the exponential factor leads to a favoritism of the states at the upper limit of the bias interval. Consequently, the major contribution to the $\mathrm{d}I/\mathrm{d}U$-signal thus results from the upper limit of the investigated potential difference of the sample, i.e. ($E_\mathrm{F}^\mathrm{sample}$ + eV). This is indicated in Fig. 2.3(b) by the different lengths of the arrows inside the interval. This way, positive biases can be used to investigate the unoccupied sample states at (E_F+ eV). Presuming the application of a negative bias the situation inverts. In this case, the tunneling current originates from electrons of occupied sample states tunneling into unoccupied tip states. Consequently, the tunneling current depends mainly on the unoccupied tip states. Provided, that the tip's DOS is flat, this method can be used to deduce information about the occupied sample states.

A more convenient way to investigate the LDOS makes use of a *lock-in amplifier*. Within this approach, the STS is performed by modulating the DC voltage utilizing a high frequency AC signal. The frequency of the AC signal has to be carefully selected (typically in the regime of kHz) not to match a mechanical resonance frequency of the experimental setup. Otherwise, the entire STM or parts of it can oscillate excluding meaningful measurements. In addition,

the frequency needs to be larger than the bandwidth of the STM's preamplifier. Otherwise, the preamplifier would compensate the modulation by changing the tip-sample separation presuming operation using the constant-current mode. For data acquisition, the reply of the system caused by the AC voltage is recorded by means of the tunneling current which is integrated for a given *time constant*. The lock-in acts as a bandpass filter for the AC frequency. It selectively amplifies the respective signal compared to the general noise, i.e. it increases the signal-to-noise ratio. This way, smaller time constants can generally be chosen leading to time saving during the experiments. The amplitude of the AC signal determines the energy resolution within STS, commonly in the range of 1 to 30 mV.

For *point spectroscopy*, spectra at a fixed location of the sample are acquired. To this end, an interval of the voltage with upper and lower limit and a number of intermediate points is specified. Once the desired tip-sample separation is achieved, the feedback loop is turned off and the voltage is ramped. At each intermediate point the $\mathrm{d}I/\mathrm{d}U$-signal is determined using Eq. 2.19. The data acquisition system finally plots the $\mathrm{d}I/\mathrm{d}U$-intensity depending on the respective voltage for the fixed *xy*-position.

Another operational mode is the $\mathrm{d}I/\mathrm{d}U$-map. In this case, not only the topographic information, but also the $\mathrm{d}I/\mathrm{d}U$-intensity is measured at each data point in the *xy*-plane. This implies that the scanning speed of the topographic acquisition needs to be adjusted to the time constant of the lock-in. For instance, a map with 256 data points per line and a time constant of 3 ms, requires a minimum time per line of 768 ms. Caused by these constraints, $\mathrm{d}I/\mathrm{d}U$-maps are more time consuming than common topographies. However, their advantage is clearly given by the spatially resolved DOS for the specified bias U.

The remaining operational mode is the *grid spectroscopy*. Within the scan area, a grid of points is defined. The topographic information and a point spectrum is acquired at each point. This ensures, that the spatially resolved full spectroscopic information is gained at each *xy*-location of the grid. The data consists of an entire set of $\mathrm{d}I/\mathrm{d}U$-slices for the bias range chosen. The disadvantage of this method is owing to its time consumption. It exceeds that of individual $\mathrm{d}I/\mathrm{d}U$-maps significantly. As a result, grid spectroscopy requires high stability of the setup.

2.3 Spin-Polarized Scanning Tunneling Microscopy

By considering another degree of freedom, i.e. the magnetism of the involved materials used for tips and samples, *spin-polarized scanning tunneling microscopy* reflects an extraordinary improvement of the conventional STM (Wiesendanger, 2009). It was first utilized in 1990 in constant current maps (Wiesendanger *et al.*, 1990). Later, SP-STM was improved by including spectroscopic measurements strongly enhancing the magnetic contrast (Bode *et al.*, 1998), even in the regime of individual adatoms (Meier *et al.*, 2008). The investigation and the interpretation of the results bases on the fact, that the tunneling current depends on the *relative alignment* of the magnetic moments of tip and sample (Slonczewski, 1989).

The phenomenon is caused by the intrinsic spin of the electrons of the participating materials. The *exchange interaction* between those electrons generally leads to different densities of spin-up $\rho_\uparrow$ and spin-down $\rho_\downarrow$ states at a given energy $\rho_\uparrow(E_\mathrm{F}) \neq \rho_\downarrow(E_\mathrm{F})$. This turns the material to be magnetic. The exchange interaction leads to exchange-split states for different orientations of

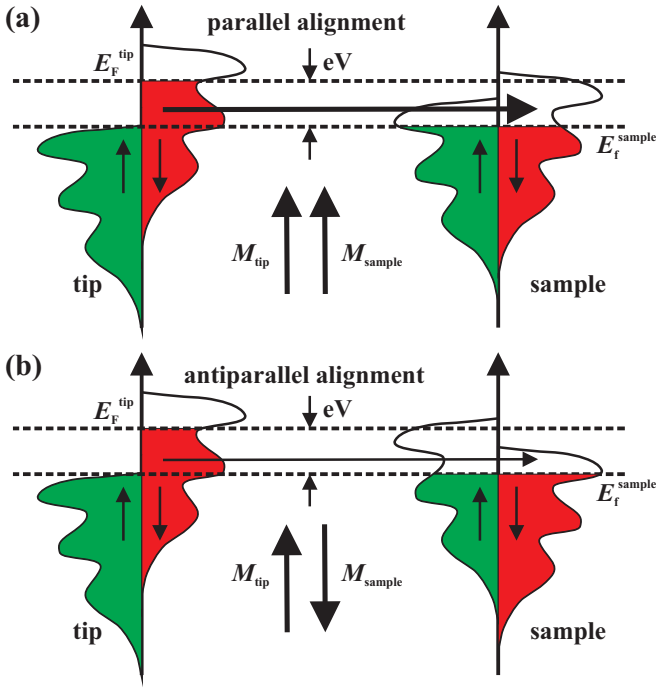

Figure 2.5: Illustration of the relative current strengths for SP-STM depending on the relative alignments of the magnetizations of tip and sample in case of spin conservation during the tunneling process. (a) For parallel alignment, the tunneling current is enhanced because the spin-down DOS of the unoccupied states of the sample exceeds the spin-down DOS for antiparallel alignment in subfigure (b). This is indicated by the smaller width of the arrow.

the magnetization. Figure 2.5 shows a ferromagnetic tip where the majority states (spin-up) are fully occupied (left panels). The tunneling current arises from the occupied minority tip states, i.e. the spin-down states above the Fermi level of the sample. Presuming spin conservation during the tunneling process, the tunneling current directly depends on the number of available unoccupied spin-down states of the sample. According to Fig. 2.5(a), for parallel alignment of the magnetizations of tip and sample, the spin-down states of the sample have to be the minority states. Thus, they exhibit a larger density of unoccupied states compared to the case of antiparallel alignment, shown in Fig. 2.5(b). Accordingly, the tunneling current is enhanced in the first case.

Bardeen's tunneling theory can be expanded to describe this situation properly. Therefore, the wave function ψ is replaced by a spinor describing spin-up and spin-down states (Reittu, 1997):

$$\psi^T = \begin{pmatrix} \psi^T_{\mu\uparrow}(\boldsymbol{r}) \\ 0 \end{pmatrix} \qquad \text{and} \qquad \psi^S = \begin{pmatrix} \psi^S_{\nu\uparrow}(\boldsymbol{r}) \\ \psi^S_{\nu\downarrow}(\boldsymbol{r}) \end{pmatrix} \tag{2.21}$$

Note, that here the spin polarization of the tip was used as a reference (Wortmann *et al.*, 2001). Therefore, it exhibits spin-up contributions only. Using this approach, the spin-dependent tunneling matrix elements are given by (Heinze, 2006):

$$M^{\sigma}_{\mu,\nu}(\boldsymbol{r}_0) = \left\langle \psi^{T}_{\mu\sigma} | U^{T}_{\sigma\sigma} | \psi^{S}_{\nu\sigma} \right\rangle = -\frac{2\pi C\hbar^2}{\kappa m}\psi^{S}_{\nu\sigma} \tag{2.22}$$

where $\boldsymbol{r}_0$ denotes the tip position vector, σ indicates the spin direction ($\uparrow, \downarrow$), C is the normalization factor according to Bardeen's theory and κ is the damping coefficient of the tunneling barrier. By defining the spin-averaged ($\rho = \rho_\uparrow + \rho_\downarrow$) and the spin-polarized DOS ($m = \rho_\uparrow - \rho_\downarrow$), the spin-averaged and spin-polarized parts of the tunneling current can be determined (Slonczewski, 1989):

$$\begin{aligned} I(\boldsymbol{r}_0, V, \theta) &= I_{\uparrow\uparrow}(\boldsymbol{r}_0, V) + I_{\uparrow\downarrow}(\boldsymbol{r}_0, V, \theta) \\ &= 2\frac{4\pi^3 C^2\hbar^3 \mathrm{e}}{\kappa^2 m^2} \cdot \left(\rho^T\rho^S(\boldsymbol{r}_0, V) + m^T m^S(\boldsymbol{r}_0, V) \cdot \cos(\theta)\right) \\ &= 2\frac{4\pi^3 C^2\hbar^3 \mathrm{e}}{\kappa^2 m^2} \cdot \rho^T\rho^S(\boldsymbol{r}_0, V) \cdot \left(1 + P^T P^S(\boldsymbol{r}_0, V) \cdot \cos(\theta)\right) \end{aligned} \tag{2.23}$$

where θ denotes the angle between the magnetizations of tip and sample $\theta = \angle(\boldsymbol{M}^S, \boldsymbol{M}^T)$ and P^i reflects the polarization parameter given by $P = m^i/\rho^i$. The cosine-dependence on θ particularly resembles the maximization of the signal for parallel alignment.

The ideal procedure of spin-polarized measurements depends on the needs for the respective experiment. Either bulk magnetic tips or nonmagnetic tips coated with a magnetic thin film can be used (Bode, 2003; Wiesendanger, 2009). The general difference is, that bulk tips in principle offer an infinite amount of magnetic material, whereas magnetic thin films can be depleted after certain time. This is especially important in view of the pulsing procedure (compare Sec. 2.1.1) usually necessary to finally achieve spin contrast. In addition, not all materials that are used for magnetic thin films, are useable for bulk magnetic tips as well.

A common material for bulk tips is Cr (Li Bassi *et al.*, 2007; Schlenhoff *et al.*, 2010). It exhibits antiferromagnetic properties. This consequently leads to an out-of-plane *magnetic uniaxial anisotropy* and to small stray fields. Thus, Cr bulk tips are mainly sensitive to the out-of-plane component of the sample's magnetization. They generally show a spin-polarization on the order of about 10 %.

In contrast, materials that are commonly used for thin films, are Co or Fe. These reveal ferromagnetic properties and, hence, larger stray fields compared to Cr bulk tips. Such thin film tips commonly exhibit coverage-dependent *spin reorientation transitions* with different anisotropies below or above a critical film thickness (Prokop *et al.*, 2006). The transition thickness is consequently chosen for the magnetic thin film tips. As a result, the tips are comparatively easy to manipulate by means of an external magnetic field. By this procedure, they can be tailored to exhibit either an in-plane or an out-of-plane sensitivity (Kubetzka *et al.*, 2005). Fe- and Co-tips generally exhibit a higher degree of spin-polarization compared to Cr-tips.

2.4 X-ray Absorption Spectroscopy

In 1895 *W. C. Röntgen* used cathode ray tubes and discovered a new type of radiation by finding fluorescent objects although the tube was hidden (Röntgen, 1895). *X-rays* received their name by Röntgen himself. They are characterized by wavelengths in the rage of 10^{-8} – 10^{-12} m. Using *L. de Broglie's* relation (De Broglie, 1970), this is equivalent to an energy range of 10^2 – 10^6 eV. The radiation is strongly ionizing and was initially used for *medical indication*, based on the fact that Ca, which is one of the main components of bones, has a comparatively high atomic number. It thus absorbs X-rays stronger compared to the remaining main elements in animal and human bodies, i.e. H, C, N, and O.

X-rays are usually generated by two different processes. The first makes use of the *photo effect*. Supposing high energetic electrons being shot toward a target, electrons from an inner core shell are removed. Subsequently, an electron from an outer shell fills up the inner hole by simultaneously emitting a photon. For an appropriate target, this photon is in the X-ray regime. By this approach only X-rays with specific energies can be generated depending on the level spacing of the target material. The second process is the emission of *deceleration radiation* by high energetic charged particles (usually electrons or positrons) if these are forced on bended trajectories. While at the beginning, in the 1970th, the X-rays from deceleration radiation were disrespectfully called the "waste product" of synchrotrons, their use has extremely grown in the past decades. Nowadays, X-rays are widely used to investigate structural, electronic, and magnetic properties in solid state physics (Schütz *et al.*, 1987; Chen *et al.*, 1995; Stöhr *et al.*, 1995; Gambardella *et al.*, 2003). Opposite to the first technique, the energy of X-rays from deceleration radiation can be easily tuned. Deceleration radiation hence turned out to be the leading technique for the production of X-rays.

Before the theory of the *X-ray absorption spectroscopy* is introduced, the main principle of the technique will be briefly described for the case of the *L*-edge X-ray absorption of a 3*d* transition metal. The layout of the experiment is schematically illustrated in Fig. 2.6. The X-rays are characterized by either positive h_+ or negative h_- helicity. These denote the projection of the intrinsic spin onto the propagation direction. The X-ray beam then illuminates the sample, which can be rotated about the *y*-axis. This way, it can be investigated with respect to its out-of-plane and in-plane properties. A magnetic field can be applied collinear to the incident beam to align the magnetic moments of the sample. This is a useful feature in view of the magnetic analysis using the *X-ray magnetic circular dichroism* effect.

Given a 3*d* TM sample, an electron of the target material can be excited from the $2p$ to the 3*d* shell. Once the photon's energy matches the $2p$-3*d* energy spacing, a strong resonance of the absorption will be detected. The particular detection is owing to the creation of a current, because the $2p$ hole state is immediately filled up by another electron from a higher energy level. This process causes the emission of an Auger electron and, thus, the rise of a current of the grounded sample. In this *total electron yield* mode, the current, given by the number of Auger electrons, is directly proportional to the number of primarily excited electrons. Therefore, it is a measure of the resonance intensity.

The actual absorption of X-rays depends on the matter's *linear absorption coefficient* μ. If the incident X-ray direction is given by *z*, the X-ray's intensity inside matter reads:

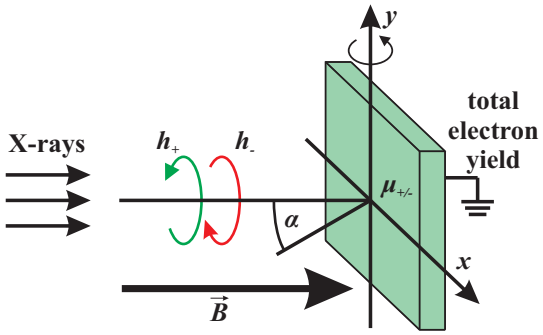

Figure 2.6: Schematic model of the XAS. h_+ and h_- denote the helicity of the X-rays. $\mu_\pm$ describes the magnetic absorption coefficient of the sample depending on the X-rays' helicity. α defines the incidence angle of the X-rays with respect to the surface plane. In addition, a magnetic field can usually be applied parallel to the incident beam.

$$I(z) = I_0 \cdot \mathrm{e}^{-\mu z} \tag{2.24}$$

where I_0 depicts the incident intensity of the X-ray. The exact value of μ is determined by the *absorption cross-section* σ^{abs} according to: $\mu = N_\mathrm{A}/A \cdot \rho_\mathrm{m}\sigma^{\mathrm{abs}}$, where N_A is Avogadro's number, A is the atomic mass number, and ρ_m is the atomic mass density. The calculation of the absorption cross-section hence depicts the main goal of the following theoretical treatment.

The description of a photon in the X-ray regime relies on the fact that this photon can be considered as an *electromagnetic wave*. Connecting electric and magnetic phenomena, electromagnetic waves (EMWs) are a key result of *Maxwell's* theory (Maxwell, 1864). EMWs can be described based on *Ampère's* circuital law, given by $\boldsymbol{\nabla} \times \boldsymbol{H} = \boldsymbol{j} + (\partial \boldsymbol{D})/(\partial t)$, where $\boldsymbol{D}$ is the dielectric field, $\boldsymbol{H}$ is the magnetizing field and $\boldsymbol{j}$ is the current density. As no particles exist in vacuum, the current density thus equals zero: $\boldsymbol{j} = 0$. With help of the equations $\boldsymbol{D} = \epsilon_0 \cdot \boldsymbol{E}$ and $\boldsymbol{B} = \mu_0 \cdot \boldsymbol{H}$, where μ_0 is the the vacuum permeability and ϵ_0 the vacuum permittivity, one obtains $\epsilon_0\mu_0(\partial \boldsymbol{E})/(\partial t) - \boldsymbol{\nabla} \times \boldsymbol{B} = 0$. This relation still depends on two fields, which is inconvenient if a simple solution is sought. After differentiating with respect to time and making use of the *Maxwell-Faraday* equation, the wave equation results in:

$$\frac{1}{\mathrm{c}^2}\frac{\partial^2 \boldsymbol{E}}{\partial t^2} - \boldsymbol{\nabla}^2 \boldsymbol{E} = 0 \tag{2.25}$$

where $\boldsymbol{E}$ is the electric field. Equation 2.25 is a differential equation of only one quantity, while its second derivative with respect to time is directly linked to its spatial variation. Any electric field $\boldsymbol{E}$ satisfying this equation is called an electromagnetic wave.

For a wave propagating with a wave vector $\boldsymbol{k}$ and a frequency ω, a solution of Eq. 2.25 is given by:

$$\boldsymbol{E}(\boldsymbol{r}, t) = \boldsymbol{\epsilon}_\mathrm{p} \cdot E_0 \mathrm{e}^{\mathrm{i}\boldsymbol{k}\boldsymbol{r} - \omega t} \tag{2.26}$$

with $\boldsymbol{\epsilon}_\mathrm{p}$ being a unit vector and indicating the *polarization* of the wave. E_0 defines the ampli-

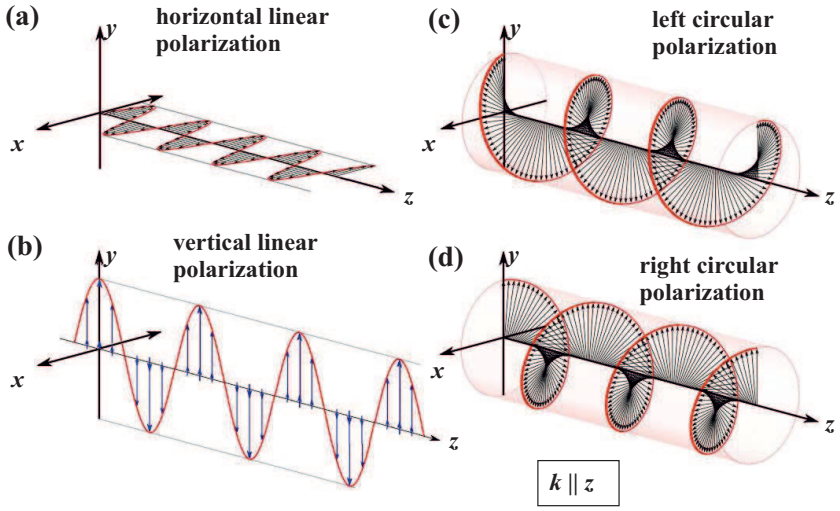

Figure 2.7: Illustration of linearly (a,b) and circularly (c,d) polarized light for the wave vector $\boldsymbol{k}$ being parallel to z. The electric field describes either a plane wave in the xz-/yz-plane or a homogeneous spiral motion about the z-direction.

tude of the electric field. To understand the concept of polarization, compare Fig. 2.7, it is important to comprehend the angular momentum of the wave. The charged particle which is circulating inside a synchrotron carries an *angular momentum* $\boldsymbol{L}$. The emission of a photon, i.e. an EMW, when the particle is forced on a bended trajectory, causes a transfer of both energy and angular momentum toward the photon. As a result of photons being Bosons, their angular momentum is $\boldsymbol{L} = 1$. According to quantum mechanics, the polarization of the EMW is then defined by the finite projection of the angular momentum L_z along the radiation emission direction z. For $\boldsymbol{L} = 1$, the allowed values of its projection are $L_z = 0, \pm\hbar$. If the radiation is emitted in the plane of the particle's orbit, the wave's propagation direction z is perpendicular to the angular momentum $\boldsymbol{L}$, compare Fig. 2.7(a,b). In these events, the wave is called *linearly polarized* ($L_z = 0$). Otherwise, the projection L_z is $+\hbar$ ($-\hbar$) where the wave is called *right (left) circularly polarized*, shown in Fig. 2.7(c,d). The polarization of an EMW is thus a direct consequence of the conservation of the angular momentum.

In the following, the polarization will be explicitly included in the definition of the wave function 2.26. For $k||z$, the vector of the electric field of the wave has to lie in the xy-plane. The linearly polarized basis states are consequently given by:

$$\begin{aligned} \boldsymbol{E}_x(z,t) &= \boldsymbol{\epsilon}_x E_0 \mathrm{e}^{\mathrm{i}(kz-\omega t)} \\ \boldsymbol{E}_y(z,t) &= \boldsymbol{\epsilon}_y E_0 \mathrm{e}^{\mathrm{i}(kz-\omega t)} \end{aligned} \tag{2.27}$$

According to Fig. 2.7(a,b), the electric field oscillates perpendicular to $\boldsymbol{k}$ along a single axis in space. Because the basis states in Eq. 2.27 are orthogonal to each other, any general polarization state of the EMW can be determined by a linear combination of these two states. Especially circularly polarized light is now easy to determine. It is characterized by equal amplitudes of the x- and y-components while these components are phase shifted by $\pi/2$. As a result, a continuous rotation of the electric field $\boldsymbol{E}$ is achieved, compare Fig. 2.7(c,d). The respective wave functions are given by:

$$\begin{aligned} \boldsymbol{E}_r(z,t) = \boldsymbol{E}_+(z,t) &= -\frac{1}{\sqrt{2}}\left(\boldsymbol{\epsilon}_x + i\boldsymbol{\epsilon}_y\right) E_0 \mathrm{e}^{\mathrm{i}(kz-\omega t)} \\ \boldsymbol{E}_l(z,t) = \boldsymbol{E}_-(z,t) &= \frac{1}{\sqrt{2}}\left(\boldsymbol{\epsilon}_x - i\boldsymbol{\epsilon}_y\right) E_0 \mathrm{e}^{\mathrm{i}(kz-\omega t)} \end{aligned} \tag{2.28}$$

Note, that it is common to use + and - to depict right and left circularly polarized light. Starting from these wave functions, the actual process of the absorption of the X-rays by an appropriate sample can be described in more detail as follows.

For the L-edge XAS of a $3d$ TM the excitation of a $2p$ core-electron to an unoccupied state of the $3d$-shell proceeds while respecting the *selection rules* of quantum mechanics. In this *one-electron approximation*, all remaining electrons are considered as being passive. This is not true in reality, but reflects an acceptable assumption and thereby a reasonable starting point.

Using the *time-dependent perturbation theory*, the transition probability per unit time T_{ab} from an initial state $|a\rangle$ to a final state $|b\rangle$ is given by *Fermi's golden rule* (Dirac, 1927):

$$T_{ab} = \frac{2\pi}{\hbar} |\langle b|\boldsymbol{H}_{\mathrm{int}}|a\rangle|^2 \, \delta\left(\epsilon_b - \epsilon_a - \hbar\omega\right) \rho\left(\epsilon_b\right) \tag{2.29}$$

where H_{int} is the Hamilton operator describing the interaction of the transition, $\rho\left(\epsilon_b\right)$ is the density of the available final states per unit energy and $\delta\left(\epsilon_b - \epsilon_a - \hbar\omega\right)$ describes the energy conservation during the transition. Presuming the absorption of an X-ray by an electron, the Hamiltonian H_{int} is given by the momentum $\boldsymbol{p}$ and the vector potential $\boldsymbol{A}$ belonging to the wave (Als-Nielsen *et al.*, 2001) according to: $\boldsymbol{H}_{\mathrm{int}} = \mathrm{e}\boldsymbol{p}\boldsymbol{A}/m_e$. In free space, the vector potential $\boldsymbol{A}$ is directly related to the electric field: $\boldsymbol{E} = -\partial\boldsymbol{A}/\partial t$. In case of a polarized wave, with the polarization unit vector $\boldsymbol{\epsilon}$ and the electron position vector $\boldsymbol{r}$ given in Cartesian coordinates, the interaction Hamiltonian reads: $\boldsymbol{H}_{\mathrm{int}} = \mathrm{e}|A_0|\boldsymbol{p}\cdot\boldsymbol{\epsilon}\cdot\mathrm{e}^{\mathrm{i}\boldsymbol{k}\boldsymbol{r}}/m_e$.

To eliminate the dependence of the transition matrix elements on the wave vector $\boldsymbol{k}$, the *electric dipole approximation* is applied. The Taylor series of the exponential function is thus used only up to first order $\mathrm{e}^{\mathrm{i}\boldsymbol{k}\boldsymbol{r}} = 1 + \mathrm{i}\boldsymbol{k}\boldsymbol{r} + \cdots \approx 1$. However, the first-order term is negligible, as: $\boldsymbol{k}\boldsymbol{r} \approx \alpha_{\mathrm{f}}/2 \ll 1$, where α_{f} is the fine structure constant. The approximation is reasonable if the size of the absorbing atomic shell is small compared to the X-ray's wavelength. The electric field can consequently be considered as being constant across the atom's volume. This condition is fulfilled in the range of *soft X-rays*, utilized within the studies at hand. The commutator: $\boldsymbol{p} = -\mathrm{i}m/\hbar[\boldsymbol{r}, \boldsymbol{H}]$ then enables to determine the transition probability (Stöhr *et al.*, 2006):

$$T_{ab} = \frac{2\pi}{\hbar}\mathrm{e}^2|A_0|^2\frac{\left(E_b - E_a\right)^2}{\hbar^2} |\langle b|\boldsymbol{\epsilon}\cdot\boldsymbol{r}|a\rangle|^2 \, \delta\left(\epsilon_b - \epsilon_a - \hbar\omega\right) \rho\left(\epsilon_b\right) \tag{2.30}$$

By means of the *Poynting vector* $\boldsymbol{S}$, that describes the energy flow of the EMW, the *absorption cross-section* σ^{abs} can be determined. It describes the ratio of the absorbed power to the incident power per unit area:

$$\sigma^{\mathrm{abs}} = \frac{\hbar\omega \cdot T_{ab}}{\mathrm{c} \cdot E_{\mathrm{dens}}} = \frac{\pi\mathrm{e}^2\omega}{\epsilon_0\mathrm{c}} |\langle b|\boldsymbol{\epsilon}\cdot\boldsymbol{r}|a\rangle|^2 \, \delta\left(\epsilon_b - \epsilon_a - \hbar\omega\right) \rho\left(\epsilon_b\right) \tag{2.31}$$

Here, the initial factor of $\hbar\omega$ describes the photon's energy taken out of the incident beam by the absorption process. Finally, the *polarization dependent X-ray absorption resonance intensity* I_{res} can be computed via the energy integral of the cross-section:

$$I_{\mathrm{res}} = 4\pi^2 \underbrace{\frac{\mathrm{e}^2}{4\pi\epsilon_0\hbar\mathrm{c}}}_{\alpha_{\mathrm{f}}} \hbar\omega \, |\langle b|\boldsymbol{\epsilon}\cdot\boldsymbol{r}|a\rangle|^2 \tag{2.32}$$

The initial and final state wave functions are now volume normalized to unity, which lets the density of final states per unit energy $\rho(\epsilon_b)$ becoming obsolete.

The transition probability (Eq. 2.30), the absorption cross-section (Eq. 2.31), and the resonance intensity (Eq. 2.32) clearly depend on the determination of the transition matrix element $\boldsymbol{\epsilon}\cdot\boldsymbol{r}$, whereas the polarization unit vector is given by Eqs. 2.27 and 2.28. A detailed analysis of this tensor operator reveals, that the matrix elements factorize into a spin part, a radial part, and an angular part. Thereby, the spherical harmonics influence only the angular part, which means, that especially the spin is unaffected. It hence needs to be preserved during the transition. An additional investigation of the radial part shows the *element-specificity* of the XAS owing to the strong localization of the core shell. These findings particularly depict the selection rules, that need to be respected during the transition. They describe the allowed changes of the quantum numbers of the orbital angular momentum l, the projection of the angular momentum m_l, the intrinsic angular momentum, i.e. the spin s, and the projection of the spin m_s along the specified axis for a given transition:

$$\begin{aligned} \Delta m_s &= 0 \\ \Delta s &= 0 \\ \Delta m_l &= 0, \pm 1 \\ \Delta l &= \pm 1 \end{aligned} \tag{2.33}$$

2.5 The X-ray Magnetic Circular Dichroism Effect

The previous section showed, that the resonance intensity depends on the density of available unoccupied final states. The SOI of the initial $2p$ states causes a separation of the resonant transitions into two resonance absorption edges ($L_{2/3}$ edges). The existence of an *exchange interaction* between localized spins in the $3d$ states furthermore causes an exchange splitting. Consequently, a different DOS for minority and majority states is obtained.

This is exemplarily described by the *Stoner model* of a half-metallic ferromagnet in Fig. 2.8. In this case, the majority states (spin-up) are fully occupied, whereas the minority states (spin-down) are only partially filled. The Stoner model and the equivalent atomic d shell model illustrate the prohibition of spin-down excitations if *spin conservation* during the transition is assumed. The *X-ray magnetic circular dichroism* effect was found in 1987 (Schütz *et al.*, 1987) and makes use of the induced asymmetry. The resonance intensity depends on the relative alignment between the spin of the polarized photons and the density of available final states which now is spin-split. The transitions from initial to final states are hence polarized with

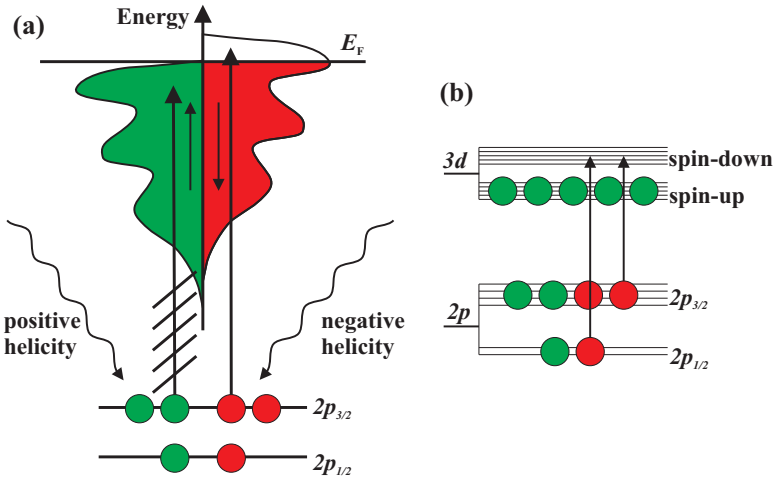

Figure 2.8: (a) Illustration of the XMCD effect using the Stoner band model. The exchange interaction causes different populations of spin-up and spin-down states. The spin-up states are entirely occupied, depicting here the case of a half-metallic ferromagnet. Hence, only spin-down transitions are allowed assuming spin conservation during the transition. (b) The respective atomic *d* shell model of the XMCD effect indicating the absence of spin-up excitations.

respect to both spin and angular momentum. The effect is maximized if the magnetization direction of the sample and the angular momentum of the incident photon are collinear. In this case the dichroic signal is measured using parallel and antiparallel alignment between the photon's angular momentum and the magnetization direction of the sample:

$$\Delta I = I^{\uparrow\downarrow} - I^{\uparrow\uparrow} = I^{-} - I^{+} \tag{2.34}$$

where I^{-} (I^{+}) describe the transition intensities with negative (positive) photon spin. Using this definition, the XMCD becomes negative for the L_3-edge, which is the common convention. Assuming spin conservation during the transition, the exact estimation of the XMCD depends on the angular part of the squared transition matrix element from the spin-orbit split *p*-states to the exchange-split unoccupied states of the 3*d*-shell. The XMCD is thus proportional to the atomic magnetic moment, i.e. the angular momentum.

Whereas for a total angular momentum of $m_j = \pm 3/2$ only single combinations according to $m_l + m_s = m_j$ exist, other values of m_j, e.g. $m_j = +1/2$ can be a result of different combinations. The weight of different transitions varies due to different transition matrix elements. This is exemplarily shown in Fig. 2.9. As a result of the XMCD given by the difference of transitions with opposite photon spin, the appropriate intensities have to be summed up. This way, the dichroism at the respective edge can be estimated with respect to both, spin and angular momentum polarization. In general, the XMCD includes also non-resonant dichroic effects from $p \rightarrow s$ transitions. Anyhow, these are usually neglected because they are smaller by a factor of > 20.

In an experiment, the alignment of the magnetization direction of the sample $\boldsymbol{M}$ and the angular momentum of the photon $\boldsymbol{L}_{\mathrm{ph}}$ can be controlled by using X-rays with opposite helicity.

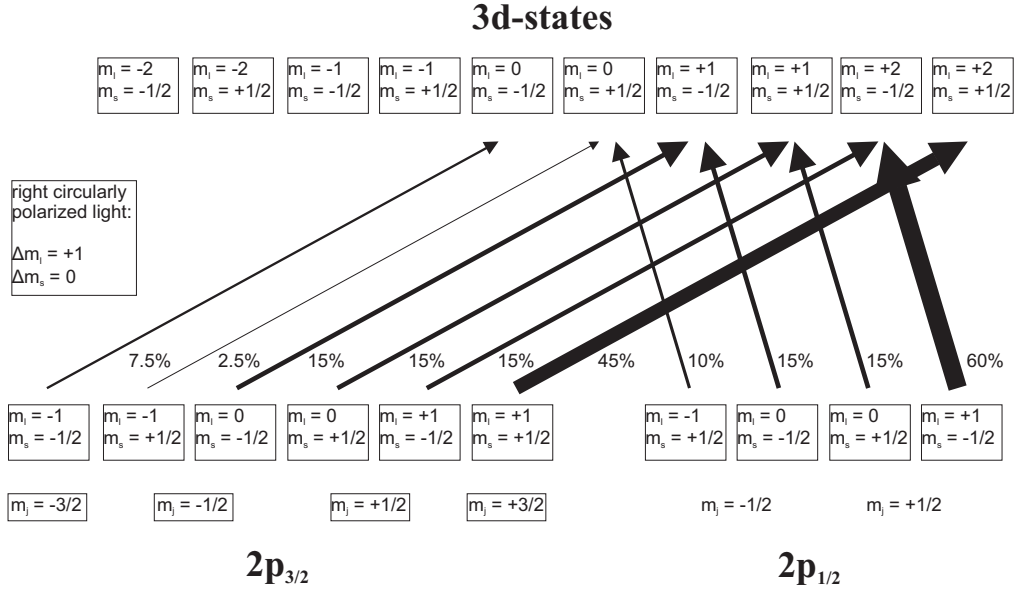

Figure 2.9: Overview of the $2p \rightarrow 3d$ transition probabilities for the excitation using right circularly polarized X-rays. The arrow widths indicate the weight of the respective channel.

Alternatively, the sample's magnetization can be inverted by means of an external magnetic field, that is applied collinear to the incident beam, compare Fig. 2.6. Considering the degree of polarization of the incident photon P_{circ}, the intensity of the XMCD basically depends on three parameters:

$$I_{\text{XMCD}} \propto P_{\text{circ}} \boldsymbol{M} \cdot \boldsymbol{L}_{\text{ph}} \tag{2.35}$$

A typical experimental spectrum obtained by means of XAS can be found in Fig. 2.10. In this case, 0.08 atomic layer equivalent (ALE) of Co nanostructures on the surface of Bi_2Se_3 were investigated. Besides the signals of positive (μ_+) and negative (μ_-) helicity, the average signal ($\mu_+ + \mu_-$) is also given. Here and in the following, $\mu(E)$ is referred to as the polarization-dependent magnetic absorption profile. The spectra are obtained by comparing the current induced in the sample (total electron yield mode) to the initially determined beam intensity. This intensity is measured by utilizing a gold foil, that is applied to a part of the X-ray beam before the actual target. As a result, the absorption intensity depending on the X-ray's energy can be computed. PyMca software is available for an initial evaluation of the data (Solé *et al.*, 2007). For the studies at hand, MatLab was used to intensify the analysis (Matlab, n. d.).

The XAS spectra of 3*d* TMs are characterized by two main resonances, separated by ≈ 10 – 15 eV, called the L_2 and L_3-absorption edges. The separation is caused by the SOI which splits the initial state into two states, namely the $2p_{1/2}$ (L_2-edge) and the $2p_{3/2}$ (L_3-edge) state. Since the $2p_{3/2}$ state has a lower binding energy, the respective L_3-edge consequently occurs lower in energy. The relative intensities of both edges are related to the transition probabilities and the unequal populations of the initial states ($2p_{1/2}$: 2 electrons; $2p_{3/2}$: 4 electrons). Besides the main resonances, a step-like background at each L-edge can be observed, compare Fig. 2.10(a). That is due to non-resonant excitation channels, e.g. by $2p \rightarrow 3s$ and $2p \rightarrow 3p$ excitations.

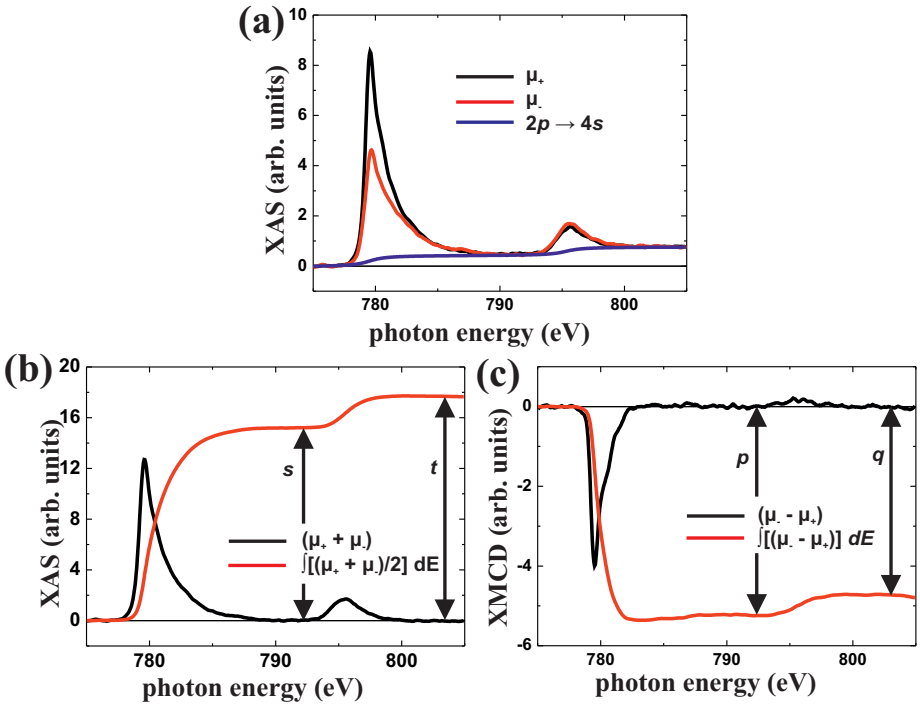

Figure 2.10: (a) Exemplary X-ray absorption spectra of Co nanostructures on Bi_2Se_3. The spectra taken with different helicity exhibit a step-like background caused by nonresonant transitions. (b) The averaged XAS spectrum after the normalization with respect to the non-resonant background and its integrated signal. (c) The according XMCD spectrum and its respective integral resulting from the difference of the XAS spectra with opposite helicity. The intensities of the integrated XAS and XMCD at the L_3-edge (s, p) and at the L_2-edge (t, q) are needed to analyze the experimental data by means of the sum rules and related quantities.

Based on the fact, that the magnetic properties are mainly related to transitions into 3*d*-states, step functions are commonly used to renormalize the spectra, compare Fig. 2.10(b). In this procedure, the actual step is simulated by an *inverse trigonometric function*: $\arctan E - E_{L_{2/3}}$, where $E_{L_{2/3}}$ depicts the energetic positions of the resonances of the $L_{2/3}$-edges. The amplitude of the arctan-function is adjusted to the XAS intensity well beyond the resonance.

Finally, the XMCD is given by the difference of the XAS spectra with opposite helicity. The dichroism at the L_3 edge is negative per definition, shown in Fig. 2.10(c). The integrated XAS and XMCD intensities are used to analyze the data in more detail, compare Sec. 2.6.

2.6 The Sum Rules

The *sum rules* allow conclusions about different valence band properties based on the experimentally obtained polarization dependent resonance intensities. In particular, they can be used to determine the number of holes in the valence band n_h, the effective magnetic spin moment m_{eff} per atom and the orbital magnetic moment m_l per atom. The calculations make use of the integrated XAS and XMCD spectra at the L_3 and L_2 edges, which are indicated in

Figs. 2.10(b,c) by the variables *s*, *t*, *p*, and *q*.

The *charge sum rule* links the number of empty states in the 3*d*-shell to the XAS intensity:

$$n_\mathrm{h} + n_\mathrm{Q} =< I > \cdot \underbrace{\frac{1}{4\pi^2\hbar\omega\alpha_\mathrm{f}\boldsymbol{R}^2\frac{L}{3(2L+1)}}}_{1/C} \tag{2.36}$$

where n_Q is a quadrupole term arising from the anisotropy of the charge density in the atomic volume, L is the orbital angular momentum of the final state and $\boldsymbol{R}$ is the radial part of the transition matrix element, given by $\boldsymbol{R} = \langle R_{n',l'}(r)|r|R_{n,l}(r)\rangle$. Here, $R_{n,l}(r)$ ($R_{n',l'}(r)$) is the radial component of the valence (core) state of shell n (n'). For a 3*d* TM, the number of holes can hence be determined by measuring the XAS intensities at the L_3/L_2 edges (Stöhr *et al.*, 1995):

$$n_\mathrm{h} + n_\mathrm{Q} = \int_{L_3+L_2} (\mu_- + \mu_+)\,\mathrm{d}E \cdot \frac{1}{C} = \frac{t}{C} \tag{2.37}$$

Angular averaging causes the quadrupole term n_Q to vanish. Acquiring the XAS along all three orthogonal directions thus enables to obtain the projection of the number of holes along these directions. In reality, measuring data along all spatial directions is usually impossible.

The second sum rule, i.e. the *spin sum rule*, requires the saturation of the magnetic moments of the sample. Furthermore, the difference of the XMCD with the wave vector $\boldsymbol{k}$ being parallel/antiparallel to the magnetization direction needs to be determined. The spin sum rule then reads (Carra *et al.*, 1993):

$$m_{S,\,eff} = -\frac{6\int_{L_3}(\mu_- - \mu_+)\,\mathrm{d}E - 4\int_{L_3+L_2}(\mu_- - \mu_+)\,\mathrm{d}E}{\int_{L_3+L_2}(\mu_+ + \mu_-)\,\mathrm{d}E} \cdot n_\mathrm{h} = -\frac{6p-4q}{t} \cdot n_\mathrm{h} \tag{2.38}$$

It connects the size of the effective spin moment $m_{S,\,eff}$ to the dichroism intensities. The effective magnetic spin moment includes the magnetic spin moment m_S and the spin dipole moment m_D according to: $m_{\mathrm{S,\,eff}} = m_S + m_D$. It is given in Bohr magnetons per atom. If the ligand field effects are comparable to the atomic SOI, the charge distribution and the spin distribution are coupled to each other. As a consequence, the intra-atomic magnetic dipole moment m_D needs to be considered, that describes an anisotropy of the spin density when the atomic cloud is distorted (Stöhr *et al.*, 2006).

The last sum rule is the *orbital moment sum rule*. It enables to determine the orbital magnetic moment according to Thole *et al.*, 1992:

$$m_L = -\frac{4}{3} \cdot \frac{\int_{L_3+L_2}(\mu_- - \mu_+)\,\mathrm{d}E}{\int_{L_3+L_2}(\mu_+ + \mu_-)\,\mathrm{d}E} \cdot n_\mathrm{h} = -\frac{4}{3} \cdot \frac{q}{t} \cdot n_\mathrm{h} \tag{2.39}$$

The orbital moment m_L also depends on the dichroism intensities. Opposite to the case of the effective spin moment, the individual contributions are differently weighted. The orbital

moment is commonly highly anisotropic due to the ligand field, that strongly affects the orbital motion of the electrons with respect to certain axes. Measuring the difference of the orbital moments along the easy and hard axis therefore opens access to the magnetocrystalline anisotropy energy (MAE).

Note, that the sum rules strictly may only be applied if the sample is fully magnetized. Owing to the individual adatoms mainly investigated within the studies at hand, this saturation is a challenging task, based on two reasons. Firstly, the available external magnetic field is limited ($B_{\mathrm{max}} = 5$ T). Secondly, the external magnetic field required to reach the saturation magnetization generally increases if the particle's size decreases.

The *ratio R* of orbital magnetic moment to effective spin moment is therefore an important quantity. It can be used to draw conclusions even if saturation is not achieved. Another advantage is, that the ratio is independent of the number of holes n_{h}, a quantity, that usually has to be gained from theoretical calculations. R can hence be independently calculated using the experimental data:

$$R = \frac{m_L}{m_S + m_D} = \frac{2\int_{L_3+L_2}(\mu_- - \mu_+)\,\mathrm{d}E}{9\int_{L_3}(\mu_- - \mu_+)\,\mathrm{d}E - 6\int_{L_3+L_2}(\mu_- - \mu_+)\,\mathrm{d}E} = \frac{2q}{9p - 6q} \tag{2.40}$$

A further interesting quantity related to the sum rules is the *branching ratio BR*. It is determined by the XAS intensity of the L_2/L_3-edges according to:

$$BR = \frac{\int_{L_3}(\mu_+ + \mu_-)\,\mathrm{d}E}{\int_{L_3+L_2}(\mu_+ + \mu_-)\,\mathrm{d}E} = \frac{s}{t} \tag{2.41}$$

BR can be used to indicate the character of the *spin ground state* of the investigated material supposing a fairly weak SOI of the valence states. This applies to 3*d* TMs (≈ 50meV). Consequently, *BR* basically reflects the value of the atomic state (Thole *et al.*, 1988). The statistical value of $BR = 0.66$ is achieved in the absence of both SOI in the initial state and electrostatic interactions (between core hole and valence electrons) in the final state. Importantly, high-spin states on average have a larger *BR* than low-spin states. Besides, the branching ratio only weakly depends on the *crystal-field splitting*, except if it produces a low-spin ground state. This is important because the crystal-field splitting, that originates from electrostatic forces caused by the charge distribution of the vicinity, can be of considerable size at surfaces owing to the broken symmetry. In view of the high-spin ground states found within all investigations at hand, this aspect has not to be considered anymore.

Chapter 3

Measurement Setups

The measurements were performed in two separate experimental setups. The home-built scanning tunneling microscope used for local scale investigations was set up in 2007 in a low-vibration laboratory particularly designed for high-standard STM measurements. The STM was part of a complex *ultrahigh vacuum* system equipped with a ^{4}He bath cryostat and a magnet operable in all three spatial directions. Therefore, this system is entitled the *Triple Axes Magnet System* and described in more detail in the following section.

Section 3.2 deals with the second experimental setup, that was used within the X-ray dependent measurements, the *ID08 beamline* at the *European Synchrotron Radiation Facility* (ESRF, n. d.) in Grenoble. The key feature was again a ^{4}He bath cryostat inside an ultrahigh vacuum (UHV) chamber which was equipped with a magnet aligned collinear to the incidence beam direction.

3.1 The Triple Axes Magnet System

The experimental setup comprised a multi-chamber UHV system which was designed in-house (Meckler *et al.*, 2009; Meckler, 2010) and fabricated by an external company (Omicron, n. d.). It served for in-situ preparation and characterization of the samples by means of STM, STS, and SP-STM. The entire system was divided into three main chambers, namely the *cryostat-*, the *growth-*, and the *preparation-chamber*, compare Fig. 3.1. The transfer of samples between separate chambers was achieved by means of vertical and horizontal *transfer rods* and *manipulators*. In addition, within the growth- and the cryostat-chamber, objects could be transferred utilizing mechanical hands. Tips were clamped inside a tip holder. Unfortunately, even this piece was too small to be handled by mechanical hands or transfer rods. Instead, *tip transporters* could be used for this purpose. They could carry the tip holder and in principle be handled similar to sample holders.

During the experiments, all chambers were operated at base pressures in the low 10^{-10} mbar range or better. The UHV was achieved by a combination of multiple pumps with varying operating mechanisms. Separate turbo pumps, ion getter pumps (IGPs), and titanium sublimation pumps (TSPs) were attached to each of the aforementioned chambers. Turbo pumps can be considered as turbines combined with a connected rough pump. As a result of their

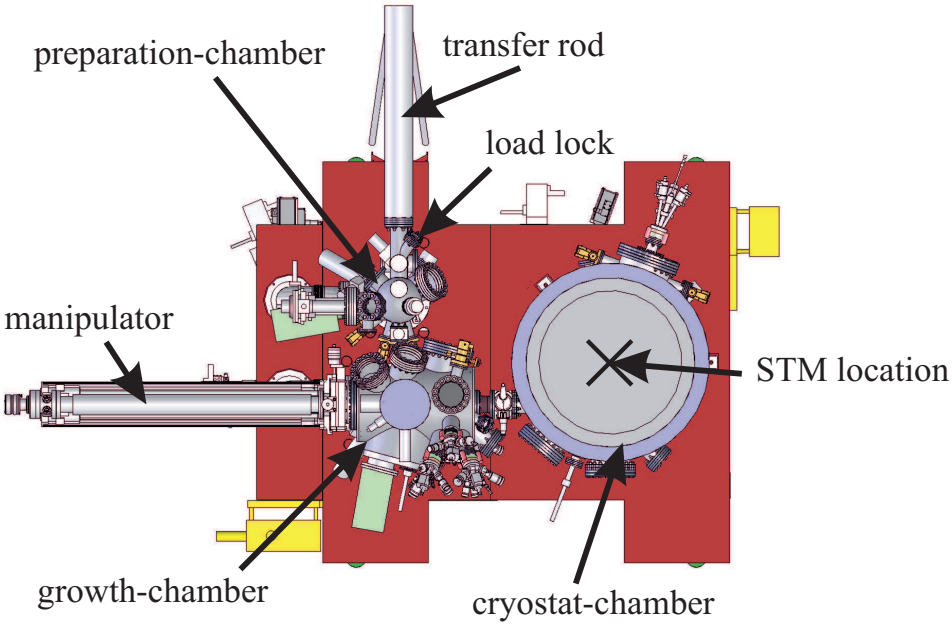

Figure 3.1: Schematic model of the triple axes magnet system (top view) including all three separate UHV chambers with the preparation facilities and the transfer devices.

extreme rotational frequencies (about 1 kHz), they are able to effectively establish UHV conditions. Turbo pumps were mainly used for the initial pump down of a chamber after venting. Additionally, they were required if process gases are involved. In contrast, they were turned off while acquiring STM data. Owing to induced vibrations the quality of the STM experiments would had suffered otherwise. Therefore, IGPs were mainly used during STM because their working principle gets along without vibrating parts. IGPs operate by ionizing rest gas molecules. These are subsequently bound on suitable surfaces which effectively reduces the respective partial pressures. The working principle of a TSP bases on the evaporation of a Ti film on the walls of the particular chamber. The pumping effect is caused by the trapping of residual gas atoms by the Ti atoms. Moreover, a non-evaporable getter pump was mounted to the cryostat-chamber exclusively. It especially traped H because the pumping efficiency of the other pump types regarding H is small.

3.1.1 The Cryostat Chamber

The cryostat-chamber involved a ^{4}He *bath cryostat*, manufactured by Cryovac (CryoVac, n. d.). According to Fig. 3.2 the STM was located in the middle of three pairs of split-coil magnets, delivered by Scientific Magnetics (Scientific Magnetics, n. d.). The combination of three magnets enabled to apply a *fully-rotatable magnetic field* to the sample. Except a *triple electron beam evaporator*, that was attached to the backside of the cryostat-chamber, all other preparation facilities were set up in the remaining two chambers.

The sectional view of the cryostat-chamber bares the general layout of the cryostat consisting of two individual dewars. During operation, the outer dewar was filled with liquid nitrogen exhibiting a temperature of 77.2 K. It was isolated from the outer UHV chamber walls by the

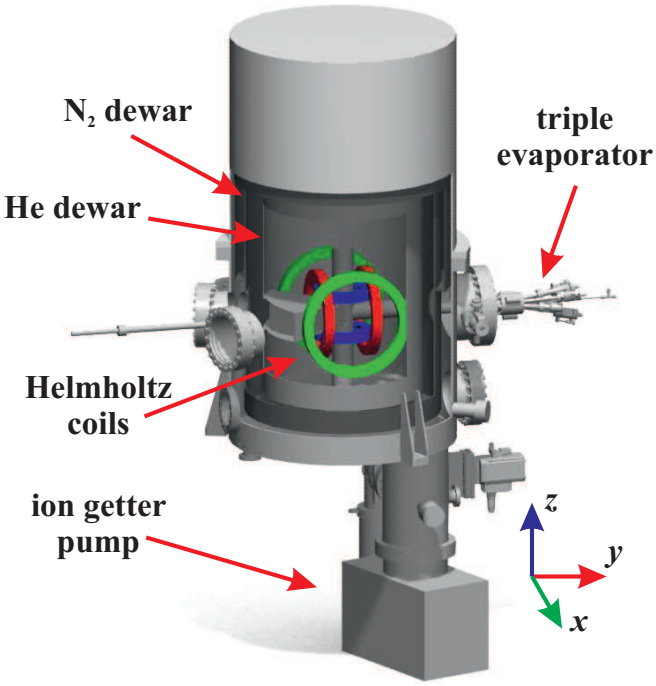

Figure 3.2: Schematic model (sectional view) of the cryostat-chamber with the split coil magnet, the LN_2 as well as the ^{4}He dewar, and a triple evaporator mounted on the backside of the transfer opening. Adapted from Gyamfi, 2012b with permission.

UHV itself. This was as well the UHV present at the microscope meaning, that the cryostat was not superinsulated. The nitrogen dewar contained another dewar, which was filled with liquid ^{4}He and facilitated a temperature of 4.2 K during operation. The capacity of this dewar was about 110 l. The large capacities of both reservoirs were chosen to guarantee a hold time of at least 48 hours before refilling of cryogenic liquids was necessary. By means of a cooling shield, that was attached to the ^{4}He dewar, the microscope was mounted from the bottom side. Its position was carefully adjusted with respect to the triple axes magnet. Additional cooling shields mounted at the front and back opening of the cryostat served for an effective thermal isolation from room temperature reservoirs. If these shields were lifted, the openings enabled access to the microscope using a mechanical hand or the electron beam (e-beam) evaporator.

The magnet represented the key feature of this setup. It was a combination of three *superconducting magnets* located inside the He reservoir, marked in blue, red, and green in Fig. 3.2. Each of the magnets consisted of a pair of *Helmholtz coils*. These coils exhibit equal winding numbers and are separated by a distance R corresponding to their radii. In general, if a current is applied to a coil, a magnetic field is created at its center. In case of a pair of Helmholtz coils, an equal current is applied in the same direction through both coils simultaneously. As a result, the magnetic field generated in the spacing between both coils can be considered as being *homogeneous*. Compared to permanent magnets, the advantage is given by the possibility to achieve much stronger magnetic fields with less volume and weight. Moreover, the magnetic field strength is easy to manipulate and can be turned off, a feature not achievable by permanent magnets.

The three pairs of Helmholtz coils were aligned along all three spatial directions around the

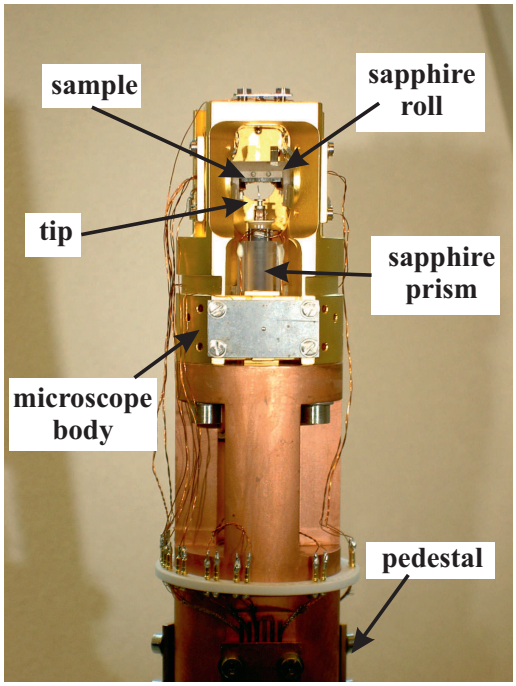

Figure 3.3: Front view of the STM before its installation into the UHV system.

STM position. This way, a magnetic field in an arbitrary direction could be applied to tip and sample. If multiple magnets were used, a maximum magnetic field strength of a cylindrical shape with $\boldsymbol{B}_x = \boldsymbol{B}_y = 1$ T, and $\boldsymbol{B}_z = 3$ T could be achieved. If the magnets were used individually, the maximum field strengths are $\boldsymbol{B}_x = \boldsymbol{B}_y = 1.3$ T, and $\boldsymbol{B}_z = 5$ T.

3.1.2 The Scanning Tunneling Microscope

Figure 3.3 depicts the *home-built scanning tunneling microscope*, that was designed and assembled by *M. Gyamfi* (Gyamfi, 2007). The pedestal was made of oxygen-free high conductivity (OFHC) copper. The material was chosen owing to its high thermal and electrical conductivity and for its capability to be easily machinable. The pedestal was used for mounting the entire microscope to the base plate of the ^{4}He dewar and for cooling the cables by clamping them in individual slots.

The microscope body, mounted on top of the pedestal, was made of *phosphorus bronze*. Opposite to OFHC copper, this material is fairly wearless. This is an important aspect because the body contained several threaded holes. A body made of Cu would suffer from tightening and loosening screws several times because the material is too soft. The microscope body was coated with a thin gold film to enhance its emissivity. As a result, the thermal radiation absorbed by the STM was reduced to optimize its base temperature.

The tip holder could be clamped in the tip receptacle. The receptacle was mounted into an insulating bushing at the upper end of a *piezoceramic tube*. As already mentioned in Sec. 2.1.1, the bendable piezoceramic tube is the key component of an STM to establish the scanning process on the sample in a controlled manner. The tube itself was glued to the *sapphire prism*, that

was clamped between three pairs of *piezoceramic stacks*. The stacks were each made of four layers of piezoceramic material with an additional aluminum oxide layer on top. Importantly, sapphire is nothing else than a different variety of Al_2O_3. This way, the touching materials exhibited a similar hardness. A movement of the sapphire prism relative to the piezoceramic stacks did thus not cause any wearing. The piezoceramic stacks could be sheared using a potential difference on opposite facets of each layer.

The actual movement can in principle be achieved by a saw-tooth like voltage signal. Applying this signal to the stacks causes a synchronous shearing of all stacks in the same direction. On the smooth slope of the signal, the sapphire prism moves simultaneously, while on the steep slope the prism is not able to follow. The transition between *static* and *dynamic friction* is the key issue for this so-called *stick-slip-approach*. It enables a movement of the sapphire prism relative to the body, while carrying the tip, toward or away from the sample. Note, that the leaf spring determining the clamping force on the sapphire prism has to be adjusted very precisely to enable this movement.

In general, samples were glued or clamped to the holder. For experiments, the holder was stuck upside down to the sample receptacle. For this microscope, the sample receptacle was also made of sapphire and has a cylindrical shape (*sapphire roll*). This layout bared the possibility to use basically an equal mounting mechanism. The sapphire roll was clamped between three pairs of piezoceramic stacks. Thereby, a rotation of the roll could be achieved and the sample's front was able facing toward the backside of the microscope. As mentioned before, a triple evaporator was mounted on the backside. This arrangement allowed the deposition of material directly on the cold sample. Another feature of this microscope was a *resistive sample heater* integrated into the roll. A temperature range between 4.2 K and 130 K was available. For the ability to precisely monitor the preparation conditions during deposition, approach, or heating a Cernox™ (Lake Shore, n. d.) *temperature sensor* was mounted next to the sample receptacle.

3.1.3 The Preparation Facilities

The preparation facilities were divided into two groups. The growth-chamber contained devices, that were used for processes which require ideal vacuum conditions, shown in the left panel in Fig. 3.4. Instead, processes which produce loads of pollution or require the use of process gases were located in the preparation-chamber, compare the right panel in Fig. 3.4. In addition, the load lock was attached as a small side chamber to the preparation-chamber. The cryostat turbo pump could be used to separately establish a vacuum in this side chamber, that however was usually not additionally baked. Therefore, its vacuum was worse than the vacua of the remaining chambers and attaching it to a different chamber than the preparation-chamber would had been counterproductive.

The Growth Chamber

The growth-chamber provided the possibility of performing *low energy electron diffraction* and *Auger electron spectroscopy*. Moreover, it contained further e-beam evaporators to grow nanostructures at variable temperatures ranging from 85 K to approximately 1400 K.

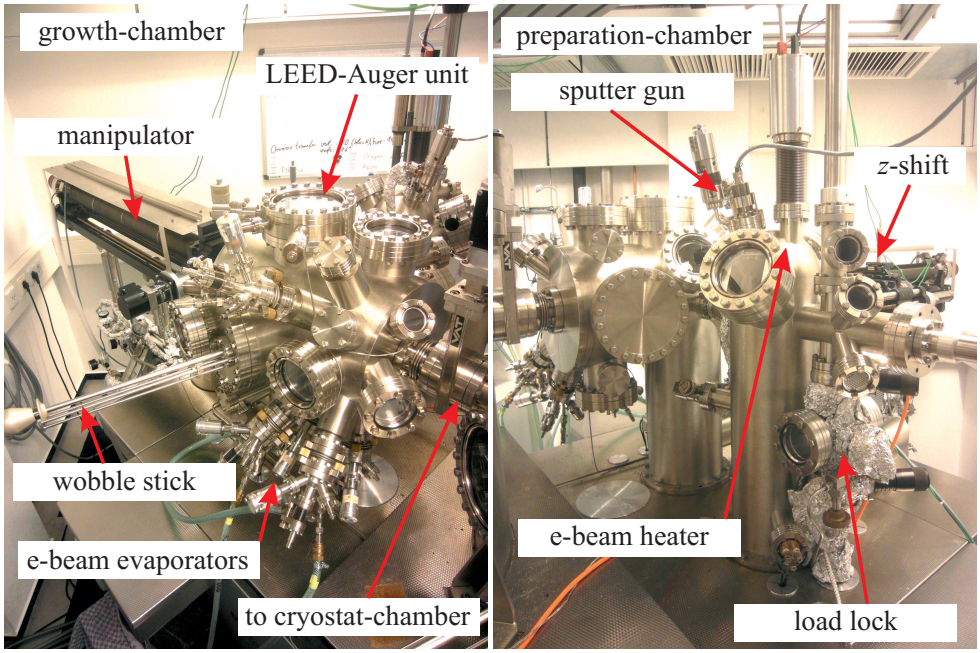

Figure 3.4: Photographies of the growth- and preparation-chamber illustrating the UHV setup. The processes that produce heavy gas loads, such as sputtering and high temperature annealing with an applied process gas, are combined in the preparation-chamber. The growth-chamber is primarily used for MBE to obtain well defined sample systems.

Low energy electron diffraction (LEED) is used to investigate the *lattice periodicity* of the surface. The low energetic electrons, emitted by a filament in front of the sample, are scattered by the crystal lattice and detected as a diffraction pattern on a luminescent screen. The obtained pattern resembles the lattice periodicity of the surface near layers in the reciprocal space. This technique is very useful to identify reconstructed surfaces. These often occur if the contamination level is too high. Alternatively, they appear as a result of insufficient preparation conditions, e.g. too low annealing temperatures.

The LEED device could be used as well for Auger electron spectroscopy (AES). This technique is sensitive to *surface contaminants*. In this process, inner-shell electrons of the surface atoms are removed by external excitation using high-energetic electrons. The remaining inner hole is filled up with a weaker bonded outer-shell electron. The energy gained by this mechanism is excited as a photon of a characteristic energy. As a result of the detection of these photons, the chemical composition of the surface can be easily investigated with respect to the degree of contamination. Note, that the detection level of AES is limited. In general, individual contaminants are beyond this detection level. AES was thus not solely able to judge the contamination level on the atomic scale. To this end STM had to be applied.

A different but very important technique for the preparation of appropriately designed samples/tips is the *molecular beam epitaxy* using e-beam evaporators. The material (evaporant) is placed near a filament in a crucible or as a rod. Heating the material by electron bombardment causes atoms to sublimate into the gas phase. Consequently, a beam of gaseous atoms (flux) can be focused toward the sample or tip. With appropriate parameters of the current- and voltage-dependent flux, the deposition rates can be precisely controlled. The desired coverage

can thus be easily achieved by adjusting the deposition time. The technique is of extreme importance because many effects, e.g. the magnetocrystalline anisotropy direction, depend critically on the coverage (Baudelet *et al.*, 1995; Hauschild *et al.*, 1998).

On the one hand, the morphology of the sample after the deposition is usually strongly correlated to the temperature during the growth process. On the other hand, post-deposition annealing might also be of high importance to achieve a smooth and well-defined surface. For this reason, the temperature of the receptacle used for samples/tips during molecular beam epitaxy (MBE) was adjustable. Cooling was established by means of an external feed through, used with liquid nitrogen. In addition, a *resistive heater*, made of pyrolytic boron nitride (pBN), was attached. This way, a wide temperature range of $\approx 85-1400$ K was available. The heatable/coolable receptacle was attached to the same *manipulator*, that also served for transferring samples/tips into the cryostat-chamber. As a result, the morphology of the sample could be maintained until the investigation by means of STM started.

The Preparation Chamber

While the aforementioned preparation devices and methods were mounted to the growth-chamber, the remaining preparation devices were attached to the preparation-chamber. It contained a *sputter ion gun*, a second resistive heater, and an additional heater offering much higher temperatures utilizing electron bombardment.

Sputtering is an important process often used to initially clean metallic surfaces. The sputter ion gun is always operated with an inert process gas, e.g. Ar. The gaseous Ar atoms are ionized using a filament and subsequently accelerated toward the sample. The sputtering current can simply be measured by the Ar-ions impinging on the grounded sample surface. The current strongly depends on the partial pressure of the Ar atmosphere and the applied acceleration voltage. It is hence easy to stabilize. The impact of the high-energy ions on the sample results in surface-near atoms blasting off the substrate. The technique was mainly used to remove initial layers of contamination from the substrate. Moreover, it can in principle also be used to increase the surface roughness or to induce defects in the sample by implanting process gas ions.

The sample receptacle used for holding the samples during the sputtering process provided the possibility to heat the sample during the process or afterward. To this end, the sample stage bore a resistive pBN heater offering temperatures between room temperature and a maximum of $\approx$ 1400 K. The pBN heater had in principle the disadvantage that the entire receptacle became warm during operation. Especially for long term annealing, the pressure usually increased significantly. This corrupted the preparation conditions and the sample quality.

For this reason, another heater type, i.e. an e-beam heater, was installed in the preparation-chamber. The device bases on electrons, that are accelerated from a filament toward the sample/tip using acceleration voltages. As a result, the object could be locally heated and the process pressure was strongly improved. Another advantage of the e-beam heater was given by the maximum temperature accessible, that was increased to more than 2500 K. These high temperatures were particularly needed for the preparation of some metallic substrates, e.g. the (110) surface of tungsten (Bode *et al.*, 2007).

3.2 The ID08 Dragon Beamline

The ID08 beamline was a measurement stage at the European Synchrotron Radiation Facility (ESRF, n. d.). This user facility is financed by more than fifteen European countries to offer their scientists the chance to perform state-of-the-art investigations. Almost fifty different apertures, the so-called *beamlines*, enable a wide range of experiments with hard as well as soft X-rays. For the investigation of individual transition metal adatoms, the ID08 beamline was chosen, because it provided *soft X-rays* with *high polarization*. Moreover, it involved a cryogenic UHV measurement stage and exhibited the opportunity to deposit atoms directly on the measurement stage. In addition, at this beamline, variable-temperature STM could be performed.

3.2.1 The X-ray Beam

The working principle of a *synchrotron* is a synchronously accelerated number of charged particles. These are collected in several bunches, each containing up to 10^{10} electrons, traveling around the synchrotron on a defined trajectory. The ability to condense the electrons in dense bunches arises from their velocity close to the speed of light c. Caused by *Einstein's special theory of relativity* (Einstein, 1905), the bunch is elongated to a length of $\approx$ 100 m in the rest frame of the electrons, As a result, the *Coulomb repulsion* is not as large as possibly assumed. However, the electrons of each bunch would drift away from each other without focusing. Therefore a system of electromagnetic lenses based on *quadrupole* or *sextupole magnets* serves this task. A single quadrupole magnet focuses the beam in one direction and defocuses it in the perpendicular direction. The combination of two quadrupole magnets rotated by 90° results in a net focusing effect in both directions.

In order to force the electron bunches on a curved trajectory *bending magnets* are used. The change of the traveling direction of a charged particle displays a variation of the momentum. It results in the emission of synchrotron radiation by means of deceleration radiation lengthwise to the curvature into a narrow cone with an opening angle of $2/\gamma$. The parameter γ depends on the velocity of the electron according to $1/\gamma^2 = 1 - \beta^2 = 1 - v^2/c^2$. The power of the photons for $v \approx c$ is given by:

$$P = \frac{2e^2 c}{3r^2}\left(\frac{E}{m_0 c^2}\right)^4 \tag{3.1}$$

with the radius of the curvature r, the energy E, and the rest mass m_0. Another interesting quantity is the frequency ω of the radiation emitted in the field of the bending magnet:

$$\omega = 2\gamma^2\omega_0 = 2\gamma^2\frac{e}{m_0}B \tag{3.2}$$

It is hence directly depending on the magnet's field strength and the energy of the particle.

The particular X-rays used at beamline ID08 were soft with a tunable energy in the range of 0.3 to 1.6 keV. Two individual *undulators* were used to provide them. An undulator is

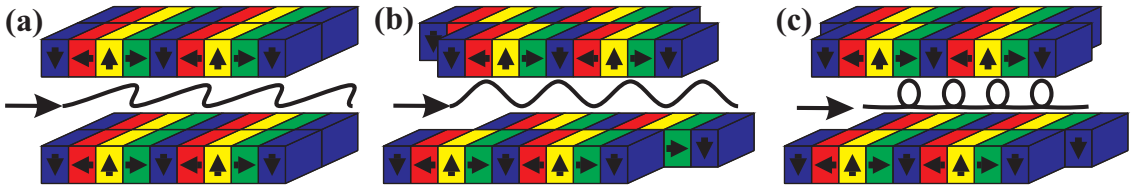

Figure 3.5: Schematic illustration of the working principle of an undulator. The individual elements are shifted with respect to each other to obtain linearly (horizontally, vertically) polarized light (a,b) and circularly polarized light (c). Right and left circular polarizations are not distinguished here for simplicity reasons.

an array of magnets (usually permanent magnets), where neighboring magnets have varying magnetization axes. Using this setup, the electron beam is weakly modulated. By shifting the individual arrays with respect to each other, linearly (horizontally/vertically oscillating) or circularly (left/right rotating) polarized light can be achieved, compare Fig. 3.5. The Apple II undulators used at ID08 achieved a degree of polarization of almost 100%.

Moreover, a single oscillation of the beam induced by the undulators causes a delay of the propagation. As a result of the beam oscillating N times, where N depicts the number of undulator periods, the delay adds up and the effective bandwidth is reduced by a factor of N. For this reason, on the one hand, the undulators strengthen the *monochromaticity* of the beam. On the other hand, the undulators increase the peak intensity of the beam. Additionally, the emission cone of the radiation after the undulator treatment is reduced by a factor of N. Thus, the *brilliance* of these devices, which depicts the photon flux emitted per unit source area and per unit radiation opening angle, exceeds that of wigglers or bending magnets by orders of magnitude. Consequently, the energy resolution available by this aperture was $\mathrm{d}E/E = 5 \cdot 10^{-4}$ at 850 eV.

The X-ray beam was focused by a system of optical lenses. As a result, a minimum beam size of about $10 \cdot 50\ \mu\mathrm{m}^2$ at the sample was achieved. As already mentioned before, this illustrates, that XAS is a spatially averaging technique, in contrast to STM. The X-rays could not be used to investigate particular adsorbates, but always probed the entire illuminated ensemble. This way, the experimental results always revealed a superposition of the individual contributions.

3.2.2 The UHV Chamber System

The setup at the ID08 beamline was a complex UHV system with three individual chambers, shown in Fig. 3.6. The measurement stage itself was centered in the analysis-chamber and connected to a ^{4}He bath cryostat operating at a base temperature of 6 K. Similar to the STM setup (compare Sec. 3.1.1), the He dewar was surrounded by another dewar filled with liquid nitrogen. In addition, a magnetic field of up to 5 T could be applied collinear to the X-ray beam. The sample holder could be screwed to the sample receptacle at the end of a rotary drive, whereas the rotation axis was perpendicular to the X-ray beam. This way, the surface normal of the sample could either point directly toward the X-ray beam at 0° (*normal incidence angle*) or could be rotated to 70° (*grazing incidence angle*). This procedure provided the opportunity to investigate the out-of-plane and in-plane electronic and magnetic properties of the sample.

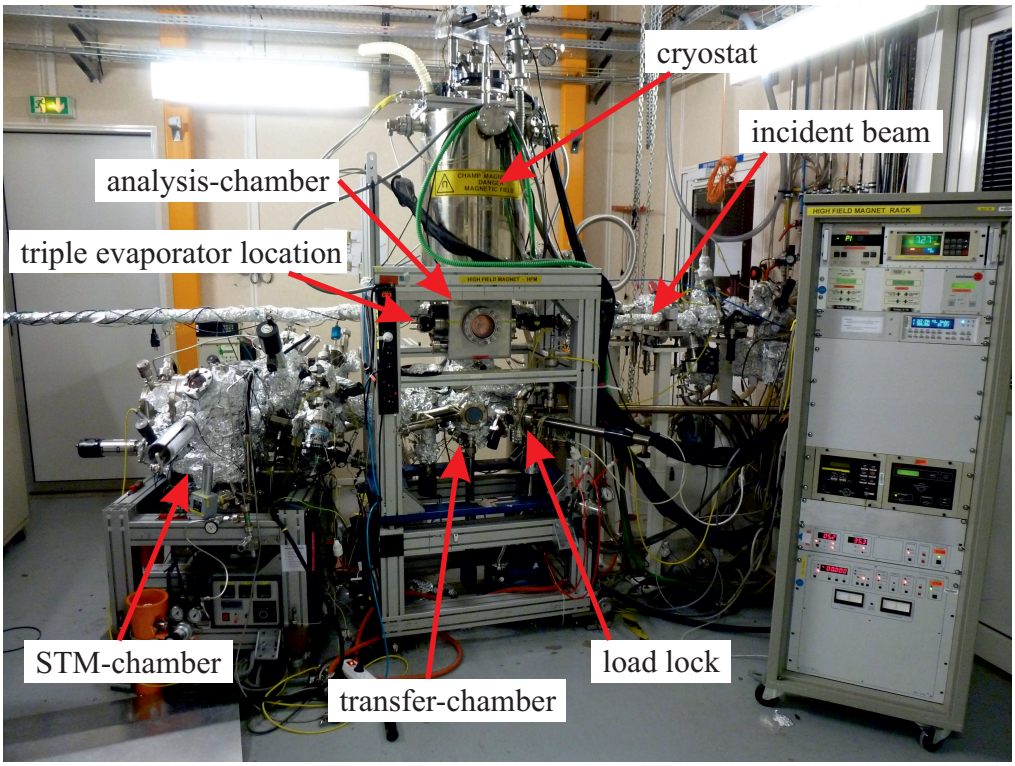

Figure 3.6: Side view on the X-ray measurement stage inside the analysis-chamber. The incident beam approaches from the right, whereas the STM-chamber is attached on the left. It is connected to the analysis-chamber via a transfer-chamber. The mounting position of the triple evaporator is indicated, directly in line with the X-ray beam tube but from the backside of the sample receptacle.

During the experiments, a triple evaporator was mounted at the backside of the sample stage. It offered the possibility to evaporate atoms directly on the cold sample if the receptacle was rotated by 180°. The base pressure of the main chamber was in the low 10^{-10} mbar range.

The sample receptacle could be bottom-loaded using a vertical transfer rod inside the transfer-chamber. This chamber connected the analysis-chamber with the STM-chamber and the load lock. The STM-chamber contained an Omicron VT-SPM (Omicron, n. d.) operating at room temperature. STM was mainly used to determine the surface quality of the samples, either before the X-ray experiments or before the MBE growth.

In contrast to the TI samples, that were just cleaved, the graphene samples needed to be cleaned prior to the experiments. To this end, they were degased at temperatures of $\approx$ 800 K using a pBN heater. The resistive heater was also installed in the STM-chamber. Further preparation facilities available were a sputter ion gun and an upgraded version of the heater using electron bombardment in case of the TI experiments.

Chapter 4

Graphene

This chapter deals with the experiments performed on *individual transition metal adatoms and clusters* on different types of *graphene*. Section 4.1 gives an overview of *free-standing graphene*. This includes carbon-based allotropes, methods to achieve high-quality graphene samples, its extraordinary structural and electronic properties and a discussion of potential applications. Subsequently, *graphene on SiC* is introduced in Sec. 4.2 motivated by its use for the experiments.

Section 4.3 bases on a recent combined experimental and theoretical study (Eelbo *et al.*, 2013a). It comprises a detailed description of the electronic and magnetic properties of individual Fe, Co, and Ni adatoms and clusters on *monolayer graphene* prepared on a SiC(0001) substrate. The samples, used within this study, were provided by the *Interface Analysis Group* of *U. Starke*. In addition to the STM and XAS/XMCD experiments, *density functional theory*-based calculations were performed by the *Theory of Magnetism and Electronic Correlations Group* of *A. Lichtenstein*.

The chapter proceeds with Sec. 4.4, which reveals, that the properties of the adatoms are drastically altered if the substrate is modified in an apparently minor way. This conclusion bases on experimental findings, that were published recently as well (Eelbo *et al.*, 2013b). The respective samples were also provided by the *Interface Analysis Group* of *U. Starke*. The chapter ends with a short summary of the graphene-based research achievements in Sec. 4.5.

4.1 Overview of Graphene

The historical background of graphene is closely related to graphite. According to Fig. 4.1, graphene is the essential building block of the remaining carbon *allotropes*, i.e. *fullerenes* (Kroto *et al.*, 1985), *nanotubes* (Iijima, 1991) and *multi-layer graphene*, which for layer numbers larger than ten exhibits the properties of bulk *graphite* (Partoens *et al.*, 2006). Interestingly, graphite was known for many years and used in practice for numerous applications, e.g. pencils, golf or tennis rackets, electrodes, lubricants, etc.. Moreover, nanotubes as well as fullerenes were investigated in detail already in the early nineties (Dresselhaus *et al.*, 1996; Saito *et al.*, 1998).

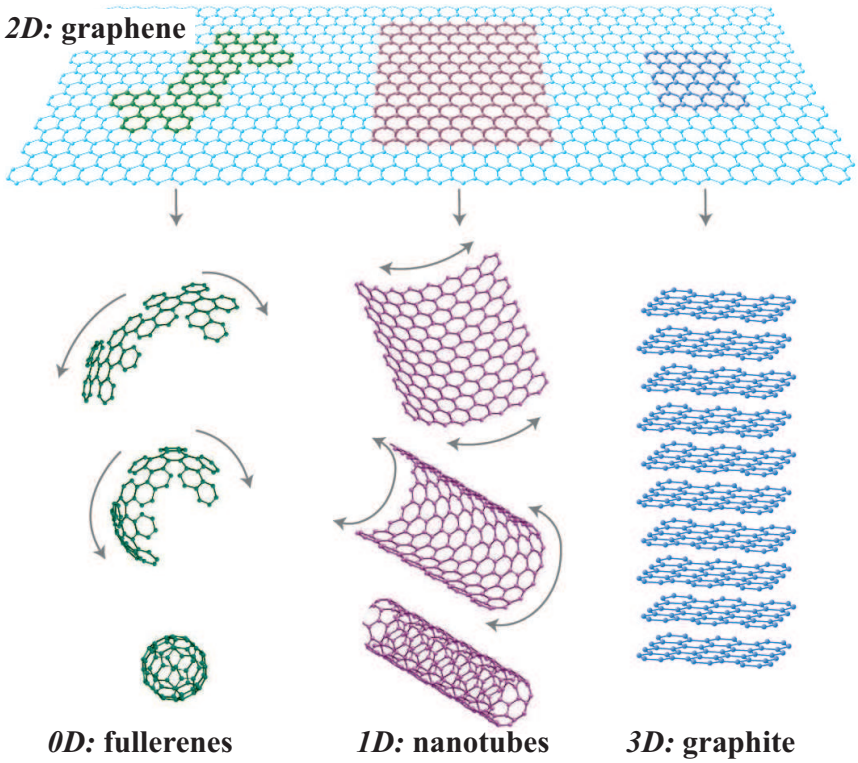

Figure 4.1: Schematic model of graphene depicting its ability to arise in different allotropes, such as fullerenes, nanotubes, multi-layer graphene, and graphite. From Geim *et al.*, 2007 with permission.

Surprisingly, high-quality single layers of graphite were not prepared until 2004. Before, graphene was considered to be an idealized but in reality non-existing system utilized to describe the properties of carbon allotropes (Wallace, 1947; McClure, 1956; Slonczewski *et al.*, 1958). Besides, it was regarded as a model system for the theoretical treatment of quantum electrodynamics (QED) (Semenoff, 1984; Haldane, 1988). Graphene was believed to be unstable at any finite temperature. This assumption was based on its strictly two-dimensional structure. It was believed, that for this type of structure thermal fluctuations would induce lattice displacements comparable to the lattice constant itself (Peierls, 1935; Landau, 1937). The idea is supported by the melting temperature which generally decreases according to the sample thickness. One thus expects a vanishing melting temperature and an instability of the truly two-dimensional graphene (Venables *et al.*, 1984). In contrast, in 2004, high-quality samples of monolayer and few-layer graphene were found revealing properties of a strictly two-dimensional electron gas and being stable even at room temperature (Novoselov *et al.*, 2004). This led to the award of the *Physics Nobel Prize* for *A. Geim* and *K. Novoselov* in 2010.

Novoselov *et al.* succeeded in the preparation of high-quality samples by the *exfoliation* of graphene from highly oriented pyrolytic graphite (HOPG) (Novoselov *et al.*, 2004). They used adhesive tape to peel off graphene flakes from HOPG bulk crystals. Moreover, they were able to determine the layer thickness accurately down to the limit of a single layer of graphene by means of an optical microscope. The crucial additive was a SiO_2 substrate with a defined

thickness (300 nm) underneath the graphene flake. This enabled to identify the number of graphene layers due to the different feeble interference-like contrast with respect to the bare wafer (Geim *et al.*, 2007). In addition, a SiO_2 substrate serves for an effective decoupling of the on top graphene. This way, it enables graphene to reveal its peculiar electronic properties.

Nowadays, various methods are established to prepare high-quality samples. They can be produced either by means of *thermal decomposition* using semiconductor surfaces such as SiC (Hass *et al.*, 2008a; Starke *et al.*, 2009), or by the *graphitization* and the *chemical vapor deposition* on metal substrates, such as Pt(111) (Sutter *et al.*, 2009), Ir(111) (Coraux *et al.*, 2008) or Ru(0001) (Marchini *et al.*, 2007).

4.1.1 Properties

Starting with the pioneering experiments in 2004 (Novoselov *et al.*, 2004), a rush in the research field of graphene was induced. This was motivated by its potential applications and peculiar properties mostly caused by graphene's strictly two-dimensional structure. Graphene is a one layer thick, flexible, and transparent crystal, made of carbon atoms. The crystal lattice is determined by the sp^2-bonding of the carbon atoms. This results in an array of benzene rings generating a *honeycomb lattice*. The lattice comprises *two sublattices* and, hence, two carbon atoms per unit cell accordingly. The in-plane lattice constant is $\approx$ 2.46 Å. Due to the weak *Van-der-Waals interaction* between adjacent layers, the layer-to-layer distance of multi-layer graphene is large, i.e. $\approx$ 3.35 Å.

The lattice of graphene enables some further astonishing structural properties. Young's modulus of graphene is the highest ever reported $\approx$ 1 TPa (Lee *et al.*, 2008) and graphene's ability to be reversibly stretchable by about 20 % (Lee *et al.*, 2008), is larger than for any other crystal structure. In addition, graphene shows a breaking strength of $\approx$ 40 N/m close to the theoretical limit (Lee *et al.*, 2008). Another record value can be found by graphene's thermal conductivity at room temperature, which is $\approx 5000\ \mathrm{Wm}{-}1\mathrm{K}^{-1}$ (Balandin *et al.*, 2010).

Graphene's electronic properties are fundamentally connected to its crystal lattice. The sp^2-hybridization of the carbon atoms entails σ-bonds between adjacent atoms and thereby the honeycomb lattice. In addition, the remaining p_z-orbital of each carbon atom binds to p_z-orbitals of neighboring atoms, where z depicts the direction perpendicular to the surface plane. This results in the formation of π- and π^*-*bands* depending on the respective sublattice of graphene. On the one hand, graphene is a semiconductor for which the band gap is driven by the intrinsic SOI. On the other hand, inside graphene, this SOI is small because carbon is a light element. Therefore, the size of the band gap is *negligible* (Min *et al.*, 2006). As a result, graphene can be considered as a zero-band gap semiconductor. This means, that the conduction and valence bands touch each other at the *Dirac points* at the Fermi level E_F, compare Fig. 4.2(a). These points coincide with the K-points of the reciprocal lattice.

Theoretically, this was already described in 1947 using a tight-binding approach for the case of graphite. In this approach electrons can hop between adjacent atoms, whereas the energy dispersion relation depending on the wave vector k_x and k_y in Cartesian coordinates is given by (Wallace, 1947):

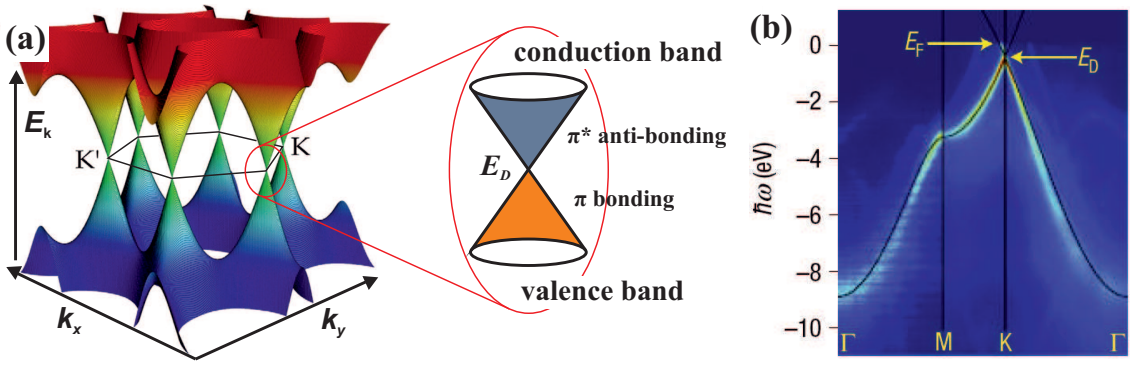

Figure 4.2: (a) Illustration of the band structure of graphene. Caused by the hexagonal structure of graphene, the unit cell of the Brillouin zone exhibits six *K*-points, each three of both sublattices. At these points the conduction and valence bands touch in the DPs and, hence, form Dirac cones as visible in the zoom-in. Adapted from Katsnelson, 2007 with permission. (b) Experimental confirmation of the linear band dispersion in the vicinity of the *K*-point for a single layer of graphene on a SiC substrate, measured by means of ARPES. The energy difference between the DP and the Fermi level is caused by a slight doping effect due to the substrate. From Bostwick *et al.*, 2007 with permission.

$$E_{\pm} = \pm\gamma_0 \sqrt{3 + \left[2\cos\left(\sqrt{3}k_y a\right) + 4\cos\left(\frac{\sqrt{3}}{2}k_y a\right)\cos\left(\frac{3}{2}k_x a\right)\right]} \tag{4.1}$$

Here, a is the in-plane lattice constant, γ_0 is the nearest-neighbor hopping energy ($\gamma_0 \approx$ 2.8 eV) and E_- (E_+) depicts the energy of the π- (π^*)-band. The combination of the cosine functions explains the wave-like energy-dispersion in Fig. 4.2(a). As a consequence of the contact of valence and conduction bands, the charge carriers can be easily tuned between electron and hole conduction with concentrations up to 10^{13} cm^{-2}. Caused by the π- and π^*-bands (Latil *et al.*, 2006), the band dispersion is *linear* in the vicinity of the sublattice-dependent and therefore inequivalent Dirac points (DPs). This is easily observable by means of angle-resolved photoemission spectroscopy (ARPES), compare Fig. 4.2(b) (Rollings *et al.*, 2006; Ohta *et al.*, 2006).

The wave function characterizing the system appropriately, is a two component spinor describing the charge carriers in either the one or the other sublattice of graphene. This feature is often referred to as a *pseudospin* of the π-states. These can also be seen as *chiral Dirac fermions*, that have lost their rest mass (Wallace, 1947) and mimic the physics of QED. In this model, chirality refers to the connection between k electrons and $-k$ hole states arising from the same sublattice. The Dirac fermions are *quasiparticles* which originate from the interaction of the charge carriers with the periodic potential of the honeycomb lattice, i.e. from graphene's two-dimensionality. They are theoretically described by the relativistic (2+1)-dimensional *Dirac equation*. The Dirac-like Hamiltonian is given by (Slonczewski *et al.*, 1958; Semenoff, 1984; Haldane, 1988):

$$\begin{aligned}\hat{H} &= v_F \cdot \sigma \cdot \boldsymbol{p} \\ &= \hbar \cdot v_F \cdot \sigma \cdot \boldsymbol{k} \\ &= \hbar \cdot v_F \cdot \begin{pmatrix} 0 & k_x - ik_y \\ k_x + ik_y & 0 \end{pmatrix}\end{aligned} \tag{4.2}$$

where v_F is the *Fermi velocity*, σ is the 2D *Pauli matrix*, $\boldsymbol{p}$ represents the quasiparticle momentum and $\boldsymbol{k}$ the quasiparticle wave vector. The Fermi velocity is given by: $v_F = \sqrt{3}a\gamma_0/2\hbar \approx c/300$. This smallness compared to the speed of light c provokes, that effects of the QED occur in a longer period of time and are often enhanced because they usually depend on a factor $c/v_F = 300$ (Katsnelson *et al.*, 2006). This was exemplarily proven in case of the half-integer quantum Hall effect (QHE) (Novoselov *et al.*, 2005; Zhang *et al.*, 2005). The half-integer characteristic of this effect relies directly on the massless Dirac fermions. The presence of electron-like and hole-like Landau states at zero energy, that can also be described by the pseudospin introduced before, depict the *sublattice-degeneracy* of graphene. Interestingly, graphene offers the possibility of observing the QHE even at room temperature due to the large cyclotron gaps characteristic for these Dirac fermions (Novoselov *et al.*, 2007).

Besides additional QED effects that are expected to be present in graphene, the *Klein paradox* was already proven experimentally (Itzykson *et al.*, 2006). It depicts the property of the Dirac fermions to be independent of potential barriers induced by external electrostatic potentials. Furthermore and interesting in view of future electronic devices, *ballistic transport* was found in graphene by means of transport measurements (Novoselov *et al.*, 2004). These reveal a propagation of the charge carriers without scattering over macroscopic distances of several micrometers. In agreement, recent investigations of suspended graphene revealed ultra-high electron mobilities of up to 2×10^5 $cm^2V^{-1}s^{-1}$ (Morozov *et al.*, 2008).

4.1.2 Preparation Methods

Since the graphene-related measurements performed within this thesis were carried out on SiC substrates, the preparation will be given in detail in Sec. 4.2. Instead, *epitaxial graphene* on metals is usually prepared with the help of *hydrocarbon* gases, such as ethylene (C_2H_4) or benzene (C_6H_6). Within the chemical vapor deposition (CVD) growth technique, the sample is heated to elevated temperatures in a hydrocarbon (HC) atmosphere after the initial removal of residual contaminants. At these temperatures, the HC molecules, adsorbed by the metal surface, break up, whereas the hydrogen desorbs from the surface and can be removed from the UHV system. The remaining carbon atoms have enough thermal energy to build up the honeycomb lattice of graphene.

The graphitization is another technique to obtain graphene or to support the CVD growth. In this case, the sample is annealed without applying HC gases but usually to higher temperatures compared to the CVD growth mode. This entails bulk carbon contaminants to segregate to the surface. There, they either build up graphene as described before or they at least increase the amount of available carbon for the graphene growth. This results in higher coverages and may reduce the defect density inside graphene.

The combination of both procedures thus enables to effectively grow flakes or entire layers

of epitaxial graphene (EG) on many metal substrates. Importantly, the properties of these graphenes significantly differ depending on the substrate. This is caused by the varying coupling strengths between the substrate and the EG. Additional influences can be induced by structural differences caused by a mismatch with the lattice constant of the substrate beneath. This can, for instance, cause the occurrence of a moiré superstructure.

4.1.3 Potential Applications

In view of its electronic properties, it is not surprising, that graphene was proposed for applications in ultra-fast future electronic devices. Indeed, graphene based *field-effect transistors* with a cutoff frequency of $\approx$ 100 GHz were already realized (Lin *et al.*, 2010). These are more than two times faster compared to Si-based field-effect transistors (FETs) of the same gate length (= 240 nm). Graphene was additionally proposed being suitable for *spintronic devices* (Wolf *et al.*, 2001). Using the difference of graphene's zigzag and armchair edges, asymmetric electronic states can in principle be realized depending on the spin of the charge carrier. This can be achieved by applying in-plane homogeneous electric fields in graphene nanoribbons (Son *et al.*, 2006).

Graphene was furthermore suggested to be suitable for *quantum computing devices* (Cerletti *et al.*, 2005). This is due to the band structure, that is degenerated with respect to both sublattices of graphene's honeycomb structure. By singly occupying the one or the other sublattice via the usage of armchair/zigzag edges the valley polarization can be lifted. As a result, a valley valve, representing a zero-magnetic-field counterpart of the spin valve, seems to be achievable (Rycerz *et al.*, 2007; Trauzettel *et al.*, 2007).

Regarding the adsorption/desorption of atoms or gaseous molecules, graphene exhibits a step-like resistance within transport measurements (Schedin *et al.*, 2007; Wehling *et al.*, 2008). This is due to the induced variation of the local charge carrier concentration if atoms or molecules are adsorbed (or detached). In combination with the low-noise character and the impermeability of graphene with respect to gas molecules (Bunch *et al.*, 2008), graphene seems to be a promising candidate for *gas sensors* with extreme sensitivities.

Related to that, graphene is capable to adsorb loads of hydrogen. Its application in the growing field of *fuel cell devices* seems hence to be reasonable due to its extreme *surface-to-volume ratio* (Sofo *et al.*, 2007). Moreover, this ratio motivates the use of graphene powder of uncoagulated micrometer-size crystallites at low manufacturing costs in mass production. Such powder can be potentially applied to *batteries* to enhance their capacities and to shorten their charging times (Yoo *et al.*, 2008).

In summary, graphene was proposed for many applications and predicted to exhibit various effects of QED. Of course, this explains the major effort in graphene-related research, though much work remains to be done in order to fulfill these expectations.

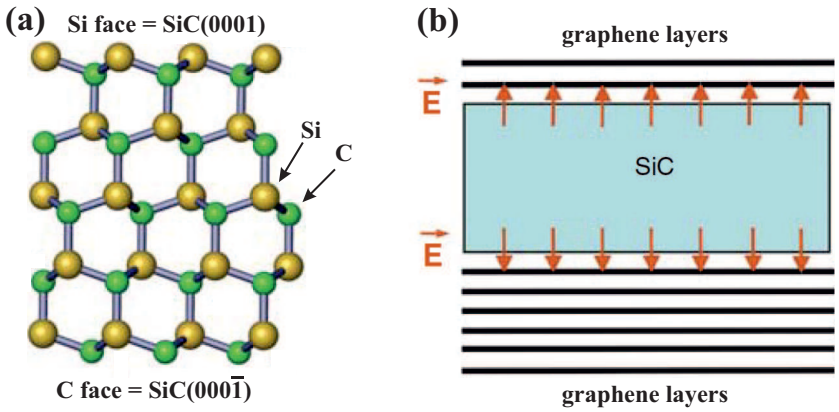

Figure 4.3: (a) Schematic model of graphene grown on both facets of 4H-SiC. The yellow and green balls represent Si and C atoms, respectively. (b) Graphene on the SiC(000$\bar{1}$) surface grows faster compared to the Si-face due to lower temperatures needed during the growth process. Adapted from First *et al.*, 2010 with permission.

4.2 Graphene on SiC

The growth of EG on SiC is currently of high interest. This is owing to the SiC substrate representing a *wide band gap semiconductor* suitable for high temperature, high electric fields, and high-speed devices. It additionally allows a direct connection to conventional electronics (Brandt *et al.*, 1998; First *et al.*, 2010).

The SiC crystal's lattice structure is described by the stacking of basal plane bilayers of Si and C, shown in Fig. 4.3(a). The in-plane lattice constant is 3.07 Å and the *z*-spacing is 2.5 Å. In general, different *polytypes* are distinguished, e.g. 4H and 6H, differing in the number of bilayers per unit cell. The unit cell in case of 4H-SiC hence exhibits a *z*-height of 10.0 Å, while the 6H-SiC shows a *z*-height of 15.1 Å. Both exhibit *band gaps* of about 3.2 eV. Note, that no polytype-dependence of the properties of the on top grown carbidic structures was found (Starke *et al.*, 2009). Furthermore, SiC enables to grow EG on both *facets* of the crystal with strong influences on the properties of the respective graphene. As a result, EG grown on the Si-terminated face, i.e. the SiC(000$\bar{1}$) surface, has to be distinguished from graphene on the C-terminated face, i.e. the SiC(0001) surface, compare Fig. 4.3. An example for the differences on both facets is given by the growth speed, compare Fig. 4.3(b). On the C-terminated facet, lower temperatures are needed to form graphene. This consequently leads to a higher growth rate compared to graphene on the Si-terminated facet (Muehlhoff *et al.*, 1986).

To increase the surface flatness after polishing and to passivate the samples, SiC is usually hydrogen-etched prior to the growth of EG. Afterward, graphitic layers on SiC are obtained by *thermal decomposition* of the bilayers of the crystal lattice which first was observed in 1975 (Van Bommel *et al.*, 1975). If the crystal is heated to typical temperatures of $\approx$ 1400 K, the covalent bonds between the Si and C atoms break up and Si is sublimated from the surface. During the growth of carbidic layers from the carbon-rich phase, the crystal surface undergoes different intermediate states depending on the facet of the crystal.

Provided the case of multiple layers of graphene, the electronic properties of each layer rely

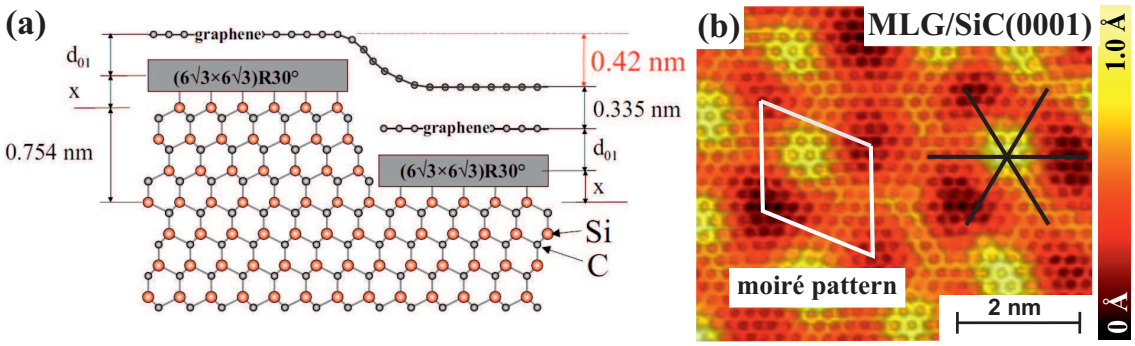

Figure 4.4: (a) Graphene on the interface layer of a SiC(0001) substrate. The topmost graphene layer is not interrupted at the substrate's steps. The second layer grows underneath the topmost closed layer starting at the substrate's steps. From Lauffer *et al.*, 2008 with permission. (b) STM constant-current map of MLG/SiC(0001). The white parallelogram indicates the moiré pattern, that is induced by the $(6\sqrt{3}\times 6\sqrt{3})$R30° reconstructed interface layer. According to the black lines, the in-plane lattice constant was determined. Tunneling parameters are $U = -0.1$ V and $I = 0.5$ nA.

on the distance to the bulk SiC substrate, compare Fig. 4.3(b). The substrate-nearest graphene layer is strongly *n-doped* with doping levels of typically 10^{13} cm^{-2}. This doping level decreases rapidly according to the distance of the SiC substrate (Lauffer *et al.*, 2008). Under normal circumstances, few-layer graphene exhibits *charge neutrality*. The doping effect has important consequences for potential applications because the mobility depends inversely proportional on the charge carrier density. Consequently, low carrier densities are desired.

For the experimental investigations of individual 3*d* TM adatoms, graphene on SiC(0001) was used as substrate. This is motivated by the Si-terminated surface being better characterized than its C-terminated counterpart. Moreover, the growth of a closed and homogeneous single layer of graphene on SiC(000$\bar{1}$) remains a challenging task although it was recently achieved for the first time (Wu *et al.*, 2009).

4.2.1 Graphene on SiC(0001)

In the case of the *Si-terminated face*, the actual preparation of MLG/SiC(0001) – in the following referred to as MLG – starts with the deposition of Si onto the simultaneously annealed surface. By this procedure, excess C, present at the surface, can be removed while the surface undergoes different reconstructions (Starke, 2004). A final annealing step at a temperature of $\approx$ 1400 K without further Si deposition causes the emergence of a $(6\sqrt{3}\times 6\sqrt{3})$R30° *reconstructed carbon layer*, compare Fig. 4.4(a).

By means of ARPES, the band dispersion of this layer's π-bands was resolved to fail the graphene-like linear behavior at the *K*-point (Emtsev *et al.*, 2008; Starke *et al.*, 2009). This first layer consisting of carbon atoms does hence not exhibit the peculiar properties of graphene. It is usually referred to as the *buffer* or *interface layer* (Charrier *et al.*, 2002). The different properties of the interface layer compared to graphene are understandable considering the π orbitals being still strongly bonded to the underneath substrate. They saturate the

dangling bonds of the topmost Si atoms, whereas the interface layer's atomic structure is in principle close to graphene's (Mattausch *et al.*, 2007; Varchon *et al.*, 2007).

The second carbon layer growing on top of the interface layer is sufficiently decoupled to depict the first layer of EG on SiC, i.e. MLG. It is obtained by further annealing the substrate at a temperature of ≈ 1500 K (Riedl *et al.*, 2007). MLG grows continuously across step edges of the underlying SiC substrate (Lauffer *et al.*, 2008). However, as shown in Fig. 4.4(b), the influence of the interface layer still remains and shows up in form of a *moiré pattern*. This moiré is easily detectable utilizing STM for certain sets of tunneling parameters. It entails a significant apparent corrugation of the surface and superimposes the atomic lattice of graphene. According to the black lines, indicated in Fig. 4.4(b), an in-plane lattice constant of 244.2 pm is determined, close to the literature value, compare Sec. 4.1.1. Moreover, due to charge transfer from the SiC substrate, MLG is electron doped exhibiting a charge carrier density of $n \approx (1.0 \pm 0.1) \times 10^{13}$ cm^{-2} (Forti *et al.*, 2011). The DP is shifted to the occupied states at ≈ -0.4 eV (Bostwick *et al.*, 2007; Zhou *et al.*, 2007). Concerning potential applications, MLG revealed mobilities up to $\approx 2.9 \times 10^4$ cm^{2}V^{-1}s^{-1}. This value was acquired after the charge carrier density was successfully lowered by the exposure of the surface to acceptor molecules (Jobst *et al.*, 2010). In view of applications, a substrate-induced band gap revealed for MLG is also of significant importance (Zhou *et al.*, 2007).

For higher coverages, further annealing at $\approx 1500 - 1600$ K is required (Riedl *et al.*, 2007). The second layer of graphene, i.e. the third layer of carbon, starts to grow at the step edges of the underlying SiC. More precisely, it grows underneath the topmost closed graphene layer in a *Bernal stacking* (ABAB...) manner (Lauffer *et al.*, 2008), compare Fig. 4.4(a). For multiple layers of graphene, the π-bands split into *bonding* and *antibonding bands*. Consequently, distinguishing the exact coverage of few-layer graphene on SiC can easily be performed by means of ARPES experiments (Latil *et al.*, 2006; Ohta *et al.*, 2007).

4.2.2 Quasi-free-standing Monolayer Graphene on SiC(0001)

The effect of the interface layer displaying a strongly bonded carbon layer can be overcome by means of *hydrogen intercalation*. If the interface layer sample is annealed in a H_2 atmosphere at temperatures of ≈ 1000 K, hydrogen intercalates underneath the interface layer. This way, it saturates the dangling bonds of the topmost Si atoms of the substrate (Riedl *et al.*, 2009), compare Fig. 4.5(a). Consequently, the π-bands of the interface layer can relax and form the graphene-characteristic linear band dispersion at the K-point.

The procedure turns the former interface layer into the first true layer of graphene (Riedl *et al.*, 2009). Upon this treatment, the charge carrier density shifts from an electron-doped surface ($n = (1.0 \pm 0.1) \cdot 10^{13}$ cm^{-2}) for MLG/SiC(0001), toward a slight *hole-doping* of the surface ($p = (3.1 \pm 1.0) \cdot 10^{11}$ cm^{-2}) in case of hydrogen intercalated graphene on SiC(0001) (Riedl *et al.*, 2009; Speck *et al.*, 2011). This effect illustrates that the hydrogen intercalation not only turns the first (former strongly bonded) carbon layer into graphene, but also effectively decreases the *coupling strength* (10^{13} cm^{-2} → 10^{11} cm^{-2}) between the respective graphene and the substrate. Therefore, hydrogen-intercalated graphene/SiC(0001), shown in Fig. 4.5(b), is usually referred to as quasi-free-standing monolayer graphene (QFMLG)/SiC(0001) – in the following QFMLG. It exhibits an

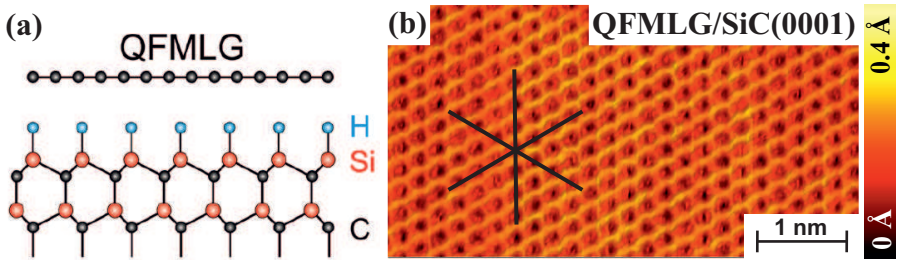

Figure 4.5: (a) Schematic model of QFMLG on SiC(0001). Adapted from Speck *et al.*, 2011 with permission. (b) Constant-current map of QFMLG/SiC(0001). The hydrogen intercalation turns the former interface layer into the first true layer of graphene. It also effectively reduces the apparent corrugation of the substrate. This can be easily seen from the color bar compared to that of Fig. 4.4(b). The black lines were used to estimate the in-plane lattice constant. Tunneling parameters are $U = -0.08$ V and $I = 0.3$ nA.

extraordinary *surface flatness* owing to the absence of the interface layer, compare Figs 4.4(b) and 4.5(b). The in-plane lattice constant was again determined according to the black lines and matches that of MLG, i.e. 244.4 pm. The remaining *p*-doping of the surface was recently ascribed to a surface charge layer induced by spontaneous polarization of the substrate (Ristein *et al.*, 2012). This is a bulk property of the underneath SiC and unavoidable for any hexagonal polytype of this material.

4.2.3 Graphene on SiC(000$\bar{1}$)

Compared to the SiC(0001) surface, the growth of few-layer graphene/SiC(000$\bar{1}$) exhibits several variations. Generally, the same preparation techniques can be applied, i.e. Si deposition on the simultaneously annealed sample and subsequent annealing without further Si deposition at higher temperatures. This procedure leads to different reconstructions of the SiC(000$\bar{1}$) surface, whereas in most cases, a coexistence of a (3×3) or a (2×2) structure was reported after annealing at 1350 K (Bernhardt *et al.*, 1999; Emtsev *et al.*, 2008). A monolayer of graphene on SiC(000$\bar{1}$) is prepared by additional heating at 1400 K (Starke *et al.*, 2009).

By means of low energy electron diffraction (LEED), graphene/SiC(000$\bar{1}$) was found to consist of individual domains rotated by varying angles with respect to the substrate (Starke *et al.*, 2009). The growth of graphene/SiC(000$\bar{1}$) is hence more *inhomogeneous* in comparison to MLG/SiC(0001). A further difference is given by the coupling between the first carbidic layer and the substrate, that is weak in case of SiC(000$\bar{1}$) (Emtsev *et al.*, 2008; Hiebel *et al.*, 2008).

As illustrated in Fig. 4.6(a), in the event of few-layer graphene, adjacent layers are usually again rotated by varying angles. They grow in a *turbostratic growth mode* different from those of Bernal stacking (Hass *et al.*, 2008b). Importantly, the rotational stacking prevents the π-bands of adjacent layers to interact with each other. Instead, each layer can be seen as individually grown EG. This was evidenced by ARPES experiments on few-layer graphene on SiC(0001) exhibiting independent Dirac cones for the three topmost layers, compare Fig. 4.6(b) (Sprinkle *et al.*, 2009). With respect to future electronic devices, few-layer

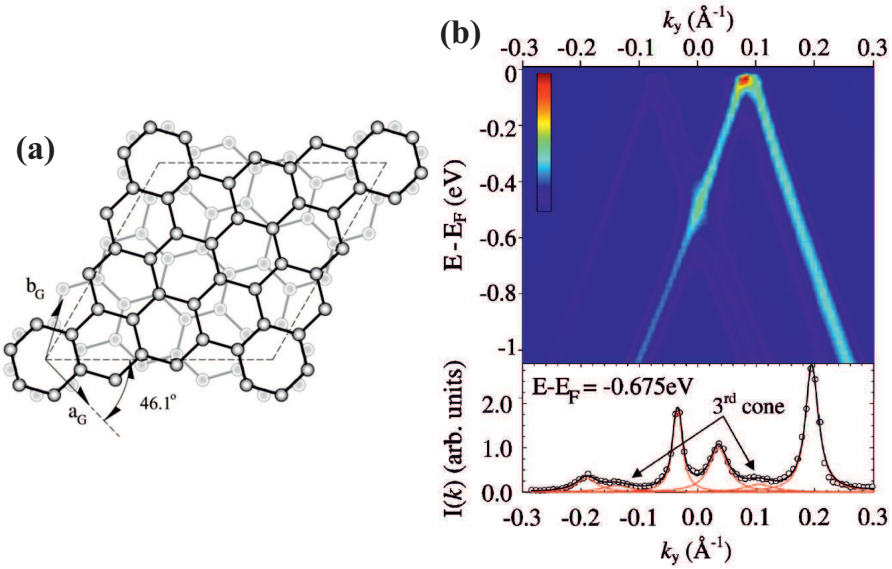

Figure 4.6: (a) Schematic model of bilayer graphene on SiC(000$\bar{1}$) indicating the rotational stacking mechanism which decouples adjacent graphene layers. Adapted from Hass *et al.*, 2008a with permission. (b) ARPES spectra and momentum dispersion curve obtained on few-layer graphene on SiC(000$\bar{1}$) revealing three independent Dirac cones. This evidences the lack of an interaction between those layers. The layers can hence be seen as individually grown EGs. Adapted from Sprinkle *et al.*, 2009 with permission.

graphene/SiC(000$\bar{1}$) reveals interesting properties. It shows discrete Landau levels at relatively weak magnetic fields even at room temperature (Orlita *et al.*, 2008). These experiments imply ultra-high charge carrier mobilities of $\approx 2.5 \times 10^5$ cm^{2}V^{-1}s^{-1}, interesting with respect to graphene-based FETs.

4.3 Individual Transition Metal Adatoms on Graphene

The MLG samples were provided by the group of *U. Starke* from the *Max Planck Institute for Solid State Research* in Stuttgart. These colleagues precharacterized the substrates by means of atomic force microscopy (AFM). Moreover, the pristine surface was investigated utilizing STM in Hamburg before the actual investigation of adsorbed TM atoms. To gain insight into the experimental findings, density functional theory (DFT)-based calculations were performed by the group of *A. Lichtenstein* from the *1st Institute of Theoretical Physics* of the University of Hamburg.

4.3.1 Pristine MLG

The samples were grown in Ar atmosphere because this improves the surface morphology. It reduces the defect density and thus provides large continuous and homogeneous layers of graphene (Emtsev *et al.*, 2009). Subsequently, the samples were precharacterized by means of

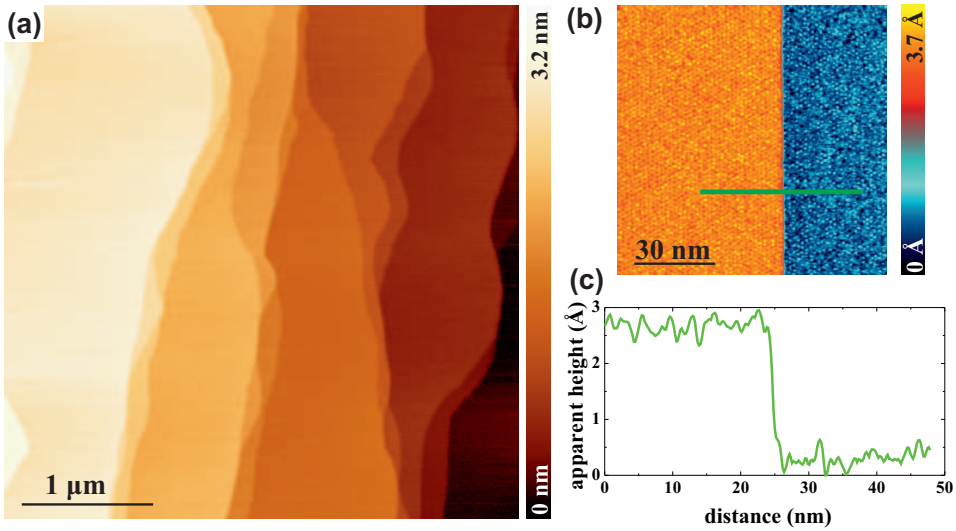

Figure 4.7: (a) Large scale topography of MLG indicating an average terrace width of ≈ 300 nm. (b) STM constant-current map of an individual SiC step edge. Neither bilayer nor uncovered interface layer contributions can be found evidencing that the desired coverage of one monolayer of graphene was perfectly achieved. Tunneling parameters are $U = -1.0$ V and $I = 0.5$ nA (c) Line profile of the step edge as indicated in (b). From Eelbo *et al.*, 2013a.

AFM with respect to their coverages and their basic properties. An exemplary image is given in Fig. 4.7(a). The large scale topography shows, that the average terrace width of the samples is about 300 nm.

Before the STM and X-ray-based investigations, further treatment of the samples was required. Although graphene is a fairly inert surface, it adsorbs contaminants if exposed to air. Therefore, the samples were degased at about 800 K prior to the experiments using pBN heaters. Fig. 4.7(b) displays a STM constant-current map of MLG with a single step edge of SiC. According to the line profile in Fig. 4.7(c), the obtained step height of ≈ 2.5 Å reflects the expected step height of a single bilayer of the substrate. No regions of bilayer graphene or an uncovered interface layer can be found. This proves that the desired coverage of one layer of graphene was perfectly achieved. Note, that the contrast variations on both steps, visible in Fig. 4.7(b), are due to the interface layer as described in Sec. 4.2.

4.3.2 STM on TM Adatoms on MLG

To investigate the properties of Fe, Co, and Ni, minute amounts of these TMs were evaporated onto MLG with the substrate located inside the STM and held at 12 K, compare Sec. 3.1.2. Subsequently, STM experiments were performed to identify the adsorption sites, as shown in Fig. 4.8. In case of Fe, the adsorption site was unfortunately *unidentifiable* because Fe adatoms were moving during the experiments. This is owing to the fact, that specific tunneling parameters are necessary to simultaneously resolve the honeycomb lattice of MLG. Lower temperatures, e.g. by using a ^{3}He-based cryo-system with typical base temperatures of 0.3 K might help stabilizing the adatoms sufficiently. However, this finding hints toward a very *low*

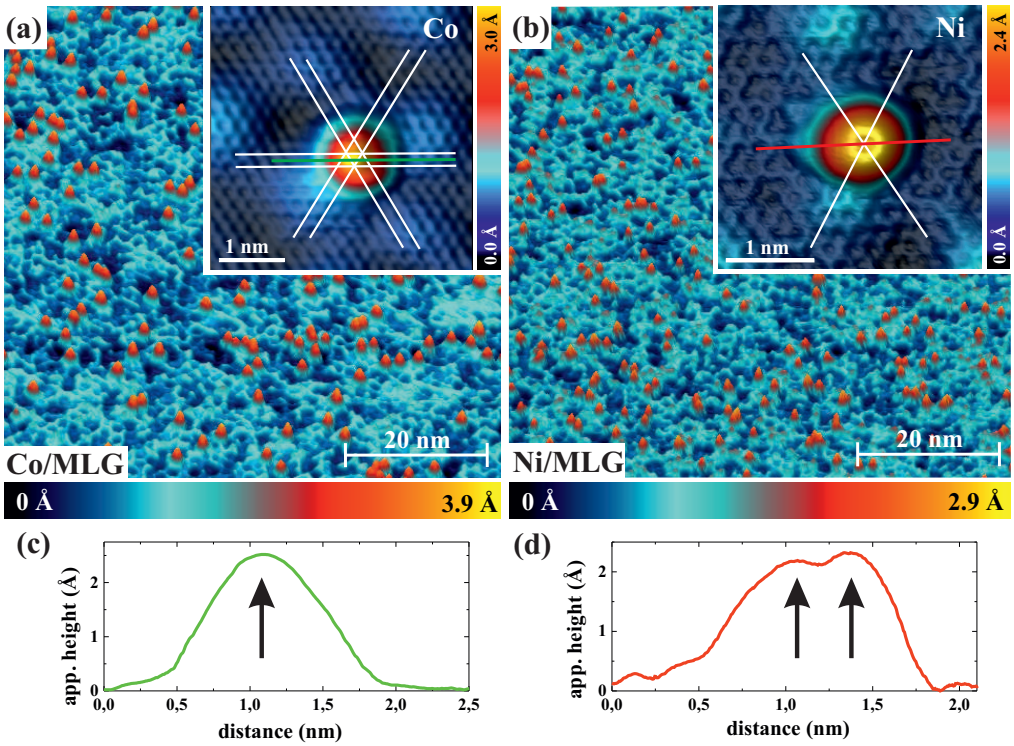

Figure 4.8: (a) STM constant-current map of individual Co adatoms on MLG. The white guidelines to the eyes indicate hollow sites of graphene's honeycomb lattice. The inset thus reveals top site adsorption for Co adatoms. Tunneling parameters are $U = 0.5$ V, $I = 0.025$ nA and $U = -0.5$ V, $I = 0.3$ nA. (b) Constant-current map of individual Ni adatoms on the same surface. According to the inset, Ni adsorbs on the hollow site. Tunneling parameters are $U = 0.4$ V, $I = 0.1$ nA and $U = -0.12$ V, $I = 0.5$ nA. (c) Line profile as indicated in (a) showing a single protrusion for the Co adatom. (d) Line profile as indicated in (b) revealing two maxima and thereby a ring-like protrusion with a depression in the center in case of the Ni adatom. The insets of (a,b) are adapted from Eelbo *et al.*, 2013b.

diffusion energy of Fe on MLG and, hence, to a weak interaction of Fe with the underlying substrate.

Provided the case of Co/MLG, several individual adatoms can be identified as red protrusions in the overview image, compare Fig. 4.8(a). The variations in the dark-blue background color of the surface is due to the interface layer (Lauffer *et al.*, 2008). The inset shows a typical high-resolution image of a Co adatom with the atomically resolved graphene lattice at the same time. The white guidelines to the eyes correspond to hollow sites of the honeycomb lattice. Since the center of the Co adatom matches a triangle spanned by these lines, the adsorption site is determined to be on top. This means, that the Co adatom adsorbs *on top of a C atom* of graphene's lattice. While most theoretical approaches predict hollow site adsorption for Co adatoms on graphene (Duffy *et al.*, 1998; Yagi *et al.*, 2004; Mao *et al.*, 2008; Sevinçli *et al.*, 2008; Johll *et al.*, 2009; Cao *et al.*, 2010; Yazyev *et al.*, 2010; Valencia *et al.*, 2010; Sargolzaei *et al.*, 2011; Rudenko *et al.*, 2012), this finding confirms calculations performed within the *generalized gradient approximation* (Perdew *et al.*, 1996) using an *on-site Coulomb potential* GGA+U of $U = 4$ eV. By means

of this model, Co atoms were found to adsorb on top of C atoms in a high-spin state with $S = 3/2$ and an electronic configuration of $3d^8 4s^1$ (Wehling *et al.*, 2010; Wehling *et al.*, 2011). Note, that individual Co adatoms on graphene were investigated before (Brar *et al.*, 2010). Unfortunately, Brar *et al.* did not identify the adsorption site for Co adsorbed on graphene/SiO_2.

The adsorption behavior differs for individual Ni adatoms, compare Fig. 4.8(b). According to the high-resolution image, the center of the adatom perfectly matches a crossing point of three guidelines indicating *hollow site* adsorption in case of Ni/MLG. This is consistent with recent experimental (Gyamfi *et al.*, 2012a) and theoretical reports (Duffy *et al.*, 1998; Yagi *et al.*, 2004; Johll *et al.*, 2009; Valencia *et al.*, 2010; Cao *et al.*, 2010; Yazyev *et al.*, 2010; Wehling *et al.*, 2011; Sargolzaei *et al.*, 2011). The Ni adatom is characterized by a ring-like protrusion with a depression in its center. The line profile of Ni thus exhibits two maxima contrary to the line profile of Co, compare Figs. 4.8(d) and 4.8(c). This strengthens the assignment of different adsorption sites for both species. The adsorption of Ni on the hollow sites was explained by an orbital selective coupling of Ni orbitals with E_1 (d_{xz}, d_{yz}) and E_2 symmetry ($d_{xy}, d_{x^2-y^2}$) to graphene's Dirac states (Gyamfi *et al.*, 2012a). The appearance of the Ni adatoms with a central depression is a result of the node along the z-axis, which the aforementioned orbitals exhibit. This node consequently appear as a depression in STM topographies. In principle, hollow site adsorption in case of Ni was theoretically predicted for a variety of electronic configurations (Wehling *et al.*, 2011). However, by means of STS experiments, Gyamfi *et al.* found strong indication, that Ni adatoms are predominantly in the $3d^{10}4s^0$ configuration (Gyamfi *et al.*, 2012a).

The generalized gradient approximation including an on-site Coulomb potential (GGA+U) model utilized by Wehling *et al.* additionally supports the STM investigations regarding another aspect. At first approximation, the difference of the binding energies of various adsorption sites ΔE_B can be used as an indication of the *diffusion barrier*. This difference is the smallest for Fe (ΔE_B(Fe) = 0.02 eV), followed by Co and Ni (ΔE_B(Co) = ΔE_B(Ni) = 0.15 eV) (Wehling *et al.*, 2011). Moreover, the absolute binding energy of Co (E_B(Co) = 0.62 eV) is smaller than that of Ni (E_B(Ni) = 0.97 eV). By definition, this illustrates a weaker binding with the substrate. Since Fe adatoms were not stable within the STM experiments and effective diffusion temperatures of T_D(Co) $\approx$ 50 K and T_D(Ni) $\approx$ 97 K (Gyamfi, 2012b) were determined, the experimental results and theoretical calculations are well in line.

4.3.3 XAS and XMCD on TM Adatoms on MLG

According to Sec. 4.3.1, the *terrace width* of MLG is about 300 nm. This is an important aspect regarding the XAS/XMCD experiments with spot sizes of the X-ray beam in the micrometer range. A large corrugation with many step edges of the underlying SiC substrate might influence the properties of the adsorbed nanostructures. Even if MLG is an uninterrupted closed layer (Lauffer *et al.*, 2008), an *indirect influence* due to the SiC step edge is possible. It can be illustrated by the local variation of the perpendicular direction. With respect to flat regions of MLG, the perpendicular direction is canted on the bended regions at the step edges. Therefore, magnetic anisotropy directions might be tilted if the nanostructures are adsorbed on these bended regions. With the obtained terrace width, the influence of the bended regions is reduced to about 0.6 %, presuming a width of the region of about 2 nm.

This corresponds to eight unit cells of MLG. Consequently, an influence on the properties of adsorbates originating from underneath SiC step edges appears to be negligible.

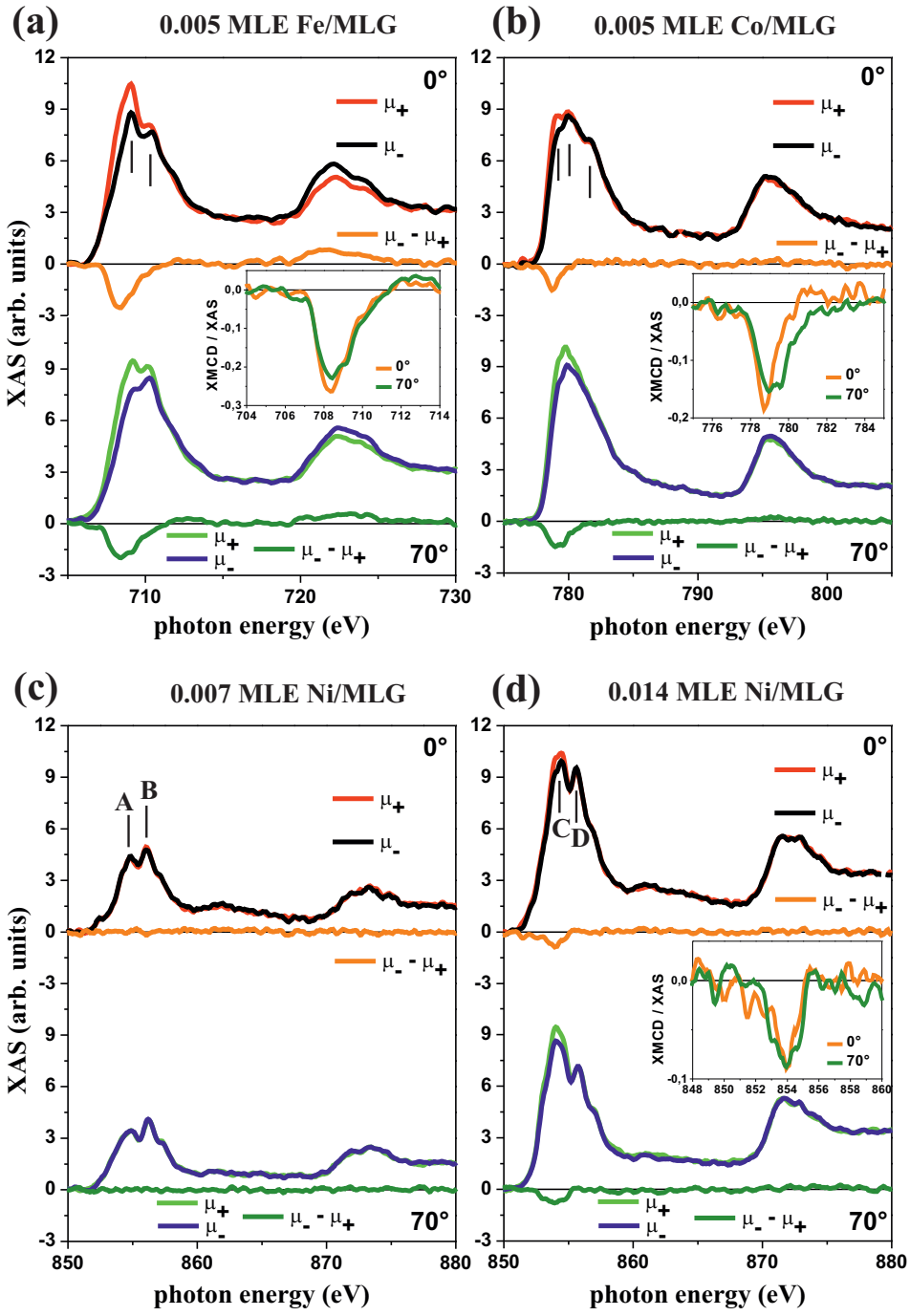

Figure 4.9: XAS and XMCD measurements performed at the $L_{2/3}$ edges for (a) 0.5% ALE Fe, (b) 0.5% ALE Co, (c) 0.7% ALE Ni and (d) 1.4% ALE Ni on MLG for a magnetic field of 5 T and a temperature of 10 K. The upper (lower) panel displays data acquired at normal, i.e. 0° (grazing, i.e. 70°) incidence angle. The insets of subfigures (a,b,d) exhibit the XMCD data obtained at both angles normalized by the XAS intensity for the L_3 edge. Adapted from Eelbo *et al.*, 2013a.

In case of the XAS/XMCD experiments, the graphene samples were of course degased utilizing the same procedure mentioned before. As a result, the preparation procedures were equal to those of the STM-based experiments. Effects provoked by the different experimental setup are hence not expected. In order to determine the coverages of the TMs correctly, calibration measurements were performed using a Cu(111) substrate. Copper was cleaned according to the procedure given elsewhere (Pietzsch *et al.*, 2004). Except the time, *equal deposition parameters* were used for the calibration measurements and the actual deposition. Because STM was performed at room temperature, the thermal energy was sufficient to enable accumulation of the TM adatoms. This decreases edge effects and enhances the precision of determining the deposition rates. As a result, the L_3 XAS intensity can be correlated to the coverage.

The characterization of the nanostructures performed by means of XAS and XMCD measurements is summarized in Fig. 4.9. The figure shows the magnetic absorption profiles (compare Sec. 2.5) for positive (μ_+) and negative (μ_-) helicity. The XAS spectra are generally used to gain information about the electronic properties of the sample. For instance, the XAS line shape can be used to indicate the *electronic configuration* of the ground state if compared to theoretical multiplet calculations. Furthermore, Fig. 4.9 shows the XMCD ($\mu_- - \mu_+$) for 0° and 70° enabling to investigate the out-of-plane and in-plane magnetic properties.

A first important observation is, that the XAS line profiles deviate from those obtained on multi-layer films of Fe, Co, and Ni (Chen *et al.*, 1990b; Chen *et al.*, 1995). In addition, they also differ from data obtained on metallic substrates (Gambardella *et al.*, 2003; Błoński *et al.*, 2010). The XAS spectra, shown in Fig. 4.9, reveal a *multiplet* structure for all configurations contrary to those earlier reports. This multiplet structure generally hints toward a rather *weak interaction* regarding two aspects. Firstly, the interaction between individual nanostructures and, secondly, the interaction between the nanostructures and the substrate. Consequently, the weak interaction explains the different behavior, because on metallic substrates or in multi-layer films the interaction is usually strengthened. The decreased interaction strength is supported by two additional expectations. Firstly, the inert-like behavior of graphene (Ohta *et al.*, 2007) suggests this behavior. Secondly, according to the fairly small binding energies (between 0.29 eV and 0.97 eV), GGA+U model calculations predict *physisorption* in case of Fe, Co, and Ni adatoms on graphene (Wehling *et al.*, 2011).

XAS and XMCD on Fe/MLG

In case of Fe, the XAS line shape reveals a broad peak for the L_2-edge and two sharp resonances at the L_3-edge, compare Fig. 4.9(a). Interestingly, the dichroism at the L_3-edge is mainly caused by the low energetic resonance. The origin of the multiplet structure remains unknown. It might trace back to *many-body*, *crystal field*, or *hybridization effects*.

A comparison of the XAS line shape to theoretical multiplet predictions (Van der Laan *et al.*, 1992) indicates a $3d^6$ *electronic configuration* of the ground state of the Fe adatoms, if a crystal field strength of $10Dq = 0.5$ eV is assumed. However, this conclusion has to be treated carefully, because the symmetry of graphene (dihedral: D_6) is lower than the symmetry used within the calculations (tetrahedral: T_d) (Van der Laan *et al.*, 1992). Additionally, the crystal field strength $10Dq$ cannot be determined from the performed experiments. These limitations may account for the deviations of

the concluded $3d^6$ configuration from the $3d^74s^1$ configuration, predicted within theoretical models for Fe/graphene (Johll *et al.*, 2009; Wehling *et al.*, 2011). Although disagreement exists regarding this issue, the predictions match the experimental results concerning a different issue. The calculations predict a high-spin ground state, that is in line with the experimentally determined branching ratio, $BR_{Fe} = 0.74$. This also suggests a high-spin ground state of Fe (compare Sec. 2.6 for further explanations about *BR*).

Unfortunately, the orbital moment and the spin sum rule cannot be applied because the magnetic moments were not saturated at the maximum magnetic field available ($B = 5$ T). Instead, the ratio *R* (compare Sec. 2.6) can be evaluated and gives $R_{Fe} = 0.05 \pm 0.03$. In view of the suggested high-spin ground state, this value indicates a *small orbital magnetic moment* of the adatoms, which is in line with recent relativistic DFT calculations (Sargolzaei *et al.*, 2011).

The inset of Fig. 4.9(a) can be used to conclude about the easy-axis of the magnetic moments. It depicts the XMCD for the L_3-edge normalized by the XAS intensity. The L_3 resonance intensity, acquired at normal incidence angle, exceeds the amplitude at grazing incidence angle by 20%. This indicates an *out-of-plane easy-axis* for Fe/MLG.

XAS and XMCD on Co/MLG

The XAS/XMCD experiments dealing with Co adatoms on MLG are depicted in Fig. 4.9(b). In this case, the L_3 edge consists of three individual resonances while for the L_2-edge again no multiplet structure can be resolved. Similar to Fe, the dichroism at the L_3 edge is mainly given by the low energy resonances. Interestingly, the multiplet features are less pronounced compared to the case of Fe which hints toward a *stronger interaction* in case of Co. This is particularly in line with the predicted binding energies of Fe (0.27 eV) and Co (0.62 eV) (Wehling *et al.*, 2011) and the STM observations concerning the stability of these species.

A comparison of the XAS line shape to the theoretical predictions (Van der Laan *et al.*, 1992) suggests a $3d^7$ *electronic configuration* of the ground state, if again a crystal field strength of $10Dq = 0.5$ eV is assumed. The branching ratio determined in case of Co matches that of Fe, i.e. $BR_{Co} = 0.74$, and again suggests a high-spin ground state. On the one hand, theory also predicts a high-spin ground state. On the other hand, this result was achieved for a $3d^84s^1$ electronic configuration (Johll *et al.*, 2009; Wehling *et al.*, 2011). The deviation between experiment and theory concerning the electronic configuration may trace back to the aforementioned discrepancies regarding the crystal symmetries and the unknown crystal field strength.

Equal to the case of Fe, the magnetic moments were not saturated. Motivated by the same branching ratios of Fe and Co, the evaluation of the ratio R_{Co}, compared to the value of Fe, is of interest. For Co, this quantity is larger, i.e. $R_{Co} = 0.35 \pm 0.02$, which indicates a *higher orbital moment*, that is in line with theory (Sargolzaei *et al.*, 2011). Furthermore, the inset of Fig. 4.9(b) exhibits, similar to Fe, an increased normalized XMCD intensity for normal incidence angle depicting an *out-of-plane easy-axis* in case of Co as well.

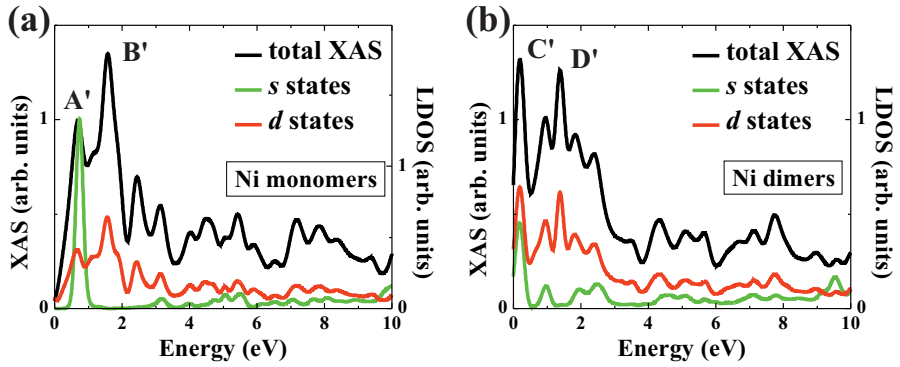

Figure 4.10: (a) Theoretical spin-averaged *s* and *d* LDOS as well as predicted XAS spectra for Ni monomers on graphene. (b) The respective calculations for Ni dimers on the same substrate. Adapted from Eelbo *et al.*, 2013a.

XAS and XMCD on Ni/MLG

Figure 4.9(c) illustrates the results of 0.007 ALE Ni/MLG, that yield an interesting peculiarity. The XMCD is *quenched* indicating that the Ni adatoms exhibit a $3d^{10}4s^0$ electronic configuration. This would be consistent with previous results (Duffy *et al.*, 1998; Yagi *et al.*, 2004; Valencia *et al.*, 2010; Cao *et al.*, 2010; Wehling *et al.*, 2011; Gyamfi *et al.*, 2012a). Due to the closed 3*d*-shell, the XAS profiles are expected to show *no absorption resonances* but only step-like features originating from non-resonant transitions, compare Sec. 2.5. In contrast, the XAS spectra depict a *multiplet structure* with basically two resonances at the L_3-edge and a broad resonance with two contributions for the L_2 edge.

In order to explain this contradiction, atomistic simulations using first-principles DFT were performed to model the Ni *s* and *d*-states and the XAS spectra at the L_3-edge. The model comprises the Vienna *ab initio* simulation package (Kresse *et al.*, 1994) with a projector augmented plane wave based code (Blöchl, 1994; Kresse *et al.*, 1999) and the WIEN2K package (Blaha *et al.*, 1990) with a full-potential linear augmented plane wave (Krogh Andersen, 1975) basis sets. The generalized gradient approximation (GGA) was employed to the exchange-correlation potential, while the results were converged carefully with respect to the number of *k* points. The system was modeled by a 3×3 graphene supercell of 18 carbon atoms with Ni placed on top. The XAS spectra were calculated within the dipole approximation using Fermi's golden rule (Dirac, 1927).

The calculated L_3 XAS spectra for Ni monomers adsorbed in hollow sites are shown in Fig. 4.10(a). They yield a *multiplet structure* with two pronounced resonances in line with the experiment. The spectra mainly follow the estimated *d*-LDOS although the *s*-LDOS provides the strongest resonance. According to Sec. 2.5, this is caused by the transition matrix element being enhanced in case of transitions to *d*-states compared to *s*-states. Comparing the theoretically determined spectra to the experimental data, reveals reasonable agreement. While the separation of the predicted L_3 resonances is given by $\Delta E_{theory} = 0.9$ eV, the experimentally determined separation is slightly larger, i.e. $\Delta E_{exp.} = 1.3$ eV, compare Fig. 4.9(c). The relative intensities of both resonances (A < B $\hat{=}$ A' < B') are in line for experiment and theory.

By this comparison the conclusion is unavoidable, that the measured XAS spectra originate almost entirely *from unoccupied Ni d-states*. This finding is only consistent with the previous report (Gyamfi *et al.*, 2012a) and with the vanishing XMCD, if the *d*-occupation of the Ni adatoms close to, but not perfectly $3d^{10}$. It is hence higher compared to bulk Ni (Chen *et al.*, 1990b). In agreement with the Anderson impurity model (Anderson, 1961), no magnetic moment can be formed if the occupation is close to a full shell. Consequently, a vanishing XMCD is expected.

The small number of holes in the Ni 3*d*-shell is due to hybridization effects. Firstly, peak A' arises from the hybridization of Ni d_{z^2}-states with Ni *s*-states, that marginally contribute to the XAS. Secondly, peak B' is dominated by the hybridization of Ni d_{xy}- and $d_{x^2-y^2}$-states with graphene's p_z-states. The origin of this feature is the exclusive coupling of conduction band states near the van Hove singularity of graphene, i.e. the discontinuity in the LDOS, to this kind of *d* orbitals exhibiting E_2 symmetry (Gyamfi *et al.*, 2012a).

In case of an increased coverage of 0.014 ALE Ni on MLG, the experiments reveal dramatically different results. According to Fig. 4.9(d), the relative XAS intensities of the leading resonances at the L_3-edge reversed. In addition, and even more important, a small but *significant* XMCD effect occurred arising from the first of both resonances.

In order to explain the experimental observations the calculations were extended to Ni dimers, shown in Fig. 4.10(b). The calculations are in accordance with the experiment regarding two aspects. Firstly, two main resonances at the L_3-edge were found, whereas, opposite to the lower coverage, in this case the low energy peak is stronger in intensity. Secondly, the predicted energetic separation between both resonances matches the experiment ($\Delta E_{theory} = \Delta E_{exp.} = 1.2$ eV). Interestingly, peak C' shifts about 0.5 eV downward in energy compared to the monomer case. This can be attributed to variations of the band structure of Ni. More precisely, the unoccupied dimer *s*-states are shifted to lower energies while the amount of unoccupied *d*-states is increased. This hints to an enhanced hybridization of Ni *s*-orbitals in the dimer case and consequently causes the *d*-orbitals to depopulate.

The effect amplifies according to the *mean cluster size*. In fact, small clusters ($n_{\mathrm{Ni}} \leq 4$) are found to be *nonmagnetic*, but for larger clusters ($n_{\mathrm{Ni}} > 4$) the magnetic moment is *stable*. It increases up to 0.85 μ_{B} per atom in case of a closed Ni layer on graphene. The occurrence of an XMCD can hence be understood with respect to the increased coverage. This causes an enhanced fraction of larger clusters ($n_{\mathrm{Ni}} > 4$) for statistical reasons. An easy-axis of the magnetization cannot be determined though. According to the inset of Fig. 4.9(d), the amplitudes of the XMCD are equal for normal and grazing incidence angle.

4.4 The Influence of the Substrate

In the foregoing section, the properties of TM adatoms on MLG were clarified. Regarding the two-dimensional electron gas, these adatoms represent perturbation centers. In general, impurities adsorbed on graphene are expected to cause electron scattering between both sublattices of graphene. This type of scattering is referred to as *intervalley scattering*. With respect to the band structure, intervalley scattering can be illustrated by scattering between both inequivalent *K*-points. The effect was already experimentally observed for the case of defects within

graphene (Rutter *et al.*, 2007) or induced by surface-adsorbed impurities (Mallet *et al.*, 2007). Interestingly, in the vicinity of TM impurities on MLG this effect was not observed.

Motivated by this lack, TM adatoms were deposited on a second type of graphene, namely QFMLG. According to Sec. 4.2.2, this type of graphene differs in an *apparently minor way* from MLG. The underlying substrate is equal, both types of graphene exhibit well-defined linear band dispersions and properties close to those of free-standing graphene. Only the decoupling mechanism differs, which results in a reduced apparent corrugation of the surface and in an even enhanced decoupling efficiency in case of QFMLG. As a result, observing or not-observing intervalley scattering on QFMLG was expected to provide insight into its mechanism. The study focused on Ni and Co adatoms due to the negative experiences made by STM investigations performed on Fe adatoms. The samples were again provided by the group of *U. Starke* from the *Max Planck Institute for Solid State Research* in Stuttgart and also grown in an Ar-atmosphere (Emtsev *et al.*, 2009; Riedl *et al.*, 2009). Prior to the STM experiments, the samples were degased inside UHV at $\approx$ 850 K to remove residual contamination.

4.4.1 STM/STS on Co/QFMLG

Figure 4.11 displays Co adatoms being adsorbed on QFMLG. In view of the STM observations obtained on MLG, it was surprising, that on QFMLG *two different species* of Co adsorbates were observed. Co_A has as a triangular appearance with a "Y"-shaped depression on its center, shown in Fig. 4.11(b). In contrast, according to Fig. 4.11(c), Co_B appears as a "usual" adatom with a sharp protrusion in its center. The differences in terms of appearance and apparent height can be easily seen from the line profile, given in Fig. 4.11(d). In order to exclude, that Co_A-type features are entailed by clustering of three Co atoms, a control experiment on a W(110) substrate was performed. By using the same deposition parameters, an average number of Co adatom per surface unit was estimated. This is only compatible with the experiments on Co/QFMLG, if Co_A features originate from a single Co atom. The high-resolution images enable to determine the adsorption sites of these species. Similar to the case of MLG, the white guidelines to the eyes display hollow sites. Hence, Co_A is adsorbed on *top* of a C atom, whereas Co_B is adsorbed on the *hollow site*.

In addition, STS was performed on both types of adsorbates, depicted in Fig. 4.11(e). While ramping the voltage a strong change of the tunneling current at ≈ -0.25 V was observed in case of Co_B. This resonance goes hand in hand with a change of the appearance toward a triangular shape. In conclusion, Co_B *changed to* Co_A. Despite this typical signature indicating a change from one type of Co into the other, one might expect other characteristic features for both types of adatoms. In general, theory predicts characteristic shapes of Fano resonances (Fano, 1961) within the differential conductance depending on the adsorption site of the particular adatom (Uchoa *et al.*, 2009). Importantly, these resonances are predicted for small tip-sample separations, at which Co usually is manipulated for the particular sample system described here. Consequently, these resonances were experimentally not detected and a comparison between theory and experiment regarding this issue is obsolete.

Figure 4.11 reveals some additional features. The overview image yields several dark depressions on the substrate. These arise from *non-hydrogen-saturated dangling bonds* of the underlying topmost Si atoms of the crystal. Note, that neither in case of Co nor in case of Ni, an

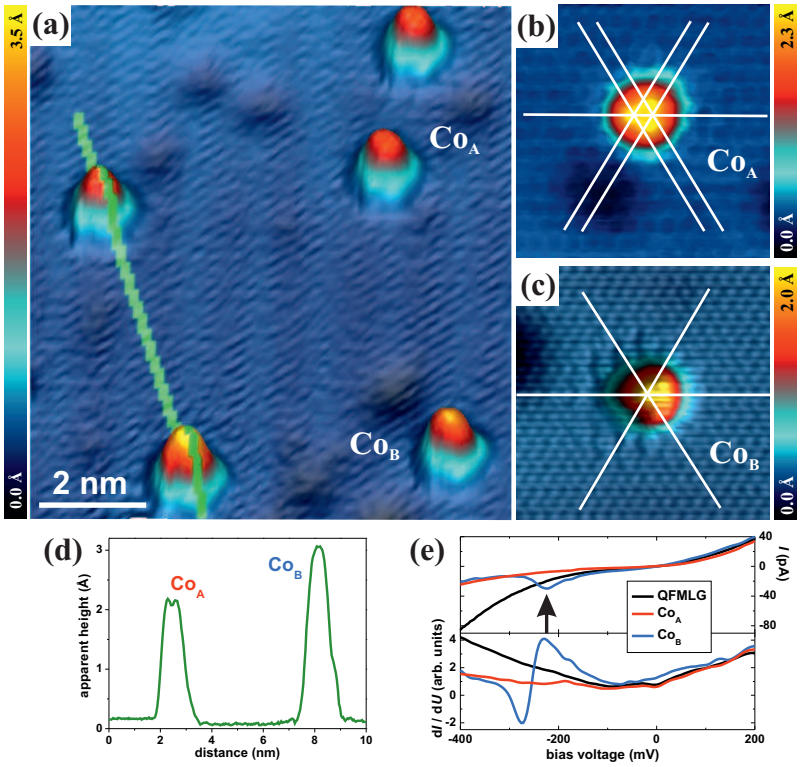

Figure 4.11: (a) Constant-current map of two types of Co monomers on QFMLG. Tunneling parameters are $U = 0.3$ V and $I = 0.1$ nA. (b,c) High-resolution images indicating top and hollow site adsorption in case of Co_A and Co_B, respectively. Tunneling parameters are $U = -0.3$ V, $I = 0.1$ nA and $U = 0.3$ V, $I = 0.1$ nA. (d) Line profile across Co_A and Co_B adatoms as indicated in (a). (e) Set of I and dI/dU spectra recorded on QFMLG and on the adsorbed Co impurities. Tunneling parameters for the STS are $U = 0.3$ V and $I = 0.07$ nA. Subfigures (a,d and e) are adapted from Eelbo *et al.*, 2013b.

influence of these features was revealed onto the adsorption geometries or on the properties of the adatoms. This suggests that the defect density was too low to have a sizable effect on the aforementioned properties.

4.4.2 STM/STS on Ni/QFMLG

In case of Ni/QFMLG, two different species of adatoms were observed as well. This can firstly be seen from the overview image, given in Fig. 4.12(a), and secondly from the indicated line profile, displayed in Fig. 4.12(d). Ni_A exhibits the same characteristic appearance as in case of MLG, namely a ring-like protrusion with a central depression. In contrast, Ni_B appears with a central protrusion only. Equal in both experiments is the adsorption site of the nodal-type Ni_A, i.e. *hollow site*, compare Fig. 4.12(b). Consequently, Ni_B is adsorbed in the *top site* according to Fig. 4.12(c). Although the adsorption site of the Ni adatoms can be manipulated by the STM tip, a switching from one type to another during STS experiments was not observed, compare Fig. 4.12(e). The spectra only show different intensities of the LDOS of both species, but neither characteristic resonances nor sudden changes.

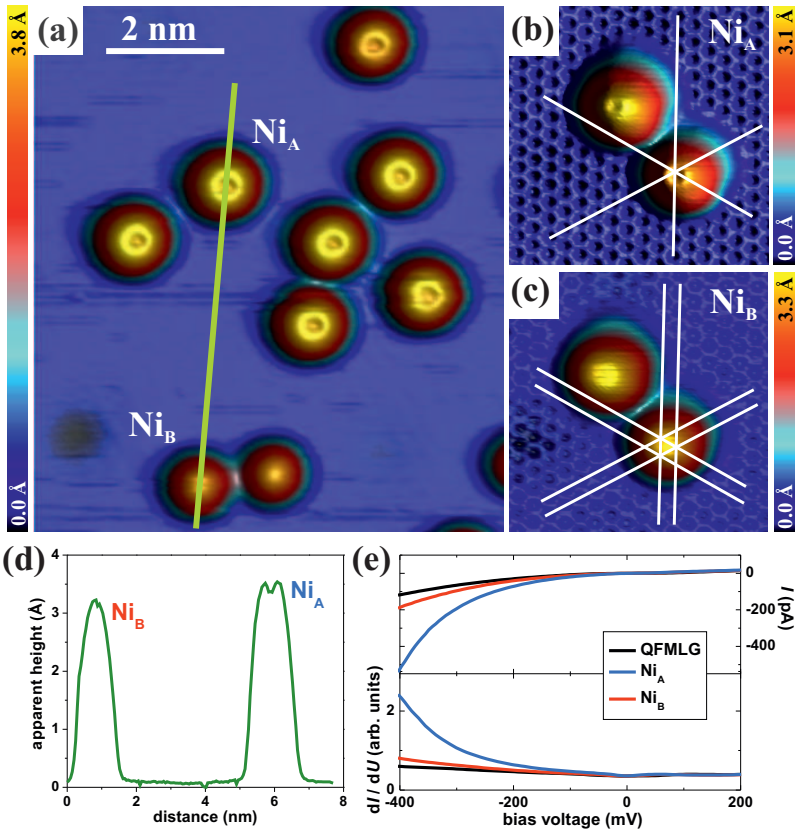

Figure 4.12: (a) Constant-current map of QFMLG after the deposition of a small amount of Ni atoms at 12 K. Tunneling parameters are $U = -0.5$ V and $I = 0.1$ nA (b,c) High-resolution images revealing the adsorption site of Ni_A and Ni_B to be hollow and top site, respectively. Tunneling parameters are $U = -0.1$ V, $I = 0.09$ nA and $U = -0.05$ V, $I = 0.09$ nA. (d) Line profile along the line indicated in (a) comparing Ni atoms located on both adsorption sites. (e) STS spectra taken on Ni atoms adsorbed on QFMLG. Tunneling parameters for STS were $U = 0.4$ V and $I = 0.05$ nA. From Eelbo *et al.*, 2013b.

4.4.3 QFMLG vs. MLG

On the one hand, the deposition procedures were identical for the studies on MLG and QFMLG. On the other hand, a completely different adsorption behavior was found. This contradiction has therefore to be related to differences induced by the substrates even though one might expect only small variations of their properties.

A first difference between those substrates is given in terms of the *surface roughness*. A sizable effect of the corrugation on the properties of adsorbed impurities was, for instance, reported in case of carbon nanotubes (Durgun *et al.*, 2004; Valencia *et al.*, 2010). Although they generally represent a different sample system, nanotubes can be considered as corrugated sheets of graphene depending on their diameter.

For the study at hand, one might hence wonder whether the adatoms' properties are influenced by the enhanced surface roughness in case of MLG. For MLG, the corrugation arises from the moiré pattern induced by the interface layer. Interestingly, this type of moiré

pattern was revealed to have a strong influence on the properties of graphene in case of MLG/Ru(0001) (Gyamfi *et al.*, 2011). By means of STS a strong bonding between substrate and valley regions and a weak bonding between substrate and hill regions was found. This indicates improved properties of the hills, which consequently are more similar to free-standing-graphene. Hence, an influence of the $(6\sqrt{3} \times 6\sqrt{3})\mathrm{R}30^\circ$ superstructure in case of MLG/SiC(0001) on the properties of graphene seems plausible. This might straightforwardly influence the properties of the adsorbed atoms. For this reason, the adsorption sites on MLG/SiC(0001) were investigated with respect to the moiré's $(6\sqrt{3} \times 6\sqrt{3})\mathrm{R}30^\circ$ unit cell. Neither in case of Co nor in case of Ni an influence of the moiré pattern on the adatoms' adsorption sites could be detected. For all cases, Co adsorbs on top, while Ni adsorbs on the hollow position. In addition, by means of STS, the electronic properties were found to be equal among all adatoms of each species, independent of the relative position within the moiré's unit cell. Consequently, an effect based on the corrugation of MLG/SiC(0001) is concluded to be negligible.

Regarding the multiple configurations, the different STS features obtained for $\mathrm{Co_A}/\mathrm{Co_B}$ on QFMLG have to be assigned to *different electronic properties*, because an atomic origin (clustering) was excluded. Multiple stable configurations of Co on graphene were predicted by means of an active space self-consistent-field approach (Rudenko *et al.*, 2012). These calculations predict different equilibrium heights above the graphene sheet and different electronic configurations. The configurations were computed to be either $3d^7 4s^2$ or $3d^9 4s^0$. However, owing to the fact, that equal adsorption sites (hollow site) were found for both configurations and top site adsorption was not predicted, this model is unsuitable to explain the experimental observations.

For a specific Coulomb potential, different adsorption sites of Co on free-standing graphene were predicted within the aforementioned GGA+U approach (Wehling *et al.*, 2011). For $U = 0$ eV, hollow site adsorption was found exhibiting a $3d^9 4s^0$ electronic configuration, whereas in case of $U = 4$ eV, a $3d^8 4s^1$ configuration and top site adsorption were computed. In contrast, the preferred adsorption site of Ni is the hollow position independent of the on-site Coulomb potential resulting in a non-magnetic electronic configuration of $3d^{10} 4s^0$. Hence, the calculations performed for free-standing graphene show *perfect agreement* with the experimental observations on MLG, presented in Sec. 4.3. For this reason, the assumption seems plausible that the GGA+U ($U = 4$ eV) model (Wehling *et al.*, 2011) might also appropriately predict the properties of Co and Ni adatoms on QFMLG.

The experimental observation of two simultaneously stable adsorption sites is consistent with this model if the *binding energies* are discussed in more detail. The energy differences important for the diffusion processes are 0.15 eV in both cases, Co and Ni. This implies diffusion temperatures of about 65 K. As a result of the deposition temperature being 12 K within the experiments, the adatoms can be assumed to be immobile. The adsorption behavior of the adatoms is thus expected to be out of *thermodynamical equilibrium*. Therefore, on the one hand, the observation of two different adsorption sites in the case of QFMLG is not surprising. On the other hand, this scenario is supposed to be valid for MLG as well. It is hence unexplainable why only one type of Co and Ni adatoms were found on MLG.

Further discrepancies occur between the experiment and the GGA+U model (Wehling *et al.*, 2011) regarding the apparent heights in the STM topographies compared to the calculated heights of top and hollow site adsorbed atoms. In case of Ni,

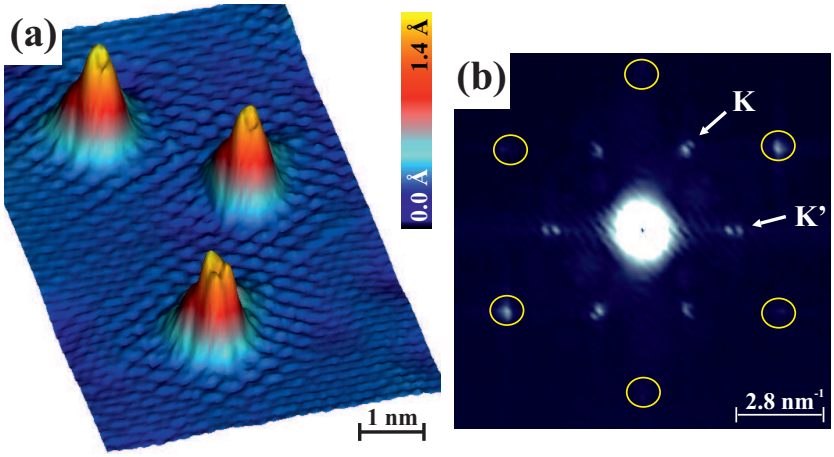

Figure 4.13: (a) Three-dimensional STM image of QFMLG revealing a ($\sqrt{3} \times \sqrt{3}$)$R30°$ pattern in the vicinity of Co_A adatoms. The z-scale is exaggerated for visual clarity. Tunneling parameters are $U = -0.3$ V and $I = 0.07$ nA. (b) 2D-FFT analysis of the STM topography. Yellow circles indicate spots originating from graphene's lattice. The inner spots are related to intervalley scattering of electrons between nonequivalent Dirac cones. Its periodicity is 3.7 Å, equal to the wavelength $\lambda_F = 2\pi/k_F = 3a/2$, where a is graphene's lattice constant. Adapted from Eelbo *et al.*, 2013b.

the theoretically predicted height difference (0.3 Å) matches the experimental estimation. In contrast, this is not the case for Co. Here, the experimentally determined difference (≈ 0.8 Å) is about twice as large as the theoretically computed one (0.4 Å).

Therefore, in view of the different observations on both types of graphene, *none* of these models predicts the properties of the adatoms consistently. This hints toward significant substrate effects, namely the *degree of decoupling*, that so far remained neglected by theory. It seems that this needs to be considered for an appropriate description of the properties of individual 3*d* TM adatoms on graphene on varying (and realistic) substrates.

4.4.4 Intervalley Scattering on QFMLG

QFMLG was chosen as a substrate due to the lack of intervalley scattering in the vicinity of TM adatoms on MLG. Importantly, the *deposition of Co* on QFMLG reveals this type of scattering. This enables to precisely investigate this effect in a controlled manner, compare Fig. 4.13(a). The graphene lattice in the vicinity of Co adatoms exhibits an interference pattern which was analyzed by means of a fast Fourier transform (FFT), shown in Fig 4.13(b). While the six outer (yellow marked) spots originate from graphene's lattice, the inner spots stem from a ($\sqrt{3} \times \sqrt{3}$)R30° superstructure. This superstructure is entailed by the intervalley scattering for which the Co adatoms induce the symmetry breaking.

Opposite to the diameter of the superstructure being ≈ 3 nm in case of the y-shaped Co_A-type adsorbates, the diameter reduces to 2 nm in case of Co_B-type adatoms. For Ni adatoms, the effect was not observed. The GGA+U model (Wehling *et al.*, 2011) predicts different electronic configurations among these adsorbates ($Co_{\text{top site}} = 3d^8$, $Co_{\text{hollow site}} = 3d^9$, Ni = $3d^{10}$).

As a result, the ruling criterion for the strength of this effect is suggested to be the valence state of the adatom. Moreover, as already mentioned, the effect was not found in case of MLG. This hints again toward an influence of the substrate-graphene interaction or an insufficient resolution caused by the superimposed corrugation due to the interface layer.

4.5 Summary

With the preceding sections deep insight was gained into the field of individual magnetic nanostructures grown on graphene. A SiC(0001) surface was selected for conceptional reasons because it is well characterized, can be prepared with high quality, and allows for a direct connection to state-of-the-art Si-based semiconductor devices.

By means of different experimental approaches, namely the STM and X-ray based spectroscopy, combined with first-principles DFT calculations, Fe, Co, and Ni adatoms and clusters on MLG/SiC(0001) were investigated (Eelbo *et al.*, 2013a). Interestingly, Fe and Co reveal paramagnetic behavior with out-of-plane easy-axes. The data of Ni adatoms yield the final proof of a previously reported nonmagnetic ground state in the regime of single atoms (Gyamfi *et al.*, 2012a). The XAS spectra support the STM findings of generally weak interactions (physisorption) between graphene and these types of adatoms. This ultimately leads to the impossibility of assigning the adsorption site of Fe with the available setup. In contrast, Co was identified to adsorb in the unusual top position. This is contrary to most theoretical results, but can be confirmed if an on-site Coulomb potential is included in the theory. Importantly, in terms of magnetism, Ni is not unusable. The experiments clearly prove that for elevated coverages a significant XMCD effect arises. Theory was able to attribute this effect to the *d*-shell occupation of Ni which scales down according to the increase of the mean cluster size *n*. This way, Ni clusters can be tuned between nonmagnetic ($n \leq 4$) and magnetic behavior ($n \geq 5$).

For MLG/SiC(0001), the first layer of graphene is decoupled by the carbon interface layer saturating the dangling bonds of the topmost Si atoms of the substrate. The intercalation of hydrogen effectively decouples the former strongly bonded interface layer and turns it into the first layer of graphene, i.e. QFMLG. At first glance, QFMLG/SiC(0001) and possibly adsorbed nanostructures are expected to exhibit properties very similar to the scenario of MLG/SiC(0001). Surprisingly, this moderate variation of the substrate alters the above mentioned observations significantly.

By a purely STM and STS based investigation dramatic changes in terms of adsorption sites and adatom-substrate interactions were revealed by exchanging the MLG to a QFMLG substrate (Eelbo *et al.*, 2013b). More precisely, both Co and Ni show up on QFMLG in two stable configurations. They are either adsorbed on the top or the hollow sites of the substrate. Another important finding is that the combination of QFMLG and Co adatoms enables to investigate the effect of intervalley scattering in a controlled manner. This effect arises from the scattering of Dirac fermions between inequivalent *K* points within the Brillouin zone of graphene.

Regarding the different observations on MLG and QFMLG, the corrugation of the substrate was concluded to have a negligible influence. Instead, the differences were assigned to the degree of decoupling of the respective graphene. To this end, QFMLG represents the "im-

proved" graphene since its chemical potential matches the DP even better than MLG. Importantly, there is no comprehensive theoretical model which can conclusively explain the different findings on the very similar substrates of QFMLG and MLG on SiC(0001).

Chapter 5

Topological Insulators

Despite graphene, another modern class of materials, namely the class of topological insulators, was investigated being subject of this chapter. Similar to the graphene-based studies, the main focus was put on the combination of promising TI candidates with small TM nanostructures. The basic concepts and properties of TIs are introduced in Sec. 5.1. The section involves a discussion of the expected phenomena and potential applications. Subsequently, the background of the experiments performed on TIs is described in detail in Sec. 5.2. This involves general aspects of the materials Bi_2Se_3 and Bi_2Te_3 and details of their preparation.

The STM/STS- and XAS/XMCD-based experiments as well as the related theoretical calculations for Co adatoms and nanostructures on Bi_2Se_3 are presented in Sec. 5.3. This work was published recently (Eelbo *et al.*, 2013c). The corresponding calculations were performed by *G. Bihlmayer* from the *Peter Grünberg Institute and Institute for Advanced Simulations*.

The proceeding section, Sec. 5.4, deals with another combined experimental and theoretical study. Individual Fe adatoms on the surface of Bi_2Te_3 were investigated, whereas the corresponding manuscript was lately published (Eelbo *et al.*, 2014). The theoretical contributions were made by the *Theory of Dirac Materials'* group of *O. V. Yazyev*. Both Bi_2Se_3 and Bi_2Te_3 samples were provided by *I. Miotkowski* from the *Purdue University* in the United States. A summary of the main TI-findings finalizes the chapter in Sec. 5.5.

5.1 Overview of Topological Insulators

The concept of topological insulators is based on the *quantum Hall effect* discovered in 1980 (Klitzing *et al.*, 1980). It represents the first experimental observation of a topologically originated effect. For his achievement *K. von Klitzing* was awarded the *Physics Nobel Prize* only five years later in 1985.

By means of transport measurements, performed on two-dimensional metal-oxide-semiconductor samples at cryogenic temperatures (4.2 K), peculiar behavior was recognized. The *bulk* of the samples remained *insulating* if perpendicular magnetic fields of the order of 15 T were applied. In contrast, current was carried by channels near the edges of the devices. Consequently, these states were referred to as so-called *edge states*. The unidirectional edge

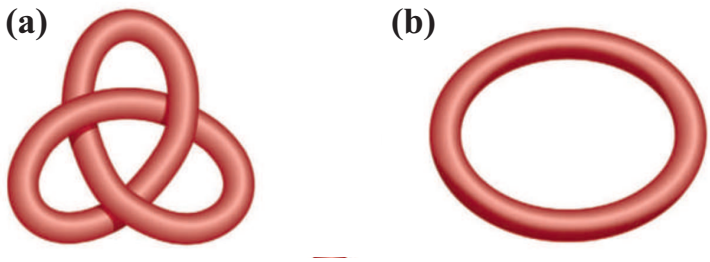

Figure 5.1: Illustration of two topologically different objects, reflecting (a) a topological insulator and (b) an ordinary insulator. The ring structure cannot be modified into the trefoil knot unless cutting the string. This is equivalent to a non-continuous change and a necessary variation of the topological invariants describing both classes. Adapted from Moore, 2010 with permission.

currents cause a quantized conductance without losses due to dissipation. The quantized conductance is a direct consequence of the electrons' circular orbit due to the topology of the sample. This means that the quantum Hall state depends on the geometry of the sample because the electrons are confined to two dimensions and subject of a strong perpendicular magnetic field. In contrast, the quantum Hall state is independent of material details (Laughlin, 1981; Thouless *et al.*, 1982).

Henceforth, the concept of topology was developed in detail (Wen, 1995). Topology depicts structural properties of objects and can this way be used to characterize a certain class of materials. The concept enables to determine topological invariants, such as the *Chern number* or the *Berry phase*. These quantities determine a material to be either an *ordinary* or a *weak/strong topological insulator*. The Chern number can be computed by an integration over the Berry curvature. Although the integrand depends on details of the surface geometry, the Chern number, due to integration, does not. Instead, it only depends on the global topology (Qi *et al.*, 2011).

To persist within the same topological class under a variation of the sample surface, the transition from the initial to the final state has to be of *smooth*, i.e. adiabatic, character. More precisely, the system is not allowed to pass a quantum phase transition. As a result, the Chern number remains constant during a smooth transition. For a two dimensional sample, different number of holes reflect different classes of topology. Therefore, a sphere is topologically equivalent to an ellipsoid, whereas a coffee cup (due to the hole at the handle) is topologically equivalent to a donut (Qi *et al.*, 2011). For both examples one can consider procedures to reform the initial to the final shape without introducing additional holes. In contrast, a non-smooth transition requires discontinuities, compare Fig. 5.1. The trefoil knot cannot be transformed into the ring structure without breaking the string. Consequently, the Chern number of both objects is different.

The concept of topology can be easily applied to condensed matter systems, that exhibit an energy gap (Zhang, 2008). In this picture, smooth transitions refer to the stability or instability of the energy gap. For a Hamiltonian of a many-particle system with an energy gap between ground and excited states, a smooth transition illustrates a process of one gapped state of the system into another gapped state without an intermediate gapless state. This action can

be more realistically illustrated by similarities of ordinary insulators and semiconductors. Although the energy gap between valence and conduction band states of the semiconductor is much smaller compared to the ordinary insulator, one can consider a transition of the respective Hamiltonian into the other without closing the gap (Hasan *et al.*, 2010).

5.1.1 Properties

A usual insulator is characterized by a large bulk band gap between the valence and the conduction band. This cannot be overcome except for strong modifications of the material's composition, e.g. by introducing electrically conductive dopants. Similar to usual insulators, TIs exhibit bulk band gaps, that can be of significant size (several hundred meV). Opposite to usual insulators, in the vicinity of phase transitions, i.e. a variation of the topological invariants, the bulk band gaps of TIs are bridged by *conductive gapless surface or edge states*. These connect the valence and the conduction bands (Kane *et al.*, 2005). Note, that the interface of a TI at a vacuum border depicts such a phase transition. The vacuum is topologically equivalent to an usual insulator. Its conduction states are given by electrons and its valence states by positrons.

Usual and topological insulators can be easily distinguished by the Chern number. The Chern number C characterizes an insulator being trivial ($C = 0$) or topological ($C \neq 0$). It can be computed via a surface integral of the respective object (Nakahara, 2003). Thereby, the Bloch wave functions $|u_n(\boldsymbol{k})\rangle$ describing the object in the reciprocal space need to be known. A line integral over a closed loop determines the according Berry curvature F_n originating from the object (Berry, 1984).

$$F_n = -\mathrm{i}\nabla_{\boldsymbol{k}} \times \langle u_n(\boldsymbol{k})|\nabla_{\boldsymbol{k}}|u_n(\boldsymbol{k})\rangle \tag{5.1}$$

The Berry phase can be seen as a geometrical phase of the object in the reciprocal space (Berry, 1984). Finally, the Chern number is given by the surface integral of the Berry curvature over the entire Brillouin zone:

$$C = \frac{1}{2\pi} \sum_n \oint F_n \mathrm{d}^2\boldsymbol{k} \tag{5.2}$$

In 2006, HgCdTe quantum wells were first proposed to be realistic candidates for strong 2D TIs (Bernevig *et al.*, 2006). They were experimentally realized only one year later (König *et al.*, 2007). The samples consist of a structure of HgTe layers sandwiched between layers of CdTe with minimum thicknesses of 6.3 nm. Above this *critical value*, a *band inversion* of the conduction-band *s*-states and the valence-band *p*-states enables the expected 2D TI behavior, compare Figs. 5.2(a,b). The edge states are illustrated in subfigure 5.2(b) by the red and blue lines connecting the valence and conduction bands.

Soon after the first experimental realization of a TI, their concept was generalized to three-dimensional systems (Fu *et al.*, 2007a; Moore *et al.*, 2007; Roy, 2009). As is the case for a 2D TI, the above described configuration is not achievable for a 3D structure without a *strong spin-orbit interaction*, that hence is a prerequisite. Figure 5.2(c) shows a model of the band structure

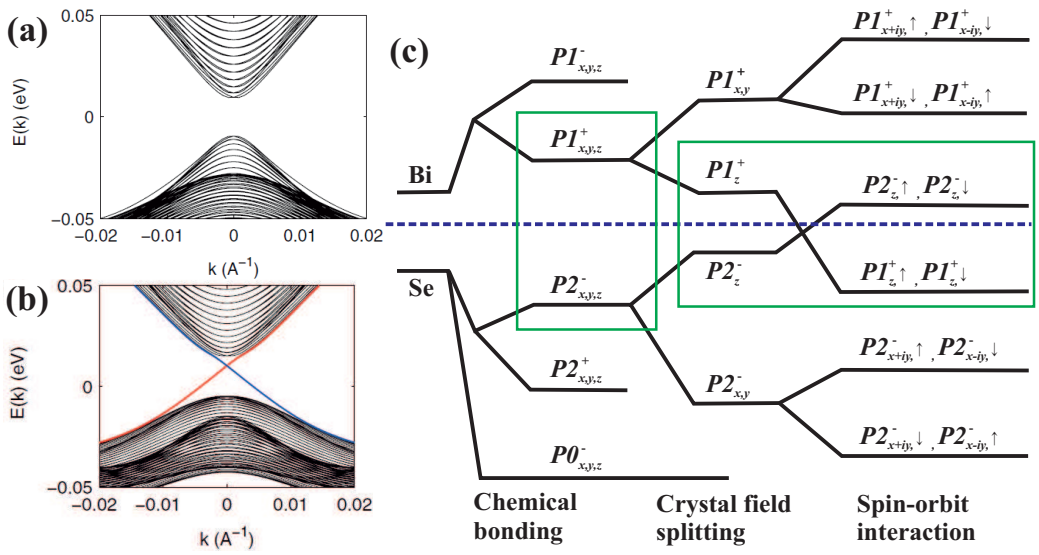

Figure 5.2: (a) Energy spectrum of the effective Hamiltonian of the HgTe layers sandwiched between layers of CdTe in a cylindrical geometry. For a thin quantum well, this setup results in an insulating bulk energy gap. (b) For thick quantum wells, gapless edge states arise. These bridge the bulk energy gap with opposite spin polarizations on both edges. Adapted from Qi *et al.*, 2010 with permission. (c) Schematic illustration of the evolution of the $p_{x,y,z}$ orbitals of Bi and Se resulting in valence and conduction band states. The evolution is driven by the chemical bonding, the crystal field splitting, and the SOI, respectively. In particular, the SOI leads to the band inversion highlighted by the green rectangles. The model neglects the *s*-orbitals, as the DOS at the Fermi surface is mainly given by the *p*-states. Adapted from Zhang *et al.*, 2009a with permission.

of the 3D TI Bi_2Se_3. It illustrates that the SOI is the crucial ingredient to cause an inversion of the *p*-orbitals. This is the characteristic feature of these materials (Zhang *et al.*, 2009a).

The SOI mimics the effect of an external magnetic field by coupling the spin and orbital angular momentum degrees of freedom of the electrons. This way, the electrons feel *spin-dependent forces* even in non-magnetic materials when they are moving through the crystal (Moore, 2010). For this reason, the electrons with different spins propagate in *opposite directions* along the edges giving rise to the quantum spin Hall effect (Murakami *et al.*, 2004). The characteristic spin-dependent movement of the Dirac fermions established the nomenclature of the so-called *helical edge states*. This is motivated by the formation of a left-handed helical texture in momentum space.

The edge states show a *linear-like dispersion*. They hence cross each other in a certain number of *Kramers degenerate points* in the reciprocal Brillouin zone. This means that the system is robust with respect to *time-reversal symmetry*. Away from these special points, the SOI lifts the degeneracy. The Kramers degenerate points therefore form 2D DPs in the surface band structure (Hasan *et al.*, 2010). These level crossings of the helical edge states prohibit a smooth transformation of a TI into an ordinary insulator not showing these edge states (Qi *et al.*, 2011).

Presuming an odd number of level crossings/DPs, the TI is called a strong TI characterized by

respecting TRS and exhibiting topologically non-trivial states at the same time. In contrast, an even number of DPs leads to a weak TI characterized by non-stable edge states of the quantum spin Hall state. According to Eq. 5.2 this property is mathematically described by the winding number of the Berry phase. This is even (odd) in case of a trivial/weak (non-trivial/strong) TI.

5.1.2 Three-Dimensional Topological Insulators

Realistic candidates for 3D TIs are expected to be semiconductors with small band gaps that consist of heavy elements. This suggestion bases on the relativistic effect of the SOI, that is strong for heavy elements. Furthermore, the SOI can only have a strong enough influence on the material to change its phase, if the material's band gap is sufficiently small. Materials with large band gaps are hence unsuitable.

The first realistic candidates of 3D TIs were $Bi_{1-x}Sb_x$ for $0.07 \leq x \leq 0.22$ and $\alpha-$Sn (Fu *et al.*, 2007b). Indeed, by means of surface-sensitive ARPES experiments, $Bi_{0.9}Sb_{0.1}$ was identified to be a TI in 2008 (Hsieh *et al.*, 2008). It also reveals the dissipationless quantum spin Hall effect (Hsieh *et al.*, 2009a). Here, ARPES is the method of choice because it utilizes a modulated photon energy. This enables a clear distinction of TSSs from that of the bulk 3D band structure. Topological surface states do not disperse along a direction perpendicular to the surface whereas the bulk states do (Hasan *et al.*, 2010).

5.1.3 2nd Generation Topological Insulators

Unfortunately, $Bi_{1-x}Sb_x$ is a randomly distributed alloy. Therefore, additional candidates of strong topological insulators were searched and found within the so-called *second generation* of strong TIs, i.e. Bi_2Se_3, Bi_2Te_3, and Sb_2Te_3 (Xia *et al.*, 2009; Zhang *et al.*, 2009a; Chen *et al.*, 2009). These materials feature several advantages compared to $Bi_{1-x}Sb_x$. Firstly, they are *stoichiometric compositions* and, thus, can in principle be grown with higher quality. This is expected to improve the signal-to-noise ratio in experiments and to enhance the observability of TI-related effects. Secondly, these materials exhibit *sizable bulk band gaps* of up to ≈ 300 meV, much larger compared to $Bi_{1-x}Sb_x$. This feature enables to observe the topological behavior even at room temperature and strongly improves the possibility of their use for applications. Thirdly, these materials exhibit the simplest surface state which is allowed for 3D TIs. According to Fig. 5.3, they are characterized by a *single Dirac point* at $\overline{\Gamma}$ whereas $Bi_{1-x}Sb_x$ shows five crossings at the Fermi energy. This simplifies data evaluation. One might think that a single DP violates the fermion doubling theorem (Nielsen *et al.*, 1983). This theorem states that for a system preserving TRS DPs must come in pairs. The doubling theorem remains valid due to the partner DP being located at the opposite surface of the TI.

With respect to their outstanding properties, 2nd generation TIs show various similarities to graphene. On the one hand, TIs and graphene are *Dirac materials*. On the other hand, due to the two sublattices, graphene exhibits two Dirac cones. These are furthermore spin-degenerate and, thus, are contrary to the single Dirac cones of 2nd generation TIs. This difference leads to interesting consequences important for applications and fundamental physics.

A first difference between TIs and graphene is given by the QHE. Although it is

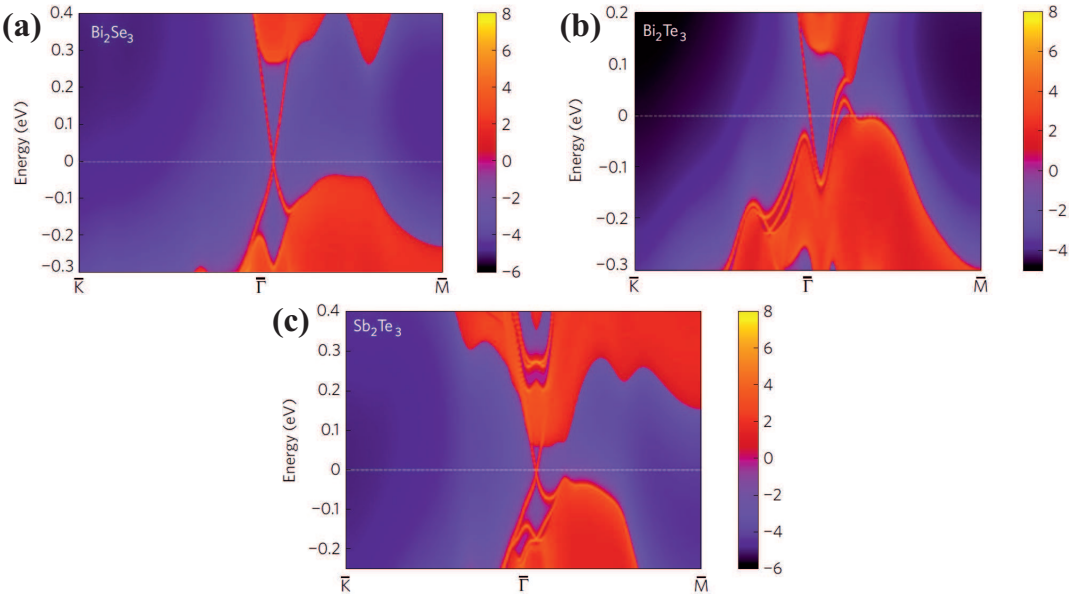

Figure 5.3: Energy and momentum dependence of the LDOS on the (111) surfaces of layered and stoichiometric crystals of Bi_2Se_3 (a), Bi_2Te_3 (b), and Sb_2Te_3 (c). The results were obtained by first-principles electronic calculations. The warmer colours represent higher LDOS, whereas red regions depict bulk valence and conduction bands. Clearly, the calculations suggest the existence of gapless TSSs. These are depicted by the thin red lines, that bridge the bulk energy gap and form DPs at $\bar{\Gamma}$. Adapted from Zhang *et al.*, 2009a with permission.

observable in both material classes, it is spin-degenerate in graphene (Haldane, 1988; Novoselov *et al.*, 2005; Zhang *et al.*, 2005) due to the *spin-degenerate* DPs mentioned before, compare Fig. 5.4(a). As a consequence, electrons can propagate in the presence of disorder with different spin orientations in graphene. In contrast, in TIs, the propagation direction is linked to the spin giving rise to the non-degenerate *quantum spin Hall effect*, shown in Fig. 5.4(b).

This directly provokes another interesting effect. In contrast to graphene, on the surfaces of strong 3D TIs, *backscattering is suppressed* in the vicinity of surface disorder, e.g. near a step edge (Roushan *et al.*, 2009; Zhang *et al.*, 2009b; Alpichshev *et al.*, 2010). Usually strong disorder centers cause a formation of an insulating state (Anderson, 1958). This is different for TIs, which are protected against this mechanism. This way, they differ from both, metal substrates, that "accidentally" exhibit surface states, and graphene, that also is expected to become localized in the presence of strong disorder (Castro Neto *et al.*, 2009).

More precisely, the effect bases on the spin-dependent motion of the electrons on the TI surface along a specific direction. TRS leads to a *destructive interference* of all possible backscattering paths and thus to the suppression of backscattering. For a nonmagnetic perturbation on the surface, backscattering can in principle be caused by SOI. If an electron with a fixed spin state impinges on the scattering center, it turns either clock- or anticlockwise around the impurity. Importantly, the electron can only propagate into the direction it came from, if its spin state inverts by an angle π or $-\pi$, compare Fig. 5.4(c,d). This way, both paths differ by 2π which leads to an inversion of the wave function, that describes this electron. As a re-

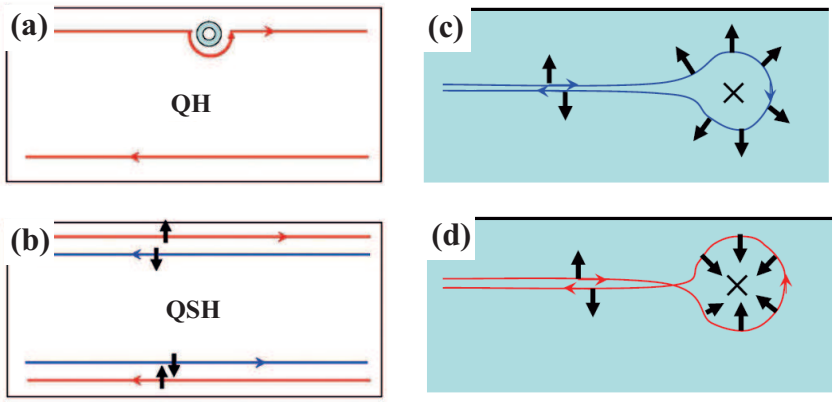

Figure 5.4: (a) In case of the quantum Hall state, propagating electrons exhibit spin-degeneracy. (b) Presuming the quantum spin Hall effect of TIs, the propagation direction is linked to the intrinsic spin. (c) and (d) In the presence of a TRS respecting (non-magnetic) perturbation, backscattering is suppressed owing to the destructive interference induced by the spin reversal. Adapted from Qi *et al.*, 2011 with permission.

sult, a destructive interference is obtained leading to *perfect transmission*. This illustrates the absence of available states for backscattering. It depicts a spin-dependent *ballistic transport* of the charge carriers. However, for $T > 0$, inelastic backscattering processes are allowed. In general, these will contribute to the conductivity and lead to *diffusive* rather than ballistic transport (Hasan *et al.*, 2010).

This can be visualized by means of ARPES experiments. Constant energy contours exhibit a hexagonal warping of *quasi-particle interference* patterns. Those arise from the interaction of the TSSs with the threefold symmetric crystal potential, that is a bulk property. By this mechanism, certain scattering channels are enhanced compared to others (Chen *et al.*, 2009; Fu, 2009; Zhang *et al.*, 2009b). An important aspect is that the hexagonal warping is strengthened in the case of Bi_2Te_3 because its bulk band gap is much smaller compared to Bi_2Se_3 (Chen *et al.*, 2010).

5.1.4 Expected Effects and Potential Applications

Concerning applications, 2nd generation TIs are most promising candidates due to their enlarged bulk band gap. Bi_2Te_3 is already well known and commonly used in thermoelectric devices for applications at room temperature.

In view of potential applications and fundamental science, a general problem to be solved is the *intrinsic doping effect* of TI substrates. This is entailed by the fact that many of the interesting effects are observable only if the chemical potential, i.e. the Fermi level, is located near the DP. Due to *imperfections* during the growth process, this condition is usually not fulfilled. The chemical potential is generally shifted to the bulk conduction band being not even in the bulk band gap anymore (Hor *et al.*, 2009; Alpichshev *et al.*, 2010; Bianchi *et al.*, 2010; Wang *et al.*, 2011).

For Bi_2Se_3 (Bi_2Te_3) the shift mainly originates from two different types of intrinsic defects.

These are firstly Se_{Bi} (Te_{Bi}) antisite defects (Cho *et al.*, 1999; Urazhdin *et al.*, 2002), where excess Se (Te) atoms occupy Bi lattice sites, or secondly Se (Te) vacancies (Scanlon *et al.*, 2012; Zhang *et al.*, 2012b). Both types of defects lead to a considerable *n*-doping of the pristine substrate. The doping effect can be reduced or compensated by a moderate Ca- or NO_2-doping (Sn-doping) of the Bi_2Se_3 (Bi_2Te_3) substrate introducing hole carriers (Chen *et al.*, 2009; Hor *et al.*, 2009; Hsieh *et al.*, 2009b). Manipulating the substrate's band structure in this way enables the ability of precisely adjusting the chemical potential near the DP. Consequently, excellent tunability by the application of electric fields is achievable, another feature interesting in view of electronic devices.

Regarding fundamental physics, a variety of effects exists, that is accessible in TI-based samples. Moreover, TIs are also potential candidates for technological applications, although some drawbacks have to be overcome for their realization, compare Sec. 6.2.

In view of the protection of the TSSs with respect to TRS, quite naturally, the breaking of this symmetry is expected to cause strong influences on the TI properties. Consequently, most effects are related to such a violation. Breaking Kramers degeneracy of the TSSs can be achieved by altering the TI surface with magnetic impurities that exhibit a net *out-of-plane magnetization* (Qi *et al.*, 2008; Liu *et al.*, 2009; Wray *et al.*, 2011). This dramatically modifies the TI properties leading to the opening of a finite energy gap at the DP. If the DP is moreover tuned toward the bulk band gap, this perturbation turns the TI into an *ordinary insulator* exhibiting insulating behavior with respect to both, bulk and surface.

The presence of TRS breaking perturbations also affects the TI in a different way. Considering the perturbation as a scattering center, the destructive interference, that is generally present on TI surfaces, is disrupted. The aforementioned suppression of backscattering of the helical edge states is thus lifted due to SOI with this impurity (Qi *et al.*, 2011).

Another consequence of lifting Kramers degeneracy by magnetic perturbations, is the expectation of a half integer quantized Hall conductance (Pankratov, 1987). This way, the proximity to magnetic insulating perturbations gives rise to the *anomalous* QHE, that is a band insulator with quantized Hall conductance but without orbital magnetic field (Qi *et al.*, 2011). It is detectable by means of transport measurements if a domain wall is introduced inside the magnet (Hasan *et al.*, 2010).

Furthermore, TRS breaking of the surface states gives rise to the magnetoelectric effect (Qi *et al.*, 2008; Essin *et al.*, 2009). This means, in the presence of TRS breaking, on the surface of a TI, an electric field generates a magnetic dipole or, alternatively a magnetic field induces a charge polarization. The phenomenon is already known from multiferroic materials (Ramesh *et al.*, 2007). Compared to multiferroics, TIs have to be seen as the superior choice for potential applications. This is owing to the greatly enhanced speed and reproducibility in TIs. Here, the effect results purely from the orbital motion of the electrons.

An outstanding prospect of a TI-based application is given by its combination with a superconductor. This is expected to enable the existence of *Majorana fermions* (Majorana, 1937). These are particles which are their own antiparticles. Hence, Majorana fermions are electrically neutral and are in most respects "half" of an ordinary Dirac fermion (Wilczek, 2009). For a heterostructure consisting of a TI and a superconductor, the surface of the superconductor may transfer Cooper-pairs into the TI. This way, the TI surface becomes superconducting it-

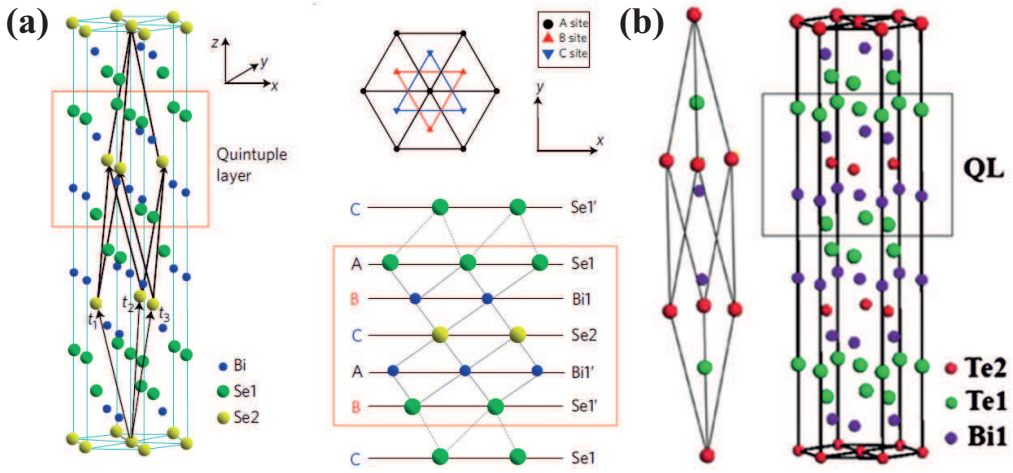

Figure 5.5: (a) Structural model of the crystal lattice of Bi_2Se_3 in a side and top view. The quintuple layers are only weakly bonded by van-der-Waals interaction between adjacent Se atoms. Adapted from Zhang *et al.*, 2009a with permission. (b) Structural model of the unit cell and the crystal lattice of Bi_2Te_3 in a side view. The quintuple layer is indicated by a black box whereas adjacent Te atoms are van-der-Waals bonded. Adapted from Hao *et al.*, 2012 with permission.

self due to the *proximity effect*. The resulting 2D superconducting state is not spin-degenerate and contains only half the degrees of freedom of an ordinary metal. This enables to induce a vortex core inside the superconducting TI surface. Since Majorana fermions are expected to exist in the vicinity of these vortex cores, both are trapped at the superconducting TI surface region (Jackiw *et al.*, 1980; Fu *et al.*, 2008). Importantly, this concept offers the opportunity for the first *direct observation* of Majorana fermions.

In view of potential quantum computing applications, a Majorana fermion depicts a degenerate two-level system, i.e. a qubit. Majorana fermions offer a *high reliability* because they obey non-Abelian quantum statistics (Moore *et al.*, 1991). This tremendously reduces potential errors in quantum computing devices (Kitaev, 2003; Collins, 2006).

5.2 Experiments on TIs

Turning to the desired experiments on TM nanostructures, appropriate TI substrates have to be chosen first. In this view, the advantages of 2nd generation TIs compared to the initially investigated topological insulators, such as $Bi_{1-x}Sb_x$, were obvious (compare Sec. 5.1.3): Growth with higher quality, the simplest possible TI band structure, and large bulk band gaps are expected to ease the investigations. As a consequence, Bi_2Se_3 and Bi_2Te_3 were chosen as appropriate substrates for the investigations of adsorbed nanostructures. In this section, the bare substrates are introduced and characterized in more detail by means of STM and STS experiments. Therefore, the presented data represent the starting point for the adsorption of magnetic Co and Fe nanostructures.

According to Fig. 5.5, the crystal structures of Bi_2Se_3 and Bi_2Te_3 are very similar. The (111)-

oriented crystals are built up of so-called *quintuple layers*. A quintuple layer consists of alternating layers of two times Bi and three times Se/Te. Inside each quintuple layer, the atoms are covalently bonded. In contrast, adjacent quintuple layers are only weakly bonded by the *van-der-Waals interaction* between adjacent Se (Te) atoms. Consequently, outer and inner Se (Te) atoms are inequivalent with respect to their electronic properties due to the differences in hybridization. The in-plane lattice constants are 412.8 pm and 438.3 pm for Bi_2Se_3 and Bi_2Te_3, respectively. The rhombohedral unit cell comprises three quintuple layers. Hence, the lattice constants in the *z*-direction are 2.864 nm and 3.049 nm, respectively. The step heights corresponding to a single quintuple layer are 0.955 nm and 1.016 nm.

The single crystals of Bi_2Se_3 (Bi_2Te_3) were similarly grown via the *Bridgman technique*. To this end, a mixture of high-purity elements was initially deoxidized and purified by multiple vacuum distillations. Subsequently, the mixture was heated to elevated temperatures ($\approx$ 1150 K) for several hours. Afterward, it was slowly cooled down inside Se (Te) atmosphere to compensate for vacancies. Finally, the crystals were zone refined at low speed to obtain samples well-oriented in the (111) direction.

Recently, significant improvements were reported concerning the quality of TI samples prepared by means of MBE (Zhang *et al.*, 2010; Li *et al.*, 2010; Wang *et al.*, 2011). These works prove that the characteristic TI properties already arise at small film thicknesses of only a few quintuple layers, i.e. about six in case of Bi_2Se_3 and about two in case of Bi_2Te_3. More importantly, a significant charge transfer from the substrates toward the TI thin films was revealed in the low-thickness range. Therefore, it is important to note that the samples, used within the experiments at hand, were single crystals with much larger thicknesses. Consequently, influences from the sample plates or the conductive adhesive were naturally avoided.

Preparation for Experiments

For the experimental investigations the crystals were mounted to sample plates made of tungsten using conductive adhesive. In addition, pieces of a molybdenum foil were glued on top of the crystals. Regarding the STM and STS measurements, the samples were transferred inside the UHV-system into the cryostat, compare Sec. 3.1. After the samples were cooled down to 4.2 K, they were cleaved inside the cryostat, whereas the mechanical hand (wobble stick) was used to grab the molybdenum foil. If the foil is actually pulled sideways relative to the sample plate, the single crystals break along the (111)-direction. This is a result of the weak van-der-Waals interaction between adjacent quintuple layers. Huge areas of *monatomic steps* can be achieved - step edges are extremely rare. Similar to the measurements on graphene, compare Sec. 4.3, this is a welcome precondition for the XAS and XMCD measurements. Step edges might falsify the experimental results due to different types of interactions with attached nanostructures.

Unfortunately, in case of the XAS and XMCD measurements a cool-down of the samples prior to the cleaving process was not possible. Hence, the samples were cleaved at room temperature inside UHV and immediately cooled down to a temperature of $\approx$ 6 K within fifteen minutes. Room temperature treatment of TIs over longer time periods usually involves a significant altering of the TI's band structure (Bianchi *et al.*, 2010). This originates from a relatively strong reactivity of these surfaces with molecules from the rest gas. Such molecules are gettered

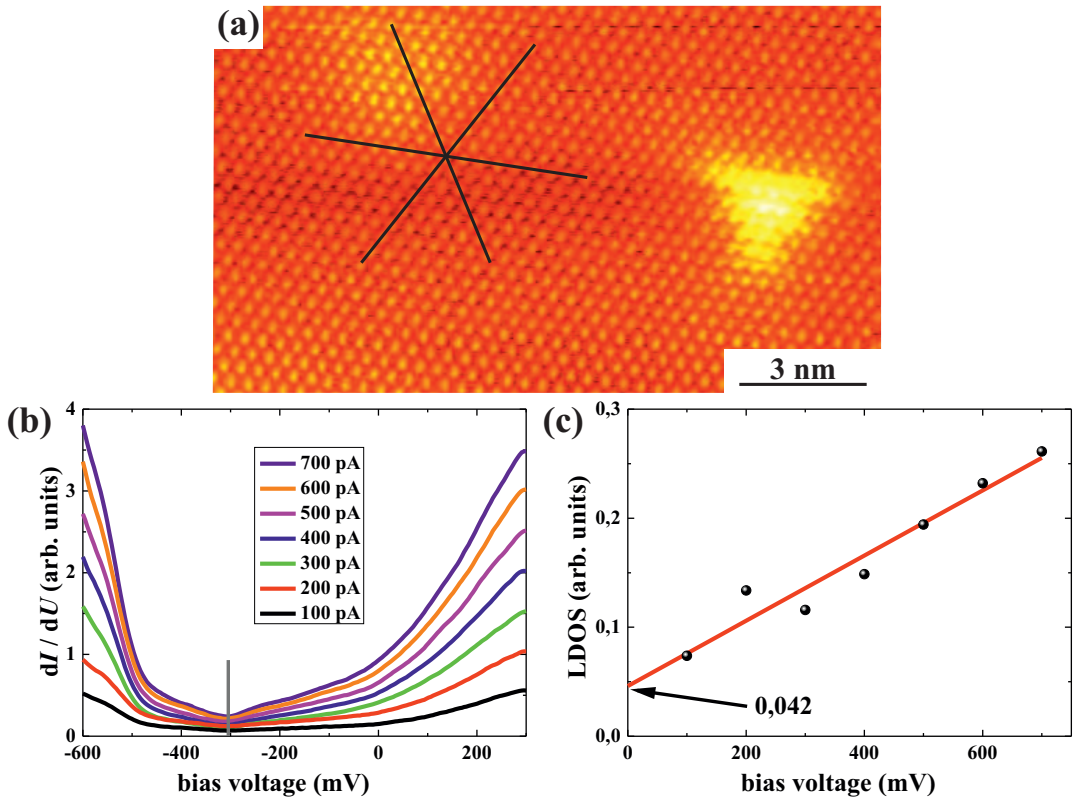

Figure 5.6: (a) STM constant-current map of the Bi_2Se_3 surface. For these tunneling parameters (U = 500 mV, I = 300 pA) topmost Se atoms are visible as yellow protrusions. The triangular feature at the right border of the image depicts a seldomly appearing pristine defect of the substrate. (b) STS performed on the surface at various tunneling currents. The stabilization voltage was U = 300 mV. The global minimum of the conductance can be assigned to the DP, that is indicated by a gray line at ≈ -310 mV. (c) Dependence of the absolute minimum of the LDOS on the applied bias voltage.

by the TI modifying its band structure significantly (Bianchi *et al.*, 2011). However, since the samples were cooled down within 15 minutes, this effect is assumed to be *negligible* for the data presented here.

5.2.1 Pristine Bi_2Se_3

Figure 5.6 shows typical results from STM and STS experiments performed on Bi_2Se_3 crystals. The constant-current image in Fig. 5.6(a) reveals a uniform surface with yellow protrusions representing topmost Se atoms. Besides, an example of *infrequent triangular defects* is visible. According to the explanation given in Sec. 5.1.4, these defects were assigned to Se_{Bi} antisite defects (Urazhdin *et al.*, 2002). Apart from that, the in-plane lattice constant was determined according to the line profiles indicated in Fig. 5.6(a). The line profiles result in a combined lattice constant of $a_{exp}(Bi_2Se_3)$ = 414.3 pm, close to the literature value.

Furthermore, the crystal was investigated by means of STS, shown in Fig. 5.6(b). Within

the series of current-dependent spectra, several characteristics can be easily identified. All spectra exhibit sharp enhancements of the LDOS at about -450 mV and -50 mV. These risings depict the *onsets of the bulk valence* and *conduction bands* of Bi_2Se_3, compare Fig. 5.3(a). In between these features, the LDOS is greatly decreased and arises mainly from the surface states of the crystal. Thereby, all spectra exhibit a global minimum at an energy of ≈ -310 mV. It is obvious from the band structure that the LDOS is minimized at the energy where the TSSs cross each other. Hence, this global minimum in the STS spectra is assigned to the DP of Bi_2Se_3. The shift of the DP with respect to the Fermi level illustrates the intrinsic *n*-doping effect (Hor *et al.*, 2009; Bianchi *et al.*, 2010) due to the presence of Se_{Bi} antisite defects (Urazhdin *et al.*, 2002) and Se vacancies (Scanlon *et al.*, 2012; Zhang *et al.*, 2012b). The absolute values of the global minimum of the LDOS can be extracted and investigated depending on the applied bias voltage U, compare Fig. 5.3(c). A straight line was fitted to the data points. This line does not match the *xy*-origin of the plot. According to Sec. 5.1.2 and Sec. 5.1.3, this indicates a *finite contribution of bulk states* to the overall conductivity.

5.2.2 Pristine Bi_2Te_3

Bi_2Te_3 investigated by means of STM is depicted in Fig. 5.7(a). Similar to Bi_2Se_3, the substrate exhibits wide and smooth areas. The topmost Te atoms are shown as yellow protrusions for the tunneling parameters used here. The infrequent protruding clover-shaped defects were identified before and assigned to Te_{Bi} antisite defects (Wang *et al.*, 2011). Again, the in-plane atom-atom distance was evaluated as indicated and results in $a_{exp}(Bi_2Te_3) = 444.3$ pm, close to the literature value.

The STS results obtained on Bi_2Te_3 are depicted in Figs. 5.7(b,c). The onsets of the bulk valence and bulk conduction bands are identified at +15 mV and +95 mV. In good agreement with the theoretical band structure calculations for Bi_2Se_3 and Bi_2Te_3, compare Figs. 5.3(a,b), the bulk band gap is much smaller in case of Bi_2Te_3. Furthermore, the global minimum in the STS spectra at $\approx +40$ mV must not be straightforwardly assigned to the DP, since in the case of Bi_2Te_3, the DP is *buried* by the onset of the bulk valence band.

To determine the energetic position of the DP the linear slopes of the “remaining” surface states in the STS spectra can be used, compare Fig. 5.7(c). By fitting straight lines to these sections of the spectra, the DP can be estimated in a simple approximation by the intersection point with the *x*-axis. This point indicates a vanishing LDOS and depicts the ideal situation of an ultimately sharp crossing of the TSSs. This way, the DP is roughly determined to be at ≈ -35 mV indicating again a pristine electron doping of the sample, that is well in line with previous observations (Alpichshev *et al.*, 2010; Wang *et al.*, 2011). The shift with respect to the Fermi level can again be assigned to the existence of Te_{Bi} antisite defects (Cho *et al.*, 1999) and Te vacancies (Scanlon *et al.*, 2012; Zhang *et al.*, 2012b). Note, that this procedure is not reliable to precisely evaluate the DP but, instead, has to be seen as a simple approximation. Errors may be due to the fitting of the straight lines. These can, for instance, originate from bulk contributions (finite temperatures, vacancies, crystal imperfections). Such influences would mask the "true" conductivity of the TSSs and result in a misleading gradient of the straight lines. Furthermore, they would affect the real conduction at the DP as well, compared to the idealized case at hand.

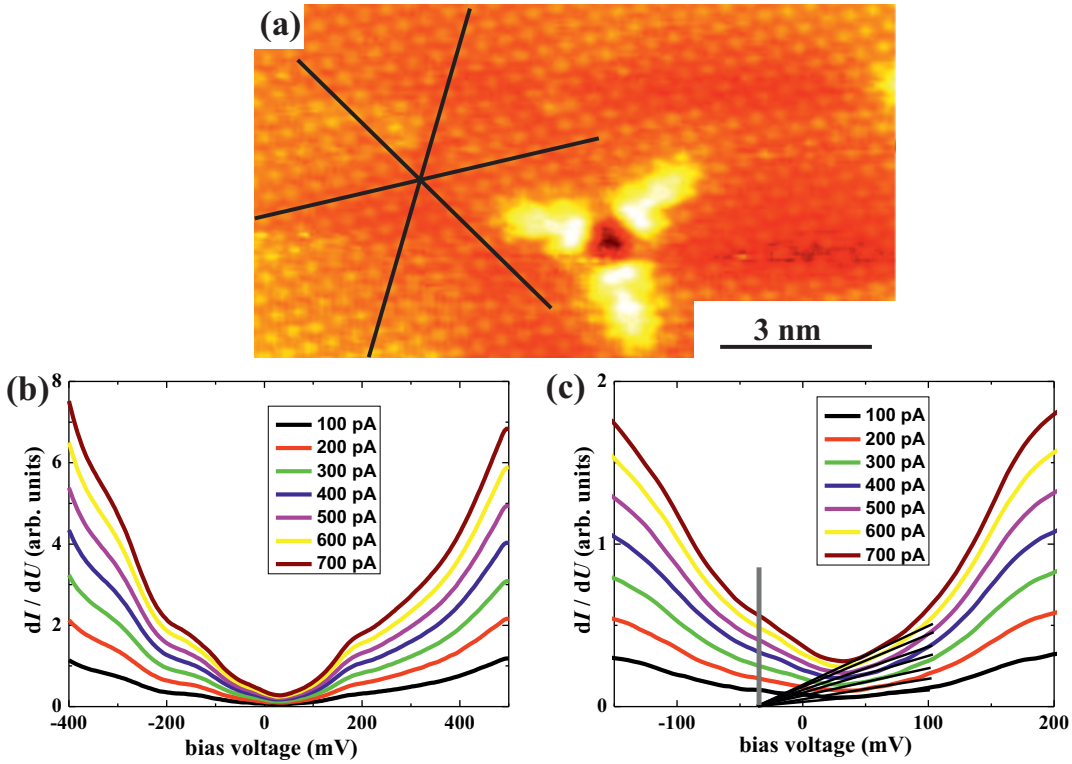

Figure 5.7: (a) STM constant-current map of the Bi_2Te_3 surface. For these tunneling parameters, $U = -400$ mV, $I = 200$ pA, topmost Te atoms are visible as yellow protrusions. The triangular clover-shape feature in the lower region of the image depicts a seldomly appearing type of a pristine defect of the substrate. It was assigned to a Te_{Bi} antisite defect. (b) STS of defect-free Bi_2Te_3 at various tunneling currents. The stabilization voltage was $U = 500$ mV. (c) Magnified view on the bulk band gap. In contrast to Bi_2Se_3, the DP is buried and, thus, has to be determined by the linear slopes of the TSSs. According to this procedure the DP is found at ≈ -35 mV.

5.3 Co on Bi_2Se_3

The first experimental investigation focused on Co nanostructures deposited on Bi_2Se_3. The Co coverages were varied in the range of 0.01 ALE up to 0.10 ALE. The samples were provided by *I. Miotkowski* from the *Purdue University*. To elucidate the findings DFT-based calculations were performed by *G. Bihlmayer* from the *Forschungszentrum Jülich*. The pristine substrate was precharacterized prior to the STM experiments, compare Sec. 5.2.1.

In view of the XAS and XMCD investigations, background spectra on the pristine crystals were acquired first. Moreover, the deposition rates were determined using a W(110) substrate, that was cleaned as described elsewhere (Bode *et al.*, 2007). Similar to the graphene-based experiments, equal deposition parameters (excluding time) were used for these calibrations and the actual measurements. Afterward, the coverage was estimated by means of STM. This way, the coverage can be assigned to the L_3 XAS intensity.

5.3.1 STM on Co/Bi_2Se_3

After the precharacterization of the bare substrate, compare Sec. 5.2.1, minute amounts of Co were deposited with the sample held at $\approx$ 12 K. A summary of the STM observations is given in Fig. 5.8. Obviously, Co appears in *two different types* of adsorbates, henceforth called Co_A and Co_B. Both types of adatoms clearly occupy different adsorption sites, which is evidenced by the white guidelines to the eyes. This is in line with a recent study dealing with Fe adatoms on the same surface, where the authors observed two different types of adsorbates after low temperature deposition as well (Honolka *et al.*, 2012).

According to Fig. 5.8(b), Co_A appears as a protrusion in an *egg-shaped fashion*. Furthermore, the corrugation of the substrate is influenced by Co_A revealing a sixfold symmetric pattern. The substrate in the close vicinity is modified to exhibit a lower intensity and six faint protrusions can be seen symmetrically located around the adatom.

In contrast, the appearance of Co_B is strongly different, shown in Fig. 5.8(d). At this bias voltage ($U = 200$ mV) Co_B appears in a *triangular fashion*. According to control experiments, performed on a W(110) substrate, Co_B-type features originate from a single Co adatom. Although Co_B exhibits also a central protrusion, the apparent height is much smaller compared to Co_A. This can be easily seen from the color scales of both subfigures. Moreover, the influence on the substrate in the event of Co_B is threefold symmetric. Note, that especially the appearance of Co_B-type adatoms is strongly bias dependent. At larger biases, Co_B appears as an egg-shaped protrusion as well, but, compared to Co_A, with a smaller apparent height. Furthermore, the influence on the substrate remains threefold symmetric.

Interestingly, both types of adatoms show up with a different commonness. This suggests that one of the adsorption sites might be energetically favorable. The relative abundance between both types is about $n_{Co_A}/n_{Co_B} = 3/1$. However, the extremely low coverage of the sample in combination with the limited scan area and scan speed of the STM calls for a careful examination of this value.

To elucidate the STM observations, DFT calculations were performed employing the GGA (Perdew *et al.*, 1996) and using the full-potential linearized augmented plane-wave method as implemented in the FLEUR-code (Krogh Andersen, 1975; Wimmer *et al.*, 1981; Weinert *et al.*, 1982; Blügel *et al.*, 2006; FLEUR, n. d.). The model comprises a $\left(\sqrt{3} \times \sqrt{3}\right) R30°$ unit cell of four quintuple layers of the substrate.

Within the theoretical modeling, the fcc hollow site is found to be energetically favorable by $\approx$ 90 meV compared to the hcp hollow site. STM constant-current maps were simulated by integrating the LDOS between the lower boundary, i.e. the Fermi level, and the upper boundary given by +100 mV. Although this value slightly deviates from the experimentally used bias of +200 mV, a *remarkable agreement* between theory and experiment concerning the appearances is found.

The simulated pristine surface, given in the inset of Fig. 5.8(a), exhibits that topmost Se atoms occur as protrusions in constant-current topographies at these biases. Hence, the Co adatoms do not occupy the top position but instead *both hollow sites* (fcc and hcp). According to Fig. 5.8(c), Co atoms adsorbed in a fcc hollow site are expected to appear as *egg-shaped protrusions*. In contrast, Co adatoms adsorbed in the hcp hollow site are computed to show up

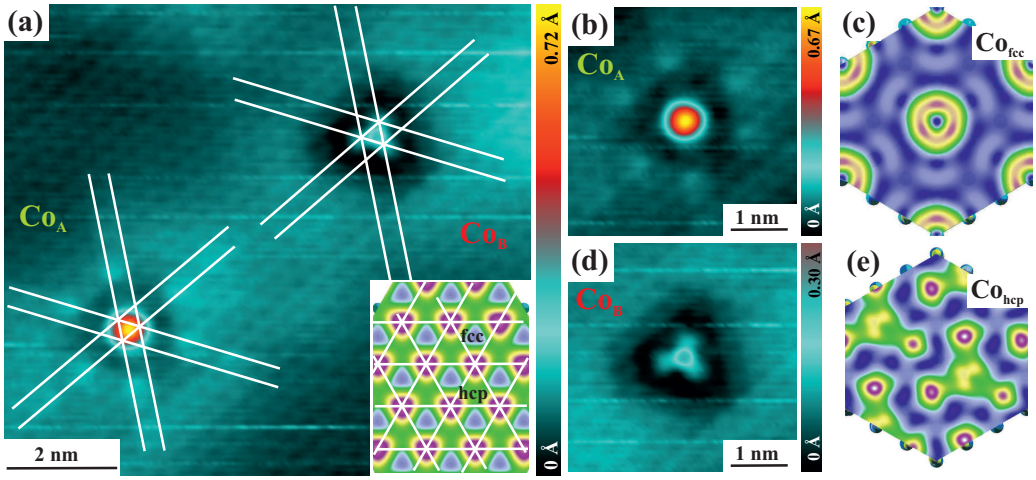

Figure 5.8: (a) STM constant-current map of two isolated and different Co impurities on the surface of Bi_2Se_3. Tunneling parameters are $U = 200$ mV and $I = 750$ pA. The inset reveals the simulated topography for a bias of $U = 100$ mV. The white guidelines to the eyes represent top positions of the surface Se layer. (b) Magnified view on Co_A revealing an egg-shaped appearance and a sixfold induced pattern in the substrate. (c) Simulated STM topography of a Co atom adsorbed in the fcc hollow site for a bias of $U = 100$ mV. (d) Magnified view on Co_B showing a triangular shape of the adatom and a threefold pattern on the substrate. (e) Simulated topography of a Co atom adsorbed in the hcp hollow site for a bias of $U = 100$ mV. Adapted from Eelbo *et al.*, 2013c.

in a *triangular fashion*, compare Fig. 5.8(e). For both hollow sites a relaxation of the Co atoms into the crystal of about 0.2 Å is found. Although the strongest intensity in the latter case is predicted to appear at the edges of the triangle, the agreement between theory and experiment is striking. This suggests that Co_A-type (Co_B-type) atoms are adsorbed in fcc (hcp) hollow sites. This assignment is particularly in line with the relative abundance of the adatoms. By this assignment, the energetically favorable fcc-adsorbed adatoms are found more often than their counterpart. Note, that the simulations can hardly be used to predict the influence on the substrate, because they were performed for an effective coverage of 0.33 ALE to keep the computational costs low. As a result, the calculations reveal an overlapped impact on the substrate originating from different adatoms within the unit cell.

Comparing these results to an experimental work reported before (Ye *et al.*, 2012), which deals with the particular sample system of Co/Bi_2Se_3, uncovers a sharp contradiction. In this work, not only a single adsorption site of Co adatoms on Bi_2Se_3 was found, but this was moreover identified being the *top position* of the surface Se layer. Although this contradiction cannot be unambiguously clarified, a possible cause might be given by the different preparation conditions. In the earlier study, both the cleaving process of the single crystals and the Co deposition were performed at *room temperature*. Even though in this case the thermal energy is high enough for the Co atoms to relax on the surface, a top site adsorption is surprising owing to the energetically favorable fcc position. Hence, it should be mentioned, that at room temperature other effects can occur as well. For instance, an *exchange process* of Fe adatoms originally deposited at low temperatures on the Bi_2Se_3 surface was found recently (Schlenk *et al.*, 2013). The authors revealed that by a very moderate annealing

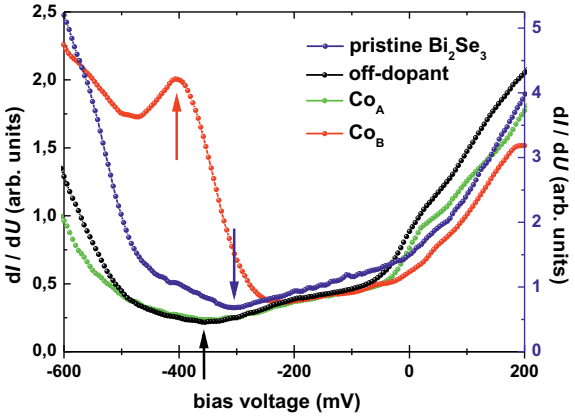

Figure 5.9: STS experiments performed on Bi_2Se_3 before (right *y*-scale) and after the deposition of Co (left *y*-scale). Tunneling parameters are $U = 200$ mV and $I = 100$ pA. The blue arrow indicates the global minimum (DP) before Co deposition. Upon this deposition, the global minimum shifts downward in energy by about −50 mV (black arrow). Furthermore, in the event of Co_B, a characteristic resonance at ≈ -400 mV was identified. From Eelbo *et al.*, 2013c.

Fe adatoms can diffuse into the bulk crystal already at $T = 260$ K. There, they substitute Bi atoms at their lattice sites. This goes hand in hand with a growth of clusters at the surface. These clusters are assumed to contain the substituted Bi atoms. It remains an open question whether similar processes can also occur for Co. However, the different preparation conditions might in principle explain the different findings of the previous work (Ye *et al.*, 2012) compared to the data at hand.

5.3.2 STS on Co/Bi_2Se_3

Besides the topographic characteristics, the electronic properties were investigated by means of STS. Therefore, prior to the deposition of Co adatoms, the pristine substrate was examined first, compare Fig. 5.6(b). After the surface was exposed to Co, point spectra were acquired on both types of adsorbates and on the surface far away from any impurity, summarized in Fig. 5.9. This so-called off-dopant spectrum reveals a shift of the global minimum of about −50 mV upon the deposition of Co from ≈ -310 mV toward ≈ -355 mV. Co hence serves for an *electron doping effect* of the sample.

As pointed out in Sec. 5.1.4, the moments of the magnetic adatoms are expected to have a strong influence on the TSSs by opening a gap at the DP (Liu *et al.*, 2009) if their magnetization is aligned perpendicular to the surface plane. Furthermore, a recent theoretical work predicts such an opening for the explicit system of Co/Bi_2Se_3 (Schmidt *et al.*, 2011). In contrast, according to Fig. 5.9, an opening was experimentally *not* observed, neither far away from the adatoms nor in their close vicinity. This finding suggests an easy-plane anisotropy for Co/Bi_2Se_3 in the low coverage regime.

Interestingly, the spectra of the adatoms reveal an additional *resonance* in case of Co_B at ≈ -400 mV. Co_A-type atoms do not reveal a similar resonance for the tunneling parameters

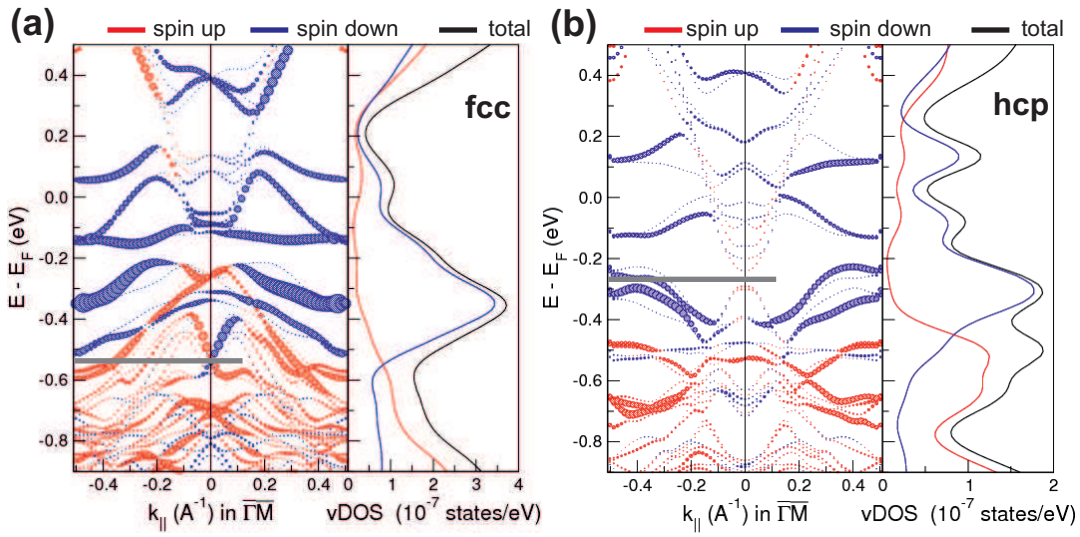

Figure 5.10: Fat band analysis and vacuum DOS of Co atoms adsorbed in the (a) fcc and (b) hcp hollow site. While spin-up states are labeled red, spin-down states are labeled blue. The size of the circles indicate the spin-polarization of the states in a region above the surface. The gray lines indicate the DPs, that are determined to be at -550 meV and -250 meV for the fcc and hcp position, respectively. From Eelbo *et al.*, 2013c.

chosen. Importantly, during the STS, a modification of Co_B adsorbates was observed several times. Thereby, the appearance and the adsorption site changed toward Co_A. A change from Co_A toward Co_B was never detected. This observation is particularly in line with the assignment of Co_A to the energetically favorable fcc-site.

The different electronic properties and the different appearances of both types of Co adatoms suggest different hybridizations with the substrate. This is further strengthened by the discrepancy between experiment and theory regarding the relaxation depths. Although theory predicts similar values for hcp- and fcc-occupation, the experimentally resolved apparent heights differ strongly, compare Fig. 5.8(b) and Fig. 5.8(d).

To gain insight, a fat band analysis of the adsorbates was performed, shown in Fig. 5.10. The figure presents the spin-resolved DOS of both types of Co with respect to their easy-axes. The easy-axes are given by the computed anisotropies which are found to be $K_{fcc} = -6$ meV (*easy-plane* anisotropy) and $K_{hcp} = +3$ meV (*out-of-plane* anisotropy). Although it might be surprising at first glance, site-dependent anisotropies were reported before for the systems of Fe and Co adatoms on Rh(111) and Fe adatoms on Pd(111) (Błoński *et al.*, 2010) as well as Fe adatoms on Pt(111) (Khajetoorians *et al.*, 2013b). Note, that the calculations at hand were again performed for an effective coverage of 0.33 ALE. Therefore, they cannot be used for a direct comparison with the STS observations.

The DPs are found at -550 meV and -250 meV for fcc or hcp occupation, respectively. Presuming fcc occupation, the band structure shows two additional Co bands at $\approx +300$ meV above the DP. These bands are shifted to ≈ -100 meV below the DP in the case of hcp. With respect to the conduction band minimum, these prominent Co-induced peaks are found -120 meV (fcc) and -220 meV (hcp) lower in energy. From this, a *stronger hybridization* (gain of bind-

ing energy) in case of hcp is evidenced. In view of the Bi p_z-states being most sensitive to the difference between fcc and hcp occupation, the Co bands thus originate mainly from the hybridization of Co minority states with Bi p_z-states. In the hcp case, these states are shifted downward in energy. Therefore, the smaller Bi-Co distance in this case leads to a stronger hybridization and a gain of binding energy at the center of the Brillouin zone. This explains the *different dispersions* of the Co bands for fcc and hcp, compare Figs. 5.10(a,b).

5.3.3 XAS and XMCD on Co/Bi_2Se_3

Furthermore, the Co nanostructures were also investigated by XAS and XMCD, summarized in Fig. 5.11. As already mentioned in Sec. 5.2, the cleaving process was performed at room temperature and the samples were subsequently cooled down as fast as possible. The deposition was done at low temperatures with the substrate held at $T \approx 6$ K. Similar to the graphene-based experiments the upper (lower) panel reveals data obtained at normal (grazing) incidence angle to examine the out-of-plane (in-plane) properties.

According to Fig. 5.11(a), the XAS line shape exhibits a single strong resonance with a high-energy shoulder at the L_3-edge and a single resonance at the L_2-edge. The comparison of the experimental data with theoretical multiplet predictions (Van der Laan *et al.*, 1992) suggests a $3d^7$ *electronic configuration* of the ground state of Co, if a crystal field strength of $10dq = 1.0$ eV is assumed. Similar to the case of graphene, this finding has to be treated carefully. The rhombohedral crystal structure of Bi_2Se_3 exhibits a dihedral D_{3d} space group and therefore shows a lower symmetry than used within the calculations (tetrahedral: T_d) (Van der Laan *et al.*, 1992). However, the electronic configuration $3d^7$ is the free-atom configuration of Co. Presuming its correctness, this observation is in line with recent reports on Fe/Bi_2Se_3 (Honolka *et al.*, 2012) and Co/Bi_2Te_3 (Shelford *et al.*, 2012). In these reports, the TM adatoms were also found to be in their pristine configuration.

Turning to the branching ratio (Thole *et al.*, 1988), a value of $BR = 0.84 \pm 0.01$ is found. This suggests a *high-spin ground state* of the Co nanostructures. From the inset of Fig. 5.11(a) the easy-axis can be estimated. The normalized L_3 signal strength is enhanced by $\approx$ 20% for the data obtained at grazing incidence angle. Consequently, an *easy-plane* anisotropy is determined for the low-coverage regime. Importantly, in view of the relative abundance of both Co species within the STM experiments ($n_{Co_A}/n_{Co_B} = 3/1$) and the prediction of an in-plane easy-axis for Co_{fcc}, this observation particularly *strengthens* the assignment of $Co_A = Co_{fcc}$. The easy-plane anisotropy is on the one hand in agreement with Fe on Bi_2Se_3 after low temperature deposition (Honolka *et al.*, 2012). On the other hand, it is contrary to predictions of an out-of-plane anisotropy for the particular system of Co/Bi_2Se_3 (Schmidt *et al.*, 2011) and to experimental studies dealing with Co and Fe adatoms on Bi_2Se_3 after room temperature deposition (Ye *et al.*, 2012; Ye *et al.*, 2013).

The results obtained at an increased coverage of 0.08 ALE reveal interesting modifications. The XAS line shape basically remains constant but reveals a faint decrease in intensity of the L_3 high-energy shoulder, compare Fig. 5.11(b). Moreover, the branching ratio is found to be independent of the coverage indicating again a high-spin ground state of Co. In contrast, the normalized XMCD, given in the inset, exhibits a surprising variation of the easy-axis which now points *out-of-plane*. According to the series of coverage-dependent normalized L_3 inten-

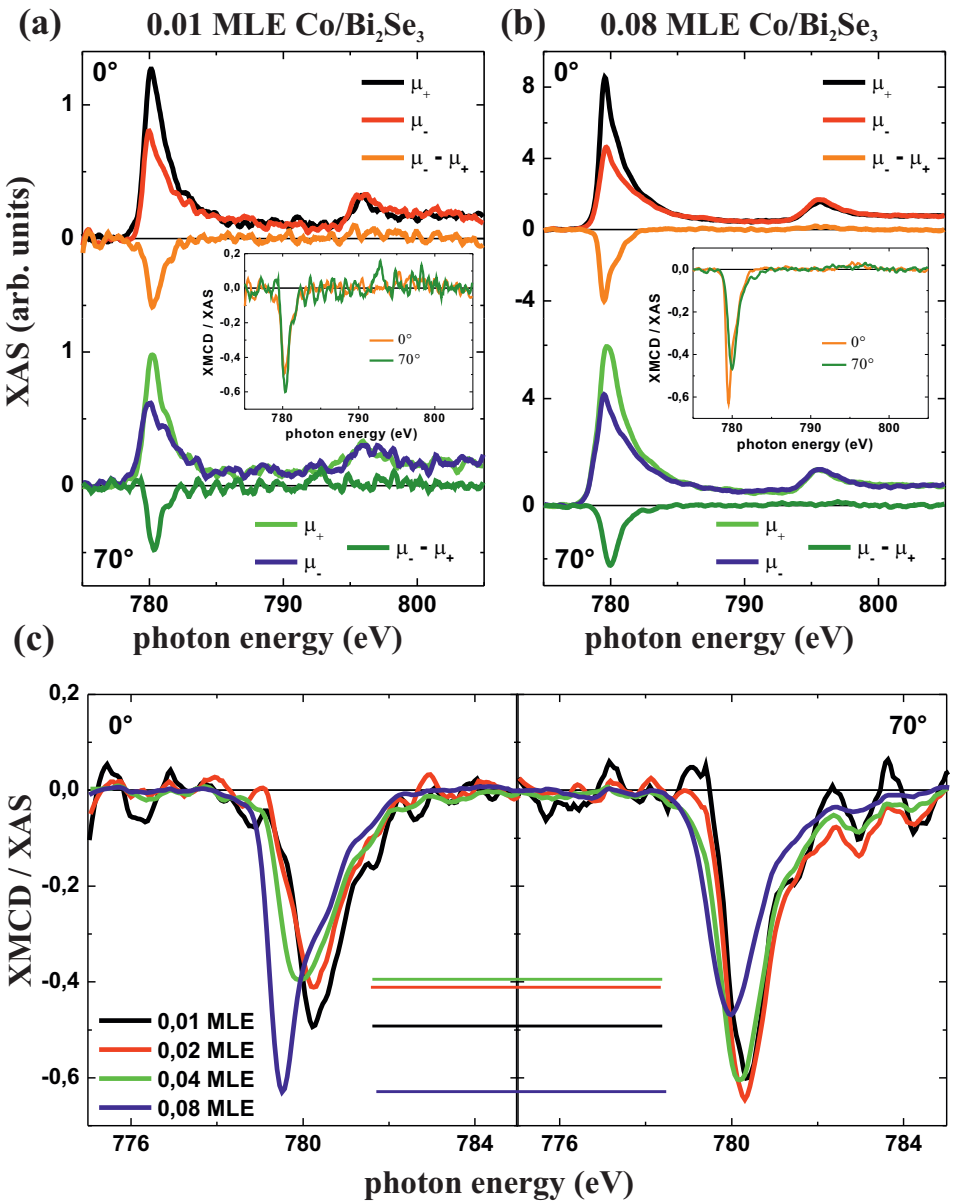

Figure 5.11: XAS and XMCD spectra for (a) 0.01 ALE and (b) 0.08 ALE of Co/Bi_2Se_3 for normal (upper panel) and grazing (lower panel) incidence angle. The insets show the XMCD signal strengths normalized by the XAS L_3 peak intensities. (c) Normalized XMCD signals of the L_3-edge for a series of coverages ranging from 0.01 ALE to 0.08 ALE for normal (left panel) and grazing (right panel) incidence angle. The colored lines are guidelines to the eyes. The series goes hand in hand with a downshift of the peak position with respect to the energy. Adapted from Eelbo *et al.*, 2013c.

sities, shown in Fig. 5.11(c), this modification of the anisotropy depicts a *spin reorientation transition* from in-plane toward out-of-plane. With respect to the accuracy level of the coverage estimation, the SRT occurs between 0.04 ALE and 0.08 ALE.

Similar to the graphene-based experiments, the magnetic field available (B = 5 T) was not sufficiently strong to saturate the magnetic moments of the Co nanostructures. The sum rules thus

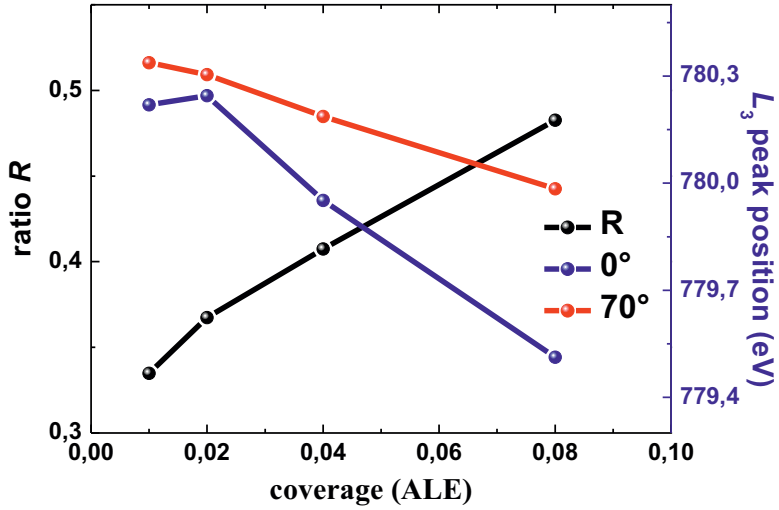

Figure 5.12: Coverage-dependence of the calculated ratio R (left y-axis) and the L_3 XMCD peak positions (right y-axis) for normal and grazing incidence angle, extracted from Fig. 5.11(c).

must not be applied. Instead, the ratio R of orbital to effective spin moment was determined. According to Fig. 5.12, this ratio is found to be $R^{0.01} = 0.33 \pm 0.02$ in the low coverage regime. Importantly, the value exceeds the Co bulk value significantly (Chen *et al.*, 1995). This indicates the character of *individual adatoms* investigated here. Furthermore, $R^{0.01}$ shows good agreement with previous results (Ye *et al.*, 2012).

Since the branching ratio and the XAS line shape are basically independent of the coverage, the same electronic configuration with a high-spin ground state is expected for the elevated coverage. Consequently, the spin moment is expected to *remain constant* upon increasing the coverage toward 0.08 ALE Co. Regarding the orbital moment, an increase of the coverage generally goes hand in hand with a lowering of m_L (Gambardella *et al.*, 2003), thus the ratio R is expected to decrease. Instead, an unexpected *rising of the ratio* according to the coverage is found, compare Fig. 5.12. For the highest coverage, the ratio is estimated as $R^{0.08} = 0.49 \pm 0.03$.

Taking a closer look, this pretended contradiction can be explained by respecting the spin reorientation transition (SRT) mentioned before. For the low coverage regime, an easy-plane anisotropy was determined, i.e. $m_L^x > m_L^z$, for z denoting the direction perpendicular to the surface plane. In this case, the ratio is thus given by $R^{0.01} = m_L^x / m_{S,\,eff}^x = 0.33 \pm 0.02$. For the high coverage regime the anisotropy has rotated to out-of-plane, which implies $m_L^x < m_L^z$ (Bruno, 1989). Moreover, within the theoretical model, the magnetic spin moments were found to be almost independent of the orientation, i.e. $m_S^x \approx m_S^z$ ($1.17\ \mu_B$/atom $\approx$ $1.15\ \mu_B$/atom). Assuming a constant ratio of in-plane orbital moment and in-plane spin moment while increasing the coverage, the experimentally determined boost of R ($R^{0.08} > R^{0.01}$) is plausible and essentially driven by the SRT. Note, that within this discussion the spin dipole moment m_D, which is part of the effective spin moment ($m_{S,\,eff} = m_S + m_D$), is assumed to have a negligible (coverage-independent) influence.

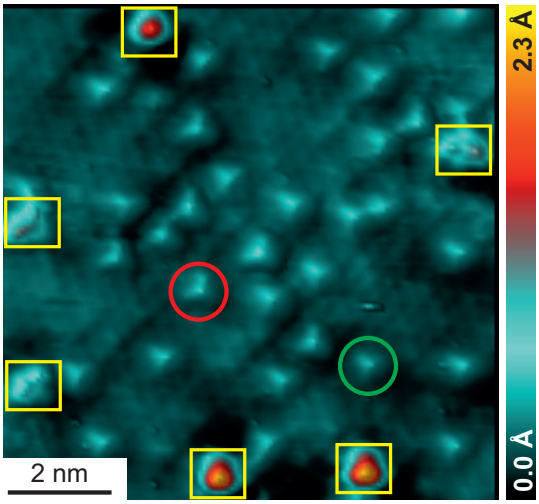

Figure 5.13: STM topography of 0.10 ALE Co/Bi_2Se_3. Tunneling parameters are $U = -200$ mV and $I = 500$ pA. At this bias, Co_A type adsorbates appear in a triangular fashion pointing to the lower border of the image (green). Co_B type adsorbates appear in a triangular fashion as well, but point to the upper border of the image (red). In addition, a significant amount of clusters (yellow) is observed.

5.3.4 Spin Reorientation Transition of Co/Bi_2Se_3

The remaining open issue concerns the origin of the SRT. A first possible explanation is given by a coverage-dependence of the relative abundance of fcc and hcp hollow site occupations. If for an increased coverage, the preferential occupation changes from the fcc toward the hcp hollow site, the SRT would be caused by the theoretically predicted out-of-plane anisotropy for this site. To this end, a series of coverage-dependent STM experiments was performed up to an overall coverage of 0.10 ALE Co/Bi_2Se_3, exemplarily shown in Fig. 5.13. According to Fig. 5.9, Co adsorbed in the hcp hollow site exhibits a resonance at -400 mV in the STS spectra. This way, for every coverage, the ratio of adatoms, that exhibit this resonance compared to the rest, can be determined. Although this ratio fluctuates while increasing the overall coverage of Co/Bi_2Se_3, the ratio does not invert. Co_A adatoms remain the predominant species, even if the coverage is raised, compare Fig. 5.13. The SRT can hence *not* be driven by an inversion of the relative fcc/hcp abundance.

Instead, a different effect is ascribed to be responsible for the SRT. When the overall coverage is raised, the *mean distance* between individual Co adatoms is decreased. Above a critical coverage, this reduced distance is likely to cause a significant increase of the *interaction of Co impurities* on the surface. As a result, Co clusters are expected to grow on the surface. In the coverage-dependent STM studies, exactly this effect was observed, compare the yellow squares in Fig. 5.13. It seems plausible that the properties including the magnetic anisotropy of the Co atoms bonded in these clusters deviate strongly from those being individually adsorbed on the Bi_2Se_3 surface in the low coverage regime. In particular, the emerging growth of clusters certainly influences the chemical state and the crystal field splitting of the involved Co atoms.

These effects are supposed to be observable by means of XAS and XMCD. Their line shapes are results of the averaged electronic properties of the ensemble of fcc/hcp Co adatoms and clusters probed by the X-ray beam. In agreement to these thoughts, a relative *decrease* of the high-energy shoulder at the L_3-edge can be determined for the elevated coverage, compare Figs. 5.11(a,b). Furthermore, Fig. 5.12 reveals that by increasing the coverage, a continuous shift downward of the peak position with respect to energy occurs.

Compared to the strongly affected magnetic properties, the described variations of the line shapes are very moderate. This basically suggests that the chemical state is not abruptly changed. When raising the coverage, the number of clusters compared to the overall number of individual adatoms is also expected to vary moderately. The assignment of the described effects to the variations of the adatom/cluster distributions when raising the coverage therefore seems to be reasonable. The SRT is thus suggested to be driven by *cluster formation* upon decreasing the mean distance between Co adatoms. The argumentation is supported by a recent investigation of bulk doped Mn-Bi_2Se_3 (Zhang *et al.*, 2012a). In this study, excess Mn clusters on the surface were assumed to cause a significant influence on the surface magnetization of the sample.

Importantly, even in the high-coverage regime, *no gap-opening* was observed by means of STS. This is contrary to the expectations (Schmidt *et al.*, 2011), because the magnetization has rotated toward the out-of-plane direction, compare Sec. 5.1.4. A gap-opening is of course only expected in the vicinity of the out-plane-magnetized Co impurities. According to the foregoing paragraph, these Co adatoms most likely are bonded in clusters. Therefore, the effect was potentially not observed, because STS near such clusters was impossible. The tunneling conditions were not sufficiently stable. Furthermore, STS was performed in the absence of external magnetic fields. The effect might thus be unobservable due to a fluctuation of the Co magnetic moments originating from an insufficient stabilization. The DFT calculations hint toward other important issues regarding this gap-opening. Even for a coverage of 0.33 ALE, the gap-opening is computed to be only 60 meV wide. As this coverage is more than three times higher than experimentally used and the gap moreover overlaps with the Co bands, it may be not resolvable at all.

5.4 Fe on Bi_2Te_3

The remaining study is motivated by the finding of Co/Bi_2Se_3. For that system, an easy-plane anisotropy was found for the low coverage regime. To gain the ability to investigate the peculiar effects, that are expected for TRS breaking perturbations on a TI, another combination of TM adatoms and TI was chosen. Therefore, the second study focuses on Fe adatoms on the (111)-surface of Bi_2Te_3. Again, the samples were provided by *I. Miotkowski* and precharacterized before the Fe deposition, compare Sec. 5.2.2. DFT-calculations were carried out by the group of *O. Yazyev* from the *Ecole Polytechnique Fédérale de Lausanne* to support the experimental findings. Calibration measurements were carried out to adjust the L_3 XAS intensity for a specified coverage. The deposition rates were determined using a W(110) substrate, that was cleaned according to the procedure given elsewhere (Bode *et al.*, 2007).

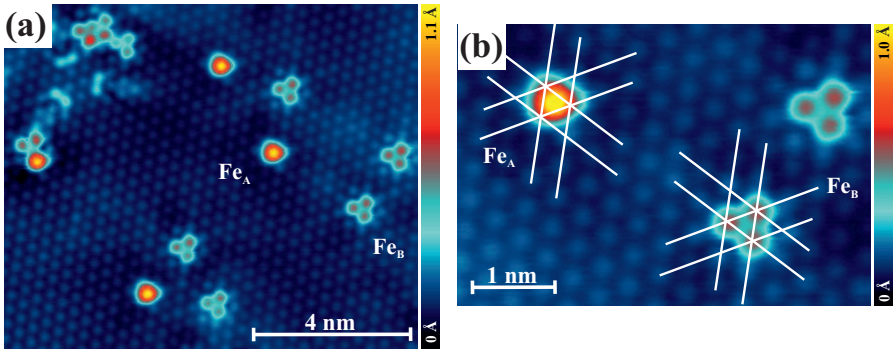

Figure 5.14: (a) STM constant-current map of an ensemble of Fe adatoms on Bi_2Te_3 revealing two different types of adsorbates. Tunneling parameters are $U = -400$ mV and $I = 300$ pA. (b) High-resolution image of two individual Fe adatoms in different adsorption sites. The white guidelines to the eyes indicate top positions of the surface Te layer. Fe_A appears as a triangular protrusion. Although the signature of Fe_B exhibits a combination of three smaller protrusions arranged in a triangle, this signature is caused by a single Fe atom. Tunneling parameters are $U = -400$ mV and $I = 300$ pA. Adapted from Eelbo *et al.*, 2014.

5.4.1 STM and STS on Fe/Bi_2Te_3

Similar to Co/Bi_2Se_3, minute amounts of Fe were deposited on the Bi_2Te_3(111) surface after its precharacterization, compare Sec. 5.2.2. This evaporation was again performed at cryogenic temperatures inside the STM at ≈ 12 K. It results in an ensemble of individual adatoms on the surface, depicted in Fig. 5.14(a).

Besides an intrinsic defect in the upper left corner that was observed on the pristine surface before, the constant-current image reveals the existence of *two different types* of signatures, called Fe_A and Fe_B. While Fe_A is characterized by a *triangular protrusion* pointing to the upper left, the signature of Fe_B is given by a combination of *three small protrusions*. These are arranged in a triangular shape and point to the lower right corner. According to the color coding, the signature of Fe_A exhibits a much larger apparent height than Fe_B. At first glance, the possibility exists that the signature of Fe_B might consist of three individual Fe atoms. To this end, a control experiment with equal deposition parameters was performed on a W(110) surface. The amount of adatoms per surface unit on both substrates is only consistent if the signature of Fe_B is generated by a single Fe atom. With respect to their apparent shapes, Fe_A atoms are independent of the bias voltage. Instead, Fe_B appears in a different and even more complicated signature with an enlarged diameter at positive biases. Note, that Fe_B neither at positive nor at negative biases appears as a triangular shaped depression. This would be a typical signature of an Fe atom that diffused into the bulk and substituted a Bi atom at its lattice position (Hor *et al.*, 2010; Okada *et al.*, 2011; Song *et al.*, 2012; Schlenk *et al.*, 2013; West *et al.*, 2012).

From the high resolution image, given in Fig. 5.14(b), it is obvious that both types of adatoms are adsorbed in *different sites*. The protrusions visible on the surface are caused by the surface Te layer. As a result, the Fe adatoms occupy fcc and hcp hollow sites. Regarding the relative abundance a distribution of 60% to 40% in advance of Fe_B is determined within the limited

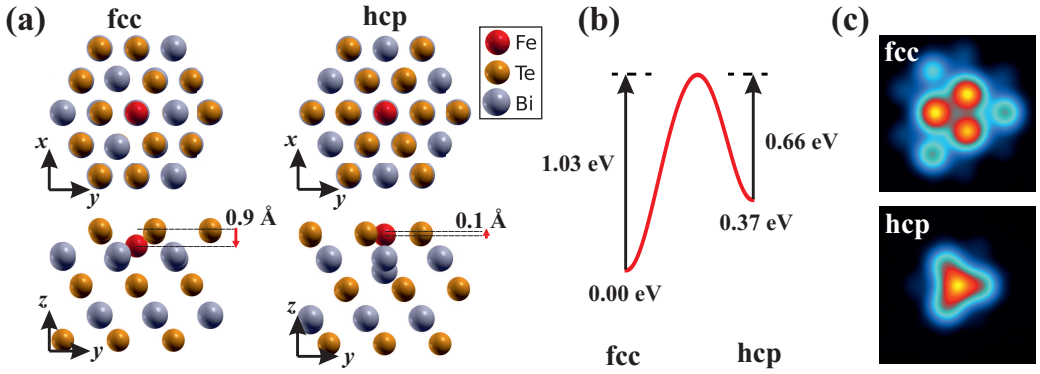

Figure 5.15: (a) Illustration of the atomic configurations of Fe atoms adsorbed in the fcc and hcp adsorption sites based on first-principles calculations. While the upper panels give a top view, side views including the vertical displacements can be found in the lower panels. (b) Schematic drawing of the potential energy surface as a result of the calculations indicating that the fcc hollow site is energetically favorable by 370 meV. (c) Simulated STM topographies of Fe adatoms in the fcc as well as hcp hollow sites for a bias voltage of $U = -400$ mV. Adapted from Eelbo *et al.*, 2014.

scan area by the STM. No indication of a movement of the adatoms between both adsorption sites was found. Consequently, the relative abundance suggests that the diffusion barrier between both adsorption sites is much higher than the available thermal energy.

The observation of two types of Fe adatoms is contrary to a recent report on the particular sample system of Fe/Bi_2Te_3(111) (West *et al.*, 2012). In that study, the existence of only a *single species* of Fe adatoms was reported. The difference might be caused by the different deposition parameters. West *et al.* deposited and investigated Fe at higher temperatures (50 K). At this temperature, the thermal energy might be sufficient to overcome the diffusion barrier between both adsorption sites. This would consequently result in the observation of only a single type of Fe adatoms.

In order to understand the STM observations, first-principles calculations were performed using the DFT framework employing the local density approximation including an on-site Coulomb potential (LDA+U) as implemented in the QUANTUM-ESPRESSO package (Giannozzi *et al.*, 2009). To reflect the Fe atoms properly, a Coulomb potential of $U = 2.2$ eV was used (Cococcioni *et al.*, 2005). Note, that for TM adatoms the on-site Coulomb potential is indispensable for correctly reproducing both the ground state magnetic moment and the magnetic anisotropy energies (Donati *et al.*, 2013). The calculation of the binding energies and the diffusion barrier between both hollow sites was performed by using the nudged elastic band approach (Henkelman *et al.*, 2000). Furthermore, SOI was included by fully relativistic pseudopotentials acting on the valence electron wave functions (Dal Corso *et al.*, 2005).

With this approach, the Fe atoms adsorbed in both hollow sites were modeled, summarized in Fig. 5.15. According to subfigure Fig. 5.15(a), the hcp adsorbed Fe atoms relax only moderately with respect to the z-direction. This effect is much stronger in the fcc position. Here, with respect to the surface, the atoms relax about 0.9 Å into the crystal. The fcc hollow

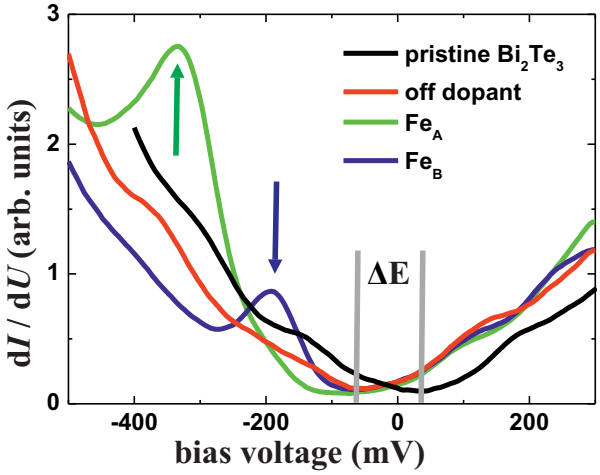

Figure 5.16: STS spectra of Bi_2Te_3 acquired before and after Fe deposition. The "off dopant" spectrum was taken after the deposition far away from any adsorbate. Both types of Fe impurities show characteristic resonances, either at -335 mV or at -190 mV, respectively. The stabilization parameters for the STS were $U = 300$ mV and $I = 200$ pA. Adapted from Eelbo *et al.*, 2014.

site is *energetically favorable* by $\approx$ 370 meV, compare Fig. 5.15(b). This difference is quite significant and much larger than in case of Fe adatoms on a Bi_2Se_3 surface, where calculations based on a GGA+U-approach determine a difference of the binding energies of only $\approx$ 70 meV (Honolka *et al.*, 2012). The variation can be assigned to the differences in the lattice constants of both substrates. The larger lattice constant of Bi_2Te_3 allows for *larger displacements*.

In view of the relative abundance within the STM topographies ($n_{Fe_A}/n_{Fe_B} \approx 40/60$), the difference in the calculated binding energies hints toward *non-equilibrium thermodynamics* during the actual adsorption process. Otherwise, a much higher or even exclusive population of Fe_B is expected. These considerations are in line with the fact that the deposition was performed at low temperatures, which effectively reduces the available thermal energy.

Moreover, the theoretical model was used to simulate STM constant-current images for the bias voltage used within the experiment ($U = -400$ mV). The comparison of Fig. 5.14(b) with Fig. 5.15(c) reveals that the signatures *clearly reflect* the experimentally observed features. They hence allow to assign Fe_A (Fe_B) to be adsorbed in the hcp (fcc) adsorption site. This assignment is particularly in line with the calculated relaxations. The relaxation is much stronger in the fcc-case and therefore in line with Fe_B-type adatoms exhibiting a much smaller apparent height, compare Fig. 5.14(b).

The magnetic spin moments were computed to be $m_S^{fcc} = 2.7\,\mu_B$/atom and $m_S^{hcp} = 2.5\,\mu_B$/atom, respectively. The orbital magnetic moments were computed to be $m_L^{fcc} = 0.7\,\mu_B$/atom and $m_L^{hcp} = 0.3\,\mu_B$/atom. Interestingly, the magnetic anisotropies, given by the MAE per atom K, were both found to point *out-of-plane* with strengths of $K^{fcc} = 12$ meV and $K^{hcp} = 10$ meV. This prediction is contrary to a recent report on the same sample system, where an *easy-plane anisotropy* due to orbital symmetry considerations was concluded (Shelford *et al.*, 2012).

The STS data acquired on this sample system are summarized in Fig. 5.16. As already mentioned in Sec. 5.2.2, the global minimum in the spectra of the pristine crystal was found at about +40 mV. Upon Fe deposition, this minimum shifts downward in energy by about 90 mV. This demonstrates the *electron doping effect* due to the Fe impurities in agreement with previous reports (Chen *et al.*, 2010; Wray *et al.*, 2011; Honolka *et al.*, 2012; Song *et al.*, 2012). In addition, *characteristic resonances* can be identified for both types of Fe adatoms: for Fe_A, a resonance at ≈ -335 mV and, in case of Fe_B, a resonance at ≈ -190 mV.

A comparison of these STS features with the theoretical calculations is *not conclusive* because the theoretical model exhibits split resonances for each type of adatom. These are a result of the supercell approximation employed within the model. Instead, the observation of single resonances for each case of Fe impurities suggests that they behave as simple scalar impurities (Biswas *et al.*, 2010). This can be understood if the magnetic moments of the Fe atoms are assumed to only *weakly couple* to the TSS. Note, that neither in case of the spectra on the adatoms themselves nor in their close or far vicinity an indication of a gap-opening was observed.

5.4.2 XAS and XMCD on Fe/Bi_2Te_3

Figure 5.17 exhibits a summary of the XAS and XMCD experiments performed on Fe/Bi_2Te_3. Again, the Fe adatoms were deposited with the substrate held at $T \approx 10$ K. According to Fig. 5.17(a), the XAS spectra reveal only a faint multiplet structure. This is assumed to be a consequence of the simultaneous investigation of the ensemble of fcc as well as of hcp adatoms.

By comparing the spectra to theoretical calculations (Van der Laan *et al.*, 1992) a $3d^6$ *electronic configuration* of the Fe ground state is determined assuming a crystal field strength of $10dq = 0.5$ eV. This is consistent with a previous report (Shelford *et al.*, 2012) but has to be treated carefully given the non-matching symmetries of the study at hand and the ones in the calculations (dihedral D_{3d} vs. tetrahedral T_d). The evaluation of the branching ratio (Thole *et al.*, 1988) results in $BR = 0.85 \pm 0.01$. Consequently, the ground state reveals a *high-spin character*. In agreement to the first-principles calculations and contrary to the recently assumed easy-plane anisotropy (Shelford *et al.*, 2012), an *out-of-plane easy-axis* is determined according to the normalized XMCD L_3 resonance intensity, compare Fig. 5.17(b). The signal strength for normal incidence angle is found to be about 50% stronger than the intensity obtained at grazing incidence angle. The out-of-plane anisotropy was further manifested by means of element specific magnetization curves, shown in Fig. 5.17(c). These show the steepest slope for the data acquired under normal incidence angle. The out-of-plane anisotropy of Fe atoms on Bi_2Te_3 is clearly contrasting the finding of an easy-plane anisotropy for Fe/Bi_2Se_3 (Honolka *et al.*, 2012). The difference may be caused by structural variations among both substrates. This might consequently lead to a different hybridization on each surface thereby causing modified electronic and magnetic properties.

To evaluate the magnetization curves, a fitting procedure was applied by using a thermodynamical model including the Zeeman splitting, a Boltzmann term, and the anisotropy energy. Therefore, the energy is estimated by (Brune *et al.*, 2009):

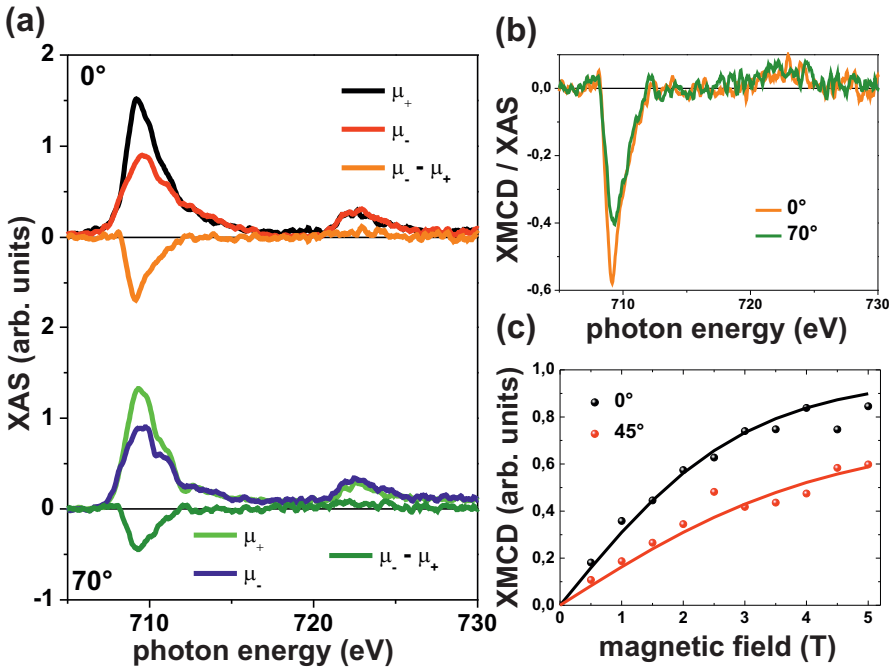

Figure 5.17: (a) XAS and XMCD spectra for 0.01 ALE Fe/Bi_2Te_3 for normal (upper panel) and grazing (lower panel) incidence angle. (b) XMCD spectra normalized by the L_3 XAS intensity indicating an out-of-plane anisotropy of the Fe adatoms. (c) Element-selective magnetization curves for the Fe adatoms at varying angles depending on the applied magnetic field. The data points represent the Fe XMCD intensity for the L_3-edge normalized by the XAS intensity. In contrast, the solid lines depict optimized results of a thermodynamical fitting procedure. The *y*-axis was renormalized to match the saturation magnetization M_{Sat} determined from this fitting procedure. From Eelbo *et al.*, 2014.

$$\begin{aligned} E &= E_{\mathrm{Zeeman}} + E_{\mathrm{Anisotropy}} \\ E(\theta_0, \theta, \phi) &= -m\mu_0 H\cos(\theta) - K(\sin(\theta_0)\sin(\theta)\cos(\phi) + \cos(\theta_0)\cos(\theta))^2 \end{aligned} \tag{5.3}$$

This equation is valid only for individual adatoms. Otherwise a mean particle size *s* must be considered for each addend. Furthermore, the magnetic moment *m*, the magnetizing field *H*, the MAE per adatom *K*, the polar and azimuthal coordinates θ and ϕ and θ_0 are used. The latter defines the easy-axis of the magnetization. As a result the magnetization can be determined including Boltzmann statistics (Gambardella *et al.*, 2002b):

$$M = M_{\mathrm{Sat}} \underbrace{\frac{\int_0^{2\pi} \mathrm{d}\phi \int_0^{\pi} \left(\sin(\theta)\cos(\phi) e^{-\frac{E(\theta_0,\theta,\phi)}{k_{\mathrm{B}}T}}\right) \mathrm{d}\theta}{\int_0^{2\pi} \mathrm{d}\phi \int_0^{\pi} \left(\sin(\theta) e^{-\frac{E(\theta_0,\theta,\phi)}{k_{\mathrm{B}}T}}\right) \mathrm{d}\theta}}_{A_{\mathrm{i}}} \tag{5.4}$$

where M_{Sat} is the saturation magnetization. Motivated by the STM observations, *two sublattices* were introduced representing fcc and hcp bonded Fe adatoms with a relative abundance of 60% to 40% in favor of Fe_{fcc}:

$$M = M_{\mathrm{Sat}}(0.6 \cdot A_{\mathrm{fcc}} + 0.4 \cdot A_{\mathrm{hcp}}) \tag{5.5}$$

According to the theoretical model and the XMCD data, total magnetic moments of $m_{\mathrm{fit}}^{\mathrm{fcc}} = 3.4\ \mu_{\mathrm{B}}$/atom and $m_{\mathrm{fit}}^{\mathrm{hcp}} = 2.8\ \mu_{\mathrm{B}}$/atom were derived and used for this fitting. The magnetic anisotropies were restricted to point out-of-plane: $\theta_0 = 0°$ for both sublattices, parallel to the surface normal. A ratio of $K^{\mathrm{fcc}}/K^{\mathrm{hcp}} = 1.2$ was fixed. The temperature and the magnetizing field at each data point are known. Straightforwardly, the magnetocrystalline anisotropy energy constants were fitted resulting in $K_{\mathrm{fit}}^{\mathrm{fcc}} = 10 \pm 4$ meV/atom and $K_{\mathrm{fit}}^{\mathrm{hcp}} = 8 \pm 4$ meV/atom. The errors are mainly caused by the scattered character of the data points given by the XMCD, compare Fig. 5.17(c). Importantly, within the error bars, the fit results are in *good agreement* with the theoretical predictions, summarized in Tab. 5.1.

The magnetization curve fitting, the theoretical calculations, and finally the XMCD results evidence the *out-of-plane anisotropy* of the Fe adatoms on Bi_2Te_3(111). In view of these facts, it is surprising that the expected gap-opening (Qi *et al.*, 2008; Liu *et al.*, 2009; Wray *et al.*, 2011) was *not observed* during the STS experiments. Interestingly, this result is similar to a recent report on bulk Fe-doped Bi_2Te_3 (Okada *et al.*, 2011). The authors revealed the breaking of Kramers degeneracy by FFT of dI/dU maps, that exhibit quasi-particle interference (QPI) patterns. Although in that report FFT evidences a broken TRS, no signature of a gap-opening was observed by means of STS. A discussion of the potential causes is given in Sec. 6.2.

5.4.3 Sum Rules of Fe/Bi_2Te_3

The XMCD spectra can be further evaluated by means of the sum rules (Thole *et al.*, 1992; Carra *et al.*, 1993), compare Sec. 2.6. According to Fig. 5.17(c), the magnetic moments were not fully saturated at the maximum magnetic field available ($B = 5$ T). However, since the magnetization curves already *flatten* at $B = 5$ T and the saturation magnetization M_{Sat}, determined by the fitting procedure, exceeds the experimental magnetization by only $\approx 10\%$, the sum rules were applied.

With help of Eq. 2.38, the effective magnetic spin moment of the ensemble of fcc and hcp adatoms was found to be $m_{S,\,eff}^{\text{sum rules}} = (2.9 \pm 0.2)\ \mu_{\mathrm{B}}$/atom. Moreover, according to Eq. 2.39, the orbital magnetic moment was calculated to be $m_L^{\text{sum rules}} = (1.1 \pm 0.1)\ \mu_{\mathrm{B}}$/atom. To particularly calculate the magnetic moments a d-shell occupation of $3d^6$ was assumed in agreement with the XAS line shape. Note, that the effective spin moment $m_{S,\,eff}$ comprises a contribution of the intra-atomic magnetic dipole moment m_D according to: $m_{S,\,eff} = m_S + m_D$. The latter accounts for an anisotropy of the spin density if the atomic cloud is distorted either by SOI or crystal-field effects (Stöhr *et al.*, 2006). For individual Fe adatoms on a surface and at cryogenic temperatures the contribution of the magnetic dipole moment has been evaluated to be about $m_D \approx 25\% \cdot m_S$ (Crocombette *et al.*, 1996). This estimation has been verified in later studies dealing with the applicability of the XMCD sum rules (Brune *et al.*, 2009; Piamonteze *et al.*, 2009; Šipr *et al.*, 2009). Furthermore, the above derived values of $m_{S,\,eff}$ and m_L need to be corrected due to the unsaturated magnetic moments. To this end, they need to be normalized by a factor $0.9^{-1} \approx 1.1$. Overall, the sum rules result in spin and orbital

Method	m_S (μ_B/atom)	m_L (μ_B/atom)	K (meV/atom)
LDA+U	2.7 (fcc) 2.5 (hcp)	0.7 (fcc) 0.3 (hcp)	12 (fcc) 10 (hcp)
Sum Rules	(2.6 ± 0.2)	(1.2 ± 0.1)	–
MC fitting			(10 ± 4) (fcc) (8 ± 4) (hcp)

Table 5.1: Summary of the magnetic moments and anisotropies of Fe/Bi_2Te_3 as determined by the sum rules, the magnetization curve fitting procedure, and calculated using the LDA+U approach.

magnetic moments of: $m_S^{\text{sum rules}} = (2.6 \pm 0.2)\ \mu_B$/atom and $m_L^{\text{sum rules}} = (1.2 \pm 0.1)\ \mu_B$/atom, compare Tab. 5.1.

Concerning the spin magnetic moment, there is *perfect agreement* between the value determined by the sum rules and the theoretically predicted one. Regarding the orbital magnetic moment, the agreement is not as good. This might be caused by an underestimation of the orbital contribution within the LDA+U approach. The theoretical model makes use of the projection of the Kohn-Sham wave functions on the Fe orbitals to determine their orbital moments. The approximation is justified for isolated adatoms and, thus, contains only the contributions of the Fe orbitals. Consequently, the theoretically computed orbital moments might underestimate the experimental value. However, compared to the Fe bulk value, the increase of the orbital moment is *well reproduced*. Alternatively, the discrepancy might be entailed or supported by a higher Fe *d*-shell occupation than assumed here. This would consequently lower the experimentally calculated spin and orbital magnetic moments. Anyhow, this disagreement cannot be clarified.

Utilizing Eq. 2.40, the ratio of orbital magnetic moment and effective spin moment was found to be $R = 0.38 \pm 0.04$. This value is in line with a recent study on the very same sample system and indicates a fairly large contribution of the orbital magnetic moment by itself (Shelford *et al.*, 2012). Similar to the experiments on Co/Bi_2Se_3, the experimentally determined ratio is much higher than the bulk value of Fe (Chen *et al.*, 1995). That illustrates the character of individual Fe atoms investigated here (Gambardella *et al.*, 2002a).

5.5 Summary

Since their first experimental realization in 2007, TIs are at the frontier of condensed matter physics. Of special interest is the combination of magnetic material with their spin-dependent TSSs, that, for certain configurations, leads to a local breaking of Kramers degeneracy. Therefore, second generation TIs were chosen for combined experimental and theoretical investigations with adsorbed 3*d* TM adatoms of Co and Fe.

In particular, Co deposited on Bi_2Se_3 at cryogenic temperatures reveals the existence of two species of Co adatoms. These were identified by DFT calculations to be adsorbed in the fcc

and hcp hollow sites of the substrate (Eelbo *et al.*, 2013c). Theory can qualitatively explain the observation of different electronic properties which those types of adatoms exhibit. Interestingly, the Co adatoms occur with a different commonness. Including this relative abundance, an *easy-plane anisotropy* is theoretically predicted and confirmed by means of XAS and XMCD experiments for the low coverage regime.

Surprisingly, while increasing the coverage, a rotation of the anisotropy toward the *out-of-plane direction*, i.e. a SRT, was found. Despite the anisotropy, the X-ray related measurements suggest a $3d^7$ high-spin ground state of Co, independent of the coverage. A possible variation of the relative abundance of fcc and hcp Co atoms upon elevating the coverage was proven to be absent. Instead, the SRT was ascribed to the *enhancement of an interaction* among the Co atoms if their density on the surface is increased. Finally, the SRT was concluded to be responsible for an unusual boost of the ratio of orbital to effective spin moment as a function of the Co coverage on Bi_2Se_3.

The second combined experimental and theoretical work deals with Fe adatoms on Bi_2Te_3 (Eelbo *et al.*, 2014). In agreement with the foregoing sample system, again two different types of adatoms were found. By first-principles DFT calculations, the adsorption sites were concluded to be the fcc and hcp hollow sites. Despite these similarities and although the structural properties of Bi_2Te_3 and Bi_2Se_3 are closely related to each other, the magnetic properties of Fe adatoms vary strongly from those of Co deposited on the sister surface.

Most importantly, already at low coverages a *strong out-of-plane anisotropy* was experimentally found by means of XMCD and theoretically confirmed. While the XAS spectra suggest a high-spin $3d^6$ electronic configuration of the ground state, the sum rules were applied to estimate the total magnetic spin besides the orbital moments. These show *reasonable agreement* with the theoretically predicted values. Furthermore, the element-selective magnetization curves were fitted by a thermodynamic model including the Zeeman splitting, the magnetic anisotropy, and a Boltzmann term. The results from the fitting procedure are *well in line* with the theoretical model and exhibit anisotropy constants on the order of 10 meV per atom. Unfortunately, by means of STS no gap-opening was revealed, although this is expected for the magnetization pointing out-of-plane. The cause remains unknown but might be given by a scalar-like behavior of the magnetic moments, that would hint toward an absence of a strong interaction between the spin-dependent TSSs and the Fe magnetic moments.

Chapter 6

Conclusions and Outlook

In the presented studies the main focus was laid on well-defined systems of a rather simple composition. This way, a foundation for the understanding of the basic properties and the behavior of 3*d* TMs was in the focus of interest. For their smallest representatives, i.e. individual adatoms, this aim was fulfilled to a *high extent*. In general, for each of the sample systems at hand, the agreement between both the experimental observations and the numerical calculations was convincing. In the following, a discussion of the main conclusions and their relevance regarding future research objectives and technological applications is given. Thereby, the chapter is divided into two parts, firstly dealing with the graphene-based experiments and afterward proceeding with the TI-related results.

6.1 Graphene

The graphene-based experiments enabled several important findings for isolated adatoms of the 3*d* TMs Fe, Co, and Ni. Firstly, the interaction of graphene with these adatoms has to be considered being *weak* as evidenced by XAS and STM experiments. Secondly, *sizable magnetic moments* were found for all investigated species by means of XMCD presuming an increased coverage of Ni. Thirdly, slight variations of the substrate influence the adsorption behavior significantly. Fourthly, *no theoretical model* currently exists that is able to predict the adatoms' properties on realistic graphene-substrates. Fifthly, the effect of intervalley scattering can now be investigated in a *controlled manner* for specific substrate-adsorbate configurations.

The importance of these findings relies on the dream of a combination of graphene's exceptional electronic properties with the magnetic properties of TMs in future nanodevices. For industrial applications, on the one hand, the technologically important materials (Fe, Co, and Ni) are commonly used to tailor the properties of modern devices. On the other hand, the *minimization of development costs* for these devices is highly desirable. A theoretical model that includes substrate effects and precisely predicts the properties of the entire system, including adsorbed nanostructures, would therefore reflect a *major step* toward a possible integration of graphene into mass production of future devices.

To investigate especially the effect of the doping level that reflects the degree of decoupling, an experiment by means of STM utilizing a third electrode can be considered. The dop-

ing level can in principle be precisely tuned by an applied *backgate* as was shown previously (Brar *et al.*, 2010). This way, graphene can be manipulated with respect to its charge carrier density. The procedure enables to shift the DP with respect to the Fermi level. It offers the possibility of mimicking the effect of hydrogen intercalation which in principle should lead to similar results as reported here. Achieving atomic resolution in this type of experiments might hence potentially provide insight into the interaction of TM adatoms with graphene.

Theoretical predictions are important in terms of magnetic properties as well. This is driven by the exceptional relevance of *magnetic data storage* devices or generally spin-dependent integrated circuits. The general layout of a possible future nanodevice consequently bases on graphene's improved transport properties compared to current standards. These are illustrated by its high charge carrier mobilities and high tunability. Straightforwardly, the most promising example for an application of graphene makes use of these peculiarities, namely its integration into already existing *flexible displays* based on organic light emitting diodes. Graphene might be used for circuit paths being flexible, highly robust, and exhibiting exceptional electronic properties at the same time. Alternatively, graphene is suitable for *field effect transistors* (Lin *et al.*, 2010), although only few graphene-based devices are available yet.

In view of magnetism, graphene can be seen as a diamagnetic semimetal. Hence, doping by 3*d* TM nanostructures, that exhibit strongly interacting inner electronic shells, offers a way to tailor the magnetic properties of the combined system both locally and globally. For instance, magnetic domains grown from TMs could be used in two ways: either in a "classical approach", such as locally storing information in a *binary code*, or in an "advanced approach" for *spintronic devices*, based on the extraordinary macroscopic spin coherence lengths already achieved in graphene at room temperature (Tombros *et al.*, 2007).

In order to precisely tailor the properties of the proposed devices, SP-STM experiments performed on TMs/graphene down to the ultimate limit of individual adatoms are highly desirable. They are expected to be able characterizing the magnetic properties on a local scale, complementary to the XMCD studies reported in the thesis at hand. An interesting effect to be examined is, for instance, given by the *size-dependent magnetic properties* observed for Ni nanostructures. In general, this feature might be present for Fe and Co as well.

A major difficulty to be overcome for the realization of the proposed structures, is the controlled growth of such systems with high quality. For SiC-related graphitic systems, experiments focusing on the diffusion barrier of TM adatoms found diffusion temperatures below 100 K (Gyamfi, 2012b). Unfortunately, above the effective diffusion temperature, no islands of the formerly distributed adatoms were found. More precisely, the consequences on the adatoms induced by the annealing were not resolvable at all. On the one hand, desorption at these temperatures seems unlikely. On the other hand, above the diffusion temperature no agglomeration of TM atoms was observed neither on flat terraces, nor at step edges of the underlying SiC. The actual behavior of the TM atoms above the diffusion temperature for graphene/SiC remains unclear. Possible scenarios could be that the TM atoms diffuse to defects in the graphene lattice itself, to defects in the interface layer underneath, or defects depicted by unsaturated dangling bonds of the SiC substrate. Last but not least, segregation into the bulk SiC crystal can not be excluded so far. To this end, element selective X-ray based investigations in combination with precisely controlled annealing might be able to lead to new conclusions regarding this issue.

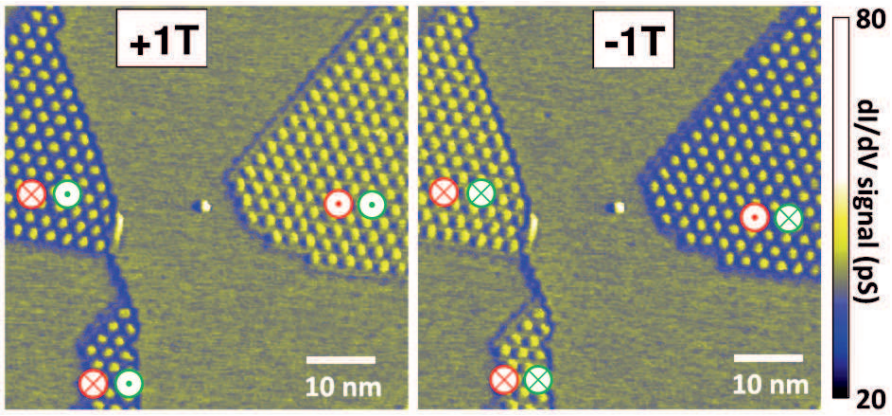

Figure 6.1: dI/dU maps revealing stable out-of-plane magnetic anisotropy of Co islands intercalated underneath graphene on Ir(111). Between both maps the external magnetic field was inverted. While the green symbols indicate the magnetic orientation of the SP-STM tip, the red symbols indicate the magnetization direction of the intercalated Co regions. The tunneling parameters are $U = -0.9$ V and $I = 1$ nA. From Decker *et al.*, 2013 with permission.

The controlled growth of extended magnetic islands on graphene would additionally simplify potential SP-STM experiments. Supposing the existence of smooth and well-defined TM islands on graphene with a sizable magnetization, a *magnetic reference* would be available to characterize the tip's magnetization.

Opposite to the SiC-based sample systems, metallic systems, such as Ir(111), offer the possibility to simultaneously grow close-packed and smooth TM islands and high-quality graphene flakes or layers. However, for these systems the original aim of decoupling the TM films by a graphene layer underneath was not established yet. If, for instance, an amount of cobalt is deposited on graphene/Ir(111) and afterward annealed to temperatures of about 450 K, Co *intercalates* beneath graphene. The Co atoms do not assemble in smooth films on graphene/Ir(111), but intercalate underneath and establish close-packed islands between the Ir substrate and the graphene layer (Decker *et al.*, 2013). Although this sample layout is far from the original idea, it offers different opportunities since the intercalated Co regions exhibit a sizable magnetic out-of-plane anisotropy, compare Fig. 6.1. They can therefore in principle be used as a *magnetic reference* to characterize the spin-polarization of the STM tip. This way, intercalated Co regions allow for the unambiguous identification of the magnetization of simultaneously deposited individual adatoms on graphene/Ir(111) on a local scale. Moreover, a magnetic reference also facilitates the investigation of the magnetism in graphene with respect to the lattice structure itself. Although the presented data in Chap. 4 suggest that TM adatoms do not significantly induce magnetism in graphene's honeycomb lattice, several numerical calculations predict unbalanced magnetic states at the zig-zag edges of graphene (Fujita *et al.*, 1996; Son *et al.*, 2006). Since the system above described naturally comprises flakes of graphene (Decker *et al.*, 2013), an investigation of this effect on a local scale seems promising.

On the one hand, the sample layout described before, in principle is interesting in view of fundamental studies on local scale magnetic properties. On the other hand, regarding industrial applications, a Si-based sample system would be incomparably more important. It would en-

able the connection to state-of-the-art Si-based semiconductor physics and electronics. Moreover, a Si-based substrate is much *cheaper* to produce and can in principle be grown with higher quality. Therefore, for the ability of precisely tailoring the properties of the combined graphene-SiC-adatom system, QFMLG is of major interest. It even offers the manipulation of adatoms with *atomic precision* among multiple adsorption sites, which in principle might provide to establish multiple magnetic states within the same sample system.

In view of future applications another major problem to be overcome is of course the *conservation* of tailored properties for the case of ambient conditions. Although graphene reveals inert-like behavior, it adsorbs gaseous molecules which are expected to alter the formerly tailored properties. To this end, significant improvements are to be made regarding the *passivation* of systems composing of graphene and adsorbed magnetic nanostructures. An example of a possible passivation was recently shown in studies on high-frequency graphene-based FETs (Farmer *et al.*, 2009; Lin *et al.*, 2011). Either polymer films or SiO_2 layers were used but it remains to be investigated whether these types of films influence the properties of adsorbed nanostructures.

6.2 Topological Insulators

For the experiments performed on topological insulators, the main findings deal with the paramagnetic behavior of the deposited 3*d* TM nanostructures. On the one hand, the magnetic properties are altered drastically with respect to the *underlying substrate* and, on the other hand, they vary strongly depending on the TM *coverage*, at least for one of the investigated substrates (Bi_2Se_3). In terms of fundamental physics even more attention has to be paid to the fact that the peculiar topological surface states appear to remain robust against this kind of doping. This indicates a rather weak and scalar-like interaction between the nanostructures' magnetic moments and the TSSs.

Some potential reasons for the lack of the observation of a broken TRS and a gap-opening were already given in Sec. 5.3.4. However, in the following, these are summarized. Firstly, the TRS breaking might induce only a very narrow gap-opening. Owing to the *smallness* of the effect, it seems plausible, that it might be unresolvable in the regime of single atoms. Secondly, this might be supported as well by the masking of the expected effect due to impurity- or substrate-induced states, which includes intrinsic antisite defects, vacancies and finite temperature effects. A masking of this kind is, for instance, present in case of Bi_2Te_3, where the DP is buried by the onset of the bulk valence band. Thirdly, a gap-opening might be restricted to a region very close to the impurity itself. This could lead to an indirect masking owing to the *lateral extent* of a perturbation center in STM constant-current images. Of course, this type of masking is simply a consequence of the overlap of the gap-opening with different states, but in topographies the effect can be investigated with respect to its lateral extent. Fourthly, external magnetic fields might be needed to sufficiently stabilize the magnetic moments. However, it remains an open question why a clear indication of a gap-opening at the DP by means of STS was not detected yet.

Similar to the graphene-based studies, magnetically-sensitive local scale experiments on TIs were not successful. Although the XMCD clearly shows some advantages (e.g. element-

specificity), it probes the magnetic properties of an ensemble. This complicates the data interpretation. For this reason, SP-STM experiments performed on TM nanostructures grown on TIs are of high priority. They are expected to enable insight into the basic mechanisms determining the electronic and magnetic properties.

Of course, the sample layout for such an experiment again comprises regions of stable magnetization with simultaneously deposited nanostructures. The usual approach for metal substrates comprises regions made of TMs, that are obtained after annealing. At first glance, a similar procedure might be applicable for TIs as well. A sample layout, where Fe is tempted to be grown pseudomorphically on, e.g., Bi_2Se_3, seems promising because the lattice mismatch is small between the (111) planes of both materials. Unfortunately, this common approach was not successful yet and entails major problems to be overcome. As was mentioned earlier, annealing of TI substrates *drastically alters* their properties by adsorbing contamination from the rest gas (Bianchi *et al.*, 2010). Improvements might be possible if, on the one hand, the procedure is applied in a carefully degased surrounding and, on the other hand, the defect density inside the TI is reduced. This would consequently lead to a decrease of available reactants and might thereby enhance the substrate's durability. Similar to graphene, a different approach would be the search for a suitable *passivating layer* that protects the TI and possibly adsorbed nanostructures if the device is exposed to ambient conditions.

Regarding the annealing of TM material on a TI surface, an even more challenging task occurs. In case of Fe on Bi_2Se_3 the Fe atoms segregate into the bulk and *substitute* Bi atoms at their lattice sites already at room temperature (Schlenk *et al.*, 2013), compare Fig. 6.2. In view of the generally similar behavior of Co and Fe on this surface and in view of the similarities among different TIs, an equivalent process can be expected as well for many other TM/TI combinations. An investigation, which seeks a particular material combination that exhibits a TM accumulation temperature below the temperature where a similar substitution process sets in, is therefore highly desirable. Although it remains speculation, these kind of studies might be successful if magnetic elements showing much *higher atomic numbers* compared to the commonly used 3*d* TM are used, e.g. Eu. Thereby, the increased atomic radius might hinder the above mentioned substitution process and enlarge the temperature range available for obtaining well-defined close-packed islands of magnetic material.

Importantly, spin-dependent information about the TI or even adsorbed nanostructures can be gained as well without the "classical" sample layout utilizing a magnetic reference in SP-STM experiments. Topological insulators exhibit *rich* QPI patterns, which display the allowed wave vectors and the relative intensities for the varying scattering processes experienced by the surface state electrons (Roushan *et al.*, 2009). Importantly, these *scattering channels* and their spin-polarization can in principle be calculated by theory.

QPI patterns can be easily obtained by experimental techniques which investigate the sample with respect to the reciprocal space. Therefore, ARPES is an ideal tool by acquiring constant energy contours which themselves reflect the QPI at the respective energy. Although STM is in principle a real space technique, it can be used for this purpose as well. FFT analysis of STS data, more precisely $\mathrm{d}I/\mathrm{d}U$ maps taken at a given bias voltage, can exhibit the QPI at the specified bias. They are thus the corresponding local scale analogue to the pattern obtained by the spatially averaging technique of ARPES (Okada *et al.*, 2011; Sessi *et al.*, 2013). Although for these kind of STS-based experiments the scan range usually needs to be quite large to include a sufficiently extended area of the scattering pattern, the simultaneously acquired sample to-

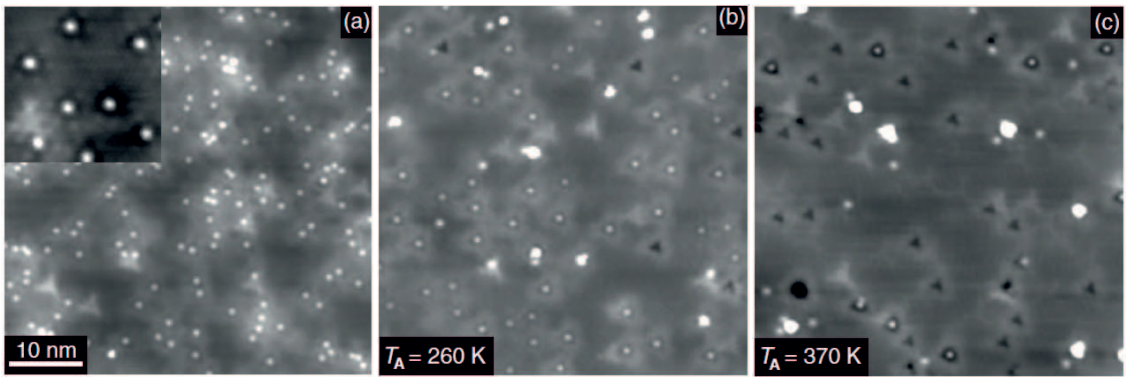

Figure 6.2: (a) STM constant-current map of 0.01 ALE Fe/Bi_2Se_3. The inset shows a magnified view of 8 individual Fe adatoms. (b) After annealing the sample at 260 K the Fe adatoms start to segregate into the bulk crystal and substitute Bi atoms at their lattice sites. Consequently, they appear as dark triangular depressions. (c) After an annealing at 370 K almost no surface-Fe is remaining. Tunneling parameters are $U = 250$ mV and $I = 0.05$ nA. Adapted from Schlenk *et al.*, 2013 with permission.

pography enables to precisely determine the local sample layout. Compared to ARPES, this is a major advantage. To obtain the scattering patterns the presence of *perturbation centers* is a necessary precondition. In a first study the QPI should hence be investigated by utilizing non-magnetic impurities on the surface. In a subsequent experiment, the introduction of magnetic impurities is of interest. This combination is generally expected to provide additional effects due to the interaction between the magnetic moments and the spin-dependent TSSs. Using SP-STM with magnetically coated tips, the *spin-dependent scattering channels* thus offer a possibility to gain information about spin-dependent properties of TIs. As a result, a stable magnetic island reflecting a magnetic reference on the sample itself is not necessarily needed.

From the above discussion the impression arises, that the handling of TIs is even more *fragile* compared to graphene substrates. This reflects a major drawback in view of possible technological applications. These generally require robust structures at ambient conditions. If the goal is achievable at all, the most straightforward application of TIs would possibly rely on the *spin-dependent transport properties*, which could be implemented in future concepts of computing devices. For spintronics and quantum computing, components that exhibit *different spin-dependent populations* or different propagation directions depending on the spin are indispensable. Another possible application of TIs could be their use as a type of *converter* at junctions where an electrical signal needs to be converted into a magnetic one utilizing the magnetoelectric effect. Unfortunately, due to the aforementioned effects present on TIs, it is unquestionable that the sample quality has to be strongly improved to achieve the ability of establishing *quasi-ballistic spin-dependent transport*. Improvements of MBE-grown TI substrates with small thicknesses (Zhang *et al.*, 2010) represent a first step to fulfill this aim.

Anyhow, it appears to be more realistic that TIs remain a class of model materials, which primarily receive attention in fundamental physics. Transport experiments precisely investigating the spin-dependency on a local scale, fundamental studies on heterostructures composed of TIs and superconductors, and investigations of heavy fermions arising from breaking Kramers degeneracy are only a few effects to be studied in detail.

Bibliography

Alpichshev, Z., J. G. Analytis, J.-H. Chu, I. R. Fisher, Y. L. Chen, Z. X. Shen, A. Fang, and A. Kapitulnik. 2010, *STM Imaging of Electronic Waves on the Surface of Bi_2Te_3: Topologically Protected Surface States and Hexagonal Warping Effects*. Phys. Rev. Lett. **104**, 016401. (cited on page(s): 72, 73, 78)

Als-Nielsen, J. and D. McMorrow. 2001, *Elements of Modern X-Ray Physics*. John Wiley & Sons. Chichester, United Kingdom. (cited on page(s): 23)

Anderson, P. W. 1958, *Absence of Diffusion in Certain Random Lattices*. Phys. Rev. **109**, 1492. (cited on page(s): 72)

Anderson, P. W. 1961, *Localized Magnetic States in Metals*. Phys. Rev. **124**, 41. (cited on page(s): 59)

Balandin, A. A., S. Ghosh, W. Bao, I. Calizo, D. Teweldebrhan, F. Miao, and C. N. Lau. 2010, *Superior Thermal Conductivity of Single-Layer Graphene*. Nano Lett. **8**, 902. (cited on page(s): 43)

Bardeen, J. 1961, *Tunnelling from a Many-Particle Point of View*. Phys. Rev. Lett. **6**, 57. (cited on page(s): 13)

Baudelet, F., M.-T. Lin, W. Kuch, K. Meinel, B. Choi, C. M. Schneider, and J. Kirschner. 1995, *Perpendicular anisotropy and spin reorientation in epitaxial Fe/Cu_3Au(100) thin films*. Phys. Rev. B **51**, 12563. (cited on page(s): 37)

Berger, L. 1996, *Emission of spin waves by a magnetic multilayer traversed by a current*. Phys. Rev. B **54**, 9353. (cited on page(s): 2)

Bernevig, B. A., T. L. Hughes, and S.-C. Zhang. 2006, *Quantum Spin Hall Effect and Topological Phase Transition in HgTe Quantum Wells*. Science **314**, 1757. (cited on page(s): 69)

Bernhardt, J., M. Nerding, U. Starke, and K. Heinz. 1999, *Stable surface reconstructions on 6H-SiC(000$\bar{1}$)*. Mater. Sci. Eng. B **61**, 207. (cited on page(s): 50)

Berry, M. V. 1984, *Quantal Phase Factors Accompanying Adiabatic Changes*. Proc. R. Soc. Lond. A **392**, 45. (cited on page(s): 69)

Bianchi, M., D. Guan, S. Bao, J. Mi, B. Brummerstedt Iversen, P. D. C. King, and P. Hofmann. 2010, *Coexistence of the topological state and a two-dimensional electron gas on the surface of Bi_2Se_3*. Nat. Commun. **1**, 128. (cited on page(s): 73)

Bianchi, M., R. C. Hatch, J. Mi, B. Brummerstedt Iversen, and P. Hofmann. 2011, *Simultaneous Quantization of Bulk Conduction and Valence States through Adsorption of Nonmagnetic Impurities on Bi_2Se_3*. Phys. Rev. Lett. **107**, 086802. (cited on page(s): 77)

Binnig, G., H. Rohrer, C. Gerber, and E. Weibel. 1982, *Tunneling through a controllable vacuum gap*. Appl. Phys. Lett. **40**, 178. (cited on page(s): 3, 7)

Binnig, G. and H. Rohrer. 1985, *Scanning Tunneling Microscopy*. Surf. Sci **11**, 157. (cited on page(s): 8)

Biswas, R. R. and A. V. Balatsky. 2010, *Impurity-induced states on the surface of three-dimensional topological insulators*. Phys. Rev. B **81**, 233405. (cited on page(s): 92)

Blaha, P., K. Schwarz, and P. Sorantin. 1990, *Full-potential, linearized augmented plane wave programs for crystalline systems*. Comput. Phys. Commun. **59**, 399. (cited on page(s): 58)

Blöchl, P. E. 1994, *Projector augmented-wave method*. Phys. Rev. B **50**, 17953. (cited on page(s): 58)

Błoński, P., A. Lehnert, S. Dennler, S. Rusponi, M. Etzkorn, G. Moulas, P. Bencok, P. Gambardella, H. Brune, and J. Hafner. 2010, *Magnetocrystalline anisotropy energy of Co and Fe adatoms on the (111) surfaces of Pd and Rh*. Phys. Rev. B **81**, 104426. (cited on page(s): 56, 83)

Blügel, S. and G. Bihlmayer. 2006, *Full-Potential Linearized Augmented Planewave Method*. in *Computational Nanoscience: Do It Yourself!* Vol. **31**, 85. Grotendorst, J., S. Blügel, and D. Marx. John von Neumann Institute for Computing. Jülich, Germany. (cited on page(s): 80)

Bode, M., M. Getzlaff, and R. Wiesendanger. 1998, *Spin-Polarized Vacuum Tunneling into the Exchange-Split Surface State of Gd(0001)*. Phys. Rev. Lett. **81**, 4256. (cited on page(s): 17)

Bode, M. 2003, *Spin-polarized scanning tunneling microscopy*. Rep. Prog. Phys. **66**, 523. (cited on page(s): 19)

Bode, M. 2004, *The Environment Matters–Even on the Atomic Scale*. Science **306**, 423. (cited on page(s): 2, 4)

Bode, M., S. Krause, L. Berbil-Bautista, S. Heinze, and R. Wiesendanger. 2007, *On the preparation and electronic properties of clean W(110) surfaces*. Surf. Sci. **601**, 3308. (cited on page(s): 37, 79, 88)

van Bommel, A. J., J. E. Crombeen, and A. Van Tooren. 1975, *LEED and Auger electron observations of the SiC(0001) surface*. Surf. Sci. **48**, 463. (cited on page(s): 47)

Bostwick, A., T. Ohta, T. Seyller, K. Horn, and E. Rotenberg. 2007, *Quasiparticle dynamics in graphene*. Nat. Phys. **3**, 36. (cited on page(s): 44, 49)

Brandt, C. D., R. C. Clarke, R. R. Siergiej, J. B. Casady, A. W. Morse, S. Sriram, and A. K. Agarwal. 1998, *SiC for Applications in High-Power Electronics*. in *SiC Materials and Devices*. Vol. **52**, 195. Park, Y. S., R. K. Willardson, and E. R. Weber. Academic Press. San Diego, United States of America. (cited on page(s): 47)

Brar, V. W., R. Decker, H.-M. Solowan, Y. Wang, L. Maserati, K. T. Chan, H. Lee, Ç. O. Girit, A. Zettl, S. G. Louie, M. L. Cohen, and M. F. Crommie. 2010, *Gate-controlled ionization and screening of cobalt adatoms on a graphene surface*. Nat. Phys. **7**, 43. (cited on page(s): 54, 98)

de Broglie, . L. V. 1970, *The reinterpretation of wave mechanics*. Found. Phys. **1**, 5. (cited on page(s): 10, 20)

Brune, H. and P. Gambardella. 2009, *Magnetism of individual atoms adsorbed on surfaces*. Surf. Sci. **603**, 1812. (cited on page(s): 92, 94)

Bruno, P. 1989, *Tight-binding approach to the orbital magnetic moment and magnetocrystalline anisotropy of transition-metal monolayers*. Phys. Rev. B **39**, 865. (cited on page(s): 86)

Bunch, J. S., S. S. Verbridge, J. S. Alden, A. M. van der Zande, J. M. Parpia, H. G. Craighead, and P. L. McEuen. 2008, *Impermeable Atomic Membranes from Graphene Sheets*. Nano. Lett. **8**, 2458. (cited on page(s): 46)

Cao, C., M. Wu, J. Jiang, and H.-P. Cheng. 2010, *Transition metal adatom and dimer adsorbed on graphene: Induced magnetization and electronic structures*. Phys. Rev. B **81**, 205424. (cited on page(s): 53, 54, 58)

Carra, P., B. T. Thole, M. Altarelli, and X. Wang. 1993, *X-Ray Circular Dichroism and Local Magnetic Fields*. Phys. Rev. Lett. **70**, 694. (cited on page(s): 28, 94)

Castro Neto, A. H., F. Guinea, N. M. R. Peres, K. S. Novoselov, and A. K. Geim. 2009, *The electronic properties of graphene*. Rev. Mod. Phys. **81**, 109. (cited on page(s): 72)

Cerletti, V., W. A. Coish, O. Gywat, and D. Loss. 2005, *Recipes for spin-based quantum computing*. Nanotechnology **16**, R27. (cited on page(s): 46)

Charrier, A., A. Coati, T. Argunova, F. Thibaudau, and Y. Garreau. 2002, *Solid-state decomposition of silicon carbide for growing ultra-thin heteroepitaxial graphite films*. J. Appl. Phys. **92**, 2479. (cited on page(s): 48)

Chen, C. J. 1988, *Theory of scanning tunneling spectroscopy*. J. Vac. Sci. Technol. A **6**, 319. (cited on page(s): 16)

Chen, C. J. 1990a, *Tunneling matrix elements in three-dimensional space: The derivative rule and the sum rule*. Phys. Rev. B **42**, 8841. (cited on page(s): 16)

Chen, C. J. 2008, *Introduction to Scanning Tunneling Microscopy*. Oxford Science Publications. New York, United States of America. (cited on page(s): 16)

Chen, C. T., F. Sette, Y. Ma, and S. Modesti. 1990b, *Soft-x-ray magnetic circular dichroism at the $L_{2,3}$ edges of nickel*. Phys. Rev. B **42**, 7262. (cited on page(s): 56, 59)

Chen, C. T., Y. U. Idzerda, H.-J. Lin, N. V. Smith, G. Meigs, E. Chaban, G. H. Ho, E. Pellegrin, and F. Sette. 1995, *Experimental Confirmation of the X-Ray Magnetic Circular Dichroism Sum Rules for Iron and Cobalt*. Phys. Rev. Lett. **75**, 152. (cited on page(s): 20)

Chen, Y. L., J. G. Analytis, J.-H. Chu, Z. K. Liu, S.-K. Mo, X. L. Qi, H. J. Zhang, D. H. Lu, X. Dai, Z. Fang, S. C. Zhang, I. R. Fisher, Z. Hussain, and Z.-X. Shen. 2009, *Experimental Realization of a Three-Dimensional Topological Insulator, Bi_2Te_3*. Science **325**, 178. (cited on page(s): 71, 73, 74)

Chen, Y. L., J.-H. Chu, J. G. Analytis, Z. K. Liu, K. Igarashi, H.-H. Kuo, X. L. Qi, S. K. Mo, R. G. Moore, D. H. Lu, M. Hashimoto, T. Sasagawa, S. C. Zhang, I. R. Fisher, Z. Hussain, and Z. X. Shen. 2010, *Massive Dirac Fermion on the Surface of a Magnetically Doped Topological Insulator*. Science **329**, 659. (cited on page(s): 73, 92)

Cho, S., Y. Kim, A. DiVenere, G. K. Wong, J. B. Ketterson, and J. R. Meyer. 1999, *Antisite defects of Bi_2Te_3 thin films*. Appl. Phys. Lett. **75**, 1401. (cited on page(s): 74, 78)

Cococcioni, M. and S. de Gironcoli. 2005, *Linear response approach to the calculation of the effective interaction parameters in the LDA+U method*. Phys. Rev. B **71**, 035105. (cited on page(s): 90)

Collins, G. P. 2006, *Computing with quantum knots*. Sci. Am. **294**, 57. (cited on page(s): 75)

Coraux, J., A. T. N'Diaye, C. Busse, and T. Michely. 2008, *Structural Coherency of Graphene on Ir(111)*. Nano. Lett. **8**, 565. (cited on page(s): 43)

Crocombette, J. P., B. T. Thole, and F. Jollet. 1996, *The importance of the magnetic dipole term in magneto-circular x-ray absorption dichroism for 3d transition metal compounds*. J. Phys.: Condens. Matter **8**, 4095. (cited on page(s): 94)

CryoVac GmbH & Co KG, Heuserweg 14, 53842 Troisdorf, Germany, http://www.cryovac.de. (cited on page(s): 32)

Dal Corso, A. and A. Mosce Conte. 2005, *Spin-orbit coupling with ultrasoft pseudopotentials: Application to Au and Pt*. Phys. Rev. B **71**, 115106. (cited on page(s): 90)

Decker, R., J. Brede, N. Atodiresei, V. Caciuc, S. Blügel, and R. Wiesendanger. 2013, *Atomic-scale magnetism of cobalt-intercalated graphene*. Phys. Rev. B **87**, 041403(R). (cited on page(s): 99)

Demtröder, W. 2010, *Experimentalphysik 3: Atome, Moleküle und Festkörper*. Springer. Berlin, Germany. (cited on page(s): 10)

Dirac, P. A. M. 1927, *The Quantum Theory of the Emission and Absorption of Radiation*. Proc. R. Soc. Lond. A **114**, 243. (cited on page(s): 10)

Donati, F., Q. Dubout, G. Autès, F. Patthey, F. Calleja, P. Gambardella, O. V. Yazyev, and H. Brune. 2013, *Magnetic Moment and Anisotropy of Individual Co Atoms on Graphene*. Phys. Rev. Lett. **111**, 236801. (cited on page(s): 90)

Dresselhaus, M. S., G. Dresselhaus, and P. C. Eklund. 1996, *Science of Fullerenes and Carbon Nanotubes: Their Properties and Applications*. Academic Press Inc. San Diego, United States of America. (cited on page(s): 41)

Duffy, D. M. and J. A. Blackman. 1998, *Magnetism of 3d transition-metal adatoms and dimers on graphite*. Phys. Rev. B **58**, 7443. (cited on page(s): 53, 54, 58)

Durgun, E., S. Dag, S. Ciraci, and O. Gülseren. 2004, *Energetics and Electronic Structures of Individual Atoms Adsorbed on Carbon Nanotubes*. J. Phys. Chem. B **108**, 575. (cited on page(s): 62)

Eelbo, T., M. Waśniowska, P. Thakur, M. Gyamfi, B. Sachs, T. O. Wehling, S. Forti, U. Starke, C. Tieg, A. I. Lichtenstein, and R. Wiesendanger. 2013a, *Adatoms and Clusters of 3d Transition Metals on Graphene: Electronic and Magnetic Configurations*. Phys. Rev. Lett. **110**, 136804. (cited on page(s): 41)

Eelbo, T., M. Waśniowska, M. Gyamfi, S. Forti, U. Starke, and R. Wiesendanger. 2013b, *Influence of the degree of decoupling of graphene on the properties of transition metal adatoms*. Phys. Rev. B **87**, 205443. (cited on page(s): 41)

Eelbo, T., M. Sikora, G. Bihlmayer, M. Dobrzański, A. Kozłowski, I. Miotkowski, and R. Wiesendanger. 2013c, *Co atoms on Bi_2Se_3 revealing a coverage dependent spin reorientation transition*. New J. Phys. **15**, 113026. (cited on page(s): 67)

Eelbo, T., M. Waśniowska, M. Sikora, M. Dobrzański, A. Kozłowski, A. Pulkin, G. Autès, I. Miotkowski, O. V. Yazyev, and R. Wiesendanger. 2014, *Strong Out-of-Plane Magnetic Anisotropy of Fe Adatoms on Bi_2Te_3*. Phys. Rev. B **89**, 104424. (cited on page(s): 67)

Einstein, A. 1905, *Zur Elektrodynamik bewegter Körper*. Ann. Phys. **322**, 891. (cited on page(s): 38)

Emtsev, K. V., A. Bostwick, K. Horn, J. Jobst, G. L. Kellogg, L. Ley, J. L. McChesney, T. Ohta, S. A. Reshanov, J. Röhrl, E. Rotenberg, A. K. Schmid, D. Waldmann, H. B. Weber, and T. Seyller. 2009, *Towards wafer-size graphene layers by atmospheric pressure graphitization of silicon carbide*. Nat. Mater. **8**, 203. (cited on page(s): 51, 60)

Emtsev, K., F. Speck, T. Seyller, L. Ley, and J. D. Riley. 2008, *Interaction, growth, and ordering of epitaxial graphene on SiC0001 surfaces: A comparative photoelectron spectroscopy study*. Phys. Rev. B **77**, 155303. (cited on page(s): 48, 50)

Essin, A. M., J. E. Moore, and D. Vanderbilt. 2009, *Magnetoelectric Polarizability and Axion Electrodynamics in Crystalline Insulators*. Phys. Rev. Lett. **102**, 146805. (cited on page(s): 5, 74)

European Synchrotron Radiation Facility, 6 Rue Jules Horowitz, BP 220, 38043 Grenoble, Cedex 9, France, http://www.esrf.eu. (cited on page(s): 31, 38)

Fano, U. 1961, *Effects of Configuration Interaction on Intensities and Phase Shifts*. Phys. Rev. **124**, 1866. (cited on page(s): 60)

Farmer, D. B., H.-Y. Chiu, Y.-M. Lin, K. A. Jenkins, F. Xia, and P. Avouris. 2009, *Utilization of a Buffered Dielectric to Achieve High Field-Effect Carrier Mobility in Graphene Transistors*. Nano Lett. **9**, 4474. (cited on page(s): 100)

Feenstra, R. M., J. A. Stroscio, and A. P. Fein. 1987, *Tunneling spectroscopy of the Si(111)2 x 1 surface*. Surf. Sci. **181**, 295. (cited on page(s): 16)

FEMTO Messtechnik GmbH, Klosterstraße 64, 10179 Berlin, Germany, http://www.femto.de. (cited on page(s): 9)

First, P. N., W. A. de Heer, T. Seyller, C. Berger, J. A. Stroscio, and J.-S. Moon. 2010, *Epitaxial Graphenes on Silicon Carbide*. MRS Bull. **35**, 296. (cited on page(s): 47)

FLEUR: The Jülich FLAPW code family, http://www.flapw.de. (cited on page(s): 80)

Forti, S., K. V. Emtsev, C. Coletti, A. A. Zakharov, C. Riedl, and U. Starke. 2011, *Large-area homogeneous quasifree standing epitaxial graphene on SiC(0001): Electronic and structural characterization*. Phys. Rev. B **84**, 125449. (cited on page(s): 49)

Fu, L., C. L. Kane, and E. J. Mele. 2007a, *Topological Insulators in Three Dimensions*. Phys. Rev. Lett. **98**, 106803. (cited on page(s): 69)

Fu, L. and C. L. Kane. 2007b, *Topological insulators with inversion symmetry*. Phys. Rev. B **76**, 045302. (cited on page(s): 71)

Fu, L. and C. L. Kane. 2008, *Superconducting Proximity Effect and Majorana Fermions at the Surface of a Topological Insulator*. Phys. Rev. Lett. **100**, 096407. (cited on page(s): 75)

Fu, L. 2009, *Hexagonal Warping Effects in the Surface States of the Topological Insulator Bi_2Te_3*. Phys. Rev. Lett. **103**, 266801. (cited on page(s): 73)

Fujita, M., K. Wakabayashi, K. Nakada, and K. Kusakabe. 1996, *Peculiar Localized State at Zigzag Graphite Edges*. J. Phys. Soc. Jpn. **65**, 1920. (cited on page(s): 99)

Gambardella, P., S. S. Dhesi, S. Gardonio, C. Grazioli, P. Ohresser, and C. Carbone. 2002a, *Localized Magnetic States of Fe, Co, and Ni Impurities on Alkali Metal Films*. Phys. Rev. Lett. **88**, 047202. (cited on page(s): 95)

Gambardella, P., A. Dallmeyer, K. Maiti, M. C. Malagoli, W. Eberhardt, K. Kern, and C. Carbone. 2002b, *Ferromagnetism in one-dimensional monatomic metal chains*. Nature **416**, 301. (cited on page(s): 93)

Gambardella, P., S. Rusponi, M. Veronese, S. S. Dhesi, C. Grazioli, A. Dallmeyer, I. Cabria, R. Zeller, P. H. Dederichs, K. Kern, C. Carbone, and H. Brune. 2003, *Giant Magnetic Anisotropy of Single Cobalt Atoms and Nanoparticles*. Science **300**, 1130. (cited on page(s): 20, 56, 86)

Geim, A. K. and K. S. Novoselov. 2007, *The rise of graphene*. Nat. Mater. **6**, 183. (cited on page(s): 42, 43)

Giannozzi, P., S. Baroni, N. Bonini, M. Calandra, R. Car, C. Cavazzoni, D. Ceresoli, G. L. Chiarotti, M. Cococcioni, I. Dabo, A. Dal Corso, S. de Gironcoli, S. Fabris, G. Fratesi, R. Gebauer, U. Gerstmann, C. Gougoussis, A. Kokalj, M. Lazzeri, L. Martin-Samos, N. Marzari, F. Mauri, R. Mazzarello, S. Paolini, A. Pasquarello, L. Paulatto, C. Sbraccia, S. Scandolo, G. Sclauzero, A. P. Seitsonen, A. Smogunov, P. Umari, and R. M. Wentzcovitch. 2009, *QUANTUM ESPRESSO: a modular and open-source software project for quantum simulations of materials*. J. Phys: Condens. Matter **21**, 395502. (cited on page(s): 90)

Gyamfi, M. 2007, *Construction of a New Scanning Tunneling Microscope for Spin-Sensitive Measurements in Ultrahigh Vacuum, at Low Temperatures, and in High Magnetic Fields*. Diploma thesis. University of Hamburg. (cited on page(s): 34)

Gyamfi, M., T. Eelbo, M. Waśniowska, and R. Wiesendanger. 2011, *Inhomogeneous electronic properties of monolayer graphene on Ru(0001)*. Phys. Rev. B **83**, 153418. (cited on page(s): 63)

Gyamfi, M., T. Eelbo, M. Waśniowska, T. O. Wehling, S. Forti, U. Starke, A. I. Lichtenstein, M. I. Katsnelson, and R. Wiesendanger. 2012a, *Orbital selective coupling between Ni adatoms and graphene Dirac electrons*. Phys. Rev. B **85**, 161406(R). (cited on page(s): 54)

Gyamfi, M. 2012b, *Scanning Tunneling Microscopy and Spectroscopy of Adatoms on Graphene*. PhD thesis. University of Hamburg. (cited on page(s): 33, 54, 98)

Haldane, F. D. M. 1988, *Model for a Quantum Hall Effect without Landau Levels: Condensed-Matter Realization of the "Parity Anomaly"*. Phys. Rev. Lett. **61**, 2015. (cited on page(s): 42, 44, 72)

Hamers, R. J. 1989, *Atomic-Resolution Surface Spectroscopy with the Scanning Tunneling Microscope*. Ann. Rev. Phys. Chem. **40**, 531. (cited on page(s): 16)

Hao, G. L., X. Qi, L. W. Yang, Z. Y. Huang, C. Y. Cai, L. Xue, S. X. Yu, and J. X. Zhong. 2012, *Fermi level shift in topological insulator-silicon heterostructures*. Solid State Commun. **152**, 2027. (cited on page(s): 75)

Hasan, M. Z. and C. L. Kane. 2010, *Colloquium: Topological insulators*. Rev. Mod. Phys. **82**, 3045. (cited on page(s): 69)

Hass, J., W. A. de Heer, and E. H. Conrad. 2008a, *The growth and morphology of epitaxial multilayer graphene*. J. Phys.: Condens. Matter **20**, 323202. (cited on page(s): 43, 51)

Hass, J., F. Varchon, J. E. Millán-Otoya, M. Sprinkle, N. Sharma, W. A. de Heer, C. Berger, P. N. First, L. Magaud, and E. H. Conrad. 2008b, *Why Multilayer Graphene on 4H-SiC(000$\bar{1}$) Behaves Like a Single Sheet of Graphene*. Phys. Rev. Lett. **100**, 125504. (cited on page(s): 50)

Hauschild, J., U. Gradmann, and H. J. Elmers. 1998, *Perpendicular magnetization and dipolar antiferromagnetism in double layer nanostripe arrays of Fe(110) on W(110)*. Appl. Phys. Lett. **72**, 3211. (cited on page(s): 37)

Heinze, S. 2006, *Simulation of spin-polarized scanning tunneling microscopy images of nanoscale non-collinear magnetic structures*. Appl. Phys. A **85**, 407. (cited on page(s): 18)

Heisenberg, W. 1927, *Über den anschaulichen Inhalt der quantentheoretischen Kinematik und Mechanik*. Z. Phys. **43**, 172. (cited on page(s): 10)

Henkelman, G., B. P. Uberuaga, and H. Jónsson. 2000, *A climbing image nudged elastic band method for finding saddle points and minimum energy paths*. J. Chem. Phys. **113**, 9901. (cited on page(s): 90)

Hiebel, F., P. Mallet, F. Varchon, L. Magaud, and J.-Y. Veuillen. 2008, *Graphene-substrate interaction on 6H-SiC(000$\bar{1}$): A scanning tunneling microscopy study*. Phys. Rev. B **78**, 153412. (cited on page(s): 50)

Honolka, J., A. A. Khajetoorians, V. Sessi, T. O. Wehling, S. Stepanow, J.-L. Mi, B. B. Iversen, T. Schlenk, J. Wiebe, N. B. Brookes, A. I. Lichtenstein, P. Hofmann, K. Kern, and R. Wiesendanger. 2012, *In-Plane Magnetic Anisotropy of Fe Atoms on Bi_2Se_3(111)*. Phys. Rev. Lett. **108**, 256811. (cited on page(s): 80)

Hor, Y. S., A. Richardella, P. Roushan, Y. Xia, J. G. Checkelsky, A. Yazdani, M. Z. Hasan, N. P. Ong, and R. J. Cava. 2009, *p-type Bi_2Se_3 for topological insulator and low-temperature thermoelectric applications*. Phys. Rev. B **79**, 195208. (cited on page(s): 73, 74, 78)

Hor, Y. S., P. Roushan, H. Beidenkopf, J. Seo, D. Qu, J. G. Checkelsky, L. A. Wray, D. Hsieh, Y. Xia, S.-Y. Xu, D. Qian, M. Z. Hasan, N. P. Ong, A. Yazdani, and R. J. Cava. 2010, *Development of ferromagnetism in the doped topological insulator $Bi_{2-x}Mn_xTe_3$*. Phys. Rev. B **81**, 195203. (cited on page(s): 89)

Horcas, I., R. Fernández, J. M. Gómez-Rodríguez, J. Colchero, J. Gómez-Herrero, and A. M. Baro. 2007, *WSXM: A software for scanning probe microscopy and a tool for nanotechnology*. Rev. Sci. Instrum. **78**, 013705. (cited on page(s): 9)

Hsieh, D., D. Qian, L. Wray, Y. Xia, Y. S. Hor, R. J. Cava, and M. Z. Hazan. 2008, *A topological Dirac insulator in a quantum spin Hall phase*. Nature **452**, 970. (cited on page(s): 71)

Hsieh, D., Y. Xia, L. Wray, D. Qian, A. Pal, J. H. Dil, J. Osterwalder, F. Meier, G. Bihlmayer, C. L. Kane, Y. S. Hor, R. J. Cava, and M. Z. Hazan. 2009a, *Observation of Unconventional Quantum Spin Textures in Topological Insulators*. Science **323**, 919. (cited on page(s): 71)

Hsieh, D., Y. Xia, D. Qian, L. Wray, J. H. Dil, F. Meier, J. Osterwalder, L. Patthey, J. G. Checkelsky, N. P. Ong, A. V. Fedorov, H. Lin, A. Bansil, D. Grauer, Y. S. Hor, R. J. Cava, and M. Z. Hazan. 2009b, *A tunable topological insulator in the spin helical Dirac transport regime*. Nature **460**, 1101. (cited on page(s): 74)

Hu, J.-M., Z. Li, L.-Q. Chen, and C.-W. Nan. 2011, *High-density magnetoresistive random access memory operating at ultralow voltage at room temperature*. Nat. Commun. **2**, 553. (cited on page(s): 2)

Hund, F. 1925, *Zur Deutung verwickelter Spektren, insbesondere der Elemente Scandium bis Nickel*. Z. Phys. **33**, 345. (cited on page(s): 10)

Iijima, S. 1991, *Helical microtubules of graphitic carbon*. Nature **354**, 56. (cited on page(s): 41)

Itzykson, C. and J.-B. Zuber. 2006, *Quantum Field Theory*. Dover Publications. New York, United States of America. (cited on page(s): 5, 45)

Jackiw, R. and P. Rossi. 1980, *Zero modes of the vortex-fermion system*. Nucl. Phys. B **190**, 681. (cited on page(s): 75)

Janak, J. F. 1977, *Uniform susceptibilities of metallic elements*. Phys. Rev. B **16**, 255. (cited on page(s): 4)

Jobst, J., D. Waldmann, F. Speck, R. Hirner, D. K. Maude, T. Seyller, and H. B. Weber. 2010, *Quantum oscillations and quantum Hall effect in epitaxial graphene*. Phys. Rev. B **81**, 195434. (cited on page(s): 49)

Johll, H., H. C. Kang, and E. S. Tok. 2009, *Density functional theory study of Fe, Co, and Ni adatoms and dimers adsorbed on graphene*. Phys. Rev. B **79**, 245416. (cited on page(s): 53, 54, 57)

Kane, C. L. and E. J. Mele. 2005, *Z_2 Topological Order and the Quantum Spin Hall Effect*. Phys. Rev. Lett. **95**, 146802. (cited on page(s): 69)

Katsnelson, M. I., K. S. Novoselov, and A. K. Geim. 2006, *Chiral tunnelling and the Klein paradox in graphene*. Nat. Phys. **2**, 620. (cited on page(s): 45)

Katsnelson, M. I. 2007, *Graphene: carbon in two dimensions*. Mater. Today **10**, 20. (cited on page(s): 44)

Khajetoorians, A. A., B. Baxevanis, C. Hübner, T. Schlenk, S. Krause, T. O. Wehling, S. Lounis, A. Lichtenstein, D. Pfannkuche, J. Wiebe, and R. Wiesendanger. 2013a, *Current-Driven Spin Dynamics of Artificially Constructed Quantum Magnets*. Science **339**, 55. (cited on page(s): 2)

Khajetoorians, A. A., T. Schlenk, B. Schweflinghaus, M. dos Santos Dias, M. Steinbrecher, M. Bouhassoune, S. Lounis, J. Wiebe, and R. Wiesendanger. 2013b, *Spin Excitations of Individual Fe Atoms on Pt(111): Impact of the Site-Dependent Giant Substrate Polarization*. Phys. Rev. Lett. **111**, 157204. (cited on page(s): 83)

Kitaev, A. Y. 2003, *Fault-tolerant quantum computation by anyons*. Ann. Phys. **303**, 2. (cited on page(s): 75)

Klitzing, K. v., G. Dorda, and M. Pepper. 1980, *New Method for High-Accuracy Determination of the Fine-Structure Constant Based on Quantized Hall Resistance*. Phys. Rev. Lett. **45**, 494. (cited on page(s): 67)

König, M., S. Wiedmann, C. Brüne, A. Roth, H. Buhmann, L. W. Molenkamp, X.-L. Qi, and S.-C. Zhang. 2007, *Quantum Spin Hall Insulator State in HgTe Quantum Wells*. Science **318**, 766. (cited on page(s): 69)

Krause, S., L. Berbil-Bautista, G. Herzog, M. Bode, and R. Wiesendanger. 2007, *Current-Induced Magnetization Switching with a Spin-Polarized Scanning Tunneling Microscope*. Science **317**, 1537. (cited on page(s): 3)

Krause, S., G. Herzog, A. Schlenhoff, A. Sonntag, and R. Wiesendanger. 2011, *Joule Heating and Spin-Transfer Torque Investigated on the Atomic Scale Using a Spin-Polarized Scanning Tunneling Microscope*. Phys. Rev. Lett. **107**, 186601. (cited on page(s): 3)

Kresse, G. and J. Hafner. 1994, *Norm-conserving and ultrasoft pseudopotentials for first-row and transition elements*. J. Phys.: Condens. Matter **6**, 8245. (cited on page(s): 58)

Kresse, G. and D. Joubert. 1999, *From ultrasoft pseudopotentials to the projector augmented-wave method*. Phys. Rev. B **59**, 1758. (cited on page(s): 58)

Krogh Andersen, O. 1975, *Linear methods in band theory*. Phys. Rev. B **12**, 3060. (cited on page(s): 58, 80)

Kroto, H. W., J. R. Health, S. C. O'Brien, R. F. Curl, and R. E. Smalley. 1985, *C60: Buckminsterfullerene*. Nature **318**, 162. (cited on page(s): 41)

Kubetzka, A., P. Ferriani, M. Bode, S. Heinze, G. Bihlmayer, K. von Bergmann, O. Pietzsch, S. Blügel, and R. Wiesendanger. 2005, *Revealing Antiferromagnetic Order of the Fe Monolayer on W(001): Spin-Polarized Scanning Tunneling Microscopy and First-Principles Calculations*. Phys. Rev. Lett. **94**, 087204. (cited on page(s): 19)

van der Laan, G. and I. W. Kirkman. 1992, *The 2p absorption spectra of 3d transition metal compounds in tetrahedral and octahedral symmetry*. J. Phys.: Condens. Matter **4**, 4189. (cited on page(s): 56)

Lake Shore Cryotronics Inc., 575 McCorkle Boulevard, Westerville, OH 43082, United States, http://www.lakeshore.com. (cited on page(s): 35)

Landau, L. D. 1937, *Theory of phase transformations. I.* Phys. Z. Sowjetunion **11**, 25. (cited on page(s): 42)

Lang, N. D. 1886, *Spectroscopy of single atoms in the scanning tunneling microscope*. Phys. Rev. B **34**, 5947. (cited on page(s): 16)

Latil, S. and L. Henrard. 2006, *Charge Carriers in Few-Layer Graphene Films*. Phys. Rev. Lett. **97**, 036803. (cited on page(s): 44, 49)

Lauffer, P., K. V. Emtsev, R. Graupner, T. Seyller, L. Ley, S. A. Reshanov, and H. B. Weber. 2008, *Atomic and electronic structure of few-layer graphene on SiC(0001) studied with scanning tunneling microscopy and spectroscopy*. Phys. Rev. B **77**, 155426. (cited on page(s): 48)

Laughlin, R. B. 1981, *Quantized Hall conductivity in two dimensions*. Phys. Rev. B **23**, 5632. (cited on page(s): 68)

Lee, C., X. Wei, J. W. Kysar, and J. Hone. 2008, *Measurement of the Elastic Properties and Intrinsic Strength of Monolayer Graphene*. Science **321**, 385. (cited on page(s): 43)

Li Bassi, A., C. S. Casari D. Cattaneo, F. Donati, S. Foglio, M. Passoni, C. E. Bottani, P. Biagioni, A. Brambilla, M. Finazzi, F. Ciccacci, and L. Duò. 2007, *Bulk Cr tips for scanning tunneling microscopy and spin-polarized scanning tunneling microscopy*. Appl. Phys. Lett. **91**, 173120. (cited on page(s): 19)

Li, Y.-Y., G. Wang, X.-G. Zhu, M.-H. Liu, C. Ye, X. Chen, Y.-Y. Wang, K. He, L.-L. Wang, X.-C. Ma, H.-J. Zhang, X. Dai, Z. Fang, X.-C. Xie, Y. Liu, X.-L. Qi, J.-F. Jia, S.-C. Zhang, and Q.-K. Xue. 2010, *Intrinsic Topological Insulator Bi_2Te_3 Thin Films on Si and Their Thickness Limit*. Adv. Mater. **22**, 4002. (cited on page(s): 76)

Lin, Y.-M., C. Dimitrakopoulos, K. A. Jenkins, D. B. Farmer, H.-Y. Chiu, A. Grill, and P. Avouris. 2010, *100-GHz Transistors from Wafer-Scale Epitaxial Graphene*. Science **327**, 662. (cited on page(s): 46, 98)

Lin, Y.-M., A. Valdes-Garcia, S.-J. Han, D. B. Farmer, I. Meric, Y. Sun, Y. Wu, C. Dimitrakopoulos, A. Grill, P. Avouris, and K. A. Jenkins. 2011, *Wafer-Scale Graphene Integrated Circuit*. Science **332**, 1294. (cited on page(s): 100)

Liu, Q., C.-X. Liu, C. Xu, X.-L. Qi, and S. C. Zhang. 2009, *Magnetic Impurities on the Surface of a Topological Insulator*. Phys. Rev. Lett. **102**, 156603. (cited on page(s): 74, 82, 94)

Majorana, E. 1937, *Teoria simmetrica dell'elettrone a del positrone*. Nuovo Cimento **14**, 171. (cited on page(s): 5, 74)

Mallet, P., F. Varchon, C. Naud, L. Magaud, C. Berger, and J.-Y. Veuillen. 2007, *Electron states of mono- and bilayer graphene on SiC probed by scanning-tunneling microscopy*. Phys. Rev. B **76**, 041403(R). (cited on page(s): 60)

Mao, Y., J. Yuan, and J. Zhong. 2008, *Density functional calculation of transition metal adatom adsorption on graphene*. J. Phys.: Condens. Matter **20**, 115209. (cited on page(s): 53)

Marchini, S., S. Günther, and J. Wintterlin. 2007, *Scanning tunneling microscopy of graphene on Ru(0001)*. Phys. Rev. B **76**, 075429. (cited on page(s): 43)

MATLAB, Mathworks, Adalperostraße 45, 85737 Ismaning, Germany, http://www.mathworks.de. (cited on page(s): 26)

Mattausch, A. and O. Pankratov. 2007, *Ab Initio Study of Graphene on SiC*. Phys. Rev. Lett. **99**, 076802. (cited on page(s): 49)

Maxwell, J. C. 1864, *A Dynamical Theory of the Electromagnetic Field*. Roy. Soc. Trans. **155**, 459. (cited on page(s): 21)

McClure, J. W. 1956, *Diamagnetism of Graphite*. Phys. Rev. **104**, 666. (cited on page(s): 42)

Meckler, S., M. Gyamfi, O. Pietzsch, and R. Wiesendanger. 2009, *A low-temperature spin-polarized scanning tunneling microscope operating in a fully rotatable magnetic field*. Rev. Sci. Instrum. **80**, 023708. (cited on page(s): 31)

Meckler, S. 2010, *Non-Collinear Magnetism in Fe on W(110)*. PhD thesis. University of Hamburg. (cited on page(s): 31)

Meier, F., L. Zhou, J. Wiebe, and R. Wiesendanger. 2008, *Revealing Magnetic Interactions from Single-Atom Magnetization Curves*. Science **320**, 82. (cited on page(s): 17)

Min, H., J. E. Hill, N. A. Sinitsyn, B. R. Sahu, L. Kleinman, and A. H. MacDonald. 2006, *Intrinsic and Rashba spin-orbit interactions in graphene sheets*. Phys. Rev. B **74**, 165310. (cited on page(s): 43)

Moore, G. and N. Read. 1991, *Nonabelions in the fractional quantum hall effect*. Nucl. Phys. B **360**, 362. (cited on page(s): 75)

Moore, J. E. and L. Balents. 2007, *Topological invariants of time-reversal-invariant band structures*. Phys. Rev. B **75**, 121306(R). (cited on page(s): 69)

Moore, J. E. 2010, *The birth of topological insulators*. Nature **464**, 194. (cited on page(s): 68, 70)

Morozov, S. V., K. S. Novoselov, M. I. Katsnelson, F. Schedin, D. C. Elias, J. A. Jaszczak, and A. K. Geim. 2008, *Giant Intrinsic Carrier Mobilities in Graphene and Its Bilayer*. Phys. Rev. Lett. **100**, 016602. (cited on page(s): 4, 45)

Muehlhoff, L., W. J. Choyke, M. J. Bozack, and J. T. Yates. 1986, *Comparative electron spectroscopic studies of surface segregation on SiC(0001) and SiC(000$\bar{1}$)*. J. Appl. Phys. **60**, 2842. (cited on page(s): 47)

Murakami, S., N. Nagaosa, and S.-C. Zhang. 2004, *Spin-Hall Insulator*. Phys. Rev. Lett. **93**, 156804. (cited on page(s): 5, 70)

Nakahara, M. 2003, *Geometry, Topology and Physics*. Institute of Physics Publishing. Bristol, United Kingdom. (cited on page(s): 69)

Nanonis SPM Controller; SPECS Zurich GmbH, Technoparkstraße. 1, 8005 Zurich, Switzerland, http://www.specs-zurich.com. (cited on page(s): 9)

Nielsen, H. B. and M. Ninomiya. 1983, *The Adler-Bell-Jackiw anomaly and Weyl fermions in a crystal*. Phys. Lett. B **130**, 389. (cited on page(s): 71)

Novoselov, K. S., A. K. Geim, S. V. Morozov, D. Jiang, Y. Zhang, S. V. Dubonos, I. V. Grigorieva, and A. A. Firsov. 2004, *Electric Field Effect in Atomically Thin Carbon Films*. Science **306**, 666. (cited on page(s): 42, 43, 45)

Novoselov, K. S., A. K. Geim, S. V. Morozov, D. Jiang, M. I. Katsnelson, I. V. Grigorieva, S. V. Dubonos, and A. A. Firsov. 2005, *Two-dimensional gas of massless Dirac fermions in graphene*. Nature **438**, 197. (cited on page(s): 5, 45, 72)

Novoselov, K. S., Z. Jiang, Y. Zhang, S. V. Morozov, H. L. Stoner, U. Zeitler, J. C. Maan, G. S. Boebinger, P. Kim, and A. K. Geim. 2007, *Room-Temperature Quantum Hall Effect in Graphene*. Science **315**, 1379. (cited on page(s): 45)

Ohta, T., A. Bostwick, T. Seyller, K. Horn, and E. Rotenberg. 2006, *Controlling the Electronic Structure of Bilayer Graphene*. Science **131**, 951. (cited on page(s): 44)

Ohta, T., A. Bostwick, J. L. McChesney, T. Seyller, K. Horn, and E. Rotenberg. 2007, *Interlayer Interaction and Electronic Screening in Multilayer Graphene Investigated with Angle-Resolved Photoemission Spectroscopy*. Phys. Rev. Lett. **98**, 206802. (cited on page(s): 49, 56)

Okada, Y., C. Dhital, W. Zhou, E. D. Huemiller, H. Lin, S. Basak, A. Bansil, Y.-B. Huang, H. Ding, Z. Wang, S. D. Wilson, and V. Madhavan. 2011, *Direct Observation of Broken Time-Reversal Symmetry on the Surface of a Magnetically Doped Topological Insulator*. Phys. Rev. Lett. **106**, 206805. (cited on page(s): 89, 94, 101)

Omicron NanoTechnology GmbH, Limburger Strasse 75, 65232 Taunusstein, Germany, http://www.omicron.de. (cited on page(s): 31, 40)

Orlita, M., C. Faugeras, P. Plochocka, P. Neugebauer, G. Martinez, D. K. Maude, A.-L. Barra, M. Sprinkle, C. Berger, W. A. de Heer, and M. Potemski. 2008, *Approaching the Dirac Point in High-Mobility Multilayer Epitaxial Graphene*. Phys. Rev. Lett. **101**, 267601. (cited on page(s): 51)

Pankratov, O. A. 1987, *Supersymmetric inhomogeneous semiconductor structures and the nature of a parity anomaly in (2+1) electrodynamics*. Phys. Lett. A **121**, 360. (cited on page(s): 74)

Partoens, B. and F. M. Peeters. 2006, *From graphene to graphite: Electronic structure around the K point*. Phys. Rev. B **74**, 075404. (cited on page(s): 41)

Peierls, R. E. 1935, *Quelques propriétés typiques des corpses solides*. Ann. I. H. Poincaré **5**, 177. (cited on page(s): 42)

Perdew, J. P., K. Burke, and M. Ernzerhof. 1996, *Generalized Gradient Approximation Made Simple*. Phys. Rev. Lett. **77**, 3865. (cited on page(s): 53, 80)

Piamonteze, C., P. Miedema, and F. M. F. de Groot. 2009, *Accuracy of the spin sum rule in XMCD for the transition-metal L edges from manganese to copper*. Phys. Rev. B **80**, 184410. (cited on page(s): 94)

Pietzsch, O., A. Kubetzka, M. Bode, and R. Wiesendanger. 2004, *Spin-Polarized Scanning Tunneling Spectroscopy of Nanoscale Cobalt Islands on Cu(111)*. Phys. Rev. Lett. **92**, 057202. (cited on page(s): 56)

Prokop, J., A. Kukunin, and H. J. Elmers. 2006, *Spin-polarized scanning tunneling microscopy and spectroscopy of ultrathin Fe/Mo(110) films using W/Au/Co tips*. Phys. Rev. B **73**, 014428. (cited on page(s): 19)

Qi, X.-L., T. L. Hughes, and S.-C. Zhang. 2008, *Topological field theory of time-reversal invariant insulators*. Phys. Rev. B **78**, 195424. (cited on page(s): 5, 74, 94)

Qi, X.-L. and S.-C. Zhang. 2010, *The quantum spin Hall effect and topological insulators*. Phys. Today **63**, 33. (cited on page(s): 70)

Qi, X.-L. and S.-C. Zhang. 2011, *Topological insulators and superconductors*. Rev. Mod. Phys. **83**, 1057. (cited on page(s): 68)

Ramesh, R. and N. A. Spaldin. 2007, *Multiferroics: progress and prospects in thin films*. Nat. Mater. **6**, 21. (cited on page(s): 74)

Reittu, H. J. 1997, *Analysis of spin-dependent tunnelling of electrons in solid state structures using the transfer-Hamiltonian method*. J. Phys.: Condens. Matter **9**, 10651. (cited on page(s): 18)

Riedl, C., U. Starke, J. Bernhardt, M. Franke, and K. Heinz. 2007, *Structural properties of the graphene-SiC(0001) interface as a key for the preparation of homogeneous large-terrace graphene surfaces*. Phys. Rev. B **76**, 245406. (cited on page(s): 49)

Riedl, C., C. Coletti, T. Iwasaki, A. A. Zakharov, and U. Starke. 2009, *Quasi-Free-Standing Epitaxial Graphene on SiC Obtained by Hydrogen Intercalation*. Phys. Rev. Lett. **103**, 246804. (cited on page(s): 49, 60)

Ristein, J., S. Mammadov, and T. Seyller. 2012, *Origin of Doping in Quasi-Free-Standing Graphene on Silicon Carbide*. Phys. Rev. Lett. **108**, 246104. (cited on page(s): 50)

Rollings, E., G.-H. Gweon, S. Y. Zhou, B. S. Mun, J. L. McChesney, B. S. Hussain, A. V. Fedorov, P. N. First, W. A. de Heer, and A. Lanzara. 2006, *Synthesis and characterization of atomically thin graphite films on a silicon carbide substrate*. J. Phys. Chem. Solids **67**, 2172. (cited on page(s): 44)

Röntgen, W. C. 1895, *Über eine neue Art von Strahlen*. Phys. Rev. (Series I) **5**, 1. (cited on page(s): 20)

Roushan, P., J. Seo, C. V. Parker, Y. S. Hor, F. Hsieh, D. Qian, A. Richardella, M. Z. Hasan, R. J. Cava, and A. Yazdani. 2009, *Topological surface states protected from backscattering by chiral spin texture*. Nature **460**, 1106. (cited on page(s): 72, 101)

Roy, R. 2009, *Topological phases and the quantum spin Hall effect in three dimensions*. Phys. Rev. B **79**, 195322. (cited on page(s): 69)

Rudenko, A. N., F. J. Keil, M. I. Katsnelson, and A. I. Lichtenstein. 2012, *Adsorption of cobalt on graphene: Electron correlation effects from a quantum chemical perspective*. Phys Rev. B **86**, 075422. (cited on page(s): 53, 63)

Rutter, G. M., J. N. Crain, N. P. Guisinger, T. Li, P. N. First, and J. A. Stroscio. 2007, *Scattering and Interference in Epitaxial Graphene*. Science **317**, 219. (cited on page(s): 60)

Rycerz, A., J. Tworzydło, and C. W. J. Beenakker. 2007, *Valley filter and valley valve in graphene*. Nat. Phys. **3**, 172. (cited on page(s): 46)

Saito, R., G. Dresselhaus, and M. S. Dresselhaus. 1998, *Physical Properties of Carbon Nanotubes*. Imperial College Press. London, United Kingdom. (cited on page(s): 41)

Sargolzaei, M. and F. Gudarzi. 2011, *Magnetic properties of single 3d transition metals adsorbed on graphene and benzene: A density functional theory study*. J. Appl. Phys. **110**, 064303. (cited on page(s): 53, 54, 57)

Scanlon, D. O., P. D. C. King, R. P. Singh, A. de la Torre, S. McKeown Walker, G. Balakrishnan, F. Baumberger, and C. R. A. Catlow. 2012, *Controlling Bulk Conductivity in Topological Insulators: Key Role of Anti-Site Defects*. Adv. Mater. **24**, 2154. (cited on page(s): 74, 78)

Schedin, F., A. K. Geim, S. V. Morozov, E. W. Hill, P. Blake, M. I. Katsnelson, and K. S. Novoselov. 2007, *Detection of individual gas molecules adsorbed on graphene*. Nat. Mater. **6**, 652. (cited on page(s): 46)

Schlenhoff, A., S. Krause, G. Herzog, and R. Wiesendanger. 2010, *Bulk Cr tips with full spatial magnetic sensitivity for spin-polarized scanning tunneling microscopy*. Appl. Phys. Lett. **97**, 083104. (cited on page(s): 19)

Schlenk, T., M. Bianchi, M. Koleini, A. Eich, O. Pietzsch, T. O. Wehling, T. Frauenheim, A. Balatsky, J.-L. Mi, B. B. Iversen, J. Wiebe, A. A. Khajetoorians, P. Hofmann, and R. Wiesendanger. 2013, *Controllable Magnetic Doping of the Surface State of a Topological Insulator*. Phys. Rev. Lett. **110**, 126804. (cited on page(s): 81)

Schmidt, T. M., R. H. Miwa, and A. Fazzio. 2011, *Spin texture and magnetic anisotropy of Co impurities in Bi_2Se_3 topological insulators*. Phys. Rev. B **84**, 245418. (cited on page(s): 82, 84, 88)

Schrödinger, E. 1926, *Quantisierung als Eigenwertproblem*. Ann. Phys. **386**, 109. (cited on page(s): 10)

Schütz, G., W. Wagner, W. Wilhelm, P. Kienle, R. Zeller, R. Frahm, and G. Materlik. 1987, *Absorption of circularly polarized x rays in iron*. Phys. Rev. (Series I) **58**, 737. (cited on page(s): 3, 20, 24)

Scientific Magnetics, 7 Suffolk Way, Abingdon, OX14 5JX, United Kingdom, http://www.scientificmagnetics.co.uk. (cited on page(s): 32)

Semenoff, G. W. 1984, *Condensed-Matter Simulation of a Three-Dimensional Anomaly*. Phys. Rev. Lett. **53**, 2449. (cited on page(s): 42, 44)

Sessi, V., M. M. Otrokov, T. Bathon, M. G. Vergniory, S. S. Tsirkin, K. A. Kokh, O. E. Tereshchenko, E. V. Chulkov, and M. Bode. 2013, *Visualizing spin-dependent bulk scattering and breakdown of the linear dispersion relation in Bi_2Te_3*. Phys. Rev. B **88**, 161407(R). (cited on page(s): 101)

Sevinçli, H., M. Topsakal, E. Durgun, and S. Ciraci. 2008, *Electronic and magnetic properties of 3d transition-metal atom adsorbed graphene and graphene nanoribbons*. Phys. Rev. B **77**, 195434. (cited on page(s): 53)

Shelford, L. R., T. Hesjedal, L. Collins-McIntyre, S. S. Dhesi, F. Maccherozzi, and G. van der Laan. 2012, *Electronic structure of Fe and Co magnetic adatoms on Bi_2Te_3 surfaces*. Phys. Rev. B **86**, 081304. (cited on page(s): 84)

Šipr, O., J. Minár, and H. Ebert. 2009, *On the importance of the magnetic dipole term T_Z in analyzing X-ray magnetic circular dichroism spectra of clusters*. Europhys. Lett. **87**, 67007. (cited on page(s): 94)

Slonczewski, J. C. and P. R. Weiss. 1958, *Band Structure of Graphite*. Phys. Rev. **109**, 272. (cited on page(s): 42, 44)

Slonczewski, J. C. 1989, *Conductance and exchange coupling of two ferromagnets separated by a tunneling barrier*. Phys. Rev. B **39**, 6995. (cited on page(s): 17, 19)

Slonczewski, J. C. 1996, *Current-driven excitation of magnetic multilayers*. J. Magn. Magn. Mater. **159**, L1. (cited on page(s): 2)

Sofo, J. O., A. S. Chaudhari, and G. D. Barber. 2007, *Graphane: A two-dimensional hydrocarbon*. Phys. Rev. B **75**, 153401. (cited on page(s): 46)

Solé, V. A., E. Papillon, M. Cotte, P. Walter, and J. Susini. 2007, *A multiplatform code for the analysis of energy-dispersive X-ray fluorescence spectra*. Acta Part B **62**, 63. (cited on page(s): 26)

Son, Y.-W., M. L. Cohen, and S. G. Louie. 2006, *Half-metallic graphene nanoribbons*. Nature **444**, 347. (cited on page(s): 46, 99)

Song, C.-L., Y.-P. Jiang, Y.-L. Wang, Z. Li, L. Wang, K. He, X. Chen, X.-C. Ma, and Q.-K. Xue. 2012, *Gating the charge state of single Fe dopants in the topological insulator Bi_2Se_3 with a scanning tunneling microscope*. Phys. Rev. B **86**, 045441. (cited on page(s): 89, 92)

Speck, F., J. Jobst, F. Fromm, M. Ostler, D. Waldmann, M. Hundhausen, H. B. Weber, and T. Seyller. 2011, *The quasi-free-standing nature of graphene on H-saturated SiC(0001)*. Appl. Phys. Lett. **99**, 122106. (cited on page(s): 49, 50)

Sprinkle, M., D. Siegel, Y. Hu, J. Hicks, A. Tejeda, A. Taleb-Ibrahimi, P. Le Fèvre, F. Bertran, S. Vizzini, H. Enriquez, S. Chiang, P. Soukiassian, C. Berger, W. A. de Heer, A. Lanzara, and E. H. Conrad. 2009, *First Direct Observation of a Nearly Ideal Graphene Band Structure*. Phys. Rev. Lett. **103**, 226803. (cited on page(s): 50, 51)

Starke, U. 2004, *Atomic Structure of SiC Surfaces*. in *Silicon Carbide: Recent Major Advances*. Vol. **79**, 281. Choyke, W. J., H. Matsunami, and G. Pensl. Springer. Berlin, Germany. (cited on page(s): 48)

Starke, U. and C. Riedl. 2009, *Epitaxial graphene on SiC(0001) and SiC(000$\bar{1}$): from surface reconstructions to carbon electronics*. J. Phys.: Condens. Matter **21**, 134016. (cited on page(s): 43)

Stöhr, J. and H. König. 1995, *Determination of Spin- and Orbital-Moment Anisotropies in Transition Metals by Angle-Dependent X-Ray Magnetic Circular Dichroism*. Phys. Rev. Lett. **75**, 3748. (cited on page(s): 20, 28)

Stöhr, J. and H. C. Siegmann. 2006, *Magnetism: From Fundamentals to Nanoscale Dynamics*. Springer. Berlin, Germany. (cited on page(s): 23, 28, 94)

Stoner, E. 1938, *Collective electron ferromagnetism*. Proc. R. Soc. Lon. Ser-A **165**, 372. (cited on page(s): 3)

Sutter, P., J. T. Sadowski, and E. Sutter. 2009, *Graphene on Pt(111): Growth and substrate interaction*. Phys. Rev. B **80**, 245411. (cited on page(s): 43)

Tersoff, J. and D. R. Hamann. 1983, *Theory and Application for the Scanning Tunneling Microscope*. Phys. Rev. Lett. **50**, 1998. (cited on page(s): 14)

Tersoff, J. and D. R. Hamann. 1985, *Theory of the scanning tunneling microscope*. Phys. Rev. B **31**, 805. (cited on page(s): 14)

Thole, B. T. and G. van der Laan. 1988, *Branching ratio in x-ray absorption spectroscopy*. Phys. Rev. B **38**, 3158. (cited on page(s): 29, 84, 92)

Thole, B. T., P. Carra, F. Sette, and G. van der Laan. 1992, *X-ray circular dichroism as a probe of orbital magnetization*. Phys. Rev. Lett. **68**, 1943. (cited on page(s): 28, 94)

Thouless, D. J., M. Kohmoto, M. P. Nightingale, and M. den Nijs. 1982, *Quantized Hall Conductance in a Two-Dimensional Periodic Potential*. Phys. Rev. Lett. **49**, 405. (cited on page(s): 68)

Tombros, N., C. Jozsa, M. Popinciuc, H. T. Jonkman, and B. J. van Wees. 2007, *Electronic spin transport and spin precession in single graphene layers at room temperature*. Nature **448**, 571. (cited on page(s): 98)

Trauzettel, B., D. V. Bulaev, D. Loss, and G. Burkhard. 2007, *Spin qubits in graphene quantum dots*. Nat. Phys. **3**, 192. (cited on page(s): 46)

Uchoa, B., L. Yang, S.-W. Tsai, N. M. R. Peres, and A. H. Castro Neto. 2009, *Theory of Scanning Tunneling Spectroscopy of Magnetic Adatoms in Graphene*. Phys. Rev. Lett. **103**, 206804. (cited on page(s): 60)

Urazhdin, S., D. Bilc, S. H. Tessmer, S. D. Mahanti, T. Kyratsi, and M. G. Kanatzidis. 2002, *Scanning tunneling microscopy of defect states in the semiconductor Bi_2Se_3*. Phys. Rev. B **66**, 161306(R). (cited on page(s): 74, 77, 78)

Valencia, H., A. Gil, and G. Frapper. 2010, *Trends in the Adsorption of 3d Transition Metal Atoms onto Graphene and Nanotube Surfaces: A DFT Study and Molecular Orbital Analysis*. J. Phys. Chem. C **114**, 14141. (cited on page(s): 53)

Varchon, F., R. Feng, J. Hass, X. Li, B. Ngoc Nguyen, C. Naud, P. Mallet, J.-Y. Veuillen, C. Berger, E. H. Conrad, and L. Magaud. 2007, *Electronic Structure of Epitaxial Graphene Layers on SiC: Effect of the Substrate*. Phys. Rev. Lett. **99**, 126805. (cited on page(s): 49)

Venables, J. A., G. D. T. Spiller, and M. Hanbucken. 1984, *Nucleation and growth of thin films*. Rep. Prog. Phys. **47**, 399. (cited on page(s): 42)

Wallace, P. R. 1947, *The Band Theory of Graphite*. Phys. Rev. **71**, 622. (cited on page(s): 42–44)

Wang, G., X.-G. Zhu, Y.-Y. Sun, Y.-Y. Li, T. Zhang, J. Wen, X. Chen, K. He, L.-L. Wang, X.-C. Ma, J.-F. Jia, S. B. Zhang, and Q.-K. Xue. 2011, *Topological Insulator Thin Films of Bi_2Te_3 with Controlled Electronic Structure*. Adv. Mater. **23**, 2929. (cited on page(s): 73, 76, 78)

Wehling, T. O., K. S. Novoselov, S. V. Morozov, E. E. Vdovin, M. I. Katsnelson, A. K. Geim, and A. I. Lichtenstein. 2008, *Molecular Doping of Graphene*. Nano Lett. **8**, 173. (cited on page(s): 46)

Wehling, T. O., A. V. Balatsky, M. I. Katsnelson, A. I. Lichtenstein, and A. Rosch. 2010, *Orbitally controlled Kondo effect of Co adatoms on graphene*. Phys. Rev. B **81**, 115427. (cited on page(s): 54)

Wehling, T. O., A. I. Lichtenstein, and M. I. Katsnelson. 2011, *Transition-metal adatoms on graphene: Influence of local Coulomb interactions on chemical bonding and magnetic moments*. Phys. Rev. B **84**, 235110. (cited on page(s): 54)

Weinert, M., E. Wimmer, and A. J. Freeman. 1982, *Total-energy all-electron density functional method for bulk solidas and surfaces*. Phys. Rev. B **26**, 4571. (cited on page(s): 80)

Wen, X.-G. 1995, *Topological orders and edge excitations in fractional quantum Hall states*. Adv. Phys. **44**, 405. (cited on page(s): 68)

West, D., Y. Y. Sun, S. B. Zhang, T. Zhang, X. Ma, P. Cheng, Y. Y. Zhang, X. Chen, J. F. Jia, and Q.-K. Xue. 2012, *Identification of magnetic dopants on the surfaces of topological insulators: Experiment and theory for Fe on Bi_2Te_3(111)*. Phys. Rev. B **85**, 081305. (cited on page(s): 89, 90)

Wiesendanger, R., H.-J. Güntherodt, G. Güntherodt, R. J. Gambino, and R. Ruf. 1990, *Observation of vacuum tunneling of spin-polarized electrons with the scanning tunneling microscope*. Phys. Rev. Lett. **65**, 247. (cited on page(s): 17)

Wiesendanger, R. 2009, *Spin mapping at the nanoscale and atomic scale*. Rev. Mod. Phys. **81**, 1495. (cited on page(s): 3, 17, 19)

Wilczek, F. 2009, *Majorana returns*. Nat. Phys. **5**, 614. (cited on page(s): 74)

Wimmer, E., H. Krakauer, M. Weinert, and A. J. Freeman. 1981, *Full-potential self-consistent linearized-augmented-plane-wave method for calculating the electronic structure of molecules and surfaces: O_2 molecule*. Phys. Rev. B **24**, 864. (cited on page(s): 80)

Wolf, S. A., D. D. Awschalom, R. A. Buhrman, J. M. Daughton, S. von Molnár, M. L. Roukes, Y. Y. Chtchelkanova, and D. M. Treger. 2001, *Spintronics: A Spin-Based Electronics Vision for the Future*. Science **294**, 1488. (cited on page(s): 46)

Wood, R. W. 1897, *A new form of Cathode Discharge and the Production of X-Rays, together with some Notes on Diffraction*. Phys. Rev. (Series I) **5**, 1. (cited on page(s): 7)

Wortmann, D., S. Heinze, P. Kurz, G. Bihlmayer, and S. Blügel. 2001, *Resolving Complex Atomic-Scale Spin Structures by Spin-Polarized Scanning Tunneling Microscopy*. Phys. Rev. Lett. **86**, 4132. (cited on page(s): 18)

Wray, L. A., S.-Y. Xu, Y. Xia, S. Hsieh, A. V. Fedorov, Y. S. Hor, R. J. Cava, A. Bansil, H. Lin, and M. Z. Hasan. 2011, *A topological insulator surface under strong Coulomb, magnetic and disorder perturbations*. Nat. Phys. **7**, 32. (cited on page(s): 74, 92, 94)

WSxM SPM Software, Nanotec Electronica S.L., Centro Empresarial Euronova 3, Ronda de Poniente 12, Planta 2a, 28760 Tres Cantos Madrid, Spain, http://www.nanotec.es. (cited on page(s): 9)

Wu, X., Y. Hu, M. Ruan, N. K. Madiomanana, J. Hankinson, M. Sprinkle, C. Berger, and W. A. de Heer. 2009, *Half integer quantum Hall effect in high mobility single layer epitaxial graphene*. Appl. Phys. Lett. **95**, 223108. (cited on page(s): 48)

Xia, Y., D. Qian, D. Hsieh, L. Wray, A. Pal, H. Lin, A. Bansil, D. Grauer, Y. S. Hor, R. J. Cava, and M. Z. Hasan. 2009, *Observation of a large-gap topological-insulator class with a single Dirac cone on the surface*. Nat. Phys. **5**, 398. (cited on page(s): 71)

Yagi, Y., T. M. Briere, M. H. F. Sluiter, V. Kumar, A. A. Farajian, and Y. Kawazoe. 2004, *Stable geometries and magnetic properties of single-walled carbon nanotubes doped with 3d transition metals: A first-principles study*. Phys. Rev. B **69**, 075414. (cited on page(s): 53, 54, 58)

Yazyev, O. V. and A. Pasquarello. 2010, *Metal adatoms on graphene and hexagonal boron nitride: Towards rational design of self-assembly templates*. Phys. Rev. B **82**, 045407. (cited on page(s): 53, 54)

Ye, M., S. V. Eremeev, K. Kuroda, E. E. Krasovskii, E. V. Chulkov, Y. Takeda, Y. Saitoh, K. Okamoto, S. Y. Zhu, K. Miyamoto, M. Arita, M. Nakatake, T. Okuda, Y. Ueda, K. Shimada, H. Namatame, M. Taniguchi, and A. Kimura. 2012, *Quasiparticle interference on*

the surface of Bi_2Se_3 induced by cobalt adatom in the absence of ferromagnetic ordering. Phys. Rev. B **85**, 205317. (cited on page(s): 81)

Ye, M., K. Kuroda, Y. Takeda, Y. Saitoh, K. Okamoto, S.-Y. Zhu, K. Shirai, K. Miyamoto, M. Arita, M. Nakatake, T. Okuda, Y. Ueda, K. Shimada, H. Namatame, M. Taniguchi, and A. Kimura. 2013, *Perpendicular magnetic anisotropy with enhanced orbital moments of Fe adatoms on a topological surface of Bi_2Se_3*. J. Phys.: Condens. Matter **25**, 232201. (cited on page(s): 84)

Yoo, E., J. Kim, E. Hosono, H.-S. Zhou, T. Kudo, and I. Honma. 2008, *Large Reversible Li Storage of Graphene Nanosheet Families for Use in Rechargeable Lithium Ion Batteries*. Nano. Lett. **8**, 2277. (cited on page(s): 46)

Zhang, D., A. Richardella, D. W. Rench, S.-Y. Xu, A. Kandala, T. C. Flanagan, H. Beidenkopf, A. L. Yeats, B. B. Buckley, P. V. Klimov, D. D. Awschalom, A. Yazdani, P. Schiffer, M. Z. Hasan, and N. Samarth. 2012, *Interplay between ferromagnetism, surface states, and quantum corrections in a magnetically doped topological insulator*. Phys. Rev. B **86**, 205127. (cited on page(s): 88)

Zhang, H., C.-X. Liu, X.-L. Qi, X. Dai, Z. Fang, and S.-C. Zhang. 2009a, *Topological insulators in Bi_2Se_3, Bi_2Te_3 and Sb_2Te_3 with a single Dirac cone on the surface*. Nat. Phys. **5**, 438. (cited on page(s): 70)

Zhang, J.-M., W. Zhu, Y. Zhang, D. Xiao, and Y. Yao. 2012, *Tailoring Magnetic Doping in the Topological Insulator Bi_2Se_3*. Phys. Rev. Lett. **109**, 266405. (cited on page(s): 74, 78)

Zhang, S.-C. 2008, *Topological states of quantum matter*. Physics **1**, 6. (cited on page(s): 68)

Zhang, T., P. Cheng, X. Chen, J.-F. Jia, X. Ma, K. He, L. Wang, H. Zhang, X. Dai, Z. Fang, X. Xie, and Q.-K. Xue. 2009b, *Experimental Demonstration of Topological Surface States Protected by Time-Reversal Symmetry*. Phys. Rev. Lett. **103**, 266803. (cited on page(s): 72, 73)

Zhang, Y., Y.-W. Tan, H. L. Stormer, and P. Kim. 2005, *Experimental observation of the quantum Hall effect and Berry's phase in graphene*. Nature **438**, 201. (cited on page(s): 5, 45, 72)

Zhang, Y., K. He, C.-Z. Chang, C.-L. Song, L.-L. Wang, X. Chen, J.-F. Jia, Z. Fang, X. Dai, W.-Y. Shan, S.-Q. Shen, Q. Niu, X.-L. Qi, S.-C. Zhang, X.-C. Ma, and Q.-K. Xue. 2010, *Crossover of the three-dimensional topological insulator Bi_2Se_3 to the two-dimensional limit*. Nat. Phys. **6**, 584. (cited on page(s): 76, 102)

Zhou, S. Y., G.-H. Gweon, A. V. Fedorov, P. N. First, W. A. de Heer, D.-H. Lee, F. Guinea, A. H. Castro Neto, and A. Lanzara. 2007, *Substrate-induced bandgap opening in epitaxial graphene*. Nat. Mater. **6**, 770. (cited on page(s): 49)

Publications

- M. Gyamfi, T. Eelbo, M. Waśniowska, and R. Wiesendanger. *Inhomogeneous electronic properties of monolayer graphene on Ru(0001).* Phys. Rev. B **83**, 153418 (2011).

- M. Gyamfi, T. Eelbo, M. Waśniowska, and R. Wiesendanger. *Fe adatoms on graphene/Ru(0001): Adsorption site and local electronic properties.* Phys. Rev. B **84**, 113403 (2011).

- M. Gyamfi, T. Eelbo, M. Waśniowska, T. O. Wehling, S. Forti, U. Starke, A. I. Lichtenstein, M. I. Katsnelson, and R. Wiesendanger. *Orbital selective coupling between Ni adatoms and graphene Dirac electrons.* Phys. Rev. B **85**, 161406(R) (2012).

- M. Gyamfi, T. Eelbo, M. Waśniowska, and R. Wiesendanger. *Impact of intercalated cobalt on the electronic properties of graphene on Pt(111).* Phys. Rev. B **85**, 205434 (2012).

- T. Eelbo, M. Waśniowska, P. Thakur, M. Gyamfi, B. Sachs, T. O. Wehling, S. Forti, U. Starke, C. Tieg, A. I. Lichtenstein, and R. Wiesendanger. *Adatoms and Clusters of 3d Transition Metals on Graphene: Electronic and Magnetic Configurations.* Phys. Rev. Lett. **110**, 136804 (2013).

- T. Eelbo, M. Waśniowska, M. Gyamfi, S. Forti, U. Starke, and R. Wiesendanger. *Influence of the degree of decoupling of graphene on the properties of transition metal adatoms.* Phys. Rev. B **87**, 205443 (2013).

- T. Eelbo, M. Sikora, G. Bihlmayer, M. Dobrzański, A. Kozłowski, I. Miotkowski, and R. Wiesendanger. *Co atoms on Bi_2Se_3 revealing a coverage dependent spin reorientation transition.* New J. Phys. **15**, 113026 (2013).

- T. Eelbo, M. Waśniowska, M. Sikora, M. Dobrzański, A. Kozłowski, A. Pulkin, G. Autès, I. Miotkowski, O. V. Yazyev, and R. Wiesendanger. *Strong out-of-plane magnetic anisotropy of Fe adatoms on Bi_2Te_3.* Phys. Rev. B **89**, 104424 (2014).

- T. Iwasaki, A. A. Zakharov, T. Eelbo, M. Waśniowska, R. Wiesendanger, J. H. Smet, and U. Starke. *Formation and structural analysis of twisted bilayer graphene on Ni(111) thin films.* Surf. Sci. **625**, 44 (2014).

Conference Contributions

- ∗T. Eelbo, M. Gyamfi, S. Meckler, O. Pietzsch, and R. Wiesendanger. *Development of an UHV Variable Temperature STM.* Poster, DPG-Meeting (2008).
- ∗M. Gyamfi, T. Eelbo, M. Waśniowska, O. Pietzsch, and R. Wiesendanger. *Electronic structure of graphene on Ru(0001) studied with STS.* Talk, DPG-Meeting (2010).
- ∗T. Eelbo, M. Gyamfi, M. Waśniowska, and R. Wiesendanger. *Growth mode and evolution of electronic properties for $Bi_{1-x}Sb_x$ alloys on W(110).* Poster, DPG-Meeting (2011).
- ∗M. Gyamfi, T. Eelbo, M. Waśniowska, and R. Wiesendanger. *Inhomogeneous electronic properties of monolayer graphene on Ru(0001).* Poster, DPG-Meeting (2011).
- T. Eelbo, M. Gyamfi, ∗M. Waśniowska, and R. Wiesendanger. *Electronic properties and localization of Fe atoms on bilayer graphene on Ru(0001).* Talk, DPG-Meeting (2011).
- M. Gyamfi, T. Eelbo, ∗M. Waśniowska, T. Wehling, A. Lichtenstein, S. Forti, U. Starke, and R. Wiesendanger. *Ni atoms on graphene: electronic properties and phonon excitations.* Poster, Graphene Week (2011).
- M. Gyamfi, T. Eelbo, ∗M. Waśniowska, T. Wehling, A. Lichtenstein, S. Forti, U. Starke, and R. Wiesendanger. *Ni atoms on graphene: electronic properties and phonon excitations.* Talk, ECOSS-28 (2011).
- ∗M. Gyamfi, T. Eelbo, M. Waśniowska, T. O. Wehling, S. Forti, U. Starke, A. I. Lichtenstein, M. I. Katsnelson, and R. Wiesendanger. *Electronic properties of Ni adatoms on graphene.* Talk, DPG-Meeting (2012).
- T. Eelbo, M. Gyamfi, S. Forti, U. Starke, ∗M. Waśniowska, and R. Wiesendanger. *Visualizing quantum interference nearby individual magnetic impurities on graphene.* Talk, DPG-Meeting (2012).
- ∗T. Eelbo, M. Sikora, M. Waśniowska, M. Dobrzański, M. Gyamfi, G. Bihlmayer, I. Miotkowski, A. Kozłowski, and R. Wiesendanger. *Electronic properties and magnetic anisotropy of individual Co adatoms adsorbed on topological insulator surfaces.* Talk, DPG-Meeting (2012).
- T. Eelbo, M. Gyamfi, S. Forti, U. Starke, ∗M. Waśniowska, and R. Wiesendanger. *Visualizing electron scattering on graphene around Co adatoms by means of STM.* Talk, Graphene Week (2012).
- T. Eelbo, M. Gyamfi, ∗M. Waśniowska, and R. Wiesendanger. *Graphene on Pt(111) intercalated by Cobalt studied with STM and STS.* Poster, ICN+T (2012).
- ∗T. Eelbo, M. Sikora, M. Waśniowska, M. Dobrzański, A. Kozłowski, M. Gyamfi, G. Bihlmayer, I. Miotkowski, and R. Wiesendanger. *Electronic and Magnetic Properties of Co Adatoms on the Bi_2Se_3 Surface.* Talk, ICN+T (2012).
- T. Eelbo, ∗M. Waśniowska, M. Sikora, G. Bihlmayer, M. Gyamfi, M. Dobrzański, A. Kozłowski, Z. Kakol, I. Miotkowski, and R. Wiesendanger. *Co atoms on Bi_2Se_3: electronic and magnetic properties.* Talk, SPS'12 & SPSTM-4 (2012).
- ∗M. Gyamfi, T. Eelbo, M. Waśniowska, and R. Wiesendanger. *Bistability of Adatoms on Graphene.* Poster, SPS'12 & SPSTM-4 (2012).

Acknowledgements

Quite naturally the results obtained were not achieved without foreign help. During the time needed to acquire, to collect, and to evaluate the data, that form the basis of my thesis, many people helped me in different ways, directly or indirectly. The list given below thus is supposed to give an overview of all the people I want to thank and has to be considered as being incomplete. I would like to thank:

- first of all, my supervisor **Prof. Dr. Wiesendanger**, who gave me the opportunity to gain the doctor's degree in his group. The experimental possibilities available and the ability to join almost any desired conference are extraordinary, which generally can not be taken for granted.
- the remaining referees **Prof. Dr. Ulrich Merkt** and **Prof. Dr. Kornelius Nielsch** for their willingness to judge my dissertation/disputation.
- especially the crew from the triple axes magnet lab, i.e. **O. Pietzsch**, **M. Gyamfi**, **S. Meckler**, **A. Pressler** and **M. Waśniowska**. The atmosphere was always very friendly, the discussions and the cooperativeness were extremely motivating.
- everybody from the **scanning probe methods group** for fruitful discussions, joint activities, and a friendly environment at any time.
- all the people who contributed to the experiments in one or the other way. That are, firstly, for their participation in the XMCD measurements: **P. Thakur**, **C. Tieg**, **M. Sikora**, **M. Dobrzański**, and **A. Kozłowski**, secondly, for providing the graphene and TI-samples: **S. Forti**, **U. Starke**, and **I. Miotkowski**, and thirdly, for the support with numerical calculations necessary to gain a detailed understanding of the experimental results: **B. Sachs**, **T. O. Wehling**, **A. I. Lichtenstein**, **G. Bihlmayer**, **A. Pulkin**, **G. Autès**, and **O. V. Yazyev**.
- the Helium-staff (**J. Völkel**, **D. Klatt**, and **W. Hatje**) for their steady supply with sufficient cryogenic liquids and the staff of the fine-mechanical workshop, who always were willing to help even on short time scales if urgent problems came up.
- last but not least, my **parents** and my entire **family** for the steady support. Special thanks go to my wife **Susanna** for her patience if I was busy with work or needed support in a different way...